INFORMATION TO USERS

This manuscript has been reproduced from the microfilm master. UMI films the text directly from the original or copy submitted. Thus, some thesis and dissertation copies are in typewriter face, while others may be from any type of computer printer.

The quality of this reproduction is dependent upon the quality of the copy submitted. Broken or indistinct print, colored or poor quality illustrations and photographs, print bleedthrough, substandard margins, and improper alignment can adversely affect reproduction.

In the unlikely event that the author did not send UMI a complete manuscript and there are missing pages, these will be noted. Also, if unauthorized copyright material had to be removed, a note will indicate the deletion.

Oversize materials (e.g., maps, drawings, charts) are reproduced by sectioning the original, beginning at the upper left-hand corner and continuing from left to right in equal sections with small overlaps. Each original is also photographed in one exposure and is included in reduced form at the back of the book.

Photographs included in the original manuscript have been reproduced xerographically in this copy. Higher quality 6" x 9" black and white photographic prints are available for any photographs or illustrations appearing in this copy for an additional charge. Contact UMI directly to order.

UMI

A Bell & Howell Information Company
300 North Zeeb Road, Ann Arbor MI 48106-1346 USA
313/761-4700 800/521-0600

Finite element modeling of transient ultrasonic waves in linear viscoelastic media

by

Paul Andrew Stucky

A dissertation submitted to the graduate faculty

in partial fulfillment of the requirements for the degree of

DOCTOR OF PHILOSOPHY

Major: Electrical Engineering (Electromagnetics)

Major Professor: William Lord

Iowa State University

Ames, Iowa

1998

Graduate College
Iowa State University

This is to certify that the Doctoral dissertation of

Paul Andrew Stucky

has met the dissertation requirements of Iowa State University

Signature was redacted for privacy.

Major Professor

Signature was redacted for privacy.

For the Major Program

Signature was redacted for privacy.

For the Graduate College

TABLE OF CONTENTS

LIST OF TABLES

LIST OF FIGURES

ABSTRACT

Linear viscoelasticity offers a minimal framework within which to construct a causal model for wave propagation in absorptive media. Viscoelastic media are often described as media with memory, that is, the present state of stress is dependent on the present strain and the complete time history of strain weighted by time convolution with an appropriate time-dependent stress relaxation modulus. An axisymmetric, displacement-based finite element method for modeling pulsed ultrasonic waves in linear, homogeneous viscoelastic media is developed that does not require storage of the complete time history of displacement at every node. This is accomplished by modeling the stress relaxation moduli as discrete or continuous spectra of decaying exponentials. The viscoelastic finite element method serves as a test bed for studying three inverse methods for recovering time dependent longitudinal moduli from pulsed ultrasonic waves transmitted through a slab of viscoelastic material with properties known *a priori*. Specifically, two existing inverse methods called propagator methods, denoted here as the two-slab method and slab-substitution method, are modeled and compared to show relative advantages and disadvantages of both. Both methods require attenuation and wave speed as a function of frequency derived from transmitted wave data for inversion and recovery of modulus data. Several different variables such as measurement location and source radius are varied to discern those variables that have greatest influence on accuracy of reconstructed moduli. It is found that an increase in source aperture radius causes the greatest improvement in modulus accuracy. Another novel inverse method known as wave splitting is applied to numerical data generated by the finite element test bed. Wave splitting requires a time-dependent transmission kernel for recovery of a viscoelastic modulus rather than frequency-dependent attenuation and wave speed. It is shown that in principle wave splitting can recover the material modulus with data derived from a simulated ultrasonic experiment, but it is not as robust as the other two frequency-domain inverse methods studied. Its main drawback is that transmission kernel data required for inversion must be known for the same thickness of viscoelastic slab implying that pulses with relatively high center frequencies must be propagated through slabs whose thickness is only appropriate for low frequency measurement. Material attenuation quickly reduces

transmitted waves at high frequencies to unacceptably low levels when propagated through thick slabs appropriate for pulses centered at lower frequencies. In general, the finite element method has been utilized as an effective tool for comparing alternative inverse methods.

CHAPTER 1 INTRODUCTION

Overview: Role of Numerical Simulation

Material property measurement is a fundamental area of basic and applied research. Precise and accurate knowledge of material properties has been and continues to be a key to solving important technological challenges. Many examples of technologically important materials exist such as the space shuttle tiles that efficiently dissipate relatively large amounts of heat and allow safe re-entry of the orbiter and graphite-epoxy composite materials that make airplanes and other structures stronger and lighter. Designing new materials requires measurements of material properties and usually some trial and error. Accurate measurement methods can reduce the iteration time in material design by reducing uncertainty in measured properities. Therefore, hand in hand with material property measurement is the study of measurement methods themselves. Active research in measurement methods includes development of practical experimental methods and theoretical development of new measurement methods. A working definition of a measurement method is a complete algorithm that takes measurable experimental data, applies signal processing, and produces an estimate of desired material properties.

An important and often essential mid-step between theory and experiment is a numerical study of new measurement methods. Assuming there exists a numerical model which accurately captures the essential physics of a proposed experimental arrangement, important questions about method feasibility can be posed and insight gained by exercising such a model. With a numerical model one can start from the most ideal and experimentally unrealistic scenario and incrementally impose more realistic conditions. At each step results show what parameters have greater or lesser effect on a measurement method's ability to estimate correctly a material property. In many cases there is more than one way to obtain the same information. A computer model or 'test bed' facilitates comparison of competing methods. From another point of view numerical simulation can indicate what is necessary technologically for a measurement method to succeed.

Measurement of mechanical material properties with ultrasonic waves is one active area for measurement method research and is a central subject of this dissertation. Generally, ultrasonic measurement

methods are inverse methods, that is, input and output are known and information that characterizes the material under test (MUT) is estimated from knowledge of input and output. Specifically, an incident wave is generated by a transducer and a scattered wave is received by a different or the same transducer. Material properties are then estimated by some sort of comparison of a reference wave with a scattered wave. A scattered wave may be reflected from or transmitted through a material under test and a reference wave may be either an incident wave or a wave reflected from or transmitted through a material medium whose properties are well known—a reference material.

A comparison of reference wave with scattered wave usually involves computer signal processing of sampled data. Signal processing algorithms are derived from theory that is assumed to represent accurately essential physics of an experimental arrangement. In the case of ultrasonic wave propagation, basic theory takes the form of a three dimensional, partial differential wave equation with appropriate boundary conditions and initial conditions. This presents an important point, that is, a measurement or inverse method is derived from a 'forward model' of the measurement process. A forward model implies that input, material under test and input/material interaction are known; therefore, an output is predictable. Usually, the more accurate the forward model the better one can assess the feasibility of an inverse method derived from it.

In summary, numerical simulation has an important role to play in modeling new materials as well as new methods to measure their properties. A computer model can serve as test bed where ideas can be tested quickly and cheaply and discarded if they appear unfeasible. Competing ideas can be compared and contrasted as more experimental reality is incorporated into the model.

Dissertation Research

Overview

This dissertation is in part a numerical feasibility study of a relatively new inverse method, wave splitting/invariant embedding (WS), and the comparison of WS with more traditional inverse methods for material property measurement denoted here as 'propagator methods.' These inverse methods are applied to measurement of viscoelastic moduli in linear, homogeneous and isotropic viscoelastic media. Another important part is the development of a finite element test bed for ultrasonic wave propagation in viscoelastic media. The numerical test bed is found to be interesting in its own right for studying ultrasonic wave propagation in linear, absorptive media. The test bed grew out of difficulties in arranging an appropriate experimental set-up for measuring viscoelastic moduli. In retrospect, a test

bed approach is a realistic way to estimate feasibility of these inverse methods from the point of view of time, flexibility and cost.

Original inspiration for this study arose from the relative success of two proof of principle electromagnetic experiments [15, 16]. In these experiments materials were placed inside a coaxial transmission line and certain properties were determined from impulse response functions, that is, time dependent reflection and transmission kernels. Response functions were recovered from measurements of plane waves incident upon, reflected from and transmitted through the MUT. In the first experiment [16] an inhomogeneous permittivity profile was reconstructed as a function of distance along the coax from reflection data. In the second experiment [15] the time dependent susceptibility of a homogenous, dispersive liquid was reconstructed as a function of time from transmission data. Material properties determined in these experiments were considered reasonable compared with previously known material properties measured with other experimental techniques [17]. Thus far no analogous experimental studies have been conducted utilizing ultrasonic waves and wave splitting inverse theory for determining mechanical properties of materials. This point begged the question: "can wave splitting inverse methods be successfully applied to ultrasonic measurement of mechanical properties?" It is this question that has motivated a numerical feasibility study. The feasibility study necessitated development of an appropriate numerical test bed. For comparison propagator inverse methods are studied in parallel as an alternative to wave splitting. Wave splitting is a general inverse method that is applicable to inhomogeneous media, but places relatively stringent requirements on the input data for the inverse algorithm. Propagator methods are relatively robust methods for recovering moduli and they exploit the pulsed nature of ultrasonic waves.

An initial question was whether to study wave splitting for ultrasonic wave propagation in nondispersive inhomogeneous, isotropic elastic media analogous with the experiment in [16] or homogeneous, isotropic viscoelastic media analogous with the experiment in [15]. Several factors influenced the choice of the latter. A major factor was that many technologically relevant materials such as polymeric solids and liquids are well modeled by linear, homogeneous and isotropic viscoelasticity theory; therefore, successful inverse methods may have broader application. A wealth of linear viscoelastic modulus data exists on polymeric materials [13] as compared with inhomogeneous elastic media; therefore, realistic values for material properties are available for input to a test bed. Also, the wave splitting inversion algorithm for viscoelastic moduli is relatively simple as a result of material homogeneity. Another point is that ultrasonic wave propagation in layered, continuously inhomogeneous elastic media results in continuous mode coupling between shear and longitudinal modes, that is, wave propagation

is relatively more complicated and corresponding WS inversion algorithms are more complicated [11]. The main point was to determine a simple test case and study it under controlled conditions that model essential physics of realistic experimental situations and determine feasibility of carrying out an actual experiment.

Research questions

A set of questions are presented that form the core of the numerical study. During investigation of these questions many other questions arose and some of these are illuminated in the text but are not enumerated here. Each question is prefaced to place it in context.

I. **Narrow-band stimuli vs. broad-band moduli**

It is well known that moduli transition from a low frequency or viscous region to a high frequency or elastic region over at least three decades in frequency for simple supercooled liquids [19] and as much as ten or more decades of frequency for some polymers [13]. On the other hand, average ultrasonic measurement equipment may have at most two decades of useful frequency bandwidth [40], therefore, a complete modulus frequency spectrum cannot be measured under a single set of experimental conditions. How can data from several band-limited experiments be combined to yield a transmission kernel suitable for input into existing one-dimensional WS inverse algorithms for viscoelastic longitudinal modulus reconstruction? How does modulus reconstruction with wave splitting compare with modulus reconstruction with propagator methods with respect to accuracy and ease of use when data from several band-limited experiments are combined?

II. **Multi-dimensional waves vs. 1D inverse algorithms**

In practice, ultrasonic waves are generated that are inherently multi-dimensional. In contrast, WS and propagator inverse algorithms are one dimensional. How is modulus reconstruction affected when data from multi-dimensional wave propagation serves as input for one-dimensional inverse algorithms?

III. **Measurable data vs. ideal data**

Data necessary for reconstruction of a viscoelastic modulus with WS is a time-dependent transmission kernel. For frequency-domain propagator methods the necessary quantity for modulus recovery is called a 'propagator.' Propagators are not directly measurable. Measurable data that are closely related to propagators quantities are incident, reflected and transmitted displacements at elastic/viscoelastic or acoustic/viscoelastic interfaces, but these displacements usually cannot

be directly measured either. In most cases, measurable quantities are total mechanical displacements at interfaces, such as an elastic/air interface, after the displacement has propagated away from the viscoelastic slab.

With a numerical test bed one can study effects on modulus reconstruction caused by measurement of displacement at positions that are not ideal. On the other hand, a test bed allows recording displacement at ideal locations and comparing modulus reconstruction with data recorded at ideal and non-ideal locations. Ideal does not imply that recorded displacement is that due to a pure plane wave, but only that the location of measurement is more desirable. How is quality of reconstructed moduli affected by utilizing displacements data measured at relatively non-ideal positions? Can simple techniques be defined to improve reconstruction when displacement recorded at such non-ideal positions are employed?

IV. **Experiment design**

An advantage of a numerical test bed that models essential physics such as finite aperture effects, band-limiting, viscoelasticity, etc., is that a variety of experimental configurations can be investigated in a relatively short amount of time. Insight gained by testing many different scenarios can suggest actual experimental arrangements which may have a greater chance of experimental success. What are 'best case' experimental arrangements for measuring a realistic longitudinal modulus with the inverse methods studied?

These questions represent some of the more important issues pertaining to feasibility of the specific inverse methods studied. These questions motivated development of a finite element model for ultrasonic wave propagation in viscoelastic media. Questions pertinent to test bed development such as choice of relevant models for viscoelastic moduli and modeling acoustic media such as water, etc., are presented in appropriate chapters.

Outline

The finite element method for axisymmetric ultrasonic wave propagation in viscoelastic media is developed in Chapter 2. An existing elastodynamic program is modified to incorporate time dependent bulk and shear moduli. Time domain convolution of nodal displacement with moduli is inherent in the formulation and requires storing time histories of each nodal displacement. Special attention is paid to developing a recursive method for storing nodal displacement histories. With this recursive method only one extra array representing one previous time step is required for storing nodal displacement

histories. Chapter 2 concludes with example calculations.

Details of wave splitting and propagator inverse methods are developed in Chapters 3 and 4, respectively, while Chapters 5 and 6 are results chapters. In Chapter 5 a simulation of a viscoelastic polymer solid in a water bath is presented. This represents a basic experimental arrangement for ultrasonic spectroscopy of solids. The water is an essential coupling medium between a solid under test and an ultrasonic transducer. Reconstruction of a longitudinal modulus with propagator and wave splitting methods is presented. The FEM test bed generates data for the inverse methods. Various physical arrangements are studied to ascertain how certain parameters affect longitudinal modulus reconstruction. In Chapter 6 propagation of ultrasonic waves in viscoelastic materials with multiple relaxation times is presented. An important point to be made in Chapter 6 is that relatively few decaying exponentials with different relaxation times are necessary to approximate a material with a continuous spectrum of relaxations when source spectra are relatively narrow compared with moduli spectra. Conclusions and further work are discussed in Chapter 7.

Contributions

Two main contributions are development of a numerical finite element model for pulsed ultrasonic waves in linear viscoelastic media and a feasibility study of one-dimensional inverse methods for reconstruction of LHI viscoelastic moduli under simulated but realistic experimental conditions. The simulated conditions include, but are not limited to: realistic frequency spectra and functional forms of bulk and shear moduli, finite aperture sources that exhibit non-planar effects, sources with relatively narrow frequency bandwidths and measured data that does not immediately correspond to data required for reconstruction. These conditions have been incorporated into a transient finite element numerical model. The finite element program is a 'numerical experiment' which includes some of the important wave physics that exists in actual ultrasonic experiments. Listed below are a set of more specific contributions. The dissertation:

- demonstrates how realistic models for linear viscoelastic (dispersive) materials are incorporated into finite element modeling of transient wave phenomena;
- shows difficulties encountered when wave splitting methods are employed for modulus reconstruction;
- demonstrates relative robustness and ease of use of propagator methods.

CHAPTER 2 VISCOELASTICITY: THEORY AND MODELING

Introduction

A basic introduction to linear viscoelasticity is given assuming infinitesimal, linear deformation. Several textbook level sources exist that describe linear viscoelasticity of which two, Christensen [8] and Ferry [13], are primary sources. Following the introduction a detailed description of the finite element method for ultrasonic waves is given with its adaptation to linear viscoelasticity. The chapter concludes with several example calculations to demonstrate the finite element model's capabilities and validity.

Linear Viscoelasticity

Linear viscoelastic material properties are time dependent whereas LHI elastic and Newtonian-viscous material properties are constants with respect to time. For comparison, stress/strain relations for LHI elastic [4], viscous [9] (neglecting thermodynamic pressure) and viscoelastic media [8] are, respectively,

$$T_{ij} = \delta_{ij}(K - \frac{2}{3}G)S_{kk} + 2GS_{ij} \tag{2.1}$$

$$T_{ij} = \delta_{ij}(\eta_v - \frac{2}{3}\eta_s)\dot{S}_{kk} + 2\eta_s\dot{S}_{ij} \tag{2.2}$$

$$T_{ij} = \delta_{ij}(K - \frac{2}{3}G) * \dot{S}_{kk} + 2G * \dot{S}_{ij} \tag{2.3}$$

where $i, j, k = 1, 2, 3$ and T_{ij}, S_{ij} and $\dot{S}_{ij}$ represent stress, strain and rate of strain tensors, respectively. Strain dependence on (x, y, z, t) has been suppressed. Strain is related to displacement by

$$S_{ij} = \frac{1}{2}[u_{i,j} + u_{j,i}] \tag{2.4}$$

assuming infinitesimal displacement. Bulk and shear viscosities are represented by η_v and η_s, respectively. The viscoelastic strain/stress relation is [49]

$$S_{ij} = \delta_{ij}(\frac{1}{9}B - \frac{1}{6}J) * \dot{T}_{kk} + \frac{1}{2}J * \dot{T}_{ij}. \tag{2.5}$$

Bulk and shear relaxation moduli, creep compliances and their interrelationships for viscoelasticity are

$$K(t) \equiv \text{bulk relaxation modulus, (Pa).} \tag{2.6}$$

$$G(t) \equiv \text{shear relaxation modulus, (Pa).} \tag{2.7}$$

$$B(t) \equiv \text{bulk compressibility or} \tag{2.8}$$

$$\text{bulk creep compliance, } (\text{Pa})^{-1}. \tag{2.9}$$

$$J(t) \equiv \text{shear creep compliance, } (\text{Pa})^{-1}. \tag{2.10}$$

$$[K * B](t) = tH(t)(s). \tag{2.11}$$

$$[G * J](t) = tH(t)(s). \tag{2.12}$$

$$[f * g](t) = \int_0^t f(t-s)g(s)ds. \tag{2.13}$$

where $H(t)$ is the Heaviside or unit step function. Lamé parameters, $\lambda(t)$ and $\mu(t)$, are related to bulk and shear relaxation moduli by $\mu(t) = G(t)$ and $\lambda(t) = K(t) - \frac{2}{3}G(t)$.

An important consequence of time dependent material properties is the capacity of viscoelastic media to store and dissipate mechanical energy. In contrast, elastic media store energy, but do not dissipate energy and viscous media dissipate energy, but do not store it. Polymers are an example of a broad class of materials that are modeled as linear and nonlinear viscoelastic media with respect to macroscopic mechanical properties [13].

Viscoelastic materials have "fading memory", that is, the present state of stress is dependent on the current strain and all previous-time strain weighted by convolution with time dependent stress relaxation moduli. Fading memory is demonstrated by integrating convolutions in the stress/strain relation, eq. 2.3, by parts which gives

$$\begin{aligned} T_{ij} &= \delta_{ij}(K_g - \frac{2}{3}G_g)S_{kk} + 2G_gS_{ij} \\ &\quad +\delta_{ij}(\dot{K} - \frac{2}{3}\dot{G}) * S_{kk} + 2\dot{G} * S_{ij} \end{aligned} \tag{2.14}$$

where $K_g = K(t=0)$ and $G_g = G(t=0)$ and subscript "g" stands for "glassy" or elastic modulus. At short times ($t = 0^+$) viscoelastic materials respond to applied strain as if they were purely elastic with moduli K_g and G_g and at later times total stress is dependent on present and past strain. Fading memory is achieved if rates of change of stress relaxation moduli are continuously decreasing functions of time [8], that is,

$$\left|\dot{K}\right| \text{ or } \left|\dot{G}\right|_{t=t_2} < \left|\dot{K}\right| \text{ or } \left|\dot{G}\right|_{t=t_1} \quad \text{for} \quad t_2 > t_1 > 0. \tag{2.15}$$

As far as is known measured relaxation moduli have never violated this "fading memory hypothesis."

A single decaying exponential is a simple prototype for relaxation moduli. Assuming exponential decay, moduli satisfying fading memory have the form

$$K(t) = \left[K_e + (K_g - K_e)e^{-t/\tau_K}\right] H(t) \tag{2.16}$$

$$G(t) = \left[G_e + (G_g - G_e)e^{-t/\tau_G}\right] H(t) \tag{2.17}$$

$$M(t) = K(t) + \frac{4}{3}G(t) \tag{2.18}$$

where subscript "e" implies equilibrium or long-time modulus and τ_K and τ_G are not necessarily equal. A new stress relaxation modulus is defined, $M(t)$, hereafter called the longitudinal modulus because it is associated with longitudinal wave propagation. A longitudinal creep compliance, $N(t)$, is defined by

$$[M * N](t) = tH(t). \tag{2.19}$$

For a viscoelastic solid $G_e \geq 0$ and for a liquid $G_e = 0$. The shear creep compliance[1] for a simple exponential type solid and fluid are, respectively,

$$J(t) = \left[\frac{1}{G_e} + (\frac{1}{G_g} - \frac{1}{G_e})e^{-t/\tau_J}\right] H(t) \tag{2.20}$$

$$J(t) = \left[\frac{1}{G_g} + \frac{t}{\eta_G}\right] H(t) \tag{2.21}$$

where $\tau_J = \frac{G_g}{G_e}\tau_G > \tau_G$ is called retardation time and η_G is shear viscosity given by [8]

$$\eta_G = \int_0^\infty G(s)ds = G_g\tau_G. \tag{2.22}$$

Under a constant shear stress a viscoelastic fluid eventually reaches a state of flow that is represented by the term proportional to time, t, in eq. 2.21. From eq. 2.20 it can be shown that there exists a short and long time correspondence between limiting values of modulus and compliance, that is,

$$\lim_{t\to 0+} J(t) = J_g = \frac{1}{G_g} \tag{2.23}$$

$$\lim_{t\to\infty} J(t) = J_e = \frac{1}{G_e}. \tag{2.24}$$

Similar relationships exist between $(K(t), B(t))$ and $(M(t), N(t))$, respectively.

Relaxation moduli in the frequency or Fourier domain can be derived by first taking the Laplace transform of eq. 2.3 and assuming zero initial conditions for strain, $S_{ij}(x, y, z, 0) = 0$. The result is

$$\tilde{T}_{ij} = \delta_{ij}(s\tilde{K} - \frac{2}{3}s\tilde{G})\tilde{S}_{kk} + 2s\tilde{G}\tilde{S}_{ij} \tag{2.25}$$

[1] The creep compliances are easily derived using Laplace transform methods on eq. 2.12.

where the Laplace domain variable, s, is taken with the bulk and shear modulus and "~" implies Laplace transform. The moduli become

$$s\tilde{K}(s) = K_e + [K_g - K_e]\frac{s\tau_K}{1+s\tau_K} \tag{2.26}$$

$$s\tilde{G}(s) = G_e + [G_g - G_e]\frac{s\tau_G}{1+s\tau_G}. \tag{2.27}$$

Upon setting $s = i\omega$ the Fourier domain relaxation or dynamic moduli become

$$\tilde{K}(\omega) = K_e + (K_g - K_e)\left[\frac{(\omega\tau_K)^2 + i\omega\tau_K}{1+(\omega\tau_K)^2}\right] \tag{2.28}$$

$$\tilde{G}(\omega) = G_e + (G_g - G_e)\left[\frac{(\omega\tau_G)^2 + i\omega\tau_G}{1+(\omega\tau_G)^2}\right] \tag{2.29}$$

with $\tilde{K}(\omega) = s\tilde{K}(s)\Big|_{s=i\omega}$ and similarly for $\tilde{G}(\omega)$ ("~" implies frequency domain). For increasing angular frequency storage moduli, $K'(\omega)$ and $G'(\omega)$, approach elastic limits, K_g and (G_g), respectively, whereas loss moduli, $K''(\omega)$ and $G''(\omega)$, approach zero for both high and low frequencies.

Stress relaxation moduli with simple exponential decay are qualitative models of real viscoelastic materials. Most real materials cannot be modeled accurately by moduli with a single characteristic relaxation time. In fact, most materials have a broad, continuous spectrum of relaxation times [13]. For example, polymers consist of molecular chains built of basic monomer units with or without sidechains or branches [13]. Molecular chains have length scales that range from intermolecular scales to the order of a complete polymer chain. Rotation, vibration and translation exist on all length scales. Associated with these motions are relaxation processes with time scales that can range over many orders of magnitude. Relaxation occurring at many different time scales is modeled by continuous distributions of relaxation times called relaxation spectrums. For example, the shear modulus can be written

$$G(t) = [G_e + (G_g - G_e)g(t)]\,H(t) \tag{2.30}$$

$$\tilde{G}(\omega) = G_e + (G_g - G_e)\tilde{g}(\omega) \tag{2.31}$$

with

$$g(t) = \int_0^\infty h_G(\tau)e^{-t/\tau}d\tau \tag{2.32}$$

$$\tilde{g}(\omega) = \int_0^\infty h_G(\tau)\frac{i\omega\tau}{1+i\omega\tau}d\tau \tag{2.33}$$

where $g(t)$ is called the shear relaxation function and $h_G(\tau)$ is the shear relaxation spectrum or spectral density. The spectrum is normalized such that

$$1 = \int_0^\infty h_G(\tau)d\tau. \tag{2.34}$$

Note that eq. 2.32 is an integral equation of the first kind, therefore, determining $h_G(\tau)$ is an ill-posed problem and any relaxation spectrum estimated from experiment is not unique. A more common form of eq. 2.32 is

$$g(t) = \ln(10)\int_{-\infty}^{\infty} \tau h_G(\tau) e^{-t/\tau} d(\log \tau) \tag{2.35}$$

where "ln" implies natural logarithm and "log" implies logarithm of base ten. Clearly, this integral must be truncated at short and long relaxation times.

There are two functions that are often used to fit measured stress relaxation data. They are known as the Kohlrausch-Williams-Watts (KWW) or "stretched exponential" function (time domain) [53] and the Havriliak-Negami (HN) function (frequency domain) [21]. They are, respectively,

$$\theta_{kww}(t) = e^{-(t/\tau_{kww})^{\beta}} H(t) \qquad 0 < \beta \leq 1 \tag{2.36}$$

$$\tilde{\theta}_{hn}(\omega) = 1 - \frac{1}{[1 + (i\omega\tau_{hn})^{\alpha}]^{\gamma}} \qquad 0 < \alpha, \gamma \leq 1 \tag{2.37}$$

where, for example, $g(t) = \theta_{kww}(t)$ or $\tilde{g}(\omega) = \tilde{\theta}_{hn}(\omega)$. These functions do not form a Fourier transform pair, but they do have similar behavior in time and frequency [1, 2]. Obviously, when $\alpha, \beta, \gamma = 1$ both functions reduce to single characteristic relaxation time model. When $0 < \alpha, \beta, \gamma < 1$ these functions can be described by continuous spectrums of relaxation times. The spectral densities for these relaxation functions are, respectively,

$$\tau h_{kww}(\tau) = -\frac{1}{\pi x}\sum_{k=0}^{\infty} \frac{(-1)^k}{k!} \sin(\pi\beta k)\Gamma(\beta k + 1)(x)^{\beta k + 1} \tag{2.38}$$

$$x = \frac{\tau}{\tau_{kww}} \tag{2.39}$$

$$\tau h_{hn}(\tau) = \frac{1}{\pi} \frac{x^{\gamma\alpha}\sin(\gamma\theta)}{[x^{2\alpha} + 2x^{\alpha}\cos(\alpha\pi) + 1]^{\gamma/2}} \tag{2.40}$$

$$\theta = \tan^{-1}\left|\frac{\sin(\alpha\pi)}{x^{\alpha} + \cos(\alpha\pi)}\right| \tag{2.41}$$

$$x = \tau/\tau_{hn}. \tag{2.42}$$

For $\beta = 0.5$ the spectral density reduces to

$$\tau h_{kww}(\tau)|_{\beta=0.5} = \sqrt{\frac{\tau}{4\pi\tau_{kww}}} e^{-\tau/4\tau_{kww}}. \tag{2.43}$$

Alvarez [1] has shown that for $0.10 \leq \beta \leq 0.95$ there exist α, γ and $\tau_{hn}/\tau_{kww} \geq 1$ such that the resulting HN stress relaxation function is a "best fit" to the KWW stress relaxation function. In other words, for a given KWW function defined by β there is a HN function defined by α and γ with corresponding $\tau_{hn} \geq \tau_{kww}$ that best approximates the KWW function. In particular, for $\beta = 0.5$ the

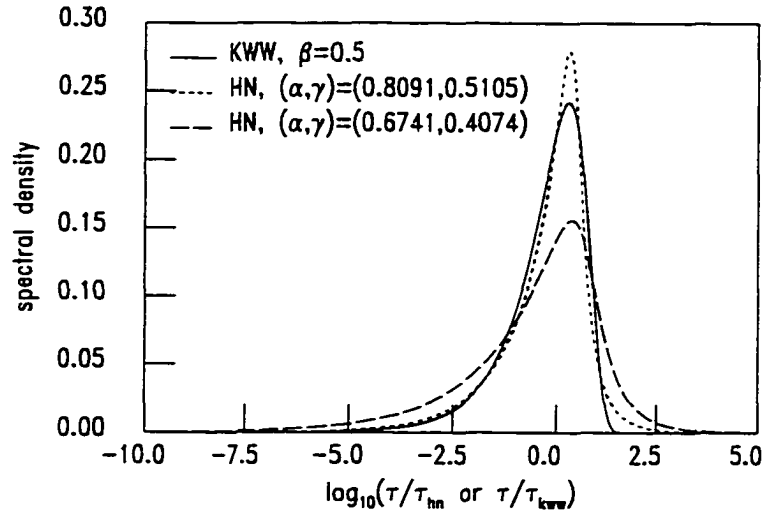

Figure 2.1 Spectral density functions for corresponding KWW relaxation functions. $\beta = 0.5$ and $\beta = 0.35$ (not shown), and their approximate HN functions: $(\alpha, \gamma) = (0.8091, 0.5105)$, $\tau_{hn}/\tau_{kww} = 2.9174$ and $(\alpha, \gamma) = (0.6741, 0.4074)$, $\tau_{hn}/\tau_{kww} = 5.3827$, respectively [1]

best fit parameters are $(\alpha, \gamma) = (0.8091, 0.5105)$ with $\tau_{hn}/\tau_{kww} = 2.9174$. The spectral densities are superimposed in Fig. 2.1 along with another pair, $(\alpha, \gamma) = (0.6741, 0.4074)$, $\tau_{hn}/\tau_{kww} = 5.3827$, that approximates the KWW relaxation function with $\beta = 0.35$. Figure 2.2 shows relaxation functions, $g(t)$ and $\hat{g}(\omega)$, derived from spectral densities shown in Fig. 2.1. The relaxation function for a single exponential is plotted for comparison.

Wave Propagation in Viscoelastic Media

For comparison the wave equations for displacement in LHI elastic and viscoelastic media are, respectively,

$$M\nabla\nabla\cdot\mathbf{u} - G\nabla\times\nabla\times\mathbf{u} = \rho\ddot{\mathbf{u}} \tag{2.44}$$

$$M*\nabla\nabla\cdot\mathbf{u} - G*\nabla\times\nabla\times\mathbf{u} = \rho\ddot{\mathbf{u}} \tag{2.45}$$

or after integrating eq. 2.45 by parts gives

$$\left[M_g + \dot{M}*\right]\nabla\nabla\cdot\mathbf{u} - \left[G_g + \dot{G}*\right]\nabla\times\nabla\times\mathbf{u} = \rho\ddot{\mathbf{u}}. \tag{2.46}$$

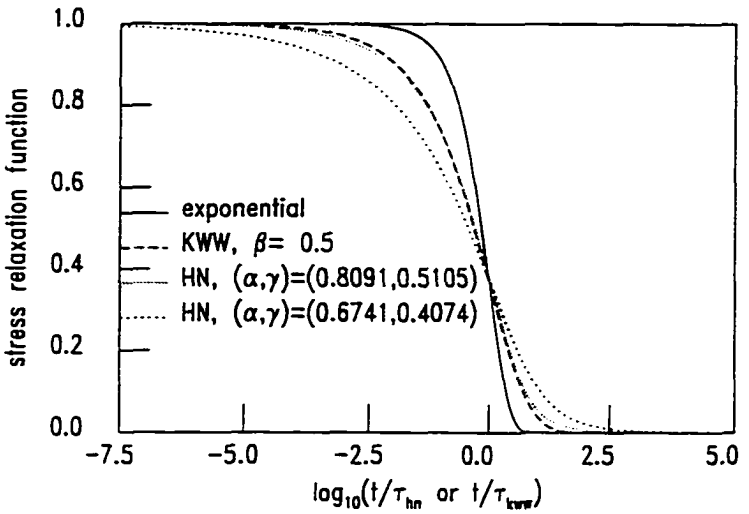

(a)

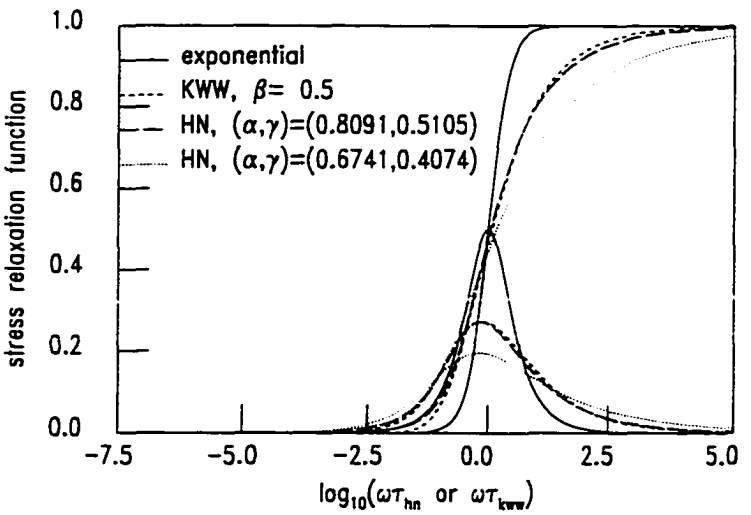

(b)

Figure 2.2 Stress relaxation functions ($g(t)$, $k(t)$ or $m(t)$), corresponding to spectral density functions in Fig. 2.1, compared with a simple exponential relaxation: time domain. (a); frequency domain. (b)

Total displacement, $\mathbf{u}$, can be subdivided into two displacements:

$$\mathbf{u} = \mathbf{u}_l + \mathbf{u}_s. \tag{2.47}$$

A longitudinal displacement, $\mathbf{u}_l$, propagates with wave speed $c_{lg} = \sqrt{M_g/\rho}$ and has the property $\nabla \times \mathbf{u}_l = 0$. Similarly, a shear displacement, $\mathbf{u}_s$, propagates with wave speed $c_{sg} = \sqrt{G_g/\rho}$ and has the property $\nabla \cdot \mathbf{u}_s = 0$.

Assuming total displacement is independent of (x, y) and varies only in (z, t) (plane wave) eq. 2.45 decouples into two one-dimensional wave equations

$$M * \partial_z^2 u_l = \rho \partial_t^2 u_l \tag{2.48}$$

$$G * \partial_z^2 u_s = \rho \partial_t^2 u_s. \tag{2.49}$$

The polarization of longitudinal displacement, u_l (u_z), is in the direction of propagation, z, and the polarization of shear displacement, u_s (u_r), is transverse to the direction of propagation, r. Assuming zero initial conditions, Laplace domain homogeneous solutions to these equations have the form

$$\tilde{u}_{l,s}(z, s) = F_{l,s}(s) e^{-sz/\tilde{c}_{l,s}} + B_{l,s}(s) e^{+sz/\tilde{c}_{l,s}} \tag{2.50}$$

with

$$\tilde{c}_l(s) = \sqrt{\frac{s\tilde{M}(s)}{\rho}} \tag{2.51}$$

$$\tilde{c}_s(s) = \sqrt{\frac{s\tilde{G}(s)}{\rho}}. \tag{2.52}$$

Letting $s = i\omega$ gives a frequency-dependent complex wave speed.

The real and imaginary parts of inverse complex wave speed equate to inverse real wave speed and real attenuation, respectively. Specifically,

$$\frac{1}{\tilde{c}_l(\omega)} = \frac{1}{c_l(\omega)} - i\frac{\alpha_l(\omega)}{\omega} \tag{2.53}$$

$$= \sqrt{\frac{\rho}{M' + iM''}} \tag{2.54}$$

$$= \sqrt{\frac{\rho}{|\tilde{M}|}} \left[\sqrt{\frac{|\tilde{M}| + M'}{2|\tilde{M}|}} - i\sqrt{\frac{|\tilde{M}| - M'}{2|\tilde{M}|}} \right] \tag{2.55}$$

$$= \sqrt{\frac{\rho}{|\tilde{M}|}} \left[\cos\left(\frac{\theta}{2}\right) - i \sin\left(\frac{\theta}{2}\right) \right] \tag{2.56}$$

$$\Longrightarrow c_l(\omega) = \sqrt{\frac{|\tilde{M}|}{\rho}} \sec\left(\frac{\theta}{2}\right) \tag{2.57}$$

$$\Longrightarrow \alpha_l(\omega) = \omega\sqrt{\frac{\rho}{|\tilde{M}|}} \sin\left(\frac{\theta}{2}\right) \tag{2.58}$$

where $\tan(\theta) = M''/M'$ and $|M| = \sqrt{M'^2 + M''^2}$ [49]. Replacing $M(\omega)$ with $G(\omega)$ and subscript "l" with "s" gives wave speed and attenuation for shear waves. It is important to note that no specific form of frequency (time) dependence (e.g., single exponential) was assumed in deriving wave speed and attenuation: they are general for LHI media. The real and imaginary components of the complex modulus, $M(\omega)$, in terms of the wave speed and attenuation are given by the following:

$$M'(\omega) = K' + \frac{4}{3}G' = \rho c^2 \left[\frac{1 - \beta^2}{[1 + \beta^2]^2}\right] \tag{2.59}$$

$$M''(\omega) = K'' + \frac{4}{3}G'' = \rho c^2 \left[\frac{2\beta}{[1 + \beta^2]^2}\right] \tag{2.60}$$

$$\beta(\omega) = \frac{\alpha(\omega)c(\omega)}{\omega} \tag{2.61}$$

These relationships are important for propagator inverse methods because they are a link between measurables, wave speed and attenuation, and modulus.

Time dependent material properties naturally give rise to frequency dependent wave speed and attenuation, hence dispersion. As a sound pulse propagates dispersion causes the pulse to undergo amplitude decay and temporal lengthening or spreading. By defining material properties directly in the time domain causality is easily and clearly enforced.

Viscoelastic Finite Element Method

The finite element method (FEM) is well established as a general numerical method for solving partial differential equations with prescribed boundary and initial conditions [22, 24]. No exhaustive literature review of finite elements for transient wave propagation is given. Instead, specific reference is made to work [34, 56, 60] that is the genesis of the computer program adapted and used for modeling LHI viscoelastic media. The transient finite element method provides a useful "test bed" for studying various aspects of ultrasonic wave propagation such as non-plane wave effects under contolled conditions.

Functional minimization

Previous elastic wave propagation studies employed energy functional minimization as an indirect method for solving the underlying displacement wave equation for isotropic [7, 33, 35, 57, 58, 59] and anisotropic [62] materials. If a functional exists whose Euler equations are the governing wave equation then minimizing the functional is equivalent to solving the wave equation directly.

For linear viscoelasticity Oden and Reddy [37] have presented a general energy functional for spatially dependent material properties. Their general functional simplifies to the following for homogeneous and

isotropic materials [7]:

$$\begin{aligned} E(\mathbf{u},t) &= \text{potential energy} + \text{kinetic energy} \\ &\quad -\text{work done by external forces} \\ &= P(\mathbf{u},t) + K(\mathbf{u},t) - W(\mathbf{u},t) \qquad (2.62) \\ &= \frac{1}{2}[S_{ij}, T_{ij}]_\Omega + \frac{\rho}{2}[\dot{u}_i, \dot{u}_i]_\Omega - [T_i^s, u_i]_{\partial\Omega} \qquad (2.63) \end{aligned}$$

where

$$[f,g]_\Omega \equiv \int_\Omega \int_0^t f(\mathbf{x}, t-\tau) g(\mathbf{x},\tau) d\tau dV \qquad (2.64)$$

$$[f,g]_{\partial\Omega} \equiv \int_{\partial\Omega} \int_0^t f(\mathbf{x}, t-\tau) g(\mathbf{x},\tau) d\tau dS. \qquad (2.65)$$

and $T_i^s(r,z,t)$ represents externally applied traction forces (Neumann boundary conditions) on the surface of the solution domain, $\partial\Omega$. It has been shown that minimization of this functional ($\delta E(\mathbf{u},t) = 0$) with respect to displacement, $\mathbf{u}$, recovers the viscoelastic wave equation, eq. 2.45 [37].

The finite element matrix equation for axisymmetric waves in viscoelastic media is developed by first writing stress, strain and displacement relations in matrix form [62]:

$$\begin{bmatrix} S_{rr} \\ S_{zz} \\ 2S_{rz} \\ S_{\phi\phi} \end{bmatrix} = \begin{bmatrix} \partial_r & 0 \\ 0 & \partial_z \\ \partial_z & \partial_r \\ r^{-1} & 0 \end{bmatrix} \begin{bmatrix} u_r \\ u_z \end{bmatrix} \qquad (2.66)$$

$$\begin{bmatrix} T_{rr} \\ T_{zz} \\ T_{rz} \\ T_{\phi\phi} \end{bmatrix} = \begin{bmatrix} K+\frac{4}{3}G & K-\frac{2}{3}G & 0 & K-\frac{2}{3}G \\ K-\frac{2}{3}G & K+\frac{4}{3}G & 0 & K-\frac{2}{3}G \\ 0 & 0 & G & 0 \\ K-\frac{2}{3}G & K-\frac{2}{3}G & 0 & K+\frac{4}{3}G \end{bmatrix} * \begin{bmatrix} \dot{S}_{rr} \\ \dot{S}_{zz} \\ 2\dot{S}_{rz} \\ \dot{S}_{\phi\phi} \end{bmatrix} \qquad (2.67)$$

or

$$\underline{S} = \underline{A}\,\underline{u} \qquad (2.68)$$

$$\underline{T} = \underline{C} * \underline{\dot{S}}. \qquad (2.69)$$

These relations are true for any element in Ω; therefore, consider a single element with solution region Ω^e and boundary $\partial\Omega^e$. Radial and axial displacements at any point within the eth element are approximated by a four-node quadrilateral finite element.

$$u_r^e(\eta,\xi,t) = \sum_{i=1}^{4} N_i(\eta,\xi) U_{ri}^e(t) = \underline{N}_s \underline{U}_r^e \qquad (2.70)$$

$$u_z^e(\eta,\xi,t) = \sum_{i=1}^{4} N_i(\eta,\xi)U_{zi}^e(t) = \underline{N}_s\underline{U}_z^e \tag{2.71}$$

with

$$\underline{N}_s = [N_1, N_2, N_3, N_4] \tag{2.72}$$

$$\underline{U}_r^e = [U_{r1}^e, U_{r2}^e, U_{r3}^e, U_{r4}^e]^T \tag{2.73}$$

$$\underline{U}_z^e = [U_{z1}^e, U_{z2}^e, U_{z3}^e, U_{z4}^e]^T. \tag{2.74}$$

In matrix form these relations are written

$$\begin{bmatrix} u_r^e \\ u_z^e \end{bmatrix} = \begin{bmatrix} \underline{N}_s & 0 \\ 0 & \underline{N}_s \end{bmatrix} \begin{bmatrix} \underline{U}_r^e \\ \underline{U}_z^e \end{bmatrix} \tag{2.75}$$

or

$$\underline{u}^e = \underline{N}\,\underline{U}^e \tag{2.76}$$

where (U_{r1}^e, U_{z1}^e) are the time dependent displacements at the quadrilateral vertices, (r_i^e, z_i^e), and $N_i(\eta,\xi)$ are bilinear shape functions:

$$N_1(\eta,\xi) = \frac{1}{4}(1-\eta)(1-\xi), \tag{2.77}$$

$$N_2(\eta,\xi) = \frac{1}{4}(1-\eta)(1+\xi), \tag{2.78}$$

$$N_3(\eta,\xi) = \frac{1}{4}(1+\eta)(1+\xi), \tag{2.79}$$

$$N_4(\eta,\xi) = \frac{1}{4}(1+\eta)(1-\xi). \tag{2.80}$$

with local or "natural" coordinates $-1 \le \eta,\xi \le 1$. The coordinates, (r^e, z^e), of a point inside of an element in terms of local coordinates and the global vertex coordinates, (r_i^e, z_i^e), are, respectively,

$$r^e(\eta,\xi) = \sum_{i=1}^{4} N_i(\eta,\xi)r_i^e = \underline{N}_s\,\underline{r}_v^e \tag{2.81}$$

$$z^e(\eta,\xi) = \sum_{i=1}^{4} N_i(\eta,\xi)z_i^e = \underline{N}_s\,\underline{z}_v^e \tag{2.82}$$

or in matrix form

$$\begin{bmatrix} r^e \\ z^e \end{bmatrix} = \begin{bmatrix} \underline{N}_s & 0 \\ 0 & \underline{N}_s \end{bmatrix} \begin{bmatrix} \underline{r}_v^e \\ \underline{z}_v^e \end{bmatrix} \tag{2.83}$$

$$\Longrightarrow \underline{x}^e = \underline{N}\,\underline{x}_v^e \tag{2.84}$$

(subscript "v" implies quadrilateral vertex point).

With these substitutions and $\underline{B}^e \equiv \underline{A}^e\ \underline{N}$, eq. 2.63 reduces to

$$E^e(\mathbf{u},t) = \frac{1}{2}\left[(\underline{B}^e\ \underline{U}^e)^T.\underline{C}^e * \underline{B}^e\ \underline{U}^e\right]_{\Omega^e} + \frac{\rho^e}{2}\left[(\underline{N}\ \dot{\underline{U}}^e)^T.\underline{N}\ \dot{\underline{U}}^e\right]_{\Omega^e} + \left[(\underline{T}^{se})^T.\underline{N}\ \underline{U}\right]_{\partial\Omega^e} \tag{2.85}$$

and the variation of $E^e(\mathbf{u},t)$ gives

$$\begin{aligned}
\delta E^e(\mathbf{u},t) &= 0 \\
&= \frac{1}{2}\left[(\underline{B}^e\ \delta\underline{U}^e)^T.\underline{C}^e * \underline{B}^e\ \underline{U}^e\right]_{\Omega^e} + \frac{1}{2}\left[(\underline{B}^e\ \underline{U}^e)^T.\underline{C}^e * \underline{B}^e\ \delta\underline{U}^e\right]_{\Omega^e} \\
&\quad + \frac{\rho^e}{2}\left[(\underline{N}\ \delta\dot{\underline{U}}^e)^T.\underline{N}\ \dot{\underline{U}}^e\right]_{\Omega^e} + \frac{\rho^e}{2}\left[(\underline{N}\ \dot{\underline{U}}^e)^T.\underline{N}\delta\dot{\underline{U}}^e\right]_{\Omega^e} \\
&\quad - \left[(\underline{T}^{se})^T.\underline{N}\ \delta\underline{U}^e\right]_{\partial\Omega^e} \\
&= \left[(\delta\underline{U}^e)^T(\underline{B}^e)^T.\underline{C}^e * \underline{B}^e\ \underline{U}^e\right]_{\Omega^e} + \rho^e\left[(\delta\dot{\underline{U}}^e)^T\ \underline{N}^T.\underline{N}\ \ddot{\underline{U}}^e\right]_{\Omega^e} \\
&\quad - \left[(\delta\underline{U}^e)^T\underline{N}^T.\underline{T}^{se}\right]_{\partial\Omega^e}.
\end{aligned} \tag{2.86}$$

Assuming $(\delta\underline{U}^e)^T$ is arbitrary the matrix equation for a single finite element follows

$$\underline{M}^e\ \ddot{\underline{U}}^e + \underline{K}^e * \underline{U}^e = \underline{R}^e \tag{2.87}$$

with initial conditions

$$\underline{U}_0^e = \underline{U}^e(t=0) \tag{2.88}$$

$$\dot{\underline{U}}_0^e = \dot{\underline{U}}^e(t=0). \tag{2.89}$$

Integrating by parts gives

$$\underline{M}^e\ \ddot{\underline{U}}^e + \underline{K}_d^e\ \dot{\underline{U}}^e + \underline{K}^e * \underline{U}^e = \underline{R}^e \tag{2.90}$$

that represents a set of nearest-neighbor coupled mass points connected by springs with damping. The mass, stiffness and surface traction matrices are, respectively,

$$\underline{M}^e = 2\pi\rho^e \int_{\Omega^e} \underline{N}^T\underline{N}\ r^e(\eta,\xi)J\,d\eta d\xi \tag{2.91}$$

$$\underline{K}^e = 2\pi \int_{\Omega^e} (\underline{B}^e)^T\underline{C}^e\ \underline{B}^e\ r^e(\eta,\xi)J\,d\eta d\xi \tag{2.92}$$

$$\underline{R}^e = \int_{\partial\Omega^e} \underline{N}^T\underline{T}^{se}\,dS \tag{2.93}$$

and integration over o is represented by 2π. Integration of the individual matrix elements is usually accomplished using a two dimensional Gauss quadrature [22]. The Jacobian, J, maps integration over infinitesimal area, $drdz$, to infinitesimal area $d\eta d\xi$:

$$J = \begin{vmatrix} \partial_\eta r^e & \partial_\xi r^e \\ \partial_\eta z^e & \partial_\xi z^e \end{vmatrix} = \partial_\eta r^e \partial_\xi z^e - \partial_\eta z^e \partial_\xi r^e. \tag{2.94}$$

Elemental mass, stiffness and surface traction are assembled to form global matrices. The resultant global matrix equation has the same form as the elemental equation, eq. 2.90, except superscript "e" is dropped.

Time dependent stiffness matrix

If the term $\underline{\dot{K}}^e * \underline{U}^e$ in eq. 2.90 is neglected, the elemental (global) matrix equation for elastic waves is recovered. Assuming bulk and shear relaxation moduli have different time dependence, $\underline{\dot{C}}^e$ is separated into two matrices such that $\dot{k}(t)$ and $\dot{g}(t)$ are factored out:

$$\underline{\dot{C}}^e = \begin{bmatrix} 1 & 1 & 0 & 1 \\ 1 & 1 & 0 & 1 \\ 0 & 0 & 0 & 0 \\ 1 & 1 & 0 & 1 \end{bmatrix} \Delta K \dot{k}(t) + \begin{bmatrix} \frac{4}{3} & -\frac{2}{3} & 0 & -\frac{2}{3} \\ -\frac{2}{3} & \frac{4}{3} & 0 & -\frac{2}{3} \\ 0 & 0 & 1 & 0 \\ -\frac{2}{3} & -\frac{2}{3} & 0 & \frac{4}{3} \end{bmatrix} \Delta G \dot{g}(t) \tag{2.95}$$

$$= \underline{C}^e_K \dot{k}(t) + \underline{C}^e_G \dot{g}(t) \tag{2.96}$$

with $\Delta K = K_y - K_e$ and $\Delta G = G_y - G_e$. The time dependent portion of the stiffness becomes

$$\underline{\dot{K}}^e = \left[2\pi \int_{\Omega^e} (\underline{B}^e)^T \underline{C}^e_K \underline{B}^e r^e(\eta, \xi) J d\eta d\xi\right] \dot{k}(t) + \left[2\pi \int_{\Omega^e} (\underline{B}^e)^T \underline{C}^e_G \underline{B}^e r^e(\eta, \xi) J d\eta d\xi\right] \dot{g}(t) \tag{2.97}$$

$$= \underline{K}^e_K \dot{k}(t) + \underline{K}^e_G \dot{g}(t). \tag{2.98}$$

therefore,

$$\underline{\dot{K}}^e * \underline{U}^e = \underline{K}^e_K \left[\dot{k} * \underline{U}^e\right](t) + \underline{K}^e_G \left[\dot{g} * \underline{U}^e\right](t) \tag{2.99}$$

or

$$\underline{\dot{K}}^e * \underline{U}^e = (\underline{K}^e_K + \underline{K}^e_G) \left[\dot{f} * \underline{U}^e\right](t) \tag{2.100}$$

if $k(t) = g(t) \equiv f(t)$, that is, time dependence of shear and bulk relaxation is the same.

The term $\left[\dot{f} * \underline{U}^e\right](t)$ implies $\dot{f}(t)$ is convolved with each member of the column matrix $\underline{U}^e(t)$, that is, the total radial and axial displacement components at each node point. Convolution requires knowledge of the complete time history of the nodal displacements, (U^e_{r1}, U^e_{z1}), and relaxation moduli time functions, $k(t)$ and $g(t)$. Such a requirement implies storing two complete displacement time histories for every node in the finite element domain Ω. Clearly this procedure will quickly consume available computer memory limiting the size of the physical domain that can be modeled as well as the length of computation time of the solution.

Fortunately, with moduli approximated by a spectrum of decaying exponentials, it has been shown that only data from the previous one or two time steps need be retained [27, 36, 47]. Assume $k(t) = y(t) \equiv f(t)$ and

$$f(t) = \int_{-\infty}^{\infty} h(\tau) e^{-t/\tau} d(\log \tau) \tag{2.101}$$

$$\approx \int_{-a}^{b} h(\tau) e^{-t/\tau} d(\log \tau) \tag{2.102}$$

$$h(\tau) = \ln(10) \tau h(\tau) \tag{2.103}$$

where $\tau_{min} = 10^{-a}$ and $\tau_{max} = 10^{b}$ and

$$1 = \int_{-a}^{b} h(\tau) d(\log \tau). \tag{2.104}$$

The convolution term is integrated numerically assuming individual nodal displacements, represented by $u(t)$, are piecewise continuous in time:

$$u(t) \approx u_k + \left\{ \frac{t - k\Delta t}{\Delta t} \right\} [u_{k+1} - u_k] \tag{2.105}$$

$$\text{for } k\Delta t \le t \le (k+1)\Delta t.$$

$$k = 0, 1, 2, \ldots, n-1$$

$$t_{max} = n\Delta t$$

then

$$\int_0^t \dot{f}(s) u(t-s) ds \approx \sum_{k=0}^{n-1} \int_{k\Delta t}^{(k+1)\Delta t} \dot{f}(s) \left[u_{n-k} + \left\{ \frac{s - k\Delta t}{\Delta t} \right\} [u_{n-k-1} - u_{n-k}] \right] ds. \tag{2.106}$$

After substituting eq. 2.102 and integrating with respect to s, eq. 2.106 reduces to

$$\left[\dot{f} * u \right](t) \approx \sum_{k=0}^{n-1} \int_{-a}^{b} [a(\tau) u_{n-k} + b(\tau) u_{n-k-1}] e^{-k\Delta t/\tau} d(\log \tau) \tag{2.107}$$

$$a(\tau) = -h(\tau) \left[1 + \frac{\tau}{\Delta t} \left(e^{-\Delta t/\tau} - 1 \right) \right] \tag{2.108}$$

$$b(\tau) = h(\tau) \left[1 + \left(1 + \frac{\tau}{\Delta t} \right) \left(e^{-\Delta t/\tau} - 1 \right) \right]. \tag{2.109}$$

Now approximating integrals over $\log \tau$ by trapezoidal rule and interchanging the summations gives

$$\left[\dot{f} * u \right](t) \approx \sum_{i=0}^{m} \left\{ \sum_{k=0}^{n-1} \left[a_i^t u_{n-k} + b_i^t u_{n-k-1} \right] e^{-k\Delta t/\tau_i} \right\} \tag{2.110}$$

where

$$\int_{-a}^{b} a(\tau)e^{-k\Delta t/\tau}d(\log\tau) \approx \sum_{i=0}^{m} a_i^t e^{-k\Delta t/\tau_i} \tag{2.111}$$

$$\int_{-a}^{b} b(\tau)e^{-k\Delta t/\tau}d(\log\tau) \approx \sum_{i=0}^{m} b_i^t e^{-k\Delta t/\tau_i} \tag{2.112}$$

$$a_i^t,\ b_i^t = \delta_i^{trap}a(\tau_i),\ \delta_i^{trap}b(\tau_i) \tag{2.113}$$

$$\delta_i^{trap} \equiv \Delta(\log\tau)\left[1 - \frac{1}{2}(\delta_{i0} + \delta_{im})\right]. \tag{2.114}$$

If the relaxation spectrum, $h(\tau)$, is assumed to be a finite sum of exponentials, that is,

$$h(\tau) = \sum_{i=0}^{m} w_i\delta(\tau - \tau_i) \tag{2.115}$$

$$1 = \sum_{i=0}^{m} w_i \tag{2.116}$$

then

$$\int_{-\infty}^{\infty} a(\tau)e^{-k\Delta t/\tau}d(\log\tau) = \sum_{i=0}^{m} a_i e^{-k\Delta t/\tau_i} \tag{2.117}$$

$$\int_{-\infty}^{\infty} b(\tau)e^{-k\Delta t/\tau}d(\log\tau) = \sum_{i=0}^{m} b_i e^{-k\Delta t/\tau_i} \tag{2.118}$$

$$a_i,\ b_i = a(\tau_i),\ b(\tau_i) \tag{2.119}$$

and

$$\left[f * u\right](t) \approx \sum_{i=0}^{m}\left\{\sum_{k=0}^{n-1}\left[a_i u_{n-k} + b_i u_{n-k-1}\right]e^{-k\Delta t/\tau_i}\right\}. \tag{2.120}$$

At time-step n define

$$I_{ni} = \sum_{k=0}^{n-1}\left[a_i u_{n-k} + b_i u_{n-k-1}\right]e^{-k\Delta t/\tau_i} \tag{2.121}$$

where $i = 0, 1, 2, \ldots, m$. It follows that

$$\begin{aligned} I_{0i} &= 0 \\ I_{1i} &= \left[a_i u_1 + b_i u_0\right] + I_{0i}e^{-\Delta t/\tau_i} \\ I_{2i} &= \left[a_i u_2 + b_i u_1\right] + I_{1i}e^{-\Delta t/\tau_i} \\ &\vdots \\ I_{ni} &= \left[a_i u_n + b_i u_{n-1}\right] + I_{n-1i}e^{-\Delta t/\tau_i} \end{aligned} \tag{2.122}$$

or

$$I_{ni} = \left[a_i^t u_n + b_i^t u_{n-1}\right] + I_{n-1i}e^{-\Delta t/\tau_i} \tag{2.123}$$

if $h(\tau)$ is a continuous distribution. Letting $u(t) \rightarrow \underline{U}^e$ and $I_n \rightarrow \underline{I}_n^e$ gives

$$\underline{I}_{ni}^e = \left[a_i^t \underline{U}_n^e + b_i^t \underline{U}_{n-1}^e\right] + \underline{I}_{n-1i}^e e^{-\Delta t/\tau_i} \tag{2.124}$$

If $h_K(\tau) \neq h_G(\tau)$ then $k(t) \neq g(t)$, therefore, define $\underline{I}_{ni}^{Ke}$ and $\underline{I}_{ni}^{Ge}$:

$$\underline{I}_{ni}^{Ke} = \left[a_i^{Kt} \underline{U}_n^e + b_i^{Kt} \underline{U}_{n-1}^e\right] + \underline{I}_{n-1i}^{Ke} e^{-\Delta t/\tau_i} \tag{2.125}$$

$$i = 0, 1, 2, \ldots, m_K \tag{2.126}$$

$$\underline{I}_{ni}^{Ge} = \left[a_i^{Gt} \underline{U}_n^e + b_i^{Gt} \underline{U}_{n-1}^e\right] + \underline{I}_{n-1i}^{Ge} e^{-\Delta t/\tau_i} \tag{2.127}$$

$$i = 0, 1, 2, \ldots, m_G \tag{2.128}$$

where m_K is not necessarily equal to m_G. This is the desired recursion result that only requires storing and updating the one-dimensional (global) matrix $\underline{I}_{n-1}$. Each element of the "recursion matrix" is a single number corresponding to the accumulated time history of every nodal displacement, u_r and u_z, convolved with the time dependent moduli that exist at that spatial node point. This recursion result allows the total convolved time history of displacement at each node point to be written in the following manner:

$$\underline{I}_n^{Ke} = \left\{\sum_{i=0}^{m_K} a_i^{Kt}\right\} \underline{U}_n^e + \left\{\sum_{i=0}^{m_K} b_i^{Kt}\right\} \underline{U}_{n-1}^e + \sum_{i=0}^{m_K} \underline{I}_{n-1i}^{Ke} e^{-\Delta t/\tau_i} \tag{2.129}$$

$$\underline{I}_n^{Ge} = \left\{\sum_{i=0}^{m_G} a_i^{Gt}\right\} \underline{U}_n^e + \left\{\sum_{i=0}^{m_G} b_i^{Gt}\right\} \underline{U}_{n-1}^e + \sum_{i=0}^{m_G} \underline{I}_{n-1i}^{Ge} e^{-\Delta t/\tau_i} \tag{2.130}$$

$$\underline{I}_n^{Ke} + \underline{I}_n^{Ge} \approx \left[\underline{k} * \underline{U}_n^e\right] + \left[\underline{g} * \underline{U}_n^e\right] \tag{2.131}$$

Global FEM matrix equation: discrete time

The global system matrix, eq. 2.90 (denoted by dropping superscript "e"), is discretized in time using a central difference scheme for $\ddot{\underline{U}}$.

$$\ddot{\underline{U}} \approx \frac{1}{\Delta t^2}\left[\underline{U}_{n+1} - 2\underline{U}_n + \underline{U}_{n-1}\right]. \tag{2.132}$$

Subscript "n" implies evaluating the quantity at $t = n\Delta t$, for example, $\underline{U}_n = \underline{U}(n\Delta t)$.

The global mass matrix, $\underline{M}$, is diagonalized using an empirical procedure known as "mass lumping" [62]:

$$M_{ij}^D = \begin{cases} \alpha M_{ij} & \text{if } i = j \\ 0 & \text{if } i \neq j \end{cases} \tag{2.133}$$

$$\alpha = \frac{\sum_i \sum_j M_{ij}}{\sum_i M_{ii}}. \tag{2.134}$$

Inverting the diagonalized mass matrix requires simply inverting each diagonal element. Combining the central difference approximation and the diagonalized mass matrix with eq. 2.90 gives

$$\begin{aligned} \underline{U}_{n+1} &= 2\underline{U}_n - \underline{U}_{n-1} - \Delta t^2 \left[\underline{M}^D\right]^{-1} \left\{\underline{K}_J \underline{U}_n - \underline{R}_n\right\} \\ &\quad -\Delta t^2 \left[\underline{M}^D\right]^{-1} \left\{\underline{K}_K \underline{U}_n^K + \underline{K}_G \underline{U}_n^G\right\}. \end{aligned} \tag{2.135}$$

Neglecting the second line of this equation recovers the original elastic equation.

For time marching solutions to remain bounded a stability condition must be satisfied. For bilinear quadrilateral finite elements employed in this study, Flanagan and Belytschko [14] have derived the following *sufficient* stability condition:

$$\Delta t \leq \frac{2}{c_{lg}\sqrt{g}} \tag{2.136}$$

$$g = \frac{4}{A^2} \sum_{i=1}^{2} \sum_{j=1}^{4} Q_{ij}^2 \tag{2.137}$$

$$\underline{Q} = \frac{1}{2} \begin{bmatrix} (r_2 - r_4) & (r_3 - r_1) & (r_4 - r_2) & (r_1 - r_3) \\ (z_4 - z_2) & (z_1 - z_3) & (z_2 - z_4) & (z_3 - z_1) \end{bmatrix} \tag{2.138}$$

where (r_i, z_i) are the coordinates of the finite element vertices and A is the area of the element. For a square and rectangular quadrilateral with side length d or d_1 and d_2, respectively, this stability condition reduces to

$$\Delta t \leq \frac{d}{\sqrt{2} c_{lg}} \tag{2.139}$$

$$\Delta t \leq \frac{1}{c_{lg}\sqrt{\frac{1}{d_1^2} + \frac{1}{d_2^2}}}. \tag{2.140}$$

Numerical studies [60, 61] have shown that for square quadrilaterals with $d_1 = d_2 = d$ the condition

$$\Delta t < \frac{d}{c_{lg}} \tag{2.141}$$

results in stable finite element solutions. This condition implies that the time step must be smaller than the time for the longitudinal wave to traverse the distance d or the shorter of the two distances d_1 and d_2.

Wave Propagation Examples

A set of examples are presented that will illustrate concepts presented in this chapter. These examples will establish confidence in the finite element method for computing transient waves in linear

viscoelastic media.

As a first example consider a viscoelastic half-space with simple exponential moduli as described in eqs. 2.16, 2.17 and 2.18. Assume that $\tau_K = \tau_G = \tau$ and the asymptotic wave speeds and moduli have the following values [43]:

$$(c_{sg}, c_{se}) = (3100.0)\ m/s \ \text{(shear)} \tag{2.142}$$

$$(c_{lg}, c_{le}) = (6300, 3150)\ m/s \ \text{(longitudinal)} \tag{2.143}$$

$$(M_g, M_e) = (\rho c_{lg}^2, \rho c_{le}^2)$$

$$= (107.2, 26.8)\ \text{GPa} \tag{2.144}$$

$$(G_g, G_e) = (\rho c_{sg}^2, \rho c_{se}^2)$$

$$= (25.9, 0)\ \text{GPa} \tag{2.145}$$

$$(K_g, K_e) = (M_g - \frac{4}{3}G_g, M_e - \frac{4}{3}G_e)$$

$$= (81.3, 26.8)\ \text{GPa} \tag{2.146}$$

$$\rho = 2700\ kg/m^3. \tag{2.147}$$

In the elastic limit ($\tau \to \infty$) the shear and longitudinal wave speeds are typical of aluminum [29].

A plane wave source is defined on the half-space surface with the following time dependent surface traction:

$$T_z(z=0,t) = Z_{lg}\dot{u}_z(z=0,t) \tag{2.148}$$

$$u_z(z=0,t) = \begin{cases} -\frac{1}{2}\left[1-\cos\left(\frac{1}{3}\omega_0 t\right)\right]\cos(\omega_0 t) & 0 \le \omega_0 t \le 6\pi \\ 0 & \text{otherwise} \end{cases} \tag{2.149}$$

where is $Z_{lg} = \rho c_{lg}$. This functional form is chosen because it represents a realistic narrow bandwidth source typical of a piezoelectric transducer. The relation between surface traction, $T_z(0,t)$, and displacement, $u_z(0,t)$, is exact in the elastic limit but the exact viscoelastic relation is

$$T_z(z=0,t) = [M * \partial_z \dot{u}_z](z=0,t). \tag{2.150}$$

For purposes of demonstration the difference in surface traction definition is unimportant. The problem geometry and source time dependence for $f_0 = 1$MHz are plotted in Fig. 2.3.

Figure 2.4 shows the frequency dependent magnitude of the source compared with the normalized longitudinal modulus, $\bar{m}(\omega)$, and normalized plane wave attenuation and wave speed, $\alpha_l(\omega)$ and $c_l(\omega)$, for three different fundamental source frequencies, $f_0 = 0.1,\ 1,\ 10$MHz. In this case $\tau = \frac{1}{2\pi}\mu s$ so that $\omega\tau = 1$ at $f = 1$MHz. At each of these frequencies transient displacement at points along the axis of

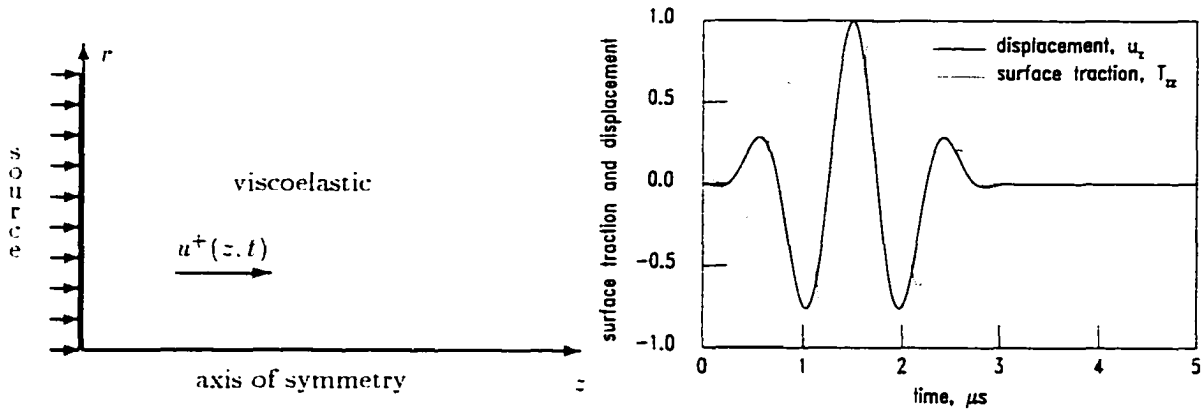

(a) (b)

Figure 2.3 Geometry of plane wave test problem. (a): time dependence of source surface traction and displacement. (b) (f_0 = 1MHz)

symmetry are plotted in Figs. 2.5(a), (b) and (c), respectively. The source radius is relatively large ($ka \approx 100$) so that only the plane portion of the transmitted wave is present at the positions where the displacement is recorded. The square symbols indicate the relative 1-D attenuation, $e^{-\alpha_l z}$. The attenuation is computed at the source center frequency and the propagation distance is noted in the figure. The exact and FE results are almost indistinguishable. The theoretical attenuation and wave speed are

$$\alpha_l(0.1\text{ MHz}) = 0.27\text{ Np/cm or }2.35\text{ dB/cm} \quad (2.151)$$

$$\alpha_l(1\text{ MHz}) = 3.12\text{ Np/cm or }27\text{ dB/cm} \quad (2.152)$$

$$\alpha_l(10\text{ MHz}) = 3.73\text{ Np/m or }32\text{ dB/cm} \quad (2.153)$$

$$c_l(0.1\text{ MHz}) = 3293\text{ m/s} \quad (2.154)$$

$$c_l(1\text{ MHz}) = 5581\text{ m/s} \quad (2.155)$$

$$c_l(10\text{ MHz}) = 6290\text{ m/s}. \quad (2.156)$$

The temporal wave spreading due to frequency dependent wave speed is relatively weak in comparison to attenuation.

If the fundamental frequency of the source is held fixed and relaxation time is varied from short to long relative to the period of the fundamental frequency, $T_0 = \frac{1}{f_0}$, then computed displacement approaches the elastic limit, see Fig. 2.6. In this case the source aperture is finite with radius a = 5mm ($ka \approx 5$)and the source traction is uniform across the entire aperture radius.

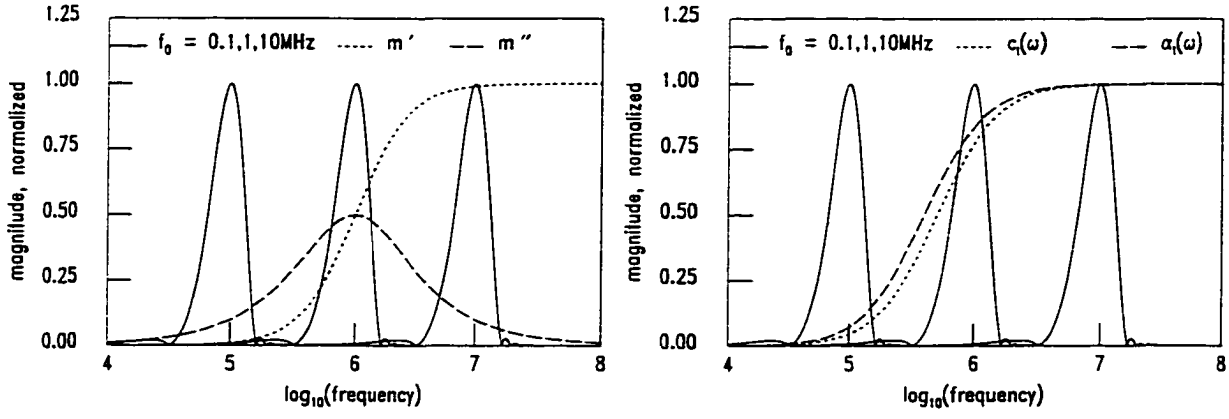

Figure 2.4 Source spectrum magnitude compared with normalized longitudinal modulus, $\hat{m}(\omega) = m' + im''$, (a), and normalized attenuation, $\alpha_l(\omega)$, and wave speed, $c_l(\omega)$, (b), versus frequency, $\log_{10}(f \text{ Hz})$

Finite element axial displacements excited by a finite aperture source, $a = 5\text{mm}$ ($ka \approx 5$), are shown in Fig. 2.5(d). In this case the medium has a continuous distribution of relaxation times. The FE displacements are compared with a Laplace-Hankel transform domain solution that has been inverted numerically to recover axial displacement at a chosen point as a function of time [43]. The finite element and Laplace-Hankel results are essentially identical. Similar correspondence exists for off-axis radial and axial displacement [43]. In Fig. 2.5(d) axial displacement, u_z, at $(r, z) = (0, 10)mm$ is shown for a material with an HN spectral distribution (denoted HN(a) in figure) that is a "best-fit" for a KWW spectral distribution with $\beta = 0.5$ [1]. For $\beta = 0.5$ the KWW spectral density is known in closed form; therefore, it can by used directly in an FE calculation. Also shown is axial displacement for an HN spectral distribution (denoted HN(b) in figure) that is a best-fit for a KWW spectral distribution with $\beta = 0.35$. See Fig. 2.1 for plots of actual spectral distributions. The KWW characteristic relaxation time is $\tau_{kww} = \frac{1}{2\pi}\mu s$ and the corresponding HN characteristic relaxation times are $\tau_{hn} = 2.9174\tau_{kww}$ for $\beta = 0.5$ and $\tau_{hn} = 5.3827\tau_{kww}$ for $\beta = 0.35$.

Summary

A brief introduction to linear viscoelasticity has been given. Specifically, models for relaxation spectra, KWW and HN spectra models, appropriate for real viscoelastic media have been described. With relaxation spectra in mind a finite element model for ultrasonic wave propagation in viscoelastic

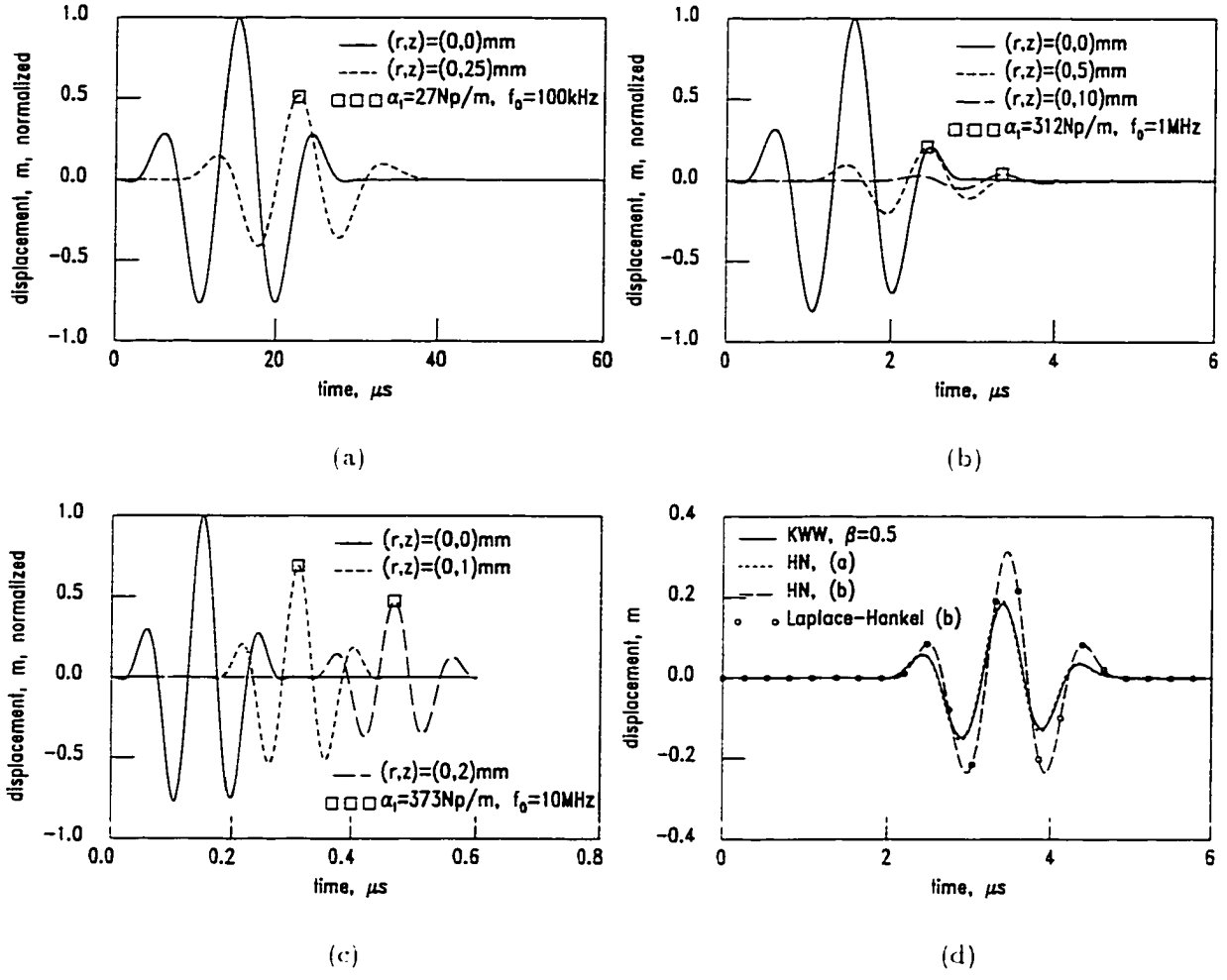

Figure 2.5 Effective 1-D FE displacement for $f_0 = 0.1,\ 1,\ 10$MHz compared with exact 1-D attenuation. (a)-(c): FE displacement computed with KWW and HN spectral distributions compared with inverse Laplace-Hankel solution. (d)

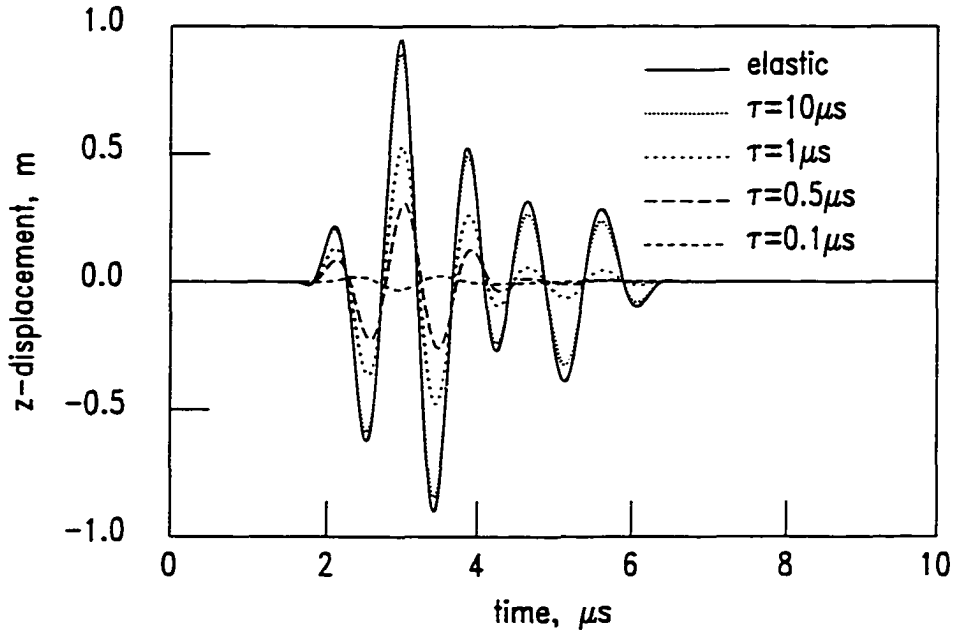

Figure 2.6 Finite element axial displacement at $(r, z) = (0, 10)mm$ for increasing relaxation time

media is developed that incorporates the distributional nature of relaxation processes. The chapter concludes with several FE examples of mechanical waves in simple, single-exponential media as well as media with a relaxation distribution. FE results are compared with an inverse Laplace-Hankel transform calculation and shown to be equivalent. These simple examples and comparisons establish initial confidence in the finite element method's ability to model accurately transient ultrasonic wave propagation in linear viscoelastic media.

CHAPTER 3 WAVE SPLITTING INVERSE METHODS

Introduction

A description of wave splitting/invariant embedding forward and inverse methods for viscoelastic media is presented. Reformulation of the one-dimensional wave equation for LHI viscoelastic media via wave splitting is developed. Wave splitting is a general method of wave field decomposition and is not limited to homogeneous media [10]. A general derivation of the differential invariant embedding equations follows wave splitting. Embedding equations interrelate one-dimensional scattering operators. Their form is general and applicable to other models of material properties such as non-dispersive, inhomogeneous media, but a splitting matrix specific to the material property model considered is required.

Following development of wave splitting and embedding equations, concrete repesentations for the reflection and transmission operators in terms of kernels are defined. Wave splitting results and embedding equations combine with scattering kernels to produce a set of integro-differential equations in time and space for the scattering kernels. The space-time PDE's for the reflection and transmission kernels would usually form the basis of the forward and inverse algorithms, but because the viscoelastic medium is homogeneous exact Laplace domain reflection and transmission kernels can be derived via a simple bounce diagram. An elegant forward algorithm is developed from the Laplace domain kernels. The forward method was first described by Fuks [15] for the analogous dispersive electromagnetic case and is adapted here to the viscoelastic case. The inversion method for recovery of the viscoelastic modulus is an ingenious method first described by Karlsson [26] that relies soley on the transmission forward model and knowledge of the transmission kernel derived from experiment.

Wave Splitting

Wave splitting is the decomposition of a total wave field into two components that propagate in opposite directions along some defined or preferred direction. In one-dimensional wave splitting for

longitudinal (shear) mechanical waves, the total wave fields are displacement, $u(z,t)$ (m), and stress, $T(z,t)$ $(N/m^2$ or $Pa)$. The split fields are (u^+, u^-) where superscript "+" implies propagation in the positive z-direction and "−" implies propagation in the negative z-direction. The split fields are often referred to as "forward and backward," "up and down" or "left and right" propagating waves.

Before wave splitting is introduced the wave equation for (u, T) is formulated as a first order system. In preparation for this formulation, define the normalized longitudinal stress relaxation modulus, $m(t)$, and the normalized creep compliance, $n(t)$, by

$$m(t) = \frac{M(t)}{M_g} \tag{3.1}$$

$$n(t) = \frac{N(t)}{N_g} \tag{3.2}$$

with the relation

$$[n * m](t) = t. \tag{3.3}$$

The stress/displacement relation is

$$T(z,t) = m * \partial_z u(z,t) \tag{3.4}$$

or after applying $n * \partial_t$ to both sides

$$\partial_z u(z,t) = n * \dot{T}(z,t) \tag{3.5}$$

$$= [1 + \dot{n} *] T(z,t). \tag{3.6}$$

Note that stress is normalized by M_g. Finally, the wave equation in terms of stress and displacement is

$$\partial_z T(z,t) = \frac{1}{c^2} \ddot{u}(z,t) \tag{3.7}$$

or rewritten as a first order system the wave equation becomes

$$\partial_z \begin{bmatrix} u \\ T \end{bmatrix} = \left\{ \begin{bmatrix} 0 & 1 \\ (\frac{\partial_t}{c})^2 & 0 \end{bmatrix} + \begin{bmatrix} 0 & \dot{n}* \\ 0 & 0 \end{bmatrix} \right\} \begin{bmatrix} u \\ T \end{bmatrix} = (\underline{A} + \underline{B}) \begin{bmatrix} u \\ T \end{bmatrix}. \tag{3.8}$$

Observe that if matrix $\underline{B}$ is neglected the one-dimensional elastic wave equation for LHI media is recovered. For reference, the wave equation written strictly in terms of displacement is

$$m * \partial_z^2 u(z,t) = \frac{1}{c^2} \ddot{u}(z,t) \tag{3.9}$$

or after operating with $n * \partial_t$ on both sides and integrating by parts it becomes

$$\partial_z^2 u(z,t) = \frac{1}{c^2} \ddot{u}(z,t) + \frac{1}{c^2} \dot{n} * \ddot{u}(z,t). \tag{3.10}$$

In order to split the total fields, (u, T), into left and right propagating fields, (u^+, u^-), a change of basis is assumed, that is,

$$\begin{bmatrix} u \\ T \end{bmatrix} = \underline{P}^{-1} \begin{bmatrix} u^+ \\ u^- \end{bmatrix} \tag{3.11}$$

$$\begin{bmatrix} u^+ \\ u^- \end{bmatrix} = \underline{P} \begin{bmatrix} u \\ T \end{bmatrix}. \tag{3.12}$$

Substituting eq. 3.11 for (u, T) in eq. 3.8 and rearranging gives

$$\partial_z \begin{bmatrix} u^+ \\ u^- \end{bmatrix} = \{\underline{P}\,\underline{A}\,\underline{P}^{-1} + \underline{P}\,\underline{B}\,\underline{P}^{-1}\} \begin{bmatrix} u^+ \\ u^- \end{bmatrix}. \tag{3.13}$$

From the chain rule for derivatives there should be a term proportional to $\partial_z \underline{P}^{-1}$, but $\partial_z \underline{P}^{-1} = 0$ because the viscoelastic medium is assumed homogeneous.

Define matrices $\underline{D} \equiv \underline{P}\,\underline{A}\,\underline{P}^{-1}$ and $\underline{E} \equiv \underline{P}\,\underline{B}\,\underline{P}^{-1}$. A transformation is sought that will diagonalize $\underline{A}$ or, in other words, will decouple left and right propagating waves in an LHI elastic medium. In this context $\underline{P}\,\underline{A}\,\underline{P}^{-1}$ is a similarity transformation from $\underline{A}$ to $\underline{D}$ where $\underline{P}^{-1}$ is a matrix whose columns are the eigenvectors of $\underline{A}$ and $\underline{D}$ is a diagonal matrix of eigenvalues of $\underline{A}$. It follows that

$$\underline{P}^{-1} = \begin{bmatrix} 1 & 1 \\ -\left(\frac{\partial_t}{c}\right) & \left(\frac{\partial_t}{c}\right) \end{bmatrix} \tag{3.14}$$

$$\underline{P} = \begin{bmatrix} 1 & -\left(\frac{\partial_t}{c}\right)^{-1} \\ 1 & \left(\frac{\partial_t}{c}\right)^{-1} \end{bmatrix} \tag{3.15}$$

and

$$\underline{D} = \begin{bmatrix} -\left(\frac{\partial_t}{c}\right) & 0 \\ 0 & \left(\frac{\partial_t}{c}\right) \end{bmatrix} \tag{3.16}$$

$$\underline{E} = \underline{P}\,\underline{B}\,\underline{P}^{-1} = \frac{1}{2c} \begin{bmatrix} -\dot{n} * \partial_t & \dot{n} * \partial_t \\ -\dot{n} * \partial_t & \dot{n} * \partial_t \end{bmatrix}. \tag{3.17}$$

where

$$\left[\left(\frac{\partial_t}{c}\right)^{-1} f\right](t) \equiv c \int_0^t f(s)ds. \tag{3.18}$$

assuming initial conditions for all field variables are zero [10]. Collecting these results together, an equivalent formulation for the 1-D wave equation, eq. 3.13, is

$$\partial_z \begin{bmatrix} u^+ \\ u^- \end{bmatrix} = \begin{bmatrix} \alpha & \beta \\ \gamma & \delta \end{bmatrix} \begin{bmatrix} u^+ \\ u^- \end{bmatrix} \tag{3.19}$$

where

$$\delta = -\alpha = \frac{1}{2c}[2 + \dot{n}*]\partial_t \tag{3.20}$$

$$\beta = -\gamma = \frac{1}{2c}\dot{n} * \partial_t. \tag{3.21}$$

With this reformulation of wave propagation in LHI viscoelastic media, wave splitting is complete.

Invariant Embedding

The split field equations, eq. 3.19, represent local 'at-a-point' dynamical relations for left and right propagating fields in an LHI viscoelastic medium. In contrast, a set of four linear scattering operators can be defined that relate incident and scattered fields for a viscoelastic slab of macroscopic thickness:

$$\begin{bmatrix} u^+(b) \\ u^-(a) \end{bmatrix} = \begin{bmatrix} \mathcal{T}^+(a,b) & \mathcal{R}^-(a,b) \\ \mathcal{R}^+(a,b) & \mathcal{T}^-(a,b) \end{bmatrix} \begin{bmatrix} u^+(a) \\ u^-(b) \end{bmatrix} \tag{3.22}$$

$$= \underline{\mathcal{S}}(a,b) \begin{bmatrix} u^+(a) \\ u^-(b) \end{bmatrix}. \tag{3.23}$$

where 'a' and 'b' indicate the boundaries of the slab and dependence on time, 't', has been suppressed (see Fig. 3.1). It is assumed that for $z < a$ and $z > b$ the material is LHI elastic media. Scattering operators are defined for a thin slab of thickness Δz and for a composite slab of thickness $\Delta z + L$, respectively, where $L = (b - a)$ is the original slab thickness:

$$\underline{\mathcal{S}}(a - \Delta z, a) = \begin{bmatrix} \mathcal{T}^+ & \mathcal{R}^- \\ \mathcal{R}^+ & \mathcal{T}^- \end{bmatrix} (a - \Delta z, a) \tag{3.24}$$

$$\underline{\mathcal{S}}(a - \Delta z, b) = \begin{bmatrix} \mathcal{T}^+ & \mathcal{R}^- \\ \mathcal{R}^+ & \mathcal{T}^- \end{bmatrix} (a - \Delta z, b). \tag{3.25}$$

where $[\cdot](a - \Delta z, a)$ implies the operators are evaluated at $(a - \Delta z, a)$, etc. Scattering operators are assumed to be time translation invariant and independent of incident fields, but the precise relationships which connect these operators to material properties and to each other are to be determined.

Invariant embedding shows how to derive operator interrelationships. The idea is to *embed* the original slab in a slab which is slightly longer by Δz and derive the scattering operators for the new, slightly longer, slab in terms of the operators for the original slab, eq. 3.22, and the dynamical relations, eq. 3.19. When Δz goes to zero the result is a set of differential equations for the scattering operators and ultimately for the operator kernels.

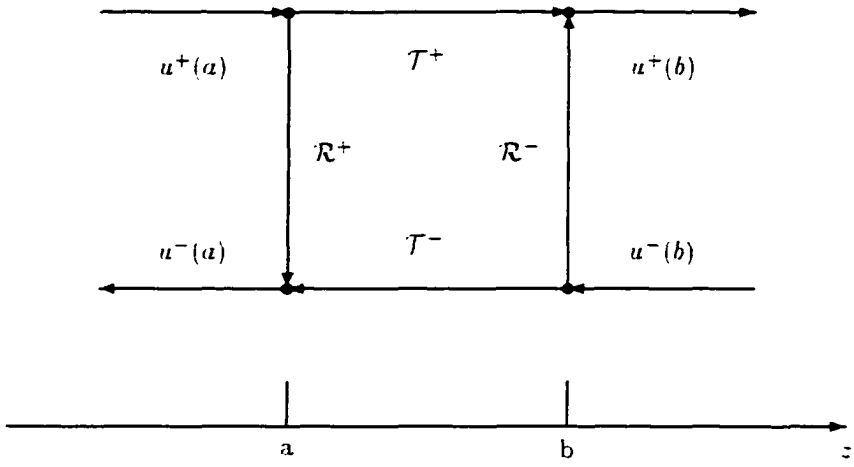

Figure 3.1 Flow graph representation of scattering process

The goal is to find mathematical relations that link scattering operators for the original, thin and composite slabs. To begin a thin slab is added to the original slab at 'a' so that the composite slab extends from $a - \Delta z \leq z \leq b$. For the moment consider only the thin slab. Assume the fields at $z = a - \Delta z$ are related to fields at "a" by a first order Taylor's series expansion about $z = a$.

$$u^+(a - \Delta z) \approx u^+(a) - \partial_z u^+(a)\Delta z \tag{3.26}$$

$$u^-(a - \Delta z) \approx u^-(a) - \partial_z u^-(a)\Delta z. \tag{3.27}$$

where $\partial_z u^\mp(a) \equiv \partial u^\mp/\partial z|_{z=a}$. With the dynamical relations, eq. 3.19, the terms $\partial_z u^\pm(a)$ in the Taylor's series expansion can be replaced so that

$$u^+(a - \Delta z) = u^+(a) - \Delta z\,(\alpha u^+(a) + \beta u^-(a)) \tag{3.28}$$

$$u^-(a - \Delta z) = u^-(a) - \Delta z\,(\gamma u^+(a) + \delta u^-(a))\,. \tag{3.29}$$

It is assumed that each operator, $(\alpha, \beta, \gamma, \delta)$, is evaluated at a. Solving for $u^-(a - \Delta z)$ and $u^+(a)$ and neglecting terms of order $(\Delta z)^2$ and higher, the scattering matrix for a thin slab becomes

$$\begin{bmatrix} u^+(a) \\ u^-(a - \Delta z) \end{bmatrix} = \begin{bmatrix} 1 + \Delta z\alpha & \Delta z\beta \\ -\Delta z\gamma & 1 - \Delta z\delta \end{bmatrix} \begin{bmatrix} u^+(a - \Delta z) \\ u^-(a) \end{bmatrix} \tag{3.30}$$

$$= \underline{S}(a - \Delta z, a) \begin{bmatrix} u^+(a - \Delta z) \\ u^-(a) \end{bmatrix}. \tag{3.31}$$

A scattering matrix for the composite slab is created from eq. 3.22 and eq. 3.30 by eliminating $u^{\pm}(a)$, neglecting terms $(\Delta z)^2$ and higher and preserving operator ordering. The scattering operator matrix for the composite slab is

$$\underline{S}(a-\Delta z, b) = \underline{S}(a-\Delta z, a) * \underline{S}(a, b). \tag{3.32}$$

The symbol, '$*$', denotes a special algebraic composition or product of the subslab scattering operators known as a 'star product' or 'Redheffer star product' in the wave splitting literature [38]. This sort of composition also appears in basic textbooks on microwave circuits [18] often set in terms of intermediate matrices known as *chain* or *T-matrices* that relate fields at 'b' to fields at 'a' and *vice versa*. The components of $\underline{S}(a-\Delta z, b)$ are

$$\mathcal{T}^+(a-\Delta z, b) = \mathcal{T}^+ \left(1-\mathcal{R}_\Delta^- \mathcal{R}^+\right)^{-1} \mathcal{T}_\Delta^+ \tag{3.33}$$

$$\mathcal{R}^+(a-\Delta z, b) = \mathcal{R}_\Delta^+ + \mathcal{T}_\Delta^- \mathcal{R}^+ \left(1-\mathcal{R}_\Delta^- \mathcal{R}^+\right)^{-1} \mathcal{T}_\Delta^+ \tag{3.34}$$

$$\mathcal{R}^-(a-\Delta z, b) = \mathcal{R}^- + \mathcal{T}^+ \mathcal{R}_\Delta^- \left(1-\mathcal{R}^+ \mathcal{R}_\Delta^-\right)^{-1} \mathcal{T}^- \tag{3.35}$$

$$\mathcal{T}^-(a-\Delta z, b) = \mathcal{T}_\Delta^- \left(1-\mathcal{R}^+ \mathcal{R}_\Delta^-\right)^{-1} \mathcal{T}^- \tag{3.36}$$

Terms $\mathcal{T}^{\pm}$ and $\mathcal{R}^{\pm}$ denote scattering operators of the original slab, $\mathcal{T}^{\pm}(a, b)$ and $\mathcal{R}^{\pm}(a, b)$, eq. 3.22, respectively, and $\mathcal{T}_\Delta^{\pm}$ and $\mathcal{R}_\Delta^{\pm}$ denote scattering operators of the thin slab, $\mathcal{T}^{\pm}(a-\Delta z, a)$ and $\mathcal{R}^{\pm}(a-\Delta z, a)$, eq. 3.30, respectively.

Substitute for $\mathcal{T}_\Delta^{\pm}$ and $\mathcal{R}_\Delta^{\pm}$ with corresponding terms in eq. 3.30 and expand terms of the form $(\cdot)^{-1}$ as a series retaining factors to first order in Δz. The composite scattering operators become

$$\mathcal{T}^+(a-\Delta z, b) \approx \mathcal{T}^+ + \Delta z \left(\mathcal{T}^+ \alpha + \mathcal{T}^+ \beta \mathcal{R}^+\right) \tag{3.37}$$

$$\mathcal{R}^+(a-\Delta z, b) \approx \mathcal{R}^+ - \Delta z \left(\gamma + \delta \mathcal{R}^+ - \mathcal{R}^+ \alpha - \mathcal{R}^+ \beta \mathcal{R}^+\right) \tag{3.38}$$

$$\mathcal{R}^-(a-\Delta z, b) \approx \mathcal{R}^- + \Delta z \mathcal{T}^+ \beta \mathcal{T}^- \tag{3.39}$$

$$\mathcal{T}^-(a-\Delta z, b) \approx \mathcal{T}^- - \Delta z \left(\delta \mathcal{T}^- - \mathcal{R}^+ \beta \mathcal{T}^-\right). \tag{3.40}$$

Upon passing to the limit $\Delta z \to 0$, the first of these equations, eq. 3.37, becomes

$$\lim_{\Delta z \to 0} \frac{\mathcal{T}^+(a, b) - \mathcal{T}^+(a-\Delta z, b)}{\Delta z} = \frac{\partial \mathcal{T}^+}{\partial a} = -\mathcal{T}^+ \alpha - \mathcal{T}^+ \beta \mathcal{R}^+ \tag{3.41}$$

where $\partial/\partial a$ implies variation with respect to the left-hand boundary, a, or

$$\frac{\partial \mathcal{T}^+}{\partial a} \equiv \left.\frac{\partial \mathcal{T}^+(z, b)}{\partial z}\right|_{z=a}. \tag{3.42}$$

In summary, the embedding equations for the scattering operators with respect to variation of the left-hand boundary, "a", are

$$\frac{\partial \mathcal{T}^+}{\partial a} = -\mathcal{T}^+ \alpha - \mathcal{T}^+ \beta \mathcal{R}^+ \tag{3.43}$$

$$\frac{\partial \mathcal{R}^+}{\partial a} = \gamma + \delta\mathcal{R}^+ - \mathcal{R}^+\alpha - \mathcal{R}^+\beta\mathcal{R}^+ \tag{3.44}$$

$$\frac{\partial \mathcal{R}^-}{\partial a} = -\mathcal{T}^+\beta\mathcal{T}^- \tag{3.45}$$

$$\frac{\partial \mathcal{T}^-}{\partial a} = \delta\mathcal{T}^- - \mathcal{R}^+\beta\mathcal{T}^- \tag{3.46}$$

with $(\alpha, \beta, \gamma, \delta)$ evaluated at a and $(\mathcal{T}^+, \mathcal{R}^+, \mathcal{R}^-, \mathcal{T}^-)$ are evaluated at (a, b). A similar set of embedding equations exist for variation of the right-hand boundary, b [10]. Equations 3.43-3.46 are a general set of operator/material property relationships for one dimensional scattering independent of incident and scattered fields. A concrete representation for the scattering operators is neccessary to derive integro-differential equations for the operator kernels from eqs. 3.43-3.46.

Scattering kernels and kernel equations

Initially assume that the viscoelastic slab is impedance matched to the elastic media at $z = a$ and $z = b$, respectively. An impedance match exists when the longitudinal (shear) acoustic impedance of each elastic medium, $Z_{le} = \rho_e c_{le}$, is equal to the high frequency acoustic impedance of the viscoelastic slab, $Z_{lve} = \rho_{ve} c_{lve} = \sqrt{\rho_{ve} M_J}$. An impedance matched condition implies reflections from the viscoelastic slab approach zero as frequency approaches infinity. Concrete representations for impedance matched scattering operators for a wave incident upon the slab from the left at $z = a$ are

$$u^-(z,t) = \mathcal{R}^+(z, L, t)u^+(z,t) \tag{3.47}$$

$$= \int_0^t R^+(z, L, t-s)u^+(z,s)ds \tag{3.48}$$

$$u^+(L, t + \tau(z)/2) = \mathcal{T}^+(z, L, t)u^+(z,t) \tag{3.49}$$

$$= d(z)u^+(z,t) + \int_0^t T^+(z, L, t-s)u^+(z,s)ds. \tag{3.50}$$

where

$$\tau(z) = 2(L - z)/c_{lve} \tag{3.51}$$

$$d(z) = e^{-\dot{n}_0 \tau(z)/4} \tag{3.52}$$

$$\dot{n}_0 \equiv \left.\frac{\partial n}{\partial t}\right|_{t=0}. \tag{3.53}$$

Explicit forms of scattering operators have been derived by Kristensson [31] from arguments based on time translation invariance and causality. An LHI viscoelastic slab impedance matched at both boundaries has symmetry with respect to waves incident at the left or right boundary; therefore, $\mathcal{R}^- = \mathcal{R}^+ = \mathcal{R}$ and $\mathcal{T}^- = \mathcal{T}^+ = \mathcal{T}$.

With scattering operators represented in terms of kernels, embedding equations for the kernels can be derived from eqs. 3.43-3.46. Embedding equations for reflection and transmission kernels are, respectively:

$$
\begin{aligned}
(2c_{lve}\partial_z - 4\partial_t)R &= -\partial_t\left[(1-R*)(1-R*)\dot{n}\right] \qquad 0<z<L \qquad (3.54)\\
&= -\ddot{n} + \dot{n}_0\left[2R - R*R\right] + \ddot{n}*\left[2R - R*R\right]\\
R(z,L,0) &= \frac{1}{4}\dot{n}_0\\
R(L,L,t) &= 0\\
R(z,L,t)\big|_{t=\tau(z)-}^{t=\tau(z)+} &= -\frac{1}{4}\dot{n}_0(d(z))^2
\end{aligned}
$$

$$
\begin{aligned}
2c_{lve}\partial_z T &= \partial_t\left[d\dot{n} - d\dot{n}*R + \dot{n}*T - \dot{n}*R*T\right] \qquad 0<z<L \qquad (3.55)\\
&= d\ddot{n} + \dot{n}_0\left[T - dR - T*R\right] + \ddot{n}*\left[T - dR - T*R\right]\\
T(z,L,0) &= -\frac{1}{4}\tau(z)d(z)\left[\ddot{n}_0 - \frac{1}{4}(\dot{n}_0)^2\right]\\
T(L,L,t) &= 0.
\end{aligned}
$$

The fourth term in eq. 3.54 is a jump discontinuity in $R(z,L,t)$ across the characteristic line, $t=\tau(z)$. When $z=0$ then $\tau(0)$ is the round trip time through the viscoelastic slab for the wavefront. Until one round trip the reflection kernel is equivalent to a reflection kernel of a viscoelastic half-space. The detailed derivations of these kernel equations is given in Karlsson [26] and will not be repeated here.

Karlsson [26] gives Laplace transform solutions to eqs. 3.54 and 3.55. This is possible because the viscoelastic medium is assumed homogeneous. Alternatively, Laplace domain scattering kernels are easily derived from a bounce diagram approach (see Appendix A). The Laplace transform kernels are

$$
\begin{aligned}
\tilde{R}(z,L,s) &= \tilde{r}(s)\left[\frac{1-d^2(z)e^{-s\tau(z)}e^{-\tilde{b}(s)}}{1-\tilde{r}^2(s)d^2(z)e^{-s\tau(z)}e^{-\tilde{b}(s)}}\right] \qquad (3.56)\\
\tilde{T}(z,L,s) &= d(z)e^{-\tilde{b}(s)/2}\left[\frac{1-\tilde{r}^2(s)}{1-\tilde{r}^2(s)d^2(z)e^{-s\tau(z)}e^{-\tilde{b}(s)}}\right] - d(z) \qquad (3.57)\\
&= d(z)e^{-\tilde{b}(s)/2}\left[1-\tilde{r}(s)\tilde{R}(z,L,s)\right] - d(z) \qquad (3.58)\\
\tilde{b}(s) &= s\tau(z)\left(\sqrt{s\tilde{n}(s)}-1\right) - \frac{1}{2}\dot{n}_0\tau(z) \qquad (3.59)\\
\tilde{r}(s) &= \frac{\sqrt{s\tilde{n}(s)}-1}{\sqrt{s\tilde{n}(s)}+1} \qquad (3.60)\\
&= \frac{1-\sqrt{s\tilde{n}(s)}}{1+\sqrt{s\tilde{n}(s)}} \qquad (3.61)
\end{aligned}
$$

The term $\tilde{r}(s)$ is the displacement reflection coefficient for an impedance matched viscoelastic half-space. The Laplace transform of the normalized creep compliance, $s\tilde{n}(s)$, comes from the Laplace transform of the modulus/compliance relation:

$$n * m = t \tag{3.62}$$

$$\Rightarrow \tilde{n}\tilde{m} = \frac{1}{s^2} \tag{3.63}$$

$$s\tilde{n} = \frac{1}{s\tilde{m}}. \tag{3.64}$$

An analogous set of Laplace domain kernels for an impedance matched slab of dispersive, electromagnetic media are presented by Fuks [15]. He showed how to invert the Laplace transform kernel equations via three intermediate variables. Their time domain kernel equations represent a forward model and form the basis of an inverse algorithm. The inverse algorithm is an ingenious method originally derived by Karlsson [26] that only requires detailed knowledge of the transmission kernel. In experimental work performed by Fuks [15] it was observed that the reflection from a dispersive fluid (an alcohol) is dominated by 'hard reflection' or reflection due to high frequency impedance mismatch; therefore, the reflected field appeared as a scaled version of the incident field and was unsuitable for recovery of the time dependent susceptibility kernel, $\chi(t)$, analogous to $\dot{n}(t)$. Fuks found that the transmitted field was relatively more sensitive to the dispersive nature of the alcohol. The transmitted wave appeared highly distorted compared with the incident field and consequently provided relatively more information about the dispersive properties of the alcohol. Fuks showed that recovery of the susceptibility kernel with transmission data only was stable and resulted in a good estimate of susceptibility [26].

The equations for the forward model based on the inverse Laplace transform are presented and their derivation is detailed in Appendix A. The time dependent reflection and transmission kernel for the slab, R and T, and the reflection kernel for a halfspace, $r(t)$, are, respectively:

$$R(0, L, t) = r(t) + \sum_{i=0}^{\infty} \mathcal{S}((i+1)\tau_0)\,(r * r * v - v)\,(*r * v)^i \tag{3.65}$$

$$T(0, L, t) = e(t) - d_0 r * R - e * r * R. \tag{3.66}$$

$$r(t) = \frac{1}{4}(\dot{n}(t) - 2\dot{n} * r - \dot{n} * r * r) \tag{3.67}$$

$$r(0) = \frac{1}{4}\dot{n}_0 \tag{3.68}$$

The equations for $b(t)$, $e(t)$ and $v(t)$ are

$$b(t) = \frac{1}{2}\tau_0\,(\ddot{n}(t) - \ddot{n} * r - \dot{n}_0 r(t)) \tag{3.69}$$

$$e(t) = -\frac{1}{2}d_0 b(t) - \frac{1}{2t}e * (tb) \tag{3.70}$$

$$v(t) = d_0^2 r(t) + 2d_0 e * r + e * e * r \tag{3.71}$$

where

$$\tau_0 \equiv \tau(z=0) \tag{3.72}$$

$$d_0 \equiv d(z=0) \tag{3.73}$$

$$\dot{n}_0 \equiv \dot{n}(t=0). \tag{3.74}$$

The term $\mathcal{S}(\tau_0)$ is a time translation operator defined by

$$\mathcal{S}(\tau_0) f(t) \equiv f(t-\tau_0). \tag{3.75}$$

A flow chart of the forward problem is presented in Fig. 3.2.

Scattering kernels for impedance mismatch

For any realistic experimental situation there will be impedance mismatches at both the front and back wall giving rise to 'hard' reflection and transmission coefficients. The longitudinal displacement reflection and transmission coefficients for the front wall, $z=0$, and back wall, $z=L$, are, respectively,

$$r_0^+ = \frac{Z_0 - Z_{we}}{Z_0 + Z_{we}} \tag{3.76}$$

$$t_0^+ = 1 + r_0^+ \tag{3.77}$$

$$r_0^- = -r_0^+ \tag{3.78}$$

$$t_0^- = 1 + r_0^- \tag{3.79}$$

$$r_L^+ = \frac{Z_{we} - Z_L}{Z_{we} + Z_L} \tag{3.80}$$

$$t_L^+ = 1 + r_L^+ \tag{3.81}$$

$$r_L^- = -r_L^+ \tag{3.82}$$

$$t_L^- = 1 + r_L^- \tag{3.83}$$

where superscripts "+" and "−" refer to the direction of the incident field upon which these scalar quantities operate (see Fig. 3.3).

If a hard reflection only exists at the back wall then two new scattering operators, $\mathcal{R}_b$ and $\mathcal{T}_b$, must be defined to take this into account. Similarly, if both front and back wall hard reflections exist then two more scattering operators must be defined, $\mathcal{R}_f$ and $\mathcal{T}_f$. These operators have been defined previously and discussed in detail elsewhere by Karlsson [26] and Fuks [15]. The operators are defined to be

$$\mathcal{R}_b u^+(0,t) = r_0^+ d_0^2 \mathcal{S}(\tau_0) u^+(0,t) + \left[R_b * u^+\right](0,t) \tag{3.84}$$

$$\mathcal{T}_b u^+(0,t) = t_L^+ d_0 u^+(0,t) + t_L^+ \left[T_b * u^+\right](0,t) \tag{3.85}$$

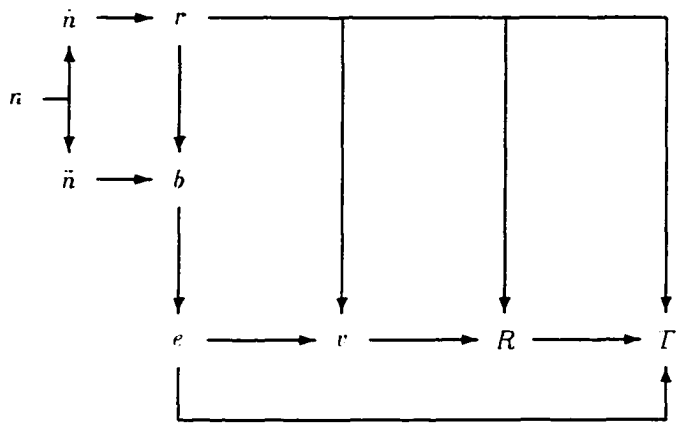

(a)

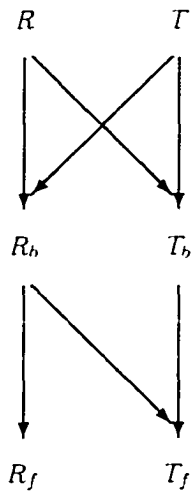

(b)

Figure 3.2 Flow chart for the forward problem: the impedance matched case. (a). and the impedance mismatched case. (b)

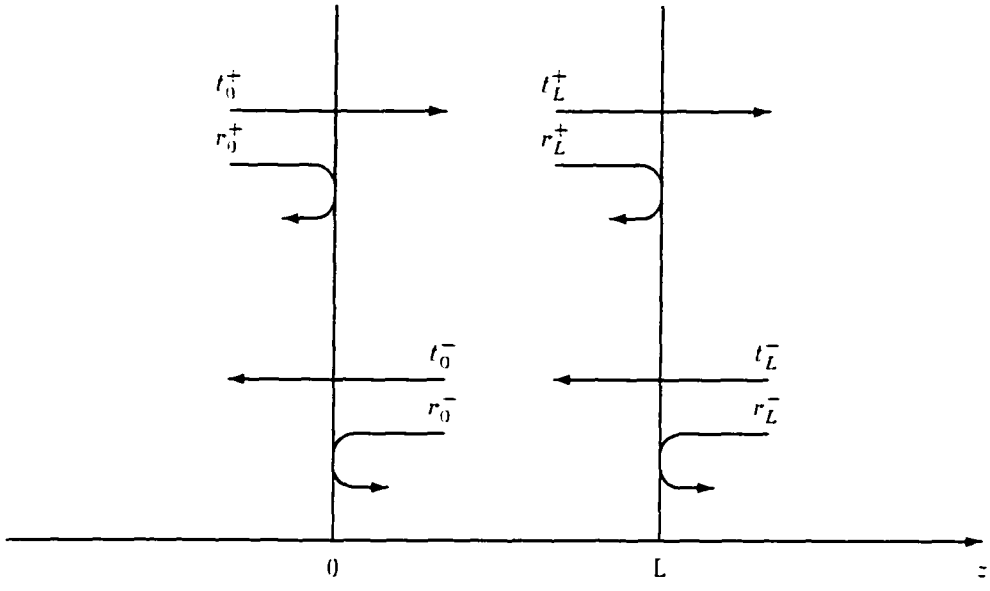

Figure 3.3 Pictorial representation of 'hard' scattering coefficients

and

$$\mathcal{R}_f u^+(0,t) = \sum_{j=0}^{\sim} a_j \mathcal{S}(j\tau_0) u^+(0,t) + \left[R_f * u^+\right](0,t) \tag{3.86}$$

$$\mathcal{T}_f u^+(0,t) = t_0^+ t_L^+ d_0 \sum_{j=0}^{\sim} b_j \mathcal{S}(j\tau_0) u^+(0,t) + t_0^+ t_L^+ \left[T_f * u^+\right](0,t) \tag{3.87}$$

where

$$\begin{aligned} a_0 &= r_0^+ \\ a_1 &= t_0^+ t_0^- r_L^+ d_0^2 \\ a_j &= r_0^- r_L^+ d_0^2 a_{j-1} \quad j = 2,3,4,\ldots \\ b_0 &= 1 \\ b_j &= r_0^- r_L^+ d_0^2 b_{j-1} \quad j = 1,2,3,\ldots \end{aligned} \tag{3.88}$$

The terms a_j and b_j with $d_0 = 1$ represent the terms that would exist if the viscoelastic slab were purely LHI elastic and impedance mismatched with respect to the LHI elastic halfspaces for $z < 0$ and $z > L$, respectively.

Fuks [15] has shown how to relate operators $\mathcal{R}_b$, $\mathcal{T}_b$, $\mathcal{R}_f$ and $\mathcal{T}_f$ to impedance matched operators $\mathcal{R}$ and $\mathcal{T}$ with a star product. When operators are replaced with their kernel representations a set of

delayed Volterra integral equations of the second kind result. The matched front wall and mismatched back wall kernel equations are

$$\begin{aligned} R_b &= R - r_L^+ [R * R - R * R_b] \\ &\quad + \mathcal{S}(\tau_0) \left[(r_L^+)^2 d_0^2 R + 2 r_L^+ d_0 T + r_L^+ T * T \right] \end{aligned} \tag{3.89}$$

$$T_b = T + r_L^+ d_0 R + r_L^+ R * T_b. \tag{3.90}$$

and for impedance mismatch at both front and back wall the Volterra equations are

$$R_f = R_b - r_0^+ R_b * R_f - r_0^+ r_L^+ d_0^2 \mathcal{S}(\tau_0) R_f - r_0^+ \sum_{j=0}^{\infty} a_j \mathcal{S}(j\tau_0) R_b \tag{3.91}$$

$$T_f = T_b - r_0^+ T_f * T_b - r_0^+ r_L^+ d_0^2 \mathcal{S}(\tau_0) T_f - r_0^+ d_0 \sum_{j=0}^{\infty} b_j \mathcal{S}(j\tau_0) R_b \tag{3.92}$$

where dependence, $(0, L, t)$, has been suppressed.

Scattering kernels: initial values and discontinuities

Initial values and discontinuities of the scattering kernels for viscoelastic media are essentially the same as for the dispersive electromagnetic case [15]. They are summarized here for completeness. Following from the previous section the initial values for the reflection and transmission kernels are, respectively,

$$r(0) = R(0) = R_b(0) = \frac{1}{4} \dot{n}_0 \tag{3.93}$$

$$R_f(0) = (1 - (r_0^+)^2) R_b(0) \tag{3.94}$$

$$T(0) = e(0) = -\frac{1}{4} \tau_0 d_0 \left[\ddot{n}_0 - \frac{1}{4} (\dot{n}_0)^2 \right] \tag{3.95}$$

$$T_b(0) = T(0) + r_L^+ d_0 R_b(0) \tag{3.96}$$

$$T_f(0) = T_b(0) - r_0^+ d_0 R_b(0). \tag{3.97}$$

At multiples of one round trip through the slab there are finite jumps which occur in the reflection and transmission kernels. There are no jumps in $r(t)$ and $T(t)$, one jump in $R(t)$ and $T_b(t)$ at $t = \tau_0$, two jumps in $R_b(t)$ at $t = \tau_0$, $2\tau_0$, and infinitely many jumps in $R_f(t)$ and $T_f(t)$ at $t = j\tau_0$ $j = 1, 2, 3, \ldots$. The notation $[R(j\tau_0)] = R(j\tau_0^+) - R(j\tau_0^-)$ is employed in what follows to denote a jump at $t = j\tau_0$. It follows that

$$[R(\tau_0)] = -\frac{1}{4} \dot{n}_0 d_0^2 \tag{3.98}$$

$$[R_b(\tau_0)] = [R(\tau_0)] + (r_L^+)^2 d_0 R(0) + 2 r_L^+ d_0 T(0) \tag{3.99}$$

$$[R_b(2\tau_0)] = (r_L^+ d_0)^2 [R(\tau_0)] \tag{3.100}$$

$$[T_b(\tau_0)] = r_L^+ d_0 [R(\tau_0)] \tag{3.101}$$

and finally for R_f and T_f

$$[R_f(\tau_0)] = (1 - r_0^+ a_0)[R_b(\tau_0)] - r_0^+ r_L^+ d_0^2 R_f(0) - r_0^+ a_1 R_b(0) \tag{3.102}$$

$$[R_f(2\tau_0)] = (1 - r_0^+ a_0)[R_b(2\tau_0)] - r_0^+ r_L^+ d_0^2 [R_f(\tau_0)] - r_0^+ a_1 [R_b(\tau_0)] - r_0^+ a_2 R_b(0) \tag{3.103}$$

$$[R_f(j\tau_0)] = (r_0^+ d_0)^2 [R_f((j-1)\tau_0)] - r_0^+ a_{j-2} [R_b(2\tau_0)] - r_0^+ a_{j-1} [R_b(\tau_0)] - r_0^+ a_j R_b(0) \quad j = 3, 4, 5, \ldots. \tag{3.104}$$

$$[T_f(\tau_0)] = r_L^+ d_0 [R_f(\tau_0)] + [T_b(\tau_0)] + r_L^+ a_1 T_b(0) \tag{3.105}$$

$$[T_f(j\tau_0)] = r_L^+ d_0 [R_f(j\tau_0)] + r_L^+ a_{j-1} [T_b(\tau_0)] + r_L^+ a_j T_b(0) \tag{3.106}$$

$$j = 2, 3, 4, \ldots.$$

For the inverse method the quantities d_0, τ_0, r_0^+, r_L^+ and $T_f(0)$ are assumed known. In the numerical experiments to follow d_0 and τ_0 are estimated from pulse transmission at asymptotically high frequency and r_0^+ is estimated from pulse reflection at high frequency. In cases to follow $r_L^+ = -r_0^+$ and $t_0^+ t_L^+ = 1 - (r_0^+)^2$. The term $T_f(0)$ is relatively difficult to estimate from measured data: therefore, it is neglected in most cases. Estimates of $\dot{n}_0$ and $\ddot{n}_0$ follow from eqs. 3.52 and 3.97, respectively: therefore,

$$\dot{n}_0 = -\frac{4}{\tau_0} \ln [d_0] \tag{3.107}$$

$$\ddot{n}_0 = \frac{1}{4}\dot{n}_0^2 - 2\tau_0^{-1} r_0^+ \dot{n}_0 - 4(\tau_0 d_0)^{-1} T_f(0). \tag{3.108}$$

The inverse algorithm requires $\dot{n}_0$, $\ddot{n}_0$ and $T_f(t)$.

The inverse algorithm employed was originally derived by Karlsson [26]. He observed that the equation which relates $T_f(t)$ to $\dot{n}(t)$ is a linear mapping from $\ddot{n}(t)$ to $T_f(t)$ so that in discretized form the mapping is

$$T_f(j\Delta t) = A_j + B_j \ddot{n}(j\Delta t) \tag{3.109}$$

where A_j and B_j are independent of $\ddot{n}(j\Delta t)$ but are dependent on $\dot{n}$ from earlier times. Fuks [15] states without proof that the reason for the mapping is that convolutions and additions are the only operations involved. This observation allows the forward algorithm to be employed as a basis for the inverse algorithm in the following manner: two dummy values for $\ddot{n}(j\Delta t)$ are chosen, $\ddot{n}_a$ and $\ddot{n}_b$, then the direct problem is solved to find dummy values for transmission kernels, T_{fa} and T_{fb}, for $t = j\Delta t$.

The values of A_j and B_j are determined from the system of two equations and two unknowns for each $j = 1, 2, 3, \ldots, N$, that is from

$$\begin{aligned} T_{fa} &= A_j + B_j \ddot{n}_a \\ T_{fb} &= A_j + B_j \ddot{n}_b. \end{aligned}$$

The last step is to estimate the true value of $\ddot{n}(j\Delta t)$ from eq. 3.109 with the values of A_j and B_j just obtained. It is assumed that $\dot{n}_0$ is known so $\dot{n}(j\Delta t)$ is determined by integrating $\ddot{n}(j\Delta t)$. Specific finite difference equations for A_j and B_j are very involved according to Karlsson [26]. The details are beyond the scope of this study. The algorithm for the inversion is as follows:

Given: r_0, d_0, r_0^+, $T_f(0)$ and T_{fi} $i = 1, 2, 3, \ldots, N$

Compute $\dot{n}_0$ and $\ddot{n}_0$ from given information

Let $c_1 = 0.9$ and $c_2 = -0.01$

Do $i = 1, N$ (N = number of time steps)

$\ddot{n}_i = \ddot{n}_{i-1}$

$\ddot{n}_{i,a} = \ddot{n}_{i-1}$

$\dot{n}_i = \dot{n}_{i-1} + (\Delta t)\ddot{n}_{i-1}$

Solve direct problem for $T_{fi,a}$

$\ddot{n}_i = c_1 \ddot{n}_{i-1} + c_2$

$\ddot{n}_{i,b} = \ddot{n}_i$

$\dot{n}_i = \dot{n}_{i-1} + (\Delta t/2)[\ddot{n}_i + \ddot{n}_{i-1}]$

Solve direct problem for $T_{fi,b}$

Compute coefficients

$B_i = (T_{fi,a} - T_{fi,b})/(\ddot{n}_{i,a} - \ddot{n}_{i,b})$

$A_i = T_{fi,a} - B_i \ddot{n}_{i,a}$

Solve for the 'true' value of $\ddot{n}_i$

$$\ddot{n}_i = (T_{f_i} - A_i)/B_i$$

Integrate $\ddot{n}_i$ to get $\dot{n}_i$

$$\dot{n}_i = \dot{n}_{i-1} + (\Delta t/2)\,[\ddot{n}_i + \ddot{n}_{i-1}]$$

End do.

The values for c_1 and c_2 are not critical. The validity of the approach is tested in Chapter 5 with wave data generated by the finite element method.

Scattering kernels: examples

The scattering kernels just presented are best interpreted by calculating and displaying kernels for some specific examples. For an example it is reasonable to assume a simple, single-exponential model for a viscoelastic medium:

$$M(t) = \left[M_e + (M_g - M_e)e^{-t/\tau}\right] H(t) \tag{3.110}$$

where

$$\rho = 1000\ kg/m^3 \tag{3.111}$$

$$V_e = 1700\ m/s \tag{3.112}$$

$$V_g = 2500\ m/s \tag{3.113}$$

$$M_e = \rho V_e^2 = 2.89\ \text{GPa} \tag{3.114}$$

$$M_g = \rho V_g^2 = 6.25\ \text{GPa}. \tag{3.115}$$

These limiting moduli are representative of a polymeric material that is a solid at room temperature. The relaxation time, τ, and the length of the viscoelastic slab, L, are variables in the calculations.

As an example, reflection and transmission kernels, (R, R_b, R_f) and (T, T_b, T_f), are shown in Fig. 3.4 for a slab thickness of $L = 5mm$ and a relaxation time of $\tau = 1\mu s$. Most notable are the jumps in the reflection kernels, Fig. 3.4(a), occurring at times equal to multiples of one round trip through the slab. For the impedance matched slab there is one jump in R at one round trip ($4\mu s$). In theory, R_f and T_f have jumps at every round trip but after about three round trips through the slab the jumps are negligible. In Fig. 3.5 kernels are plotted for $L = 5mm$ and increasing relaxation time. In this

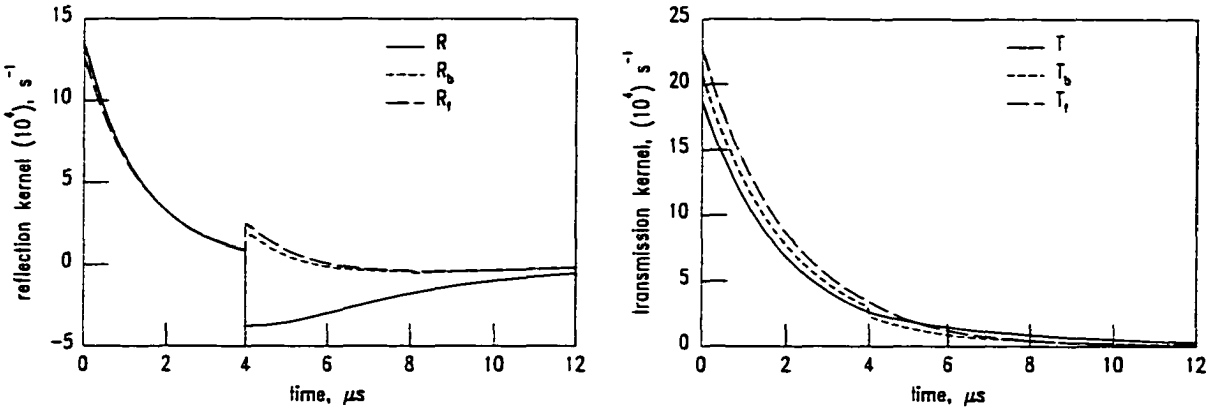

(a) (b)

Figure 3.4 Reflection kernels. (a). and transmission kernels. (b). for impedance matched. (R, T). mismatched back wall. (R_b, T_b). and mismatched front and back wall. (R_f, T_f). with $\tau = 1\mu s$ and $L = 5mm$

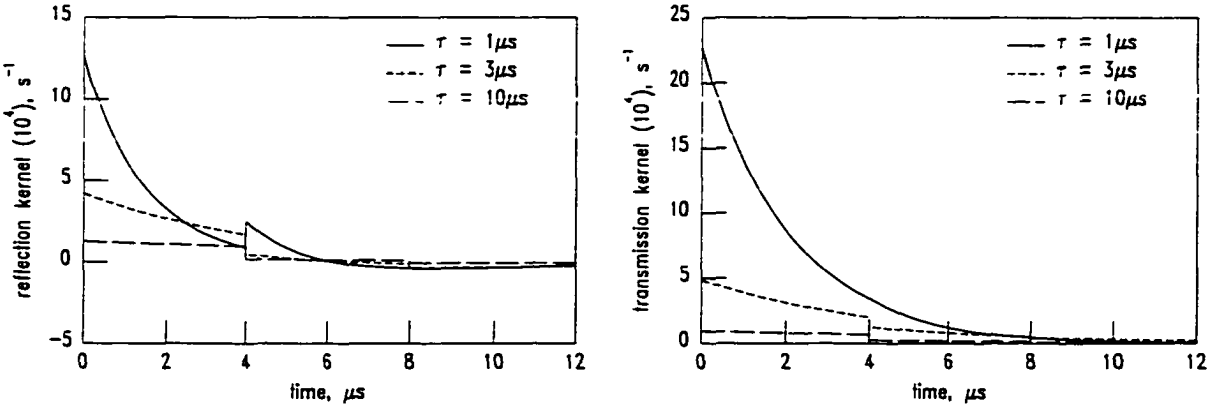

(a) (b)

Figure 3.5 Reflection kernels. R_f. and transmission kernels. T_f. in (a) and (b). respectively. for various relaxation times. τ. and $L = 5mm$

case initial values of kernels approach zero as relaxation time increases representing the approach to an essentially elastic regime. The elastic limit is achieved when $\tau \to \infty$ then $M(t) \to M_g$.

The effect of decreasing slab thickness is demonstrated in Fig. 3.6. In this case the transmission kernels have reduced initial amplitude and faster overall decay for decreasing slab thickness for the specified relaxation time. Intuitively this is reasonable because the attenuation and wave spreading

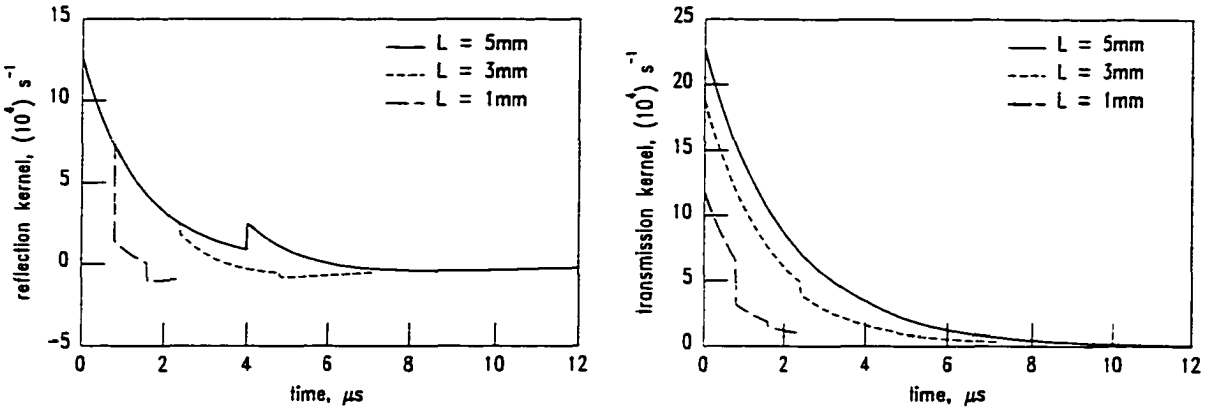

Figure 3.6 Reflection kernels, R_f, and transmission kernels, T_f, in (a) and (b), respectively, for various slab thicknesses, L, and $\tau = 1\mu s$

inherent in a viscoelastic medium have a cumulative effect on waves as they propagate; therefore, there will be relatively less overall effect on a transmitted wave if the slab is thinner. A less intuitive result is demonstrated in Figs. 3.7 and 3.8. Figure 3.7 shows that for a fixed relaxation time the transmission kernel has a maximum at time zero for a given slab thickness. It is possible that a wave transmitted through a slab with thickness such that its transmission kernel is maximum at time zero can carry relatively more information about the viscoelastic nature of the slab. In other words there may exist an optimal slab thickness for measuring viscoelastic moduli. Figure 3.8 shows the same characteristic, but in this case the slab width is held constant and the relaxation time is varied. In this case one notices that as the relaxation time decreases the peak of the reflection kernel becomes centered around one microsecond. One microsecond is approximately the difference in time delay for a wave to traverse the slab at asymptotically high and low frequencies, that is, $(5mm) \cdot (1/1.7km/s - 1/2.5km/s) = 0.94\mu s$ where the limiting high frequency wave speed is $2.5km/s$. These effects are made more clear when these kernels are convolved with an incident wave.

A model incident wave is plotted in Fig. 3.9(a) that is representative of a band-limited ultrasonic

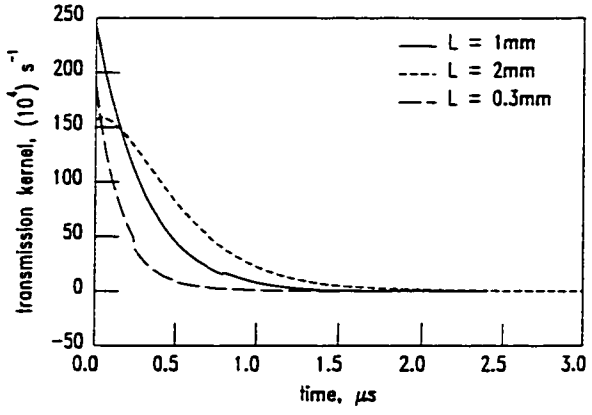

Figure 3.7 Transmission kernels, T_f, for various slab thicknesses, L, and $\tau = 100ns$, demonstrating maximum in T_f for a specific slab thickness, $L = 1mm$

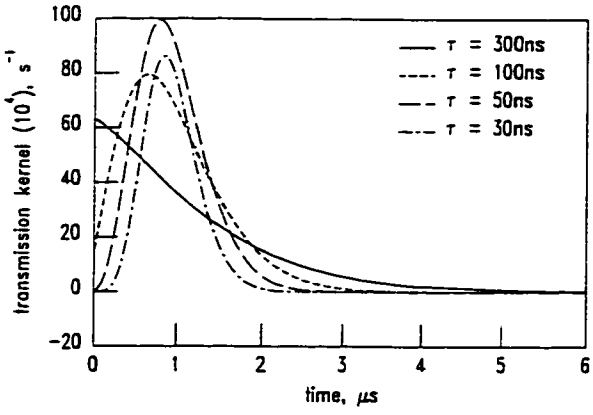

Figure 3.8 Transmission kernels, T_f, for various relaxation times, τ, and $L = 5mm$, demonstrating maximum in T_f for a specific relaxation time, $\tau = 50ns$

pulse. The pulse's normalized frequency spectrum magnitude is plotted in Fig. 3.9(b) along with normalized attenuation and wavespeed for a single-exponential viscoelastic medium with different relaxation times. As relaxation time lengthens attenuation and wavespeed curves move to the left or lower frequency and the incident wave magnitude lies more in the slab's high-frequency elastic region where little wave spreading and attenuation occur. Figures 3.10(a)-(c) show reflected waves and Figures 3.10(d)-(f) show transmitted waves for various relaxation times. Specifically, Figs. 3.10(a) and (d) show the portion of reflected and transmitted field that are due strictly to the hard reflection and transmission coefficients, $(r^{\pm}_{0,L}, t^{\pm}_{0,L})$, from eqs. 3.86 and 3.87; no convolutions are involved, only scalar multiplication. Figures 3.10(b) and (e) are reflected and transmitted portions of the field arising from convolution with R_f and T_f, respectively. The strongest reflection and transmission with respect to R_f and T_f occurs when $\tau = 0.1\mu s$ and the incident wave spectrum lies in the transition region between the viscous or low frequency region and the glassy, elastic or high frequency region (see Fig. 3.9(b)). Figures 3.10(c) and (f) are total reflected and transmitted fields, that is, they are sums of hard and convolutional or soft reflections and transmissions.

Figure 3.11 shows the shift in dominance from the directly transmitted wave, $t_0^+ t_L^+ \, d_0 u^+(0,t)$, to the 'indirect' wave, $t_0^+ t_L^+ T_f * u^+(0,t)$, when relaxation time shortens from $\tau = 300ns$ to $\tau = 50ns$. Ultimately, when relaxation time becomes short enough attenuation again decreases and the wave propagates relatively unattenuated in the slab's low frequency or viscous region. This point is made more clear in Chapter 4 when propagator inverse methods are discussed.

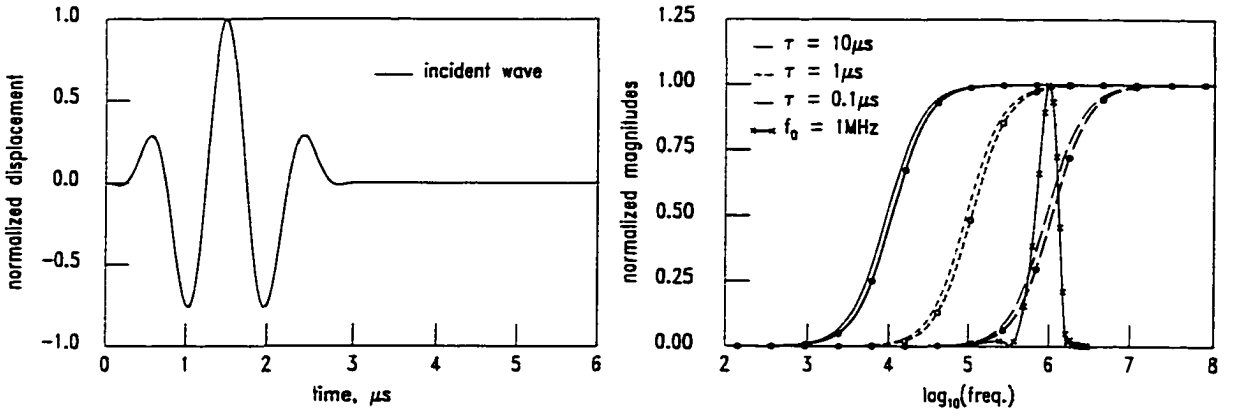

Figure 3.9 Example of incident waveform, (a), and normalized frequency spectrum compared with normalized attenuation and wavespeed (curves with symbols) versus relaxation time, (b)

Summary

Wave Splitting methods are a unique method for reformulating transient wave propagation from a second order hyperbolic PDE in terms of total displacement into an equivalent system of first order PDE's with left and right propagating waves. This decomposition naturally leads to definitions for reflection and transmission operators and their respective kernels. Wave splitting and invariant embedding allow formulation of integro-differential kernel equations that interrelate transmission and reflection kernels and material properties. Due to homogeneity of the viscoelastic medium, Laplace domain reflection and transmission kernels can be derived. A time-domain forward model for reflection and transmission is developed from Laplace domain kernels and is solved by finite difference methods. The forward-model kernel equations provide a well posed relationship between material properties and kernels or system impulse response functions. By an ingenious method due to Karlsson [26], the forward model becomes a basis for an inverse method that utilizes transmission kernel, $T_f(t)$. The inversion method has been demonstrated in a proof-of-principle experiment on a dispersive electromagnetic material [15] where the time dependent susceptibility, $\chi(t)$, was recovered. The susceptibility is analogous to the rate of change of the normalized creep compliance, $\dot{n}(t)$. Unfortunately, application of this wave splitting inversion method to the viscoelastic case is subject to severe technological constraints that are made more clear in subsequent chapters.

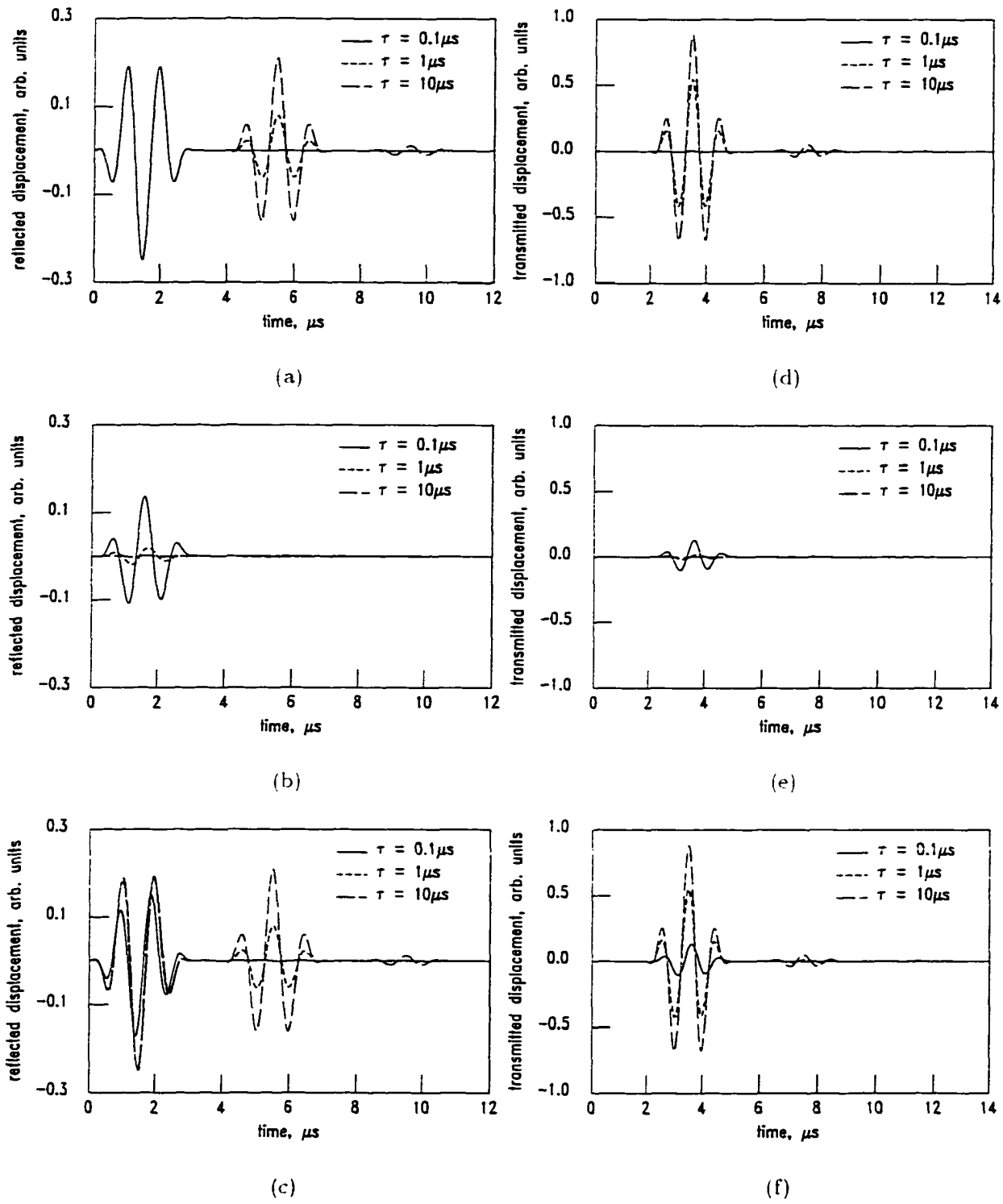

Figure 3.10 Reflected fields: hard. (a): soft. (b): total. (c): transmitted fields: hard. (d): soft. (e): total. (f). for slab thickness $L = 5mm$

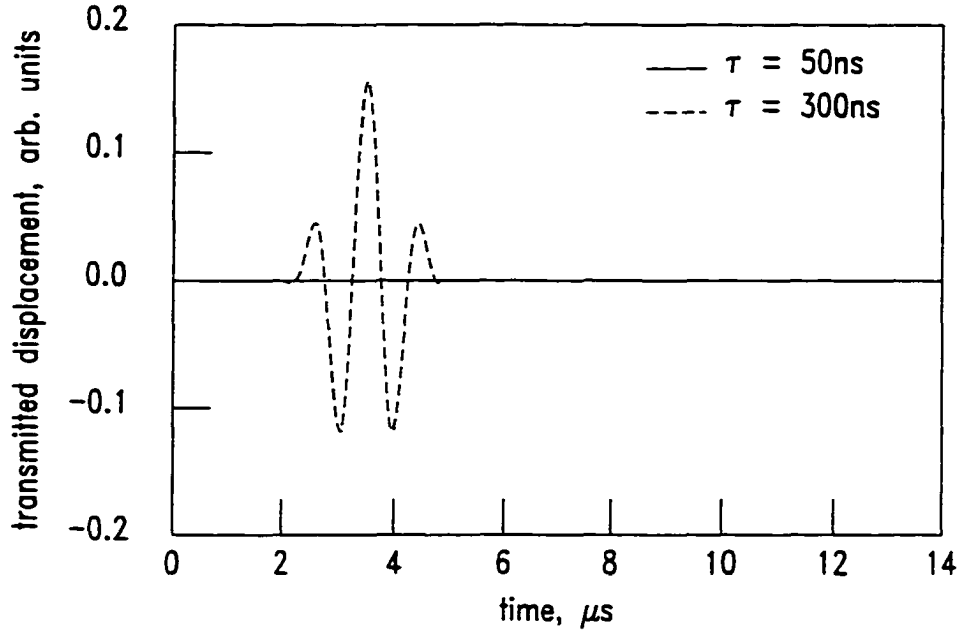

(a)

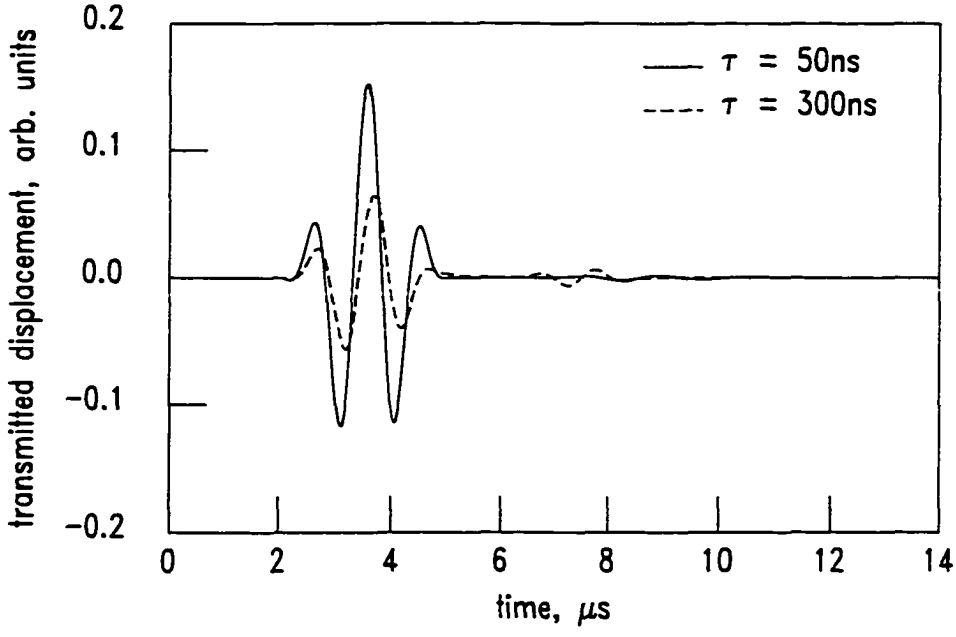

(b)

Figure 3.11 Transmitted wave for $\tau = 50ns, 300ns$: direct wave $(t_0^+ t_L^+ d_0 \sum_{j=0}^{3} b_j \mathcal{S}(j\tau_0) u^+(0,t))$, (a), and indirect wave $(t_0^+ t_L^+ T_f * u^+(0,t))$, (b)

CHAPTER 4 PROPAGATOR INVERSE METHODS

Introduction

Wave splitting methods require knowledge of system input and output: therefore, measurement of an incident wave is required which is not easily accomplished in most practical experimental situations. Recovering viscoelastic moduli from the transmission kernel also requires knowledge of attenuation at asymptotically high frequency, that is, knowledge of d_0 as well as n_0 and τ_0. 'Asymptotically high frequency' is not a well defined concept for real materials. All measurement apparatus has a limit to its shortest measurable time scale; therefore, requiring certain quantities be known at time equal to zero is practically impossible. To know material properties at a given time scale requires a measurement technique with time scales of the same order. Viscoelastic materials generally have time scales that span several orders of magnitude. More practical techniques for estimating moduli relate attenuation and wave speed measured over a frequency bandwidth to the real and imaginary components of the frequency-domain modulus. Several measurements with overlapping bandwidths can be combined to construct a composite modulus.

Methods described in this chapter are called 'propagator methods.' Propagator refers to the exponential propagator, $\exp(\pm\tilde{\gamma}z)$, that is a mathematical description of wave propagation from one point to another. Three propagator methods are described that rely on measurement of transmitted waves analogous to the wave splitting method. The methods in the order that they are described are the two-slab method, the slab substitution method and the Hankel transform method. In the two-slab method transmission measurements are made on two slabs of different thicknesses. For the slab substitution method a transmission measurement is made with and with out the slab in the propagation path. A calibration reflection measurement is required for the slab substitution method. Finally, the Hankel transform method specifies that the transmitted wave be measured with a point-like receiver along a radial line from the beam center. The measured signal is then integrated along this radial line effectively removing dependence on the radial coordinate. The Hankel transform method is combined with the first two methods. It is not a distinctly separate method, but it is another way to collect and process

data to remove beam spreading effects.

The basic theory for the two-slab and slab substitution method is one dimensional. A 1-D theory gives the simplest relation between measurable data and attenuation and wave speed. Propagator methods have been applied experimentally in a number of studies for solids [20, 23, 30, 32, 55, 63] and liquids [25, 50]. Pure plane waves do not exist in ultrasonic experiments. Real waves undergo decay due to geometrical spreading. An approximate diffraction correction is often included with one dimensional theory to account for the beam spreading [23, 30]. In other cases the correction is ignored entirely [20, 32] or some argument is offered to justify neglecting it [55, 63]. With the finite element test bed, numerical experiments are performed under controlled conditions with known material properties to test the validity of the one-dimensional theories with and without a diffraction correction.

Two-Slab Method

Assume a purely one dimensonal system with an ultrasonic source positioned a distance, L_1, to the left of a viscoelastic slab of thickness L as in Fig. 4.1. A receiver is situated to the right of the slab at distance L_2. In most cases the slab is a solid and the medium to the left and right of the slab is a fluid, usually water. An ultrasonic pulse is launched from the source, passes through the slab and arrives at the receiver. This process is repeated on a second slab of the same material with a different thickness, $L + \Delta L$, where ΔL can be positive or negative. The description of this process in the frequency domain is the following:

$$\hat{A}_L(\omega) = e^{-\tilde{\gamma}_w L_2} \hat{T}_L^+ e^{-\tilde{\gamma} L} \hat{T}_0^+ e^{-\tilde{\gamma}_w L_1} \hat{A}_i(\omega) \tag{4.1}$$

$$\hat{A}_{L+\Delta L}(\omega) = e^{-\tilde{\gamma}_w L_2 - \Delta L} \hat{T}_L^+ e^{-\tilde{\gamma}(L+\Delta L)} \hat{T}_0^+ e^{-\tilde{\gamma}_w L_1} \hat{A}_i(\omega) \tag{4.2}$$

where

$$\tilde{\gamma}_w(\omega) = \alpha_w(\omega) + i\frac{\omega}{c_w} \tag{4.3}$$

$$\tilde{\gamma}(\omega) = \alpha(\omega) + i\frac{\omega}{c(\omega)} \tag{4.4}$$

$$\hat{T}_0^+(\omega) = \frac{2Z_w}{Z_w + \tilde{Z}(\omega)} \tag{4.5}$$

$$\hat{T}_L^+(\omega) = \frac{2\tilde{Z}(\omega)}{Z_w + \tilde{Z}(\omega)} \tag{4.6}$$

$$Z_w = \rho_w c_w \tag{4.7}$$

$$\tilde{Z}(\omega) = \rho \tilde{c}(\omega) \tag{4.8}$$

$$\hat{A}_L(\omega) = A_L(\omega) e^{i\phi_L(\omega)} \tag{4.9}$$

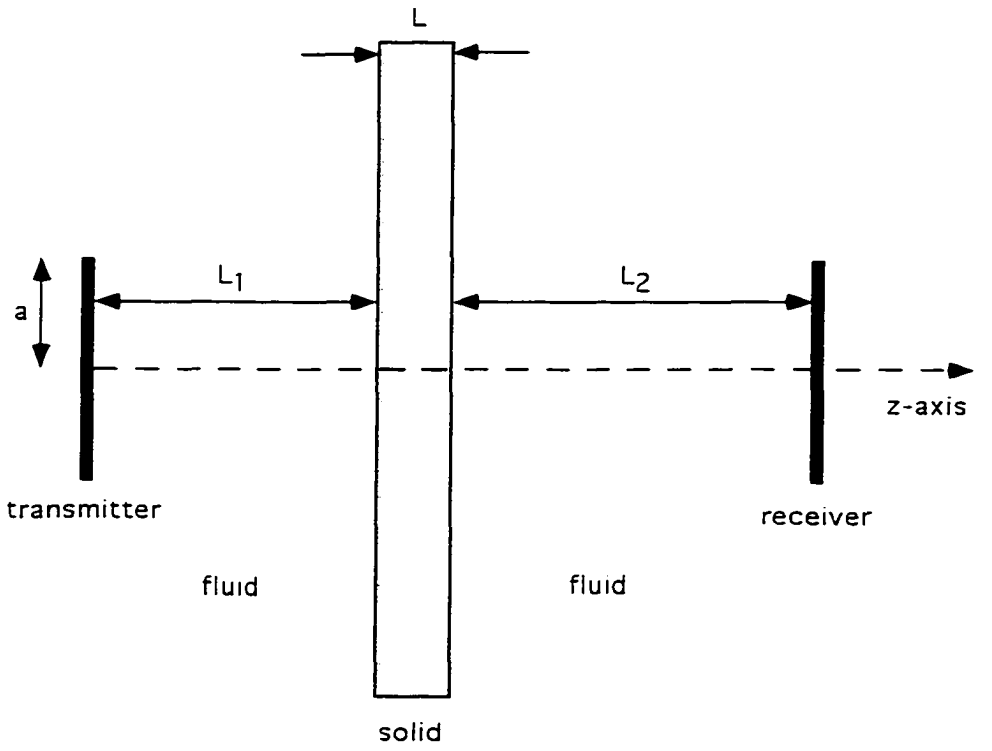

Figure 4.1 Geometry for two-slab and slab substitution methods

$$\tilde{A}_{L+\Delta L}(\omega) = A_{L+\Delta L}(\omega)e^{i\Phi_{L+\Delta L}(\omega)} \tag{4.10}$$

$$\tilde{A}_i(\omega) = A_i(\omega)e^{i\Phi_i(\omega)}. \tag{4.11}$$

The terms, $\tilde{A}_i(\omega)$ and $\tilde{A}_L(\omega)$ and $\tilde{A}_{L+\Delta L}(\omega)$ represent the Fourier transforms of the incident pulse, subscript 'i', and the received or transmitted pulse with slab of length L and $L + \Delta L$, respectively. $\tilde{\gamma}_w(\omega)$ and $\tilde{\gamma}(\omega)$ are the propagation factors for water and the slab and $\tilde{T}_0^+(\omega)$ and $\tilde{T}_L^+(\omega)$ are the transmission coefficients at the left and right interface, respectively. The term $L_2 - \Delta L$ implies that the transducers are not repositioned when the second slab is placed between them. In practice it may be necessary to reposition the receiver in order to bring the received signal within the digitizing window when a second slab is placed in the propagation path or when the slab is removed completely [32]. The wave speed in water is usually assumed independent of frequency to a relatively high frequency when operating at a given temperature,

$$c_w \approx 1500\ m/s. \tag{4.12}$$

The attenuation increases with the square of the frequency:

$$\alpha_w(\omega) = \alpha_0 f^2 \tag{4.13}$$

where $\alpha_0 = (21.20 \pm 0.05)10^{-17}\ s^2/cm$ for distilled water at 25°C [50].

To recover the attenuation and wave speed from the useful bandwidth of the measurement system, the ratio of $\tilde{A}_{L+\Delta L}$ to $\tilde{A}_L$ is taken which gives

$$\frac{\tilde{A}_{L+\Delta L}(\omega)}{\tilde{A}_L(\omega)} = e^{(\alpha_w - \alpha(\omega))\Delta L} \tag{4.14}$$

$$= e^{(\alpha_w - \alpha(\omega))\Delta L} e^{i\omega\left(\frac{1}{c_w} - \frac{1}{c(\omega)}\right)\Delta L} \tag{4.15}$$

where

$$\left|\frac{\tilde{A}_{L+\Delta L}(\omega)}{\tilde{A}_L(\omega)}\right| = e^{(\alpha_w - \alpha(\omega))\Delta L} \tag{4.16}$$

$$\phi_{\Delta L}(\omega) = \arctan\left[\frac{\Im\left(\tilde{A}_{L+\Delta L}/\tilde{A}_L\right)}{\Re\left(\tilde{A}_{L+\Delta L}/\tilde{A}_L\right)}\right] \tag{4.17}$$

$$= \omega\left(\frac{1}{c_w} - \frac{1}{c(\omega)}\right)\Delta L \tag{4.18}$$

Attenuation and wave speed of the slab follow from the magnitude and phase angle:

$$\alpha(\omega) = \alpha_w(\omega) - \frac{1}{\Delta L}\ln\left|\frac{\tilde{A}_{L+\Delta L}(\omega)}{\tilde{A}_L(\omega)}\right| \tag{4.19}$$

$$c(\omega) = \frac{c_w}{1 - \frac{c_w \phi_{\Delta L}(\omega)}{\omega \Delta L}}. \tag{4.20}$$

Accurate determination of slab attenuation and wavespeed depends on accurate knowledge of the water attenuation versus frequency and wavespeed which is assumed constant at the measurement temperature. If the receiving transducer's original position, L_2, is adjusted to compensate for the length difference of the second slab, ΔL, then the effects of the water can be eliminated. For example, if the second slab is longer than the first slab then ΔL is positive and the receiving transducer must move to the right in Fig. 4.1 when the second slab is inserted. The corresponding attenuation and wavespeed simplify to

$$\alpha(\omega) = -\frac{1}{\Delta L}\ln\left|\frac{\tilde{A}_{L+\Delta L}(\omega)}{\tilde{A}_L(\omega)}\right| \tag{4.21}$$

$$c(\omega) = -\frac{\omega \Delta L}{\phi_{\Delta L}(\omega)}. \tag{4.22}$$

Diffraction corrections

Equations 4.1 and 4.2 are valid for one-dimensional plane waves. Plane waves do not decay due to geometric spreading. In contrast waves produced by axisymmetric finite apertures have a complex sound

field composed of planar and non-planar waves that decay with distance from their source. For a plane piston source the non-planar effects emanate from the rim or edge of the transducer. 'Edge waves' are a source of diffraction or beam spreading for on-axis propagating displacement. Diffraction correction factors have been derived that account for geometric decay of waves in an approximate manner when included in eqs. 4.1 and 4.2. Diffraction correction coefficients have been described in a number of works [5, 6, 28, 39, 41, 51, 52] and employed in ultrasonic forward-scattering models [48] and recently in experimental measurement situations [23].

Diffraction corrections are derived from knowledge of the pressure field due to a circular plane-piston source with finite radius 'a'. The piston resides in an infinite rigid baffle and oscillates with angular frequency ω (see Fig. 4.2). The amplitude of the speed of the piston's harmonic motion is V_0 and the piston radiates into an LHI acoustic medium, for example water, with wave speed c_w. Rogers and Van Buren [39] give the equation, originally derived by Lord Rayleigh, for the pressure field due to a piston

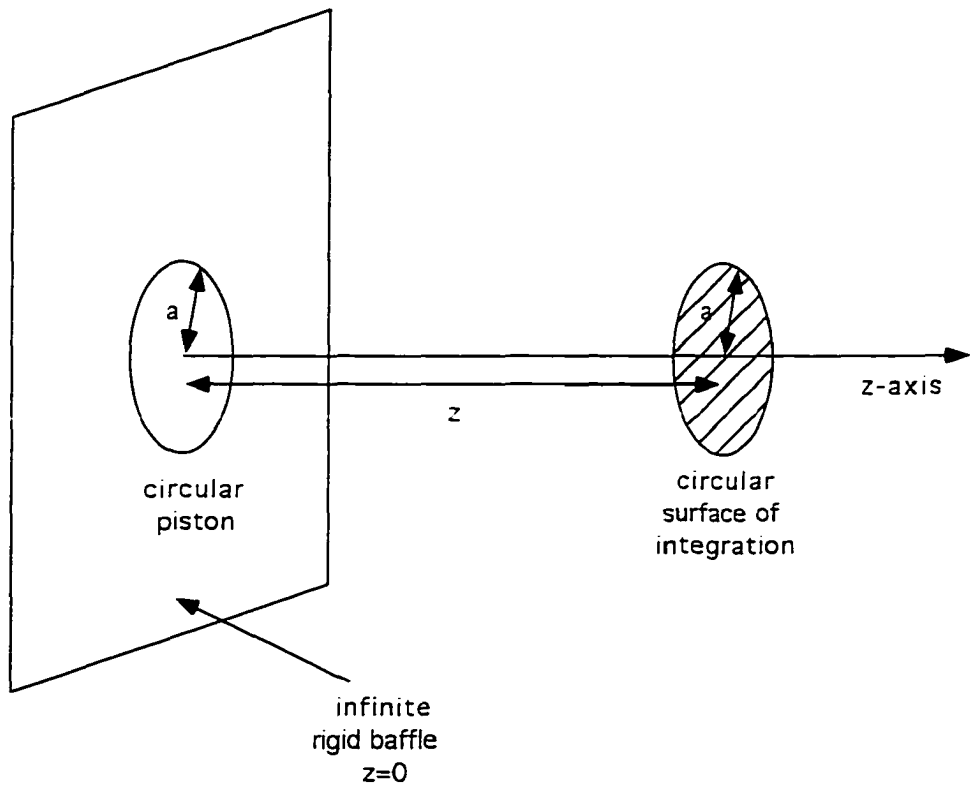

Figure 4.2 Geometry for diffraction correction calculation of a piston transmitter

source as

$$P(r,z,\omega) = \frac{i\omega\rho_0 V_0}{2\pi}\int_0^a\int_0^{2\pi}\frac{\exp\left[-ik(r^2+r_0^2-2rr_0\cos(\theta_0)+z^2)^{1/2}\right]}{\left[r^2+r_0^2-2rr_0\cos(\theta_0)+z^2\right]^{1/2}}r_0 dr_0 d\theta_0 \qquad (4.23)$$

where the term $(\cdots)^{1/2}$ is the distance between the field point, $(r,0,z)$, and the source point, $(r_0,\theta_0,0)$. From Williams [51] the average acoustic pressure over a disk of radius a that is coaxial with and a distance z in front of the piston source is given by

$$\langle P(z,\omega)\rangle = \rho_0 c_w V_0\left[e^{-ikz} - \frac{4}{\pi}\int_0^{\pi/2}\exp\left[-ik(z^2+4a^2\cos^2(x))^{1/2}\right]\sin^2(x)dx\right]. \qquad (4.24)$$

Assuming a pressure sensitive receiver exists that has an output proportional to the average pressure over its face then the diffraction correction, $\bar{D}(z,\omega)$, for such a receiver with radius a (equal to the radius of the transmitter) is defined as the ratio of the average pressure to that of an ideal plane wave, $P_0(z,\omega) = \rho_0 c V_0 e^{-ikz}$:

$$\bar{D}(z,\omega) = \langle P(z,\omega)\rangle / P_0(z,\omega) = 1 - \frac{4}{\pi}e^{ikz}\int_0^{\pi/2}\exp\left[-ik(z^2+4a^2\cos^2(x))^{1/2}\right]\sin^2(x)dx. \qquad (4.25)$$

Rogers and Van Buren [39] showed that in the limit $ka \to \infty$ the diffraction correction in eq. 4.25 becomes

$$\bar{D}^{\infty}(S) = 1 - e^{-i(2\pi/S)}\left[J_0(2\pi/S) + iJ_1(2\pi/S)\right] \qquad (4.26)$$

where $S = 2\pi c_w z/\omega a^2 = z\lambda_w/a^2$ and J_0 and J_1 are Bessel functions of order zero and one, respectively.

It is not obvious how to incorporate diffraction corrections into eqs. 4.1 and 4.2 because corrections have been derived assuming no intervening slab of material between transmitter and receiver. Thompson [18] and Jeong [23] both employ a limiting form of the diffraction correction, eq. 4.26, for cases involving propagation through one or more materials. They assume diffraction corrections, $\bar{D}^{\infty}(S)$, for a propagation path with slabs of thickness L and $L+\Delta L$, respectively, placed between the transducers are, respectively,

$$\bar{D}_L^{\infty} = \bar{D}^{\infty}(S_w + S_L) \qquad (4.27)$$

$$\bar{D}_{L+\Delta L}^{\infty} = \bar{D}^{\infty}(S_w + S_L + S_{\Delta L}) \qquad (4.28)$$

where

$$S_w = (L_1 + L_2)c_w\left[\frac{2\pi}{\omega a^2}\right] \qquad (4.29)$$

$$S_L = Lc(\omega)\left[\frac{2\pi}{\omega a^2}\right] \qquad (4.30)$$

$$S_{\Delta L} = (c(\omega) - c_w)\Delta L\left[\frac{2\pi}{\omega a^2}\right]. \qquad (4.31)$$

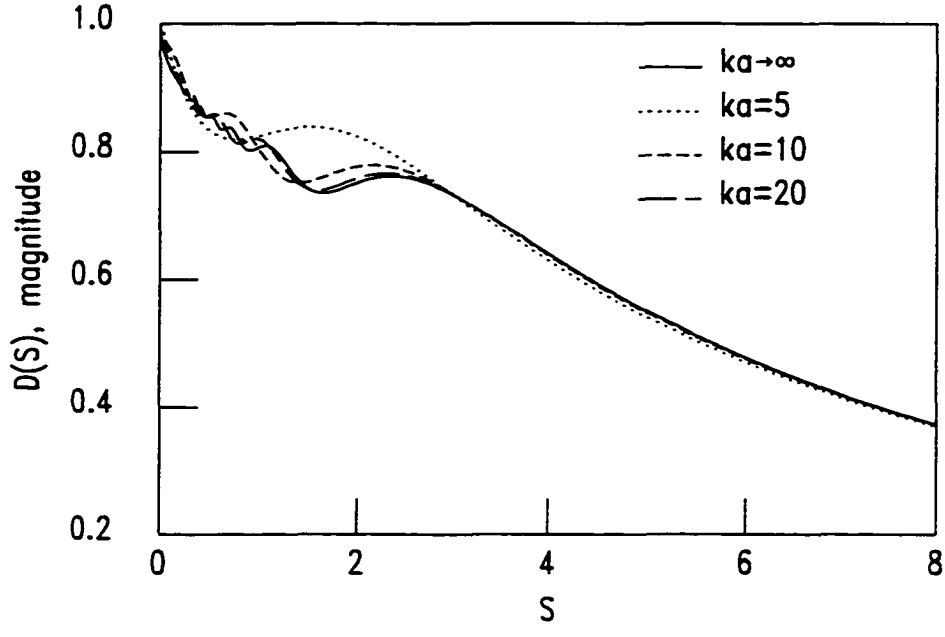

(a)

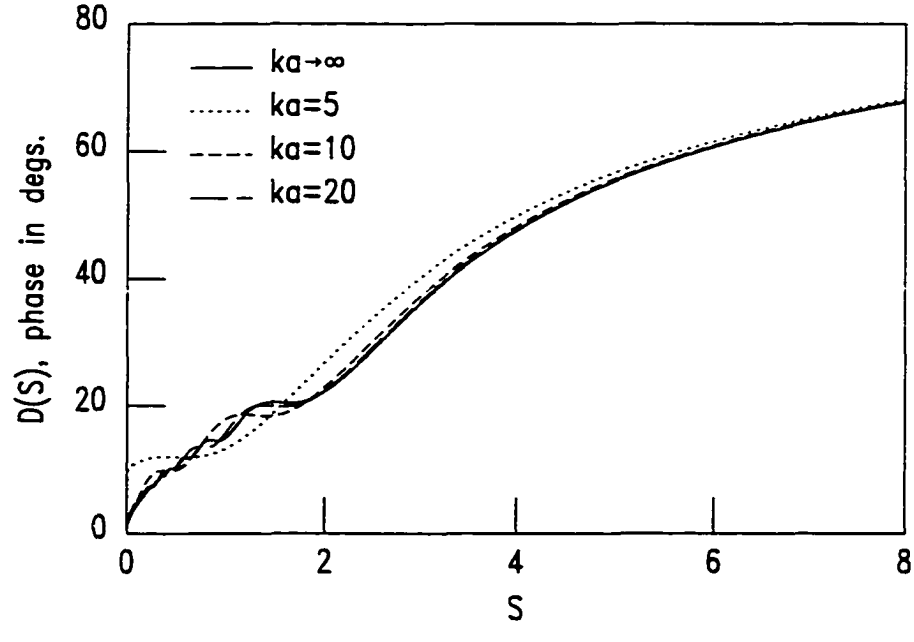

(b)

Figure 4.3 Exact diffraction correction, $D(S)$, versus ka and normalized distance, $S = 2\pi c_w z/\omega a^2$, compared with $D^{\infty}(S)$, magnitude (a) and phase in degrees (b)

Attenuation in water and the slab is neglected in $\tilde{D}^{\sim}(S)$ but is accounted for in the propagator terms, $e^{-\gamma_w(L_1+L_2)}$ and $e^{-\gamma L}$, respectively. Notice that $c(\omega)$ is required to compute S, but $c(\omega)$ is one of the unknowns to be measured. This point is taken up in Chapter 5.

Diffraction corrected received signals, denoted by superscript 'D', become

$$\tilde{A}_L^D(\omega) = \tilde{D}_L^{\sim}\tilde{A}_L(\omega) \tag{4.32}$$

$$\tilde{A}_{L+\Delta L}^D(\omega) = \tilde{D}_{L+\Delta L}^{\sim}\tilde{A}_{L+\Delta L}(\omega). \tag{4.33}$$

In a real measurement actual measured signals correspond to $\tilde{A}_L^D(\omega)$ and $\tilde{A}_{L+\Delta L}^D(\omega)$ for two different slab lengths. The goal is to remove beam spreading to recover effective plane wave signals. This is accomplished by dividing measured signals by appropriate diffraction corrections. The extent to which beam spreading can be removed and material properties recovered via plane wave theory is one theme of this work and is facilitated by an FEM test bed.

The equations for attenuation and wave speed, eqs. 4.19 and 4.20, including diffraction corrections become

$$\alpha(\omega) = \alpha_w(\omega) - \frac{1}{\Delta L}\ln\left[\frac{|\tilde{A}_{L+\Delta L}^D/\tilde{A}_L^D|}{|\tilde{D}_{L+\Delta L}^{\sim}/\tilde{D}_L^{\sim}|}\right] \tag{4.34}$$

$$c(\omega) = \frac{c_w}{1 - \frac{c_w(\phi_{\Delta L} - \phi_D)}{\omega\Delta L}} \tag{4.35}$$

where

$$\phi_D(\omega) = \arctan\left[\frac{\Im(\tilde{D}_{L+\Delta L}^{\sim}/\tilde{D}_L^{\sim})}{\Re(\tilde{D}_{L+\Delta L}^{\sim}/\tilde{D}_L^{\sim})}\right] \tag{4.36}$$

Figure 4.3 shows exact diffraction correction, $\tilde{D}$, eq. 4.25, versus S for increasing ka compared with correction, $\tilde{D}^{\sim}$, eq. 4.26, valid for $ka \to \infty$. For ka greater than about twenty exact and limiting diffraction corrections are practically indistinguishable.

Slab Substitution Method

Slab substitution requires removing the slab under test and replacing it with a 'known' material, that is, a material whose properties are relatively well characterized versus frequency and temperature. The usual test situation is a solid slab immersed in water. When the slab is removed water takes the place of the slab. This technique is more common than the two-slab method [23, 32, 63].

The slab substitution method is described by the following equations:

$$\tilde{A}_L(\omega) = e^{-\gamma_w L_2}\tilde{T}_L^+ e^{-\gamma L}\tilde{T}_0^+ e^{-\gamma_w L_1}\tilde{A}_i(\omega) \tag{4.37}$$

$$\tilde{A}_w(\omega) = e^{-\gamma_w(L_1+L_2+L)}\tilde{A}_i(\omega) \tag{4.38}$$

where $\tilde{A}_w(\omega)$ represents the Fourier transform of the received signal when water (or other known fluid) replaces the slab. The ratio $\tilde{A}_L/\tilde{A}_w$ is

$$\frac{\tilde{A}_L(\omega)}{\tilde{A}_w(\omega)} = \tilde{T}_L^+\tilde{T}_0^+ e^{(\cdots)L} \tag{4.39}$$

$$= \left|\tilde{T}_L^+\tilde{T}_0^+\right| e^{i\phi_T} e^{(\alpha_w - \alpha(\omega))L} e^{i\omega\left(\frac{1}{c_w} - \frac{1}{c(\omega)}\right)L} \tag{4.40}$$

where the magnitude and phase angle are

$$\left|\frac{\tilde{A}_L(\omega)}{\tilde{A}_w(\omega)}\right| = \left|\tilde{T}_L^+\tilde{T}_0^+\right| e^{(\alpha_w - \alpha(\omega))L} \tag{4.41}$$

$$\phi(\omega) = \arctan\left[\frac{\Im\left(\tilde{A}_L/\tilde{A}_w\right)}{\Re\left(\tilde{A}_L/\tilde{A}_w\right)}\right]. \tag{4.42}$$

$$= \phi_T(\omega) + \phi_L(\omega) \tag{4.43}$$

$$\phi_T(\omega) = \arctan\left[\frac{\Im\left(\tilde{T}_L^+\tilde{T}_0^+\right)}{\Re\left(\tilde{T}_L^+\tilde{T}_0^+\right)}\right] \tag{4.44}$$

$$\phi_L(\omega) = \omega\left(\frac{1}{c_w} - \frac{1}{c(\omega)}\right)L. \tag{4.45}$$

Usually media on the left and right side of the slab are the same; therefore, transmission coefficient terms can be written in terms of the reflection coefficient: $\tilde{T}_L^+\tilde{T}_0^+ = 1 - \left(\tilde{R}_0^+\right)^2$. Attenuation and wave speed are recovered from the magnitude and phase angle of the ratio of the signals, with and without the slab, in the following manner:

$$\alpha(\omega) = \alpha_w(\omega) - \frac{1}{L}\ln\left[\frac{\left|\tilde{A}_L(\omega)/\tilde{A}_w(\omega)\right|}{\left|1 - \left(\tilde{R}_0^+\right)^2\right|}\right] \tag{4.46}$$

$$c(\omega) = \frac{c_w}{1 - \frac{c_w(\phi - \phi_T)}{\omega L}}. \tag{4.47}$$

A reflection measurement is necessary to estimate the reflection coefficient, $\tilde{R}_0^+$, as compared with the two-slab approach where only transmission data are required.

Analogous to the previous section, diffraction corrections can be incorporated into the attenuation and wave speed relationships for the slab substitution method. In this case diffraction corrections are

$$\tilde{D}_s^\infty = \tilde{D}^\infty(S_w + S_{sL}) \tag{4.48}$$

$$\tilde{D}_w^\infty = \tilde{D}^\infty(S_w + S_{wL}) \tag{4.49}$$

with

$$S_w = (L_1 + L_2)c_w\left[\frac{2\pi}{\omega a^2}\right] \tag{4.50}$$

$$S_{sL} = Lc(\omega)\left[\frac{2\pi}{\omega a^2}\right] \tag{4.51}$$

$$S_{wL} = Lc_w\left[\frac{2\pi}{\omega a^2}\right]. \tag{4.52}$$

Received signals with diffraction correction are

$$\tilde{A}_L^D(\omega) = \tilde{D}_s^{\infty} \tilde{A}_L(\omega) \tag{4.53}$$

$$\tilde{A}_w^D(\omega) = \tilde{D}_w^{\infty} \tilde{A}_w(\omega) \tag{4.54}$$

and attenuation and wave speed with correction are

$$\alpha(\omega) = \alpha_w(\omega) - \frac{1}{L} \ln \left[\frac{\left| \tilde{A}_L(\omega) / \tilde{A}_w(\omega) \right|}{\left| 1 - (\tilde{R}_0^+)^2 \right| \left| \tilde{D}_s^{\infty} / \tilde{D}_w^{\infty} \right|} \right] \tag{4.55}$$

$$c(\omega) = \frac{c_w}{1 - \frac{c_w (\phi_D - \phi_T - \phi_{D'})}{\omega L}} \tag{4.56}$$

where

$$\phi_D = \arctan \left[\frac{\Im \left(\tilde{D}_s^{\infty} / \tilde{D}_w^{\infty} \right)}{\Re \left(\tilde{D}_s^{\infty} / \tilde{D}_w^{\infty} \right)} \right]. \tag{4.57}$$

As was mentioned previously, a reflection measurement is required to estimate $\tilde{R}_0^+$. This is usually accomplished by making a 'calibration' reflection measurement [32]. Calibration requires measuring a reflected signal from a material whose impedance is relatively well known, for example aluminum or fused quartz. The calibration reflection coefficient is

$$R_{0,cal}^+ = \frac{Z_w - Z_{cal}}{Z_w + Z_{cal}} \tag{4.58}$$

with Z_w and Z_{cal} assumed known. The reflected signals, subsript r, with diffraction correction are

$$\tilde{A}_{r,L_1}^D(\omega) = \tilde{D}_{L_1}^{\infty} e^{-2\gamma_w L_1} \tilde{R}_0^+ \tilde{A}_1(\omega) \tag{4.59}$$

$$\tilde{A}_{r,L_1}^{D,cal}(\omega) = D_{L_1}^{\infty} e^{-2\gamma_w L_1} R_{0,cal}^+ \tilde{A}_1(\omega). \tag{4.60}$$

Diffraction correction, $\tilde{D}_{L_1}^{\infty}$, is evaluated at $S_{L_1} = 2L_1 c_w \left[2\pi / \omega a^2 \right]$. Upon dividing $\tilde{A}_{r,L_1}^D$ by $\tilde{A}_{r,L_1}^{D,cal}$ the unknown reflection coefficient is

$$\tilde{R}_0^+(\omega) = \left[\frac{\tilde{A}_{r,L_1}^D(\omega)}{\tilde{A}_{r,L_1}^{D\,cal}(\omega)} \right] R_{0,cal}^+. \tag{4.61}$$

Notice that the calibration reflection coefficient is not considered a function of frequency.

Hankel Transform Method

Diffraction corrections that have been described are an approximate method to account for geometrical spreading and decay of waves emitted from a finte aperture transmitter. These corrections transform the original one-dimensional theory into an approximate axisymmetric theory. Another approximate method is described that effectively integrates out the radial dependence of an axisymmetric field via a

Hankel transform. When the transform parameter, ξ, is set to zero the Hankel transformed equations revert to one-dimensional equations. The set of transmission equations without diffraction correction presented for the two-slab, eqs. 4.1 and 4.2, and slab substitution method, eqs. 4.37 and 4.38, can be used directly except that the transmitted wave must be collected along a radial line outward from the beam axis. The method is dependent on how well the receiver approximates a point receiver relative to transmitter beam width and diameter.

The viscoelastic wave equation for displacement is

$$M * \nabla\nabla \cdot \dot{\mathbf{u}} - G * \nabla \times \nabla \times \dot{\mathbf{u}} = \rho\ddot{\mathbf{u}}. \tag{4.62}$$

The shear relaxation modulus is $G(t)$ and the longitudinal relaxation modulus is $M(t) = K(t) + \frac{4}{3}G(t)$ where $K(t)$ is the bulk relaxation modulus. If only longitudinal waves are of interest then neglecting the second term on the left hand side simplifies the wave equation to

$$M * \nabla\nabla \cdot \dot{\mathbf{u}} = \rho\ddot{\mathbf{u}}. \tag{4.63}$$

With this approximation all shear wave phenomena are neglected within the viscoelastic slab. On the other hand this approximation simplifies the scattering process because all longitudinal to shear and shear to longitudinal mode conversions that occur at slab/water interfaces are eliminated. The appropriate displacement wave equation for water, the immersion fluid, is

$$K_w \nabla\nabla \cdot \mathbf{u} = \rho_w \ddot{\mathbf{u}}. \tag{4.64}$$

where water is aasumed inviscid, compressible and lossless.

A Laplace Hankel transform for a time dependent, axisymmetric function is given by

$$\tilde{f}^{\nu}(\xi, s) = \mathcal{L}\left[\mathcal{H}_{\nu}\left[f(r,t)\right]\right] = \int_0^{\infty}\int_0^{\infty} f(r,t) r J_{\nu}(r\xi) e^{-st} dr ds \tag{4.65}$$

where ν is usually a positive integer or zero [42]. A Laplace-Hankel transform of order zero and one of the axial and radial components of the vector wave equation, respectively, replaces dependence on radial coordinate, r, and time, t, with transform parameters ξ and s, respectively. Resultant transformed equations are

$$s\tilde{M}\partial_z\left[\xi\tilde{u}_r^1 + \partial_z\tilde{u}_z^0\right] = \rho s^2\tilde{u}_z^0 \quad (z) \tag{4.66}$$

$$-s\tilde{M}\xi\left[\xi\tilde{u}_r^1 + \partial_z\tilde{u}_z^0\right] = \rho s^2\tilde{u}_r^1 \quad (r) \tag{4.67}$$

where it is assumed that $u_z(r, z, 0) = \dot{u}_z(r, z, 0) = 0$. After decoupling the radial and axial components these equations become

$$\partial_z^2\tilde{u}_z^0 = \left[\xi^2 + \frac{s^2}{\tilde{c}_l^2}\right]\tilde{u}_z^0 \quad (z) \tag{4.68}$$

$$\partial_z^2 \tilde{u}_r^1 = \left[\xi^2 + \frac{s^2}{\tilde{c}_l^2}\right] \tilde{u}_r^1 \quad (r) \tag{4.69}$$

where $\tilde{u}_z^0 \equiv \tilde{u}_z^0(\xi, z, s)$, $\tilde{u}_r^1 \equiv \tilde{u}_r^1(\xi, z, s)$ and $\tilde{c}_l^2 = s\tilde{M}/\rho$. The homogeneous solution for $\tilde{u}_z^0$ is

$$\tilde{u}_z^0(\xi, z, s) = \tilde{F}_{z,s}(\xi, s)e^{-\tilde{\jmath}_s z} + \tilde{B}_{z,s}(\xi, s)e^{+\tilde{\jmath}_s z} \tag{4.70}$$

$$\tilde{\jmath}_s = \sqrt{\xi^2 + s^2/\tilde{c}_l^2}. \tag{4.71}$$

From eqs. 4.66 and 4.67 it can be shown that $\partial_z \tilde{u}_r^1 = -\xi \tilde{u}_z^0$; therefore

$$\tilde{u}_r^1(\xi, z, s) = \frac{\xi}{\tilde{\jmath}_s}\left[\tilde{F}_{z,s}(\xi, s)e^{-\tilde{\jmath}_s z} - \tilde{B}_{z,s}(\xi, s)e^{+\tilde{\jmath}_s z}\right]. \tag{4.72}$$

Subscript z denotes z-component of displacement and subscript $w1$, s, and $w2$ denote water half-spaces and slab. Coefficients F and B denote forward and backward (left and right) moving waves, respectively. A similar set of equations for water can be written assuming that $c_w \to \tilde{c}_w(s)$.

Reflection and transmission coefficients for both interfaces of the fluid-slab-fluid system are easily determined by enforcing continuity of axial displacement and pressure, $\tilde{p}(\xi, z, s) = s\tilde{M}(\xi \tilde{u}_r^1 + \partial_z \tilde{u}_z^0)$, at interfaces $z = 0$ and $z = L$. Note that this definition of pressure is different by a minus sign from usual definitions; it is analogous with definition of stress in elasticity. Acoustic impedance of the slab is defined to be minus the ratio of pressure to particle speed, $s\tilde{u}_z^0$, for waves propagating in the $+z$ direction or

$$-\frac{\tilde{p}(\xi, z, s)}{s\tilde{u}_z^0(\xi, z, s)} = \frac{\rho_s s}{\tilde{\jmath}_s}. \tag{4.73}$$

Figure 4.4 gives a pictorial representation of the fluid-solid-fluid system. The displacement reflection and transmission coefficients at the interfaces are

$$\tilde{R}_0^+(\xi, s) = \frac{(\rho_w s/\tilde{\jmath}_w) - (\rho_s s/\tilde{\jmath}_s)}{(\rho_w s/\tilde{\jmath}_w) + (\rho_s s/\tilde{\jmath}_s)} \tag{4.74}$$

$$\tilde{T}_0^+(\xi, s) = \frac{2(\rho_w s/\tilde{\jmath}_w)}{(\rho_w s/\tilde{\jmath}_w) + (\rho_s s/\tilde{\jmath}_s)} = 1 + \tilde{R}_0^+(\xi, s) \tag{4.75}$$

$$\tilde{T}_L^+(\xi, s) = \frac{2(\rho_s s/\tilde{\jmath}_s)}{(\rho_w s/\tilde{\jmath}_w) + (\rho_s s/\tilde{\jmath}_s)} = 1 - \tilde{R}_0^+(\xi, s). \tag{4.76}$$

When $s \to i\omega$ and $\xi = 0$ eqs. 4.70, 4.72–4.76 revert to one-dimensional equations equivalent to those presented for the two-slab method. When $\xi = 0$ the Hankel transform of $u_z(r, z, t)$ is simply

$$u_z^0(z, t) = \int_0^\infty u_z(r, z, t) r dr \tag{4.77}$$

where $J_0(0) = 1$; therefore, radial dependence of the field is effectively eliminated. Assuming an ideal point receiver, displacement is recorded as a function of time at a $z = \textit{constant}$ plane in front of

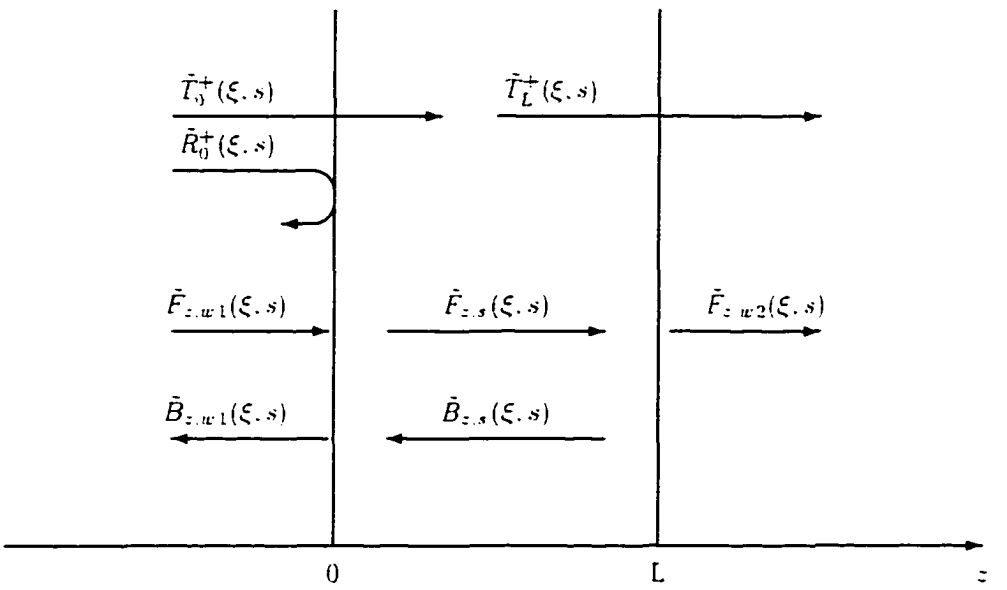

Figure 4.4 Pictorial representation of fluid-solid-fluid system

the transmitter for successive radial positions. Assuming a relatively well collimated beam, a limit in radial direction can be defined beyond which the field is considered negligible. The radial integral is approximated at each time step by summing over recorded displacements. The result is a function dependent only on time, $u_z^0(z,t) \rightarrow u_z^0(t)$. Equations for attenuation and wave speed without diffraction correction that were developed previously in the two-slab, eqs. 4.19 and 4.20, and slab substitution method, eqs. 4.46 and 4.47, can be employed directly if, for example, $\tilde{A}_L(\omega) \equiv \tilde{u}_z^0(\omega)$ in eq. 4.1.

Summary

Two different transmission methods for recovering viscoelastic moduli have been presented: the two-slab method and the slab substitution method. A third method, a Hankel transform method with $\xi = 0$, utilizes the same set of fundamental equations as the two-slab and slab substitution methods but requires that a received signal be collected with a point-like receiver and integrated along a radial line from the beam axis. The first two methods have been used in practice with and without diffraction corrections while the Hankel transform method is untried as far as is known. In practice diffraction corrections are applied in an *ad lib* manner. Within a finite element test bed material properties are known *a priori*; therefore, a numerical experiment is conducted to compare known material properties with material properties recovered with proposed inverse methods. The goals of such a numerical

experiment are to visualize the fields as they propagate throughout the system and to show under what conditions inverse methods give material properties within acceptable engineering tolerance. The ultimate hope is that such insight can suggest modifications to real experimental systems.

CHAPTER 5 MODULUS MEASUREMENT WITH INVERSE METHODS

Introduction

One-dimensional and axisymmetric wave propagation results are presented for a model of a water-immersion through-transmission system for determining longitudinal viscoelastic moduli, $M(t) = K(t) + \frac{4}{3}G(t)$, of solid polymers. First, a set of 1-D results for the two-slab method are presented and serve as a benchmark for comparison with axisymmetric results that follow. Next, a standard correction for geometric beam spreading known as the 'diffraction correction' is discussed. Most realistic measurement systems employ finite diameter receivers as well as finite diameter transmitters. Finite aperture transmitters produce waves that undergo beam spreading or diffraction as they propagate away from the transmitter. In addition, finite aperture receivers effectively average fields incident upon their face. To account for beam spreading, a diffraction correction is applied to the received signal. Ideally, diffraction correction removes decay due to geometric spreading leaving only intrinsic losses due to the material itself. With a FE test bed finite aperture receivers that average incident fields can be simulated to demonstrate systematic errors that are introduced into measurement of material properties. For each of the simulated measurement methods: two-slab, slab substitution and wave splitting, a finite aperture receiver is modeled, but a diffraction correction is applied in the two-slab case only. For simplicity moduli with single-exponential time dependence are employed. Although a simple exponential model is an unrealistic model for real viscoelastic materials it does contain all essential physics and is sufficient to exercise multiple frequency-bandwidth techniques. Also the frequency bandwidth of the source is already smaller than the low to high frequency transition region of a simple exponential moduli; therefore, a broader moduli spectrum would just require more sources with overlapping bandwiths and essentially nothing more about various measurement methods' efficacy would be demonstrated.

Preliminaries

Recall that the bulk and shear moduli for a single-exponential material are given by the following:

$$K(t) = \left[K_e + (K_g - K_e)\, e^{-t/\tau}\right] H(t) \tag{5.1}$$

$$G(t) = \left[G_e + (G_g - G_e)\, e^{-t/\tau}\right] H(t). \tag{5.2}$$

Relaxation times for the bulk and shear modulus are assumed equal. Limiting wave speeds and moduli for the slab are:

$$V_{le},\ V_{lg} = 1700,\ 2500\ m/s \tag{5.3}$$

$$V_{se},\ V_{sg} = 0,\ 1000\ m/s \tag{5.4}$$

$$\rho_s = 1000\ kg/m^3 \tag{5.5}$$

$$G_e = \rho_s V_{se}^2 = 0\ \text{Pa} \tag{5.6}$$

$$G_g = \rho_s V_{sg}^2 = 1\ \text{GPa} \tag{5.7}$$

$$K_e = \rho_s \left(V_{le}^2 - \frac{4}{3} V_{se}^2\right) = 2.25\ \text{GPa} \tag{5.8}$$

$$K_g = \rho_s \left(V_{lg}^2 - \frac{4}{3} V_{se}^2\right) = 6.25\ \text{GPa} \tag{5.9}$$

$$\tau_s = 8.75\ ns. \tag{5.10}$$

The equilibrium shear modulus, G_e, is set to zero as a model for an amorphous, uncross-linked solid polymer. It is also valid for a viscoelastic liquid. The choice of relaxation time is made clear in Fig. 5.1. With this choice of relaxation time, normalized attenuation and wave speed make their transition from low to high frequency centered within the range of source spectrums. Obviously this is a contrived choice made to fit the current FEM's ability to model dispersive wave propagation for center frequencies commonly available in off-the-shelf transducers.

A viscoelastic slab is considered immersed in water. Water has attenuation that is proportional to the square of frequency, $\alpha_w(f) = \alpha_{w0} f^2$, to relatively high frequency ($\sim$ 1 GHz) while wave speed is essentially constant. A set of viscoelastic material parameters that model this behavior are

$$V_{le},\ V_{lg} = 1500,\ 1750\ m/s \tag{5.11}$$

$$V_s = 0\ m/s \tag{5.12}$$

$$\rho_w = 1000\ kg/m^3 \tag{5.13}$$

$$G = 0\ \text{Pa} \tag{5.14}$$

$$K_e = \rho_s V_{le}^2 = 2.25\ \text{GPa} \tag{5.15}$$

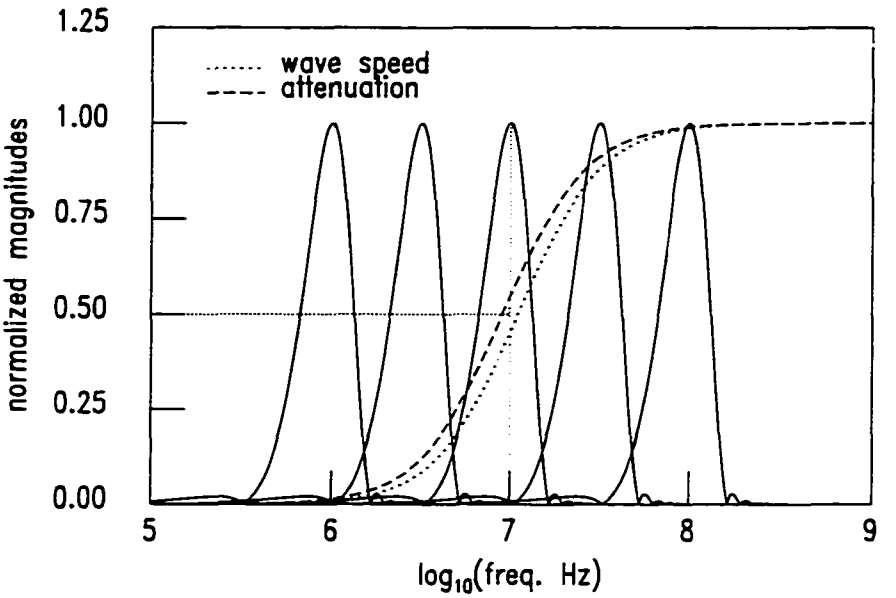

Figure 5.1 Normalized source spectrums compared with normalized material attenuation and wave speed

$$K_g = \rho_s V_{lg}^2 = 3.06\ \text{GPa} \tag{5.16}$$

$$\tau_w = 4.21\ ps. \tag{5.17}$$

Notice that the shear modulus is zero: therefore, water is modeled as an inviscid, compressible 'viscoacoustic' fluid. Figure 5.2 shows absolute attenuation and wave speed to 300MHz. For comparison $\alpha_{w0} f^2$ is also plotted where

$$\alpha_{w0} = \frac{4\pi^2 (K_g - K_e)\tau_w}{2\rho_w V_{le}^3} = 20.0(10^{-15})\ \text{Np}/(m\text{Hz}^2). \tag{5.18}$$

For one-dimensional calculations water attenuation is included.

The five center frequencies for the frequency bands that span the transition region in the model material are f_0 = 1, 3.16, 10, 31.6, 100 MHz, respectively. For each frequency a set of numbers that define finite element calculations are given in Table 5.1. The time increments satisfy the stability criterion. $\Delta t \leq h/V_{lg}$ where $\Delta r = \Delta z = h$. For the given frequencies the number of elements per longitudinal wavelength in water is about 60 and ranges from 68–100 for the viscoelastic solid depending on center frequency. Fifteen elements per wavelength is usually sufficient, but because computer resources were not a limitation and numerical dispersion is desired to be a minimum a relatively large number of elements per wavelength was chosen.

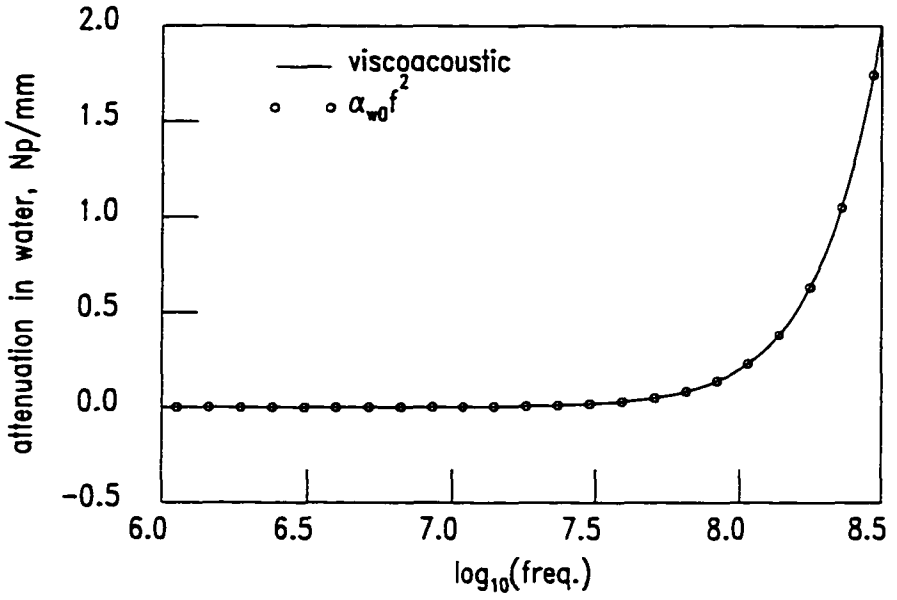

Figure 5.2 Absolute attenuation in water: viscoacoustic model compared with $\alpha_{w0}f^2$ in Np/mm

Two-Slab Method: One Dimension

The model parameters given in Table 5.1 are used for calculating transient displacement transmitted through a slab of various thicknesses. Figures 5.3 and 5.4 show transmitted displacement at the right-most boundary, $L_1 + L$, of the slab and at a distance, $L_1 + L + L_2$, beyond the slab representing propagation through water to a receiver. In this case an ideal receiver records displacement at the water/vacuum interface. For a plane wave normally incident on a traction free interface the surface displacement is twice the incident displacement: therefore, dividing recorded displacement by two recovers the incident field. Distance L_2 is kept constant which translates into moving the receiver to the right to

Table 5.1 Parameters for FE calculations at each center frequency

f_0 (MHz)	h (μm)	Δt (ns)	L_1 (μm)	L_2 (μm)	L (μm)
1.0	25.0	8.0	7500.0	7500.0	1000–8000
3.16	8.0	2.5	2400.0	2400.0	496–3000
10.0	2.5	0.8	750.0	750.0	100–800
31.6	0.8	0.25	240.0	240.0	49.6–300
100.0	0.25	0.08	75.0	75.0	10–80

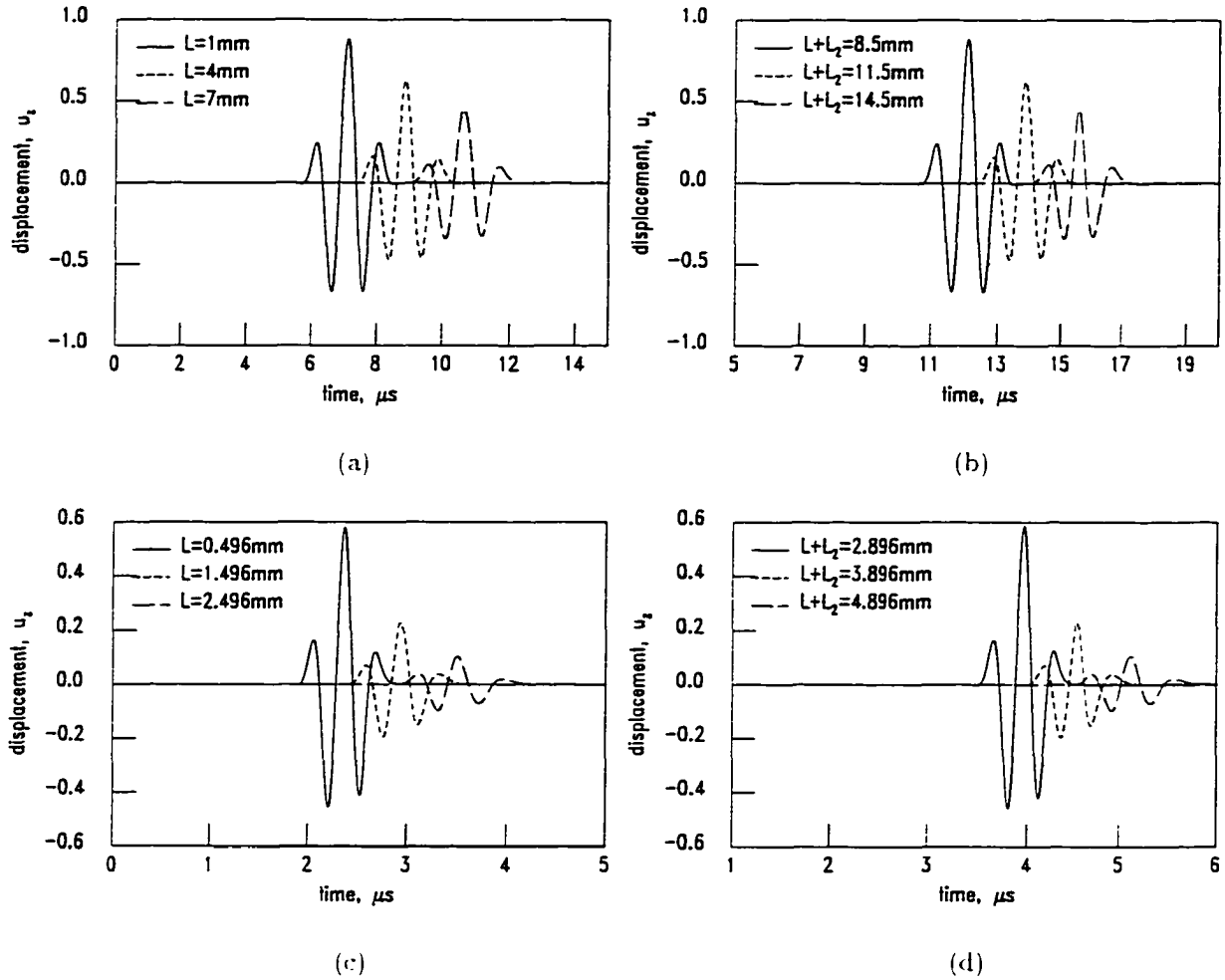

Figure 5.3 Transmitted plane-wave displacement for three different slab thicknesses at f_0 = 1MHz. (a)-(b). f_0 = 3.16MHz. (c)-(d)

compensate for increased slab thickness. A visual comparison of waveforms at $L_1 + L$ and $L_1 + L + L_2$ in Figs. 5.3 and 5.4 shows that for frequencies and propagation distances chosen losses in the water are negligible; therefore, water losses will be neglected in all subsequent axisymmetric calculations.

Recovery of attenuation, wave speed, frequency and time dependent moduli proceeds as described in Fig. 5.5. Figures 5.6 and 5.7 show recovered attenuation and wave speed for transmitted waves recorded at $L_1 + L$ and $L_1 + L + L_2$, respectively. For each frequency bandwidth attenuation and wave speed were determined with three different combinations of transmitted waves shown in Figs. 5.3 and 5.4 corresponding to three seperate slab thicknesses. Also shown is the percent difference between numerical and exact values for each frequency bandwidth. In all cases and for all combinations the percent difference is less than five percent except at band edges where the first null occurs in the wave's

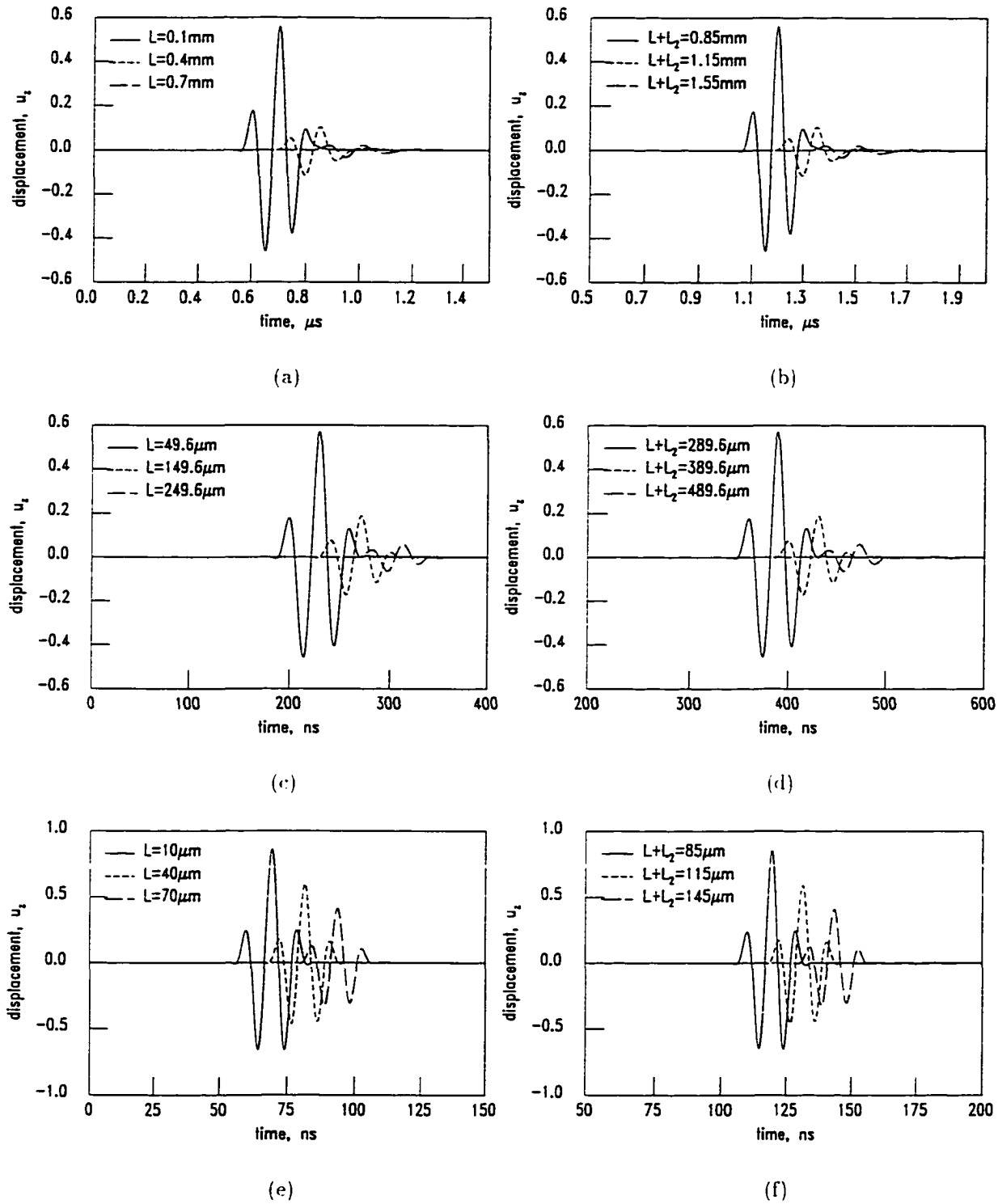

Figure 5.4 Transmitted plane-wave displacement for three different slab thicknesses at f_0 = 10MHz. (a)-(b): f_0 = 31.6MHz. (c)-(d): and f_0 = 100MHz. (e)-(f)

frequency spectrum on either side of center frequency. These results demonstrate that in principle the FE model can serve as test bed for ultrasonic wave propagation in linear viscoelastic media and that numerical errors can be kept within respectable 'engineering tolerance' ($< 5\%$).

Ultimately, it is the time dependent longitudinal relaxation modulus that is of interest. Figure 5.8 shows reconstruction of the time dependent modulus from the frequency dependent modulus recovered from the one-dimensional wave propagation model. Specifically, Fig. 5.8(b) compares the reconstructed modulus when the frequency dependent modulus is truncated at the highest frequency ($f_{max} = 157$MHz) of measurement and when the frequency dependent modulus is extended to $f_{max} = 1$GHz by assuming the real part of the modulus, $M'(\omega)$, at f_{max} is equal to M' at the highest frequency of measurement and imaginary part, $M''(\omega)$, goes to zero linearly above the highest frequency of measurement. When $f_{max} = 157$MHz there is clearly some ripple in the time dependent modulus and deterioration is greatest at small time which is equivalent to high frequency. When $f_{max} = 1$GHz ripple is negligible and there is less short-time deterioration.

In Fig. 5.8(c) the modulus is approximated by excluding some of the five frequency bands. In one case the lowest and highest frequency bands have been dropped which correspond to center frequencies $f_0 = 1$ and 100MHz. In this case almost no change is noted in the time dependent modulus, Fig. 5.8(d). In the other two cases the three highest bands and three lowest bands have been dropped. When the three highest bands are dropped short time response is clearly degraded but long time response is adequate. The opposite is true when the three lowest bands are dropped. Generally, loss of low frequency information destroys important overall trends in the data whereas loss of high frequency information imposes small ripples in the data. Accurate measurements of low frequency information is essential. Approximating the frequency dependent modulus outside its measured range is equivalent to imposing *a priori* knowledge about its behavior in those frequency ranges. If interest is in a limited frequency range then making reasonable assumptions outside of this range may have negligible effect on a forward model. Making such assumptions is akin to knowing the appropriate time/frequency scales of interest.

Understanding Diffraction Corrections

In all real experimental situations where basic material properties are to be determined, for example, wave speed and attenuation, ultrasonic transmitters and receivers have finite radius. In general, it is advantageous to have a relatively large transmitting aperture. Assuming the transmitter behaves like an ideal piston, it will produce a plane wave region on the axis of symmetry that can be exploited

1. Given: raw time trace of transmitted wave at source center frequency, f_0
2. Window in time the first transmitted pulse without internal re-reflections (if possible)
3. FFT the windowed transmitted wave and calculate spectrum, $\bar{A}_L(\omega)$
4. Window the useful frequency bandwidth of transmitted wave spectrum
5. Repeat steps 1-4 for a slab of different thickness to obtain $\bar{A}_{L+\Delta L}(\omega)$
6. Compute attenuation and wave speed:

$$\alpha(\omega) = -\frac{1}{\Delta L}\ln\left|\frac{\bar{A}_{L+\Delta L}(\omega)}{\bar{A}_L(\omega)}\right|; \qquad c(\omega) = -\frac{\omega\Delta L}{\phi_{\Delta L}(\omega)}$$

7. Compute estimate of modulus for useful bandwidth centered at f_0:

$$\begin{aligned} M'(\omega) &= K' + \frac{4}{3}G' = \rho c^2\left[\frac{1-\beta^2}{[1+\beta^2]^2}\right] \\ M''(\omega) &= K'' + \frac{4}{3}G'' = \rho c^2\left[\frac{2\beta}{[1+\beta^2]^2}\right] \\ \beta(\omega) &= \frac{\alpha(\omega)c(\omega)}{\omega} \end{aligned}$$

8. Repeat steps 2-7 for another f_0
9. Combine modulus estimates for various bandwidths to form an overall estimate
10. Extend low and high frequency modulus data to zero frequency and 1GHz, respectively
11. Compute estimate of time domain modulus (IFFT):

$$M(t) = \mathcal{F}^{-1}\left[\bar{M}(\omega)\right]$$

Figure 5.5 Data processing for modulus recovery with two-slab propagator method in one dimension

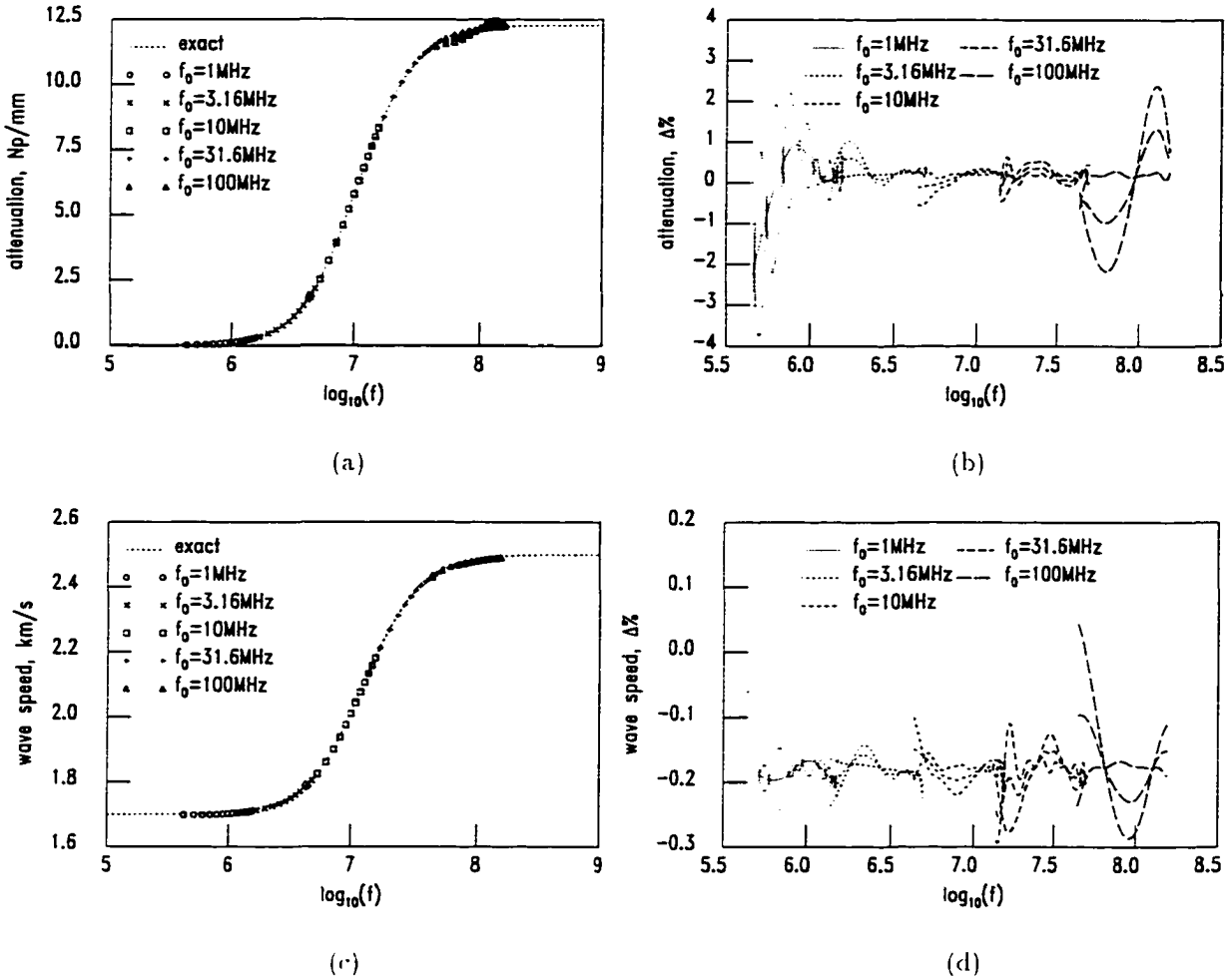

Figure 5.6 Recovered slab attenuation, (a), wave speed, (c), and percent difference from exact, (b) and (d), for displacement recorded at right-most solid-fluid boundary, L

for plane wave-like measurements. A large radius receiving aperture ($ka \gg 1$) coaxially aligned with the transmitter intercepts a portion of the transmitted field. Usually, by the time the transmitted field reaches the receiver, edge waves emanating from the rim of the transmitter have become 'mixed up' with the central plane wave region. The wave striking the receiver is a complex combination of plane and edge waves. To account for this 'diffraction' or 'beam spreading' in an approximate manner a diffraction correction is often employed. The diffraction correction assumes there exists a pressure sensitive receiver, for example a piezoelectric transducer, that effectively averages incident pressure. While it is not clear that a piezoelectric transducer exactly averages incident pressure it is at least a reasonable assumption. A transient finite element method provides an excellent test bed to study

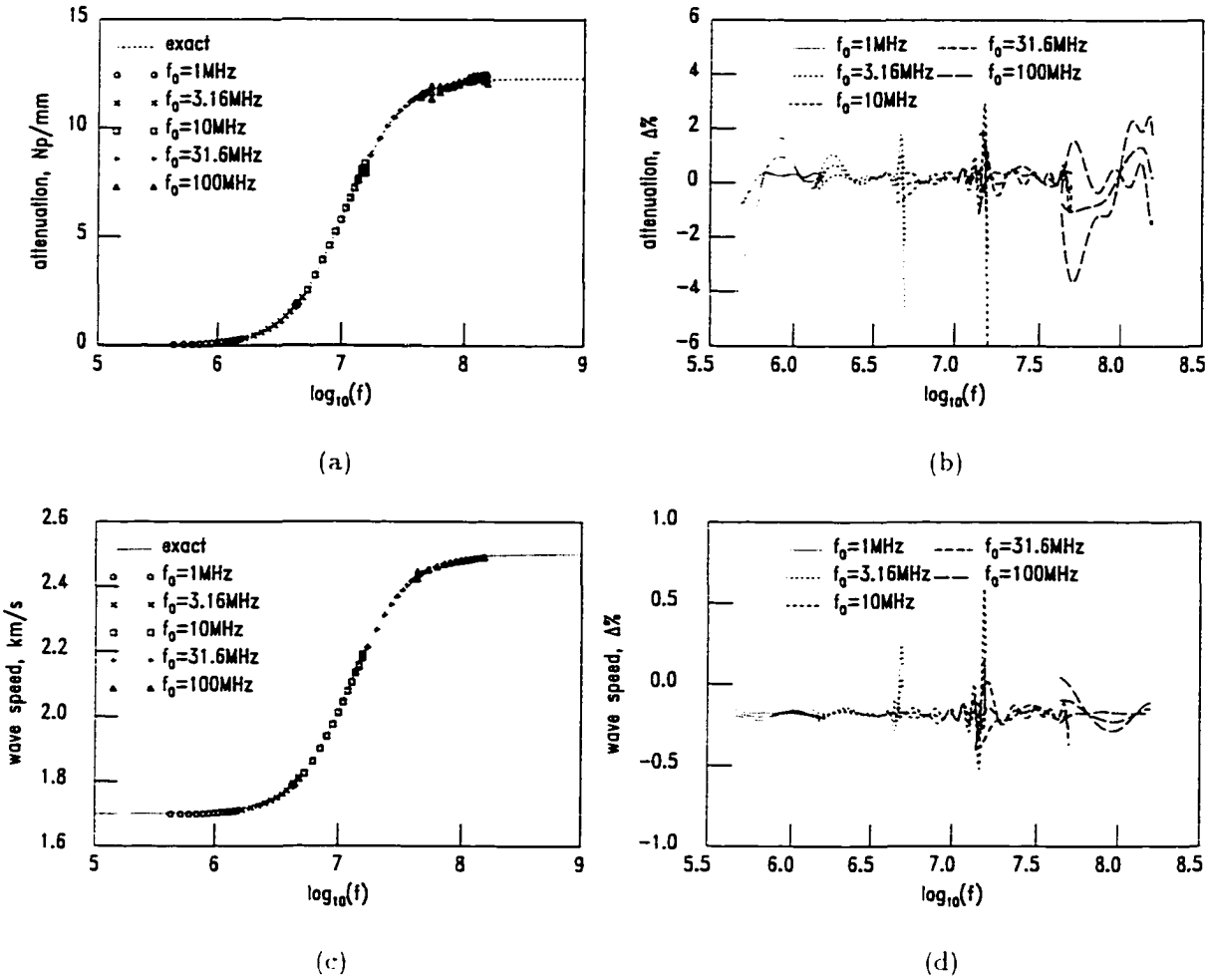

Figure 5.7 Recovered slab attenuation, (a), wave speed, (c), and percent difference from exact, (b) and (d), for displacement recorded at $L+L_2$

diffraction (beam spreading), diffraction corrections and effects of both of these things on material property measurement.

For model situations considered a displacement vector is computed in the acoustic fluid instead of scalar acoustic pressure because a displacement-based FEM is directly compatible with the usual displacement FE formulation for an elastic or viscoelastic medium. The usual diffraction correction is derived assuming a pressure field radiated by a piston source in an infinite rigid baffle: therefore, it is of interest to know how significant is the difference when a diffraction correction is applied to the average received displacement, $\langle u_z(r,z,t)\rangle$, instead of the pressure, $\langle p(r,z,t)\rangle = K_f \nabla \cdot \mathbf{u}(r,z,t)$[1]. In what follows diffraction corrections for pressure and axial displacement are compared directly. In addition

[1] Usually the pressure is defined to be positive in compression, that is, $p(r,z,t) = -K_f \nabla \cdot \mathbf{u}(r,z,t)$, but in cases considered here it is chosen to be postive in tension analogous to stress.

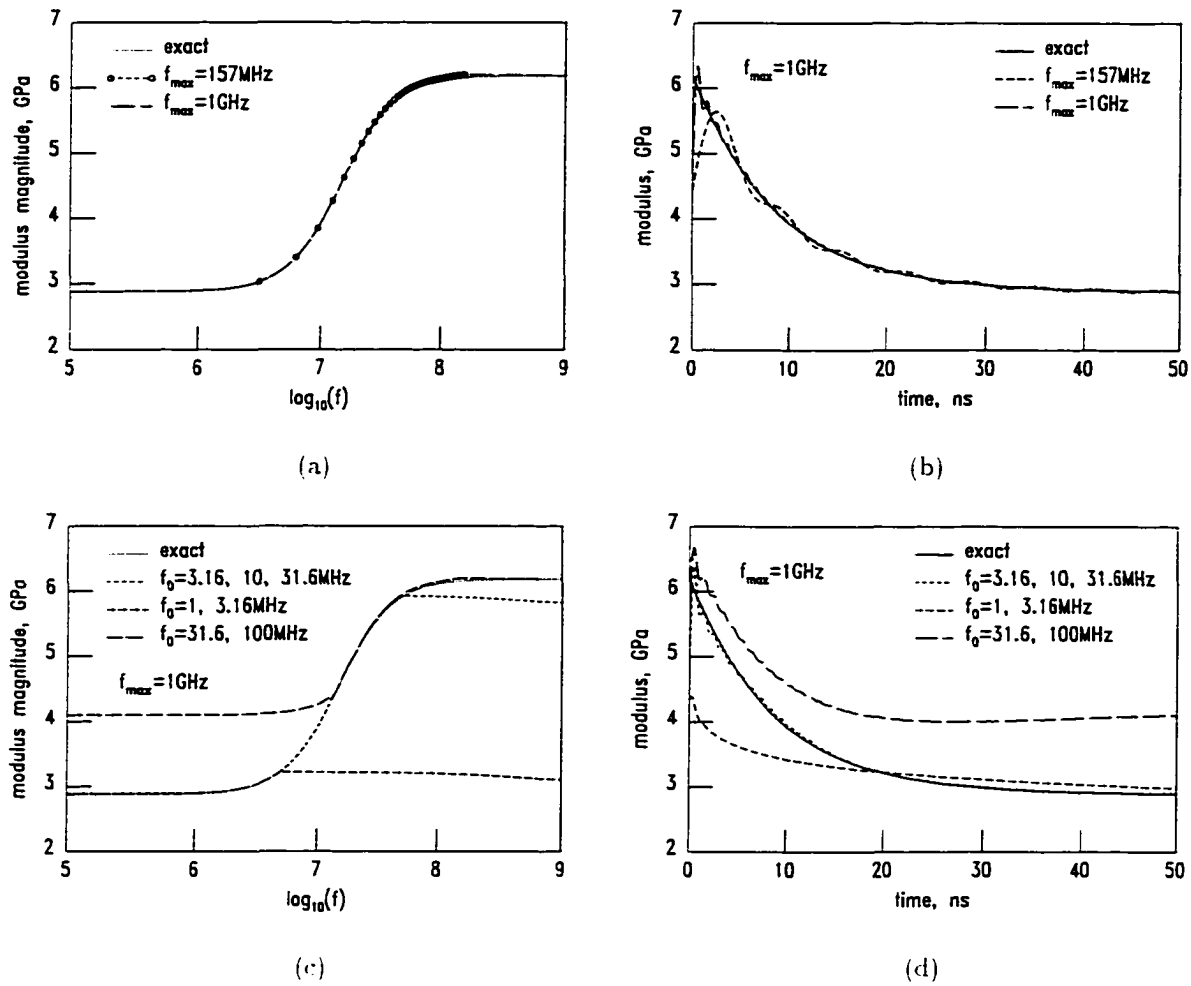

Figure 5.8 Frequency dependent modulus, (a) and (c), and corresponding time dependent modulus, (b) and (d)

the received pressure averaged over a receiving aperture is compared with received axial displacement, $u_z(r, z, t)$, averaged over the same aperture. Both are computed with the finite element method in an axisymmetric mode. Average received pressure (axial displacement) is compared with an equivalent diffraction corrected plane wave. A diffraction correction derived specifically for axial displacement is given and applied. Finally, average received pressure (displacement) is diffraction corrected to account for or 'divide out' geometric beam spreading in order to recover a plane wave field. Examples are given for waves in a homogeneous acoustic half-space.

Acoustic Pressure and Displacement FE Models

The finite element model is easily adapted for modeling pressure fields due to a piston source [56]. The displacement wave equation can be written as

$$\left(K + \frac{1}{3}G\right)\nabla\nabla\cdot\mathbf{u} + G\nabla^2\mathbf{u} = \rho\ddot{\mathbf{u}}. \tag{5.19}$$

When $K = -\frac{1}{3}G$ and $u_r(r,z,t) = 0$ the resulting equation for $u_z(r,z,t)$ is formally analogous to the acoustic pressure with $K_f = G$, that is, let $p(r,z,t) = u_z(r,z,t)$ then

$$K_f\nabla^2 p = \rho_f\ddot{p}. \tag{5.20}$$

For a one dimensional model pressure and axial displacement propagating in the positive z-direction are related by

$$p(z,t) = -Z_f\dot{u}_z(z,t). \tag{5.21}$$

that is, pressure and displacement are related by a time derivative. For ease of comparison pressure and axial displacement are forced to have the same time variation. For an acoustic displacement model set $G = 0$ and $K_f = K$ then

$$K_f\nabla\nabla\cdot\mathbf{u} = \rho_f\ddot{\mathbf{u}} \tag{5.22}$$

with $c_f = \sqrt{K_f/\rho_f}$.

Average pressure (axial displacement) over a receiver of radius, b, located at axial position, z, is defined by

$$\begin{aligned}
\langle p\rangle(z,t) &= \frac{1}{\pi b^2}\int_0^{2\pi}\int_0^b p(r,z,t)\,r\,dr\,d\theta && (5.23)\\
&= \frac{2}{b^2}\int_0^b p(r,z,t)\,r\,dr && (5.24)\\
&\approx \frac{2}{N^2}\sum_{i=1}^{N} i\,p_i(i\Delta r,z,t) - \frac{1}{N}p_N(N\Delta r,z,t) && (5.25)
\end{aligned}$$

where $b = N\Delta r$ and trapezoidal rule is employed to approximate the integral. The same formula is valid for average axial displacement by replacing $p(r,z,t)$ with $u_z(r,z,t)$. Average pressure (displacement) at a chosen axial distance, z, and receiver radius, b, is easily computed and output as the FEM marches in time. In addition, the FE model can be set to run in a plane wave mode. The plane wave output can then be modified by an appropriate diffraction correction and compared with the average pressure or axial displacement already computed.

Figures 5.9 and 5.10 show pressure and displacement wave fields radiated into an acoustic half space due to a plane piston source on the fluid surface. The source has a radius, $a = 2.5mm$ ($ka \approx 10$).

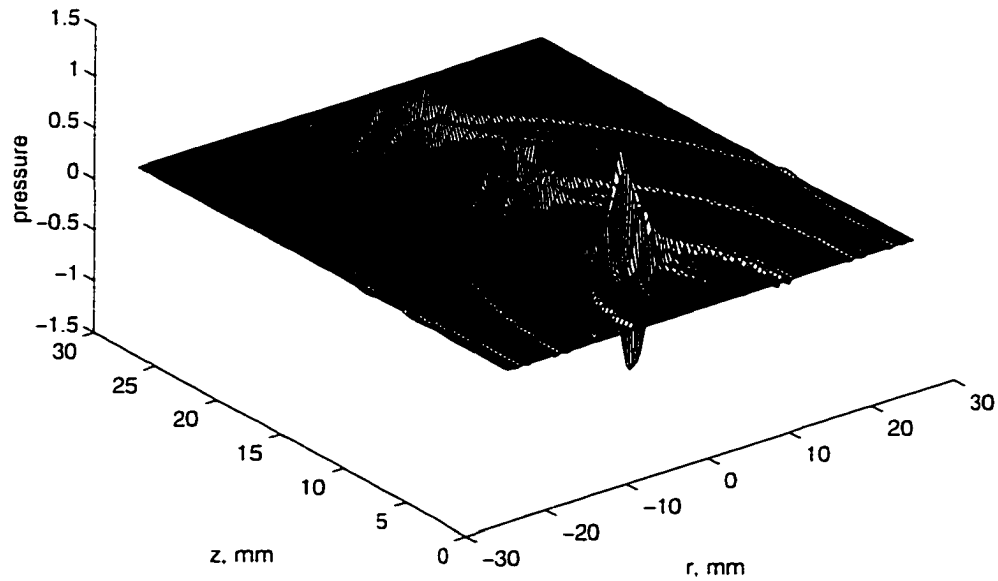

Figure 5.9 Acoustic pressure in fluid half-space for $t = 6,\ 12,\ 18\mu s$ for source radius, $a = 2.5mm$, and center frequency, $f_0 = 1$MHz

and a center frequency, $f_0 = 1$MHz. Three different times are superimposed to clearly demonstrate beam diffraction. A simple visual comparison shows the similarity between pressure, Fig. 5.9, and axial displacement, Fig. 5.10(a). Differences are noticeable in the amplitude of the edge wave. For the displacement FE model a smooth roll-off of applied surface force at the aperture edge is necessary to suppress spurious shear modes that are generated at the source edge when the source is an ideal piston [44]. These modes are only a problem in a displacement-only FE fluid model when the shear modulus is zero. Roll-off has eliminates shear modes and reduces amplitude of longitudinal edge waves; therefore, some of the difference in amplitude between edge waves for pressure and axial displacement is due to this smoothing at the source edge.

Comparison of diffraction corrections

A rigid baffle is defined by $u_z(r, 0, t) = f(t)$ when $r \leq a$ and $u_z(r, 0, t) = 0$ when $r > a$. The pressure diffraction correction, eq. 4.25, for the case when transmitter and receiver have the same radius, $a = b$, and the transmitter is an ideal piston placed in a rigid baffle is

$$\tilde{D}(z, \omega) = 1 - \frac{4}{\pi}\int_0^{\pi/2} e^{-ik(q(x)-z)}\sin^2(x)dx \tag{5.26}$$

$$q(x) = \sqrt{z^2 + 4a^2\cos^2(x)}. \tag{5.27}$$

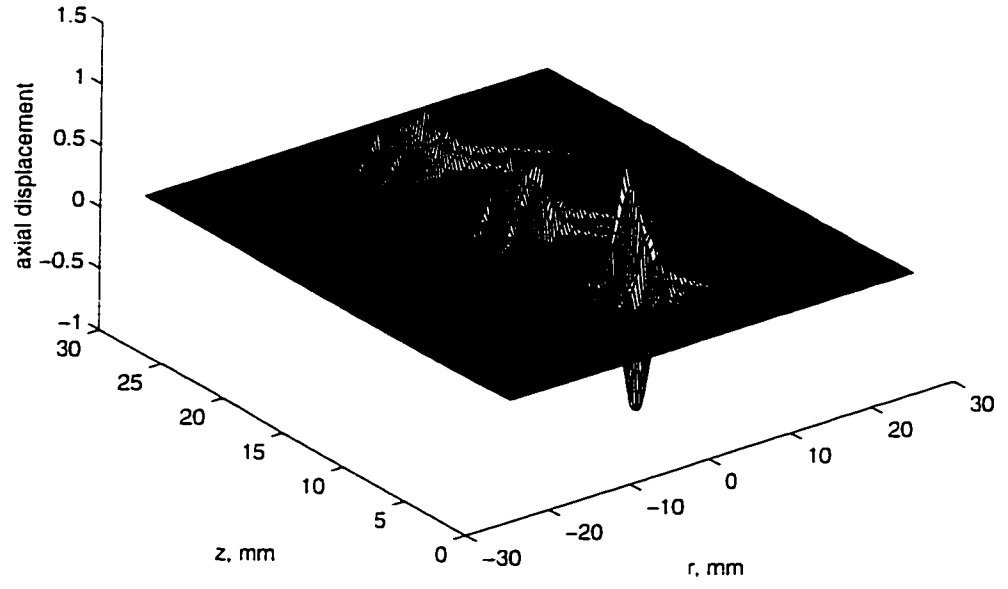

(a)

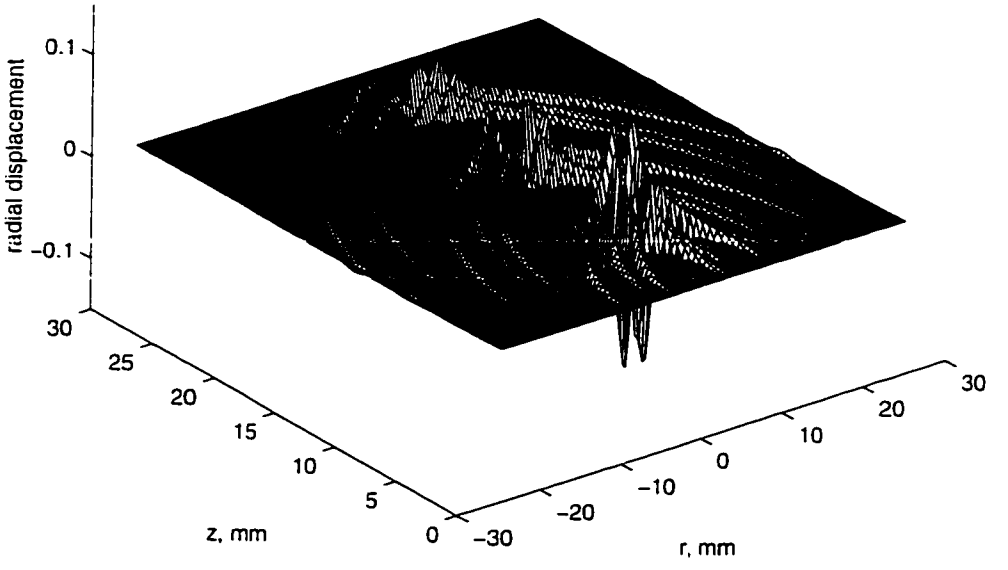

(b)

Figure 5.10 Axial, (a), and radial, (b) displacement in fluid half-space for $t = 6,\ 12,\ 18\mu s$ for source radius, $a = 2.5mm$, and center frequency, $f_0 = 1$MHz

When $ka \gg 1$ and $a = b$ this equation becomes (eq. 4.26) [5. 39]

$$\bar{D}^{\infty}(S) = 1 - e^{-i(2\pi/S)}\left[J_0(2\pi/S) + iJ_1(2\pi/S)\right] \tag{5.28}$$

$$S = z\lambda/a^2. \tag{5.29}$$

The equation for $\bar{D}^{\infty}(S)$ is widely used because of its simplicity. Williams [52] extended this simple result to higher order. His result is

$$\bar{D}_2^{\infty}(z,\omega) = 1 - e^{-i\zeta}\left\{\left(1 - \frac{A}{2}\right)\left[J_0(\zeta) + iJ_1(\zeta)\right] + \frac{A}{\zeta}J_1(\zeta)\right\} \tag{5.30}$$

$$A = \eta + \frac{1}{4}\eta^2 \tag{5.31}$$

$$\eta = \left(\frac{\zeta}{ka}\right)^2 \tag{5.32}$$

$$\zeta = \frac{k}{2}\left[\sqrt{z^2 + 4a^2} - z\right]. \tag{5.33}$$

A comparison of this slightly more complicated result with the exact integral expression, eq. 5.29, shows that it is almost indistinguishable from the exact equation for all cases tested. The more common result, eq. 5.29, is compared with the exact diffraction correction for cases considered. For the case when $a \neq b$ Williams [52] has derived the following formula:

$$\bar{D}(z,\omega) = \left[1, \frac{a^2}{b^2}\right] - \frac{4a^2}{\pi}\int_0^{\pi/2} \frac{e^{-ik(q(x)-z)}}{q^2(x) - z^2}\sin^2(2x)dx \tag{5.34}$$

$$q(x) = \sqrt{z^2 + (a-b)^2 + 4ab\cos^2(x)}. \tag{5.35}$$

where $\left[1, a^2/b^2\right]$ implies 1 for $b \leq a$ and a^2/b^2 for $b > a$.

A diffraction correction for axial displacement, $u_z(r,z,t)$, with pressure release or traction free boundary conditions on the fluid surface ($u_z(r,0,t) = f(t)$ $r \leq a$ and $p(r,0,t) = 0$ $r > a$) is easily derived from a velocity potential given by Archer-Hall [3].

$$o(r,z,\omega) = \frac{V_0}{ik}\left\{e^{-ikz} + \frac{1}{\pi}\int_0^{\pi} e^{-ikq(x)}\frac{z}{q(x)}\left[\frac{ar\cos(x) - a^2}{q^2(x) - z^2}\right]dx\right\} \tag{5.36}$$

$$q(x) = \sqrt{r^2 + a^2 - ar\cos(x) + z^2} \tag{5.37}$$

where $u_z(r,z,\omega) = \partial_z o/i\omega$ and $V_0 \equiv i\omega U_0$. After taking a derivative with respect to z, averaging axial displacement over the radius of the receiver and dividing by a plane wave of displacement, $u_z(z,\omega) = -U_0 e^{-ikz}$, the result is a diffraction correction for axial displacement for traction free boundary conditions:

$$\bar{D}_d(z,\omega) = \left[1, \frac{a^2}{b^2}\right] + \frac{2}{\pi b^2}\int_0^b\int_0^{\pi} e^{-ik(q(x)-z)}\frac{z}{q(x)}f(x)\left[\frac{ar\cos(x) - a^2}{q^2(x) - z^2}\right]rdxdr \tag{5.38}$$

$$f(x) = \frac{z}{q(x)}\left[1 - \frac{q(x)}{ikz^2} + \frac{1}{ikq(x)}\right] \tag{5.39}$$

where subscript 'd' implies displacement and $q(x)$ is a given by eq. 5.37. Double integration is approximated with 4×4-point double Gaussian integration over a patch in the xr-plane with one hundred patches in the x and r directions, respectively.

Figures 5.11 and 5.12 compare pressure and axial displacement diffraction corrections, eqs. 5.29, 5.35 and 5.39, respectively, for a source with center frequency, $f_0 = 1$MHz, and radius, $a = 2.5mm$, transmitting into water. For this case $ka \approx 10$ which is relatively small so that significant diffraction effects exist for axial distances considered. In Fig. 5.11 the source and receiver have equal radii ($a = b$) and distance between transmitter and receiver is varied. In Fig. 5.12 separation distance is held constant and ratio of receiver and transmitter radii, b/a, is varied. An important point demonstrated by these plots is that relatively small variations in magnitude exist between pressure and axial displacement diffraction corrections. When $a = b$ the simple formula for $ka \rightarrow \infty$, eq. 5.29, appears completely adequate as an approximation for exact cases.

Figure 5.13 represents a 'forward' application of a diffraction correction, that is, a plane wave is 'adjusted' by a diffraction correction to make it equivalent to a field of a finite aperture source averaged over a finite aperture receiver. Figure 5.13(a) is a plane wave computed with the FEM and plotted versus increasing distance from the source. In Fig. 5.13(b) FE axisymmetric pressure and axial displacement averaged over a receiver with $a = b$ are compared. When pressure and axial displacement are forced to have the same time dependence they are almost indistinguishable for cases considered. In Figs. 5.13(c)-(e) averaged FE axial displacement is compared with a plane wave adjusted by a diffraction correction for axial displacement, pressure (exact) and pressure ($ka \rightarrow \infty$), respectively. In each case differences are slight and diminish with distance from the source. Other cases were compared when $a \neq b$ and a similar level of correspondence was noted. The only noticeable differences occur as distance to the source goes to zero.

In principle the inverse of the diffraction correction is applied to a measured axisymmetric field to remove or 'divide out' beam spreading and return the field to a plane wave. Any attenuation not due to beam spreading can then be recovered with plane wave techniques described previously. A simple test case for diffraction removal is presented in Fig. 5.14 where fluid bulk modulus is time dependent (viscoacoustic). For this calculation the following parameters were set:

$$V_{le},\ V_{lg} = 1500,\ 1750\ m/s \tag{5.40}$$

$$\rho = 1000\ kg/m^3 \tag{5.41}$$

$$\tau = 8.75\ ns. \tag{5.42}$$

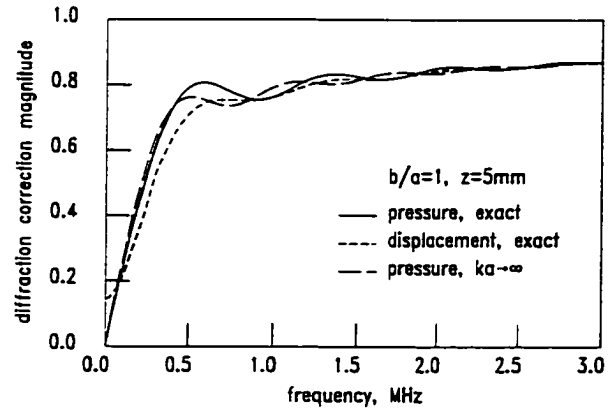

(a)

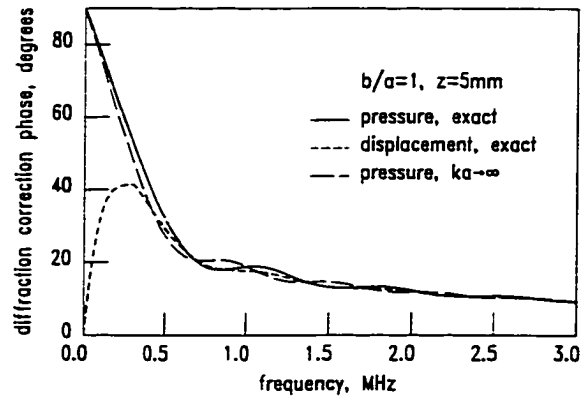

(b)

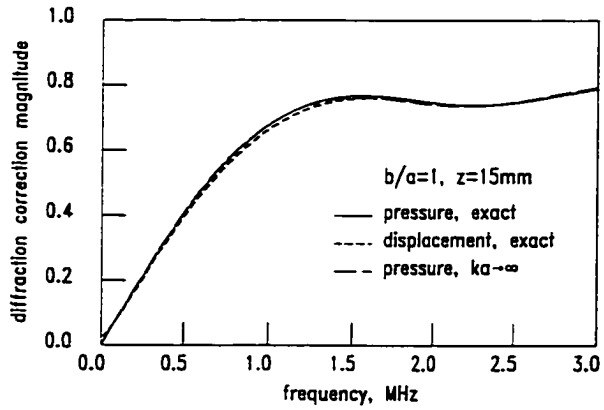

(c)

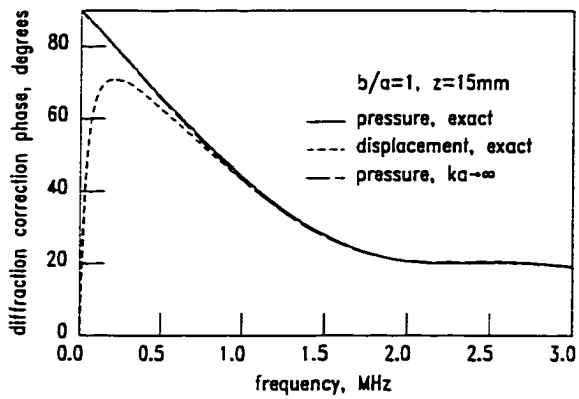

(d)

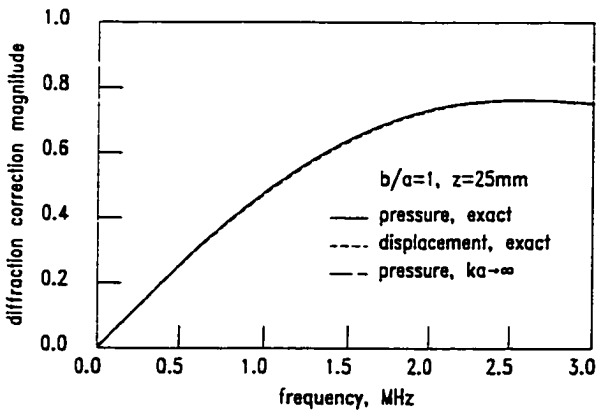

(e)

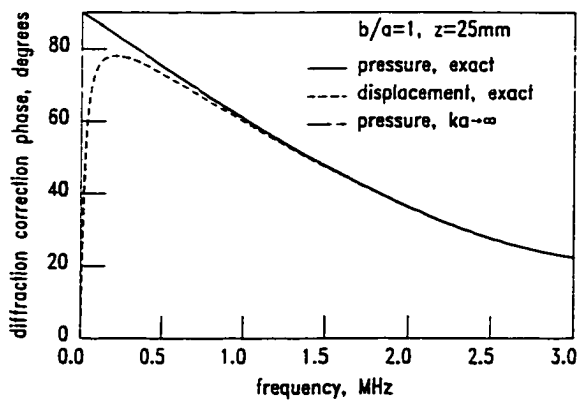

(f)

Figure 5.11 Diffraction correction (d.c.), magnitude and angle, versus frequency for $b/a = 1$ at $z = 5mm$, (a)-(b), $z = 15mm$, (c)-(d), $z = 25mm$, (e)-(f)

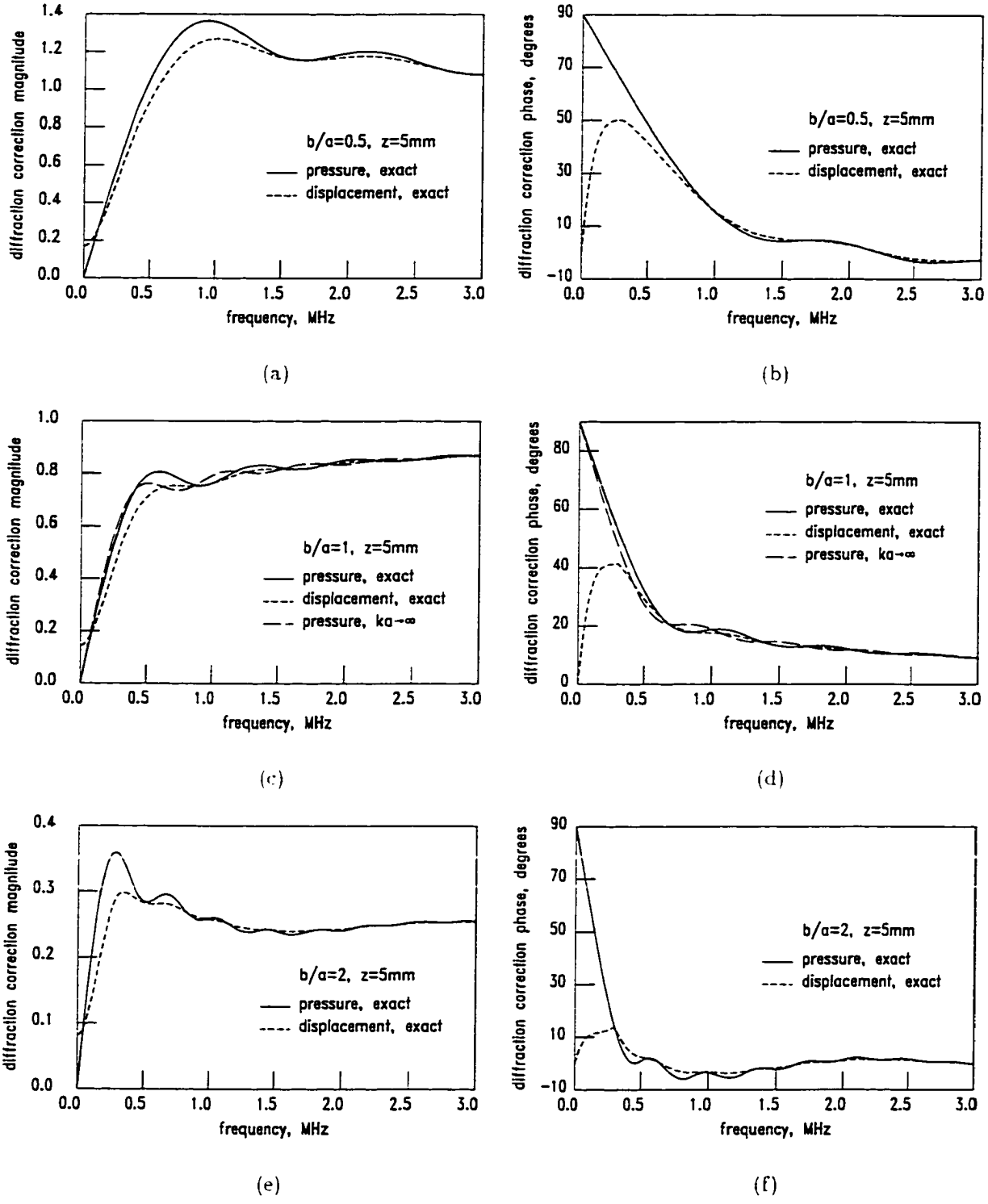

Figure 5.12 Diffraction correction (d.c.). magnitude and angle. versus frequency at $z = 5mm$ for $b/a = 0.5$. (a)-(b). $b/a = 1$. (c)-(d). $b/a = 2$. (e)-(f)

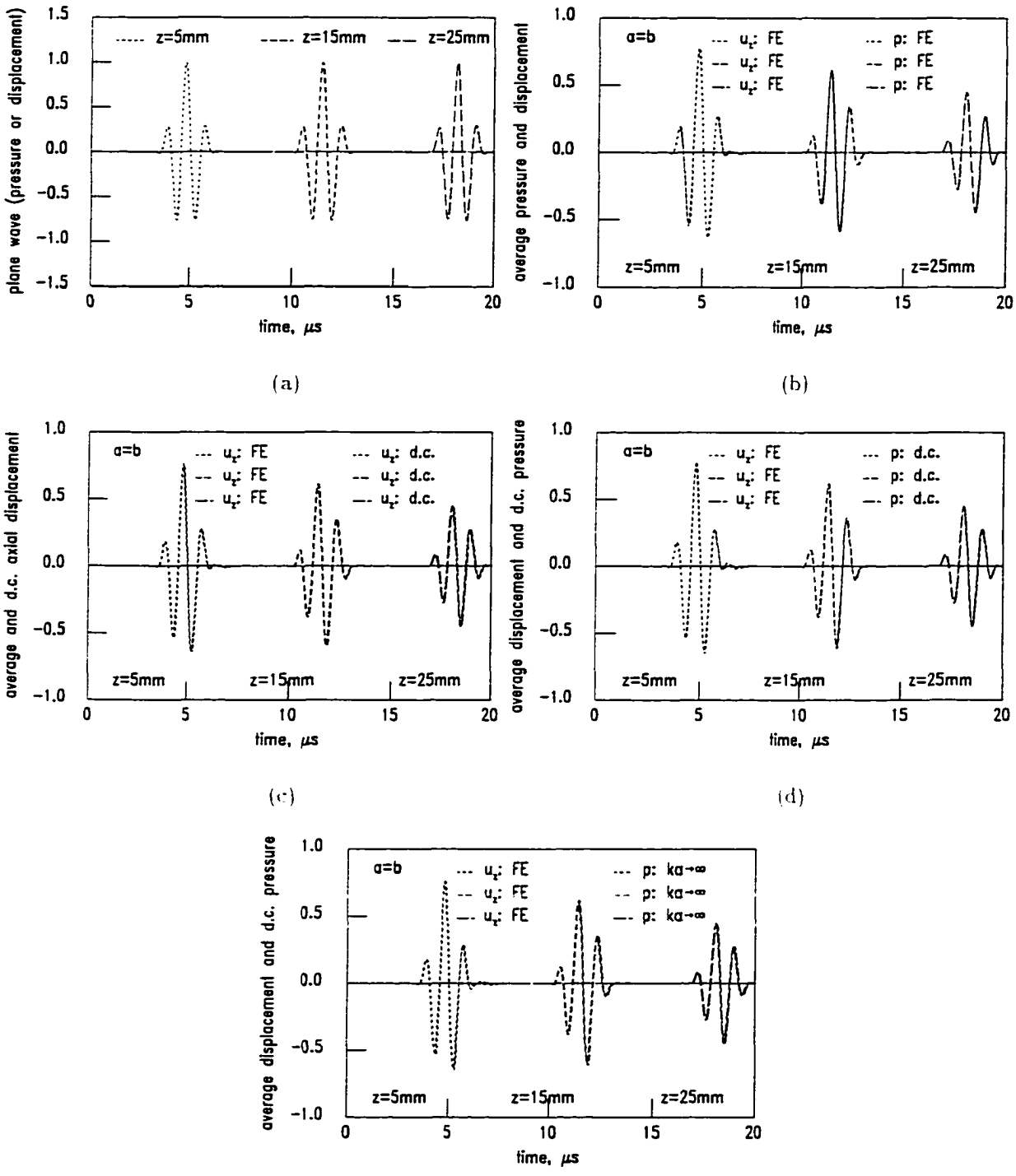

Figure 5.13 Plane wave. (a): FE $\langle u_z \rangle$ and $\langle p \rangle$ for $(a = b)$. (b): FE $\langle u_z \rangle$ compared with plane wave adjusted for diffraction with axial displacement diffraction correction (d.c.). (c) eq. 5.39: with pressure d.c.: (d) eq. 5.35: and with pressure d.c. for $ka \to \infty$. (e) eq. 5.29

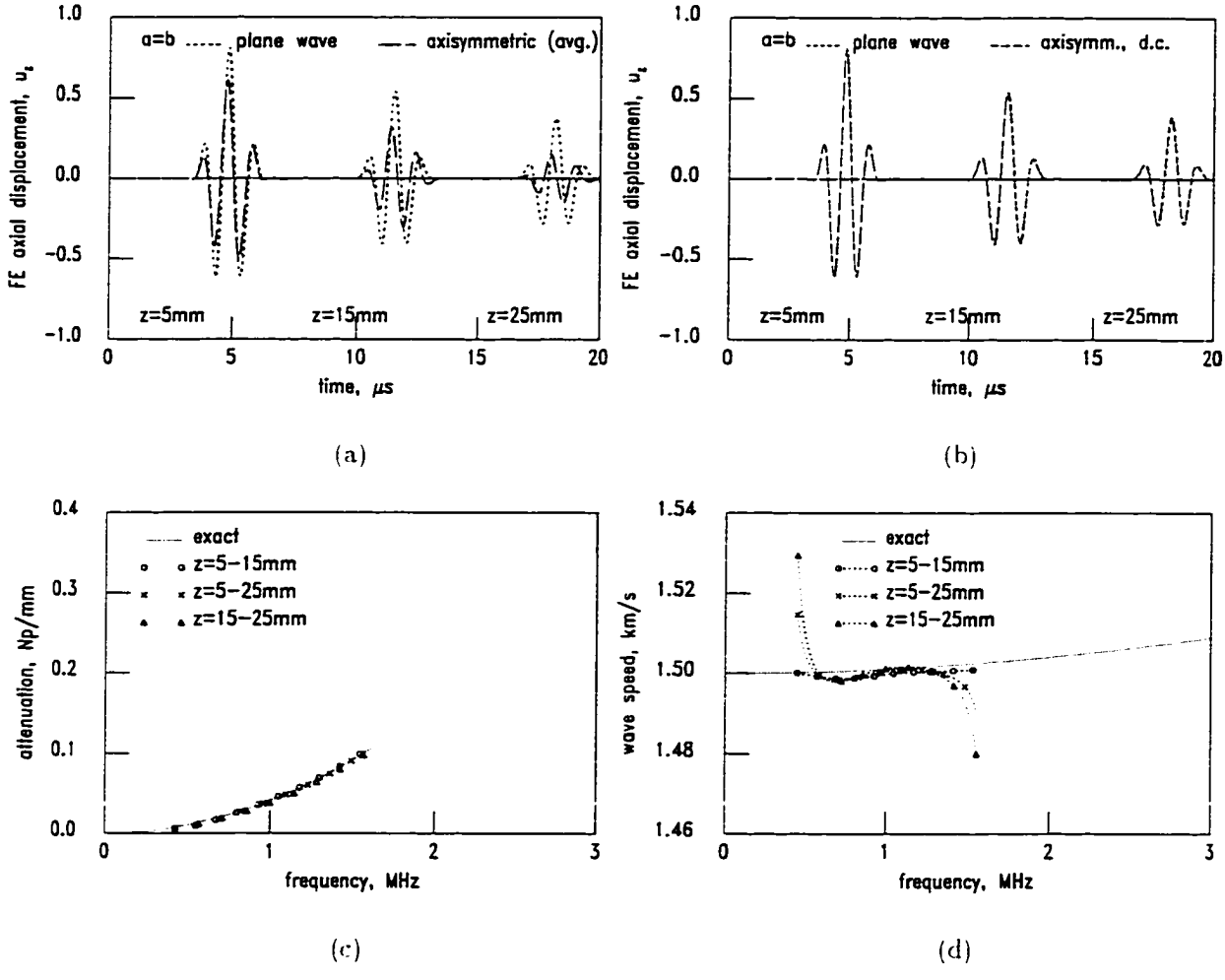

Figure 5.14 Plane wave and averaged FE axial displacement. (a): plane wave and averaged FE axial displacement with diffraction correction. (b) eq. 5.39: recovered attenuation and wave speed. (c) and (d)

Figure 5.14(a) compares a plane wave calculation with attenuation with a corresponding axisymmetric wave along the z-axis. Additional decrease in amplitude due to beam spreading is apparent. Figure 5.14(b) shows an axisymmetric wave after a diffraction correction has been applied. Clearly, beam spreading has been removed and the axisymmetric wave has been returned to an equivalent plane wave traveling in an attenuating material. The attenuation and wave speed, Fig. 5.14(c)-(d), are recovered with a one dimensional method such as the two-slab method previously discussed. This simple test case is representative of experimental methods for measuring mechanical properties of viscoelastic fluids [25, 50]. Recording the wave at two different positions corresponds to a receiving transducer that has been repositioned relative to the transmitter. Both receiver and transmitter are immersed in the viscoelastic fluid which is a simpler measurement compared with measurement of a viscoelastic solid. In the case of a solid it must be immersed in fluid (water) to ensure adequate and consistent coupling of ultrasound into the specimen. To be studied in succeeding sections are systematic errors that occur in material property measurement when a diffraction correction is applied to an axisymmetric wave that has undergone transmission through a fluid-solid-fluid system that includes partial reflections at interfaces.

Two-Slab and Slab-Substitution Inverse Method Results

In this section, the longitudinal stress relaxation modulus of a viscoelastic slab is reconstructed from transmitted ultrasonic waves with two-slab and slab-substitution propagator methods. The slab is assumed to be immersed in water and is defined to have material properties as given in eqs. 5.3, 5.4 and 5.5. The real and imaginary components of the frequency domain modulus are calculated from wave speed and attenuation. The wave speed and attenuation are the quantities computed directly from transmitted displacement with relevant equations from Chapter 4 on propagator inverse methods. First, a brief discussion of data processing is presented then a discussion of results follows.

Data processing

Figures 5.15 and 5.16 give an outline of the scheme for transforming recorded wave data at a given source center frequency, f_0, into an estimate for the longitudinal modulus with two-slab and slab-substitution methods, respectively. It has been noted previously that diffraction corrections require wave speed as a function of frequency for calculation, but wave speed is unknown in principle unknown. Typically, a reasonable estimate of wave speed at center frequency is obtained from comparing the difference in time of arrival for some prominent feature of the transmitted wave for two different slab

thicknesses, for example. Wave speed estimated in this way is assumed to be constant over the useful bandwidth at a given center frequency. For calculations here wave speed is taken to be the exact wave speed at center frequency, see Table 5.2. In addition the slab-substitution method requires a reflection measurement to estimate a slab's reflection coefficient, $R_0^+(\omega)$. It is assumed that the reflection coefficient is a real constant and is approximated by the magnitude of the exact reflection coefficient at center frequency (see Table 5.2):

$$R_0^+ \approx \frac{Z_w - |\hat{Z}_s(f_0)|}{Z_w + |\hat{Z}_s(f_0)|} \tag{5.43}$$

$$\hat{Z}_s(f_0) = \sqrt{\rho_s \hat{M}(f_0)} \tag{5.44}$$

$$Z_w = \rho_w c_w. \tag{5.45}$$

There are a variety of different variables such as source and receiver radius that could be varied to show their influence on modulus reconstruction. A select few are chosen that are considered most influential. They are aperture radius given in terms of ka, data measurement location, diffraction correction and slab thickness. For each method attenuation and wave speed are estimated over a band of frequencies centered at f_0. A simple method of concatenation is employed to create composite attenuation and wave speed curves. Where bandwidths overlap a simple average of the two curves is taken. Resultant composite curves may have sharp jumps at the overlaps. Some method of data smoothing could be applied but this was not attempted. Because the source is band limited attenuation and wave speed do not extend down to zero frequency. If the frequency domain modulus were simply set to zero below its low frequency limit, about 400kHz, then the reconstructed time domain modulus would be severely degraded because low frequencies contain general overall trends of the data. With *a priori* knowledge of viscoelastic materials it is reasonable to extend low frequency data directly to zero frequency assuming data at zero frequency is equal to data at 400kHz. A similar argument is made for high frequency data. In this case the last high frequency data point, at about 157MHz, is extended to 1GHz. The choice of 1GHz is arbitrary.

For axisymmetric calculations Table 5.3 gives mesh spatial parameters. Basically, spatial step sizes were doubled compared with earlier one-dimensional calculations so that spatial domains of sufficient extent could be modeled without interference from unwanted reflections from sidewalls. For a given source aperture radius the outside wall in the radial direction was set to four times the aperture radius to ensure no reflections from sidewalls interfered with recorded wave forms. The largest mesh contained 960 × 456 four-node quadrilateral elements (437,760 elements) and a total of 878,345 displacement variables.

1. For diffraction correction assume wave speed has been estimated at f_0
2. Given: raw time trace of transmitted wave at f_0 and averaged over radius, a
3. Window in time the first transmitted pulse without internal re-reflections (if possible)
4. FFT the windowed transmitted wave and calculate spectrum, $\tilde{A}^D_L(\omega)$
5. Window the useful frequency bandwidth of transmitted wave spectrum
6. Repeat steps 2-5 for a slab of different thickness to obtain $\tilde{A}^D_{L+\Delta L}(\omega)$
7. Compute and apply diffraction correction, eq. 5.30, to remove geometric wave spreading:

$$\begin{aligned} \tilde{D}^{\infty}_{2,L} &= \tilde{D}^{\infty}_{2}(S_w + S_L) \\ \tilde{D}^{\infty}_{2,L+\Delta L} &= \tilde{D}^{\infty}_{2}(S_w + S_L + S_{\Delta L}) \\ \tilde{A}_L(\omega) &= \tilde{A}^D_L(\omega)/\tilde{D}^{\infty}_{2,L} \\ \tilde{A}_{L+\Delta L}(\omega) &= \tilde{A}^D_{L+\Delta L}(\omega)/\tilde{D}^{\infty}_{2,L+\Delta L} \end{aligned}$$

8. Compute attenuation and wave speed:

$$\alpha(\omega) = -\frac{1}{\Delta L}\ln\left|\frac{\tilde{A}_{L+\Delta L}(\omega)}{\tilde{A}_L(\omega)}\right| : \qquad c(\omega) = -\frac{\omega \Delta L}{\phi_{\Delta L}(\omega)}$$

9. Compute estimate of modulus for useful bandwidth centered at f_0:

$$\begin{aligned} M'(\omega) &= K' + \frac{4}{3}G' = \rho c^2\left[\frac{1-\beta^2}{[1+\beta^2]^2}\right] \\ M''(\omega) &= K'' + \frac{4}{3}G'' = \rho c^2\left[\frac{2\beta}{[1+\beta^2]^2}\right] \\ \beta(\omega) &= \frac{\alpha(\omega)c(\omega)}{\omega} \end{aligned}$$

10. Repeat steps 2-9 for another f_0
11. Combine modulus estimates for various bandwidths to form an overall estimate
12. Extend low and high frequency modulus data to zero frequency and 1GHz, respectively
13. Compute estimate of time domain modulus (IFFT):

$$M(t) = \mathcal{F}^{-1}\left[\tilde{M}(\omega)\right]$$

Figure 5.15 Data processing for modulus recovery with two-slab propagator method including diffraction correction for axisymmetric case

1. Assume reflection calibration has been performed to recover $R_0^+ = |\tilde{R}_0^+(f_0)|$ at f_0
2. Given: raw time trace of transmitted wave at f_0 and averaged over radius, a
3. Window in time the first transmitted pulse without internal re-reflections (if possible)
4. FFT the windowed transmitted wave and calculate spectrum, $\tilde{A}_L^D(\omega)$
5. Window the useful frequency bandwidth of transmitted wave spectrum
6. Repeat steps 2-5 for the case with slab removed to obtain $\tilde{A}_w^D(\omega)$
7. Compute attenuation and wave speed (assume phase angle, ϕ_T, of $\tilde{R}_0^+$ is zero):

$$\alpha(\omega) = -\frac{1}{\Delta L}\ln\left[\frac{\left|\tilde{A}_L^D(\omega)/\tilde{A}_w^D(\omega)\right|}{\left|1-(R_0^+)^2\right|}\right]; \qquad c(\omega) = \frac{c_w}{1-\frac{c_w\phi_L(\omega)}{\omega\Delta L}}$$

8. Compute estimate of modulus for useful bandwidth centered at f_0:

$$M'(\omega) = K' + \frac{4}{3}G' = \rho c^2\left[\frac{1-\beta^2}{[1+\beta^2]^2}\right]$$

$$M''(\omega) = K'' + \frac{4}{3}G'' = \rho c^2\left[\frac{2\beta}{[1+\beta^2]^2}\right]$$

$$\beta(\omega) = \frac{\alpha(\omega)c(\omega)}{\omega}$$

9. Repeat steps 2-8 for another f_0
10. Combine modulus estimates for various bandwidths to form an overall estimate
11. Extend low and high frequency modulus data to zero frequency and 1GHz, respectively
12. Compute estimate of time domain modulus (IFFT):

$$M(t) = \mathcal{F}^{-1}\left[\tilde{M}(\omega)\right]$$

Figure 5.16 Data processing for modulus recovery with slab-substitution propagator method for axisymmetric case (no diffraction correction)

Table 5.2 Wave speed and reflection coefficient at center frequency, f_0

f_0 (MHz)	$c_l(f_0)$ (m/s)	R_0^+
1.0	1706.0	-0.06412
3.16	1752.0	-0.07743
10.0	2018.0	-0.1472
31.6	2388.0	-0.2284
100.0	2487.0	-0.2475

Table 5.3 Parameters for axisymmetric FE calculations at each center frequency

f_0 (MHz)	h (μm)	Δt (ns)	L_1 (μm)	L_2 (μm)	L (μm)	
1.0	50.0	18.0	7500.0	7500.0	1000.0,	7000.0
3.16	16.0	5.76	2400.0	2400.0	496.0,	2496.0
10.0	5.0	1.8	750.0	750.0	100.0,	700.0
31.6	1.6	0.576	240.0	240.0	49.6,	249.6
100.0	0.5	0.18	75.0	75.0	10.0,	70.0

Discussion of results

With each FEM run one can easily generate megabytes of output. Plots in this section have been 'distilled' from much larger amounts of data. Each composite modulus includes numerical approximation errors from data processing routines as well as from the finite element method itself. Intimately entwined with numerical errors are 'systematic errors' defined to be those aspects of the total recorded waveform whose sole source is beam spreading. Beam spreading is essentially the main source of corruption in recovered moduli. In order to reduce numerical approximation errors, a relatively large number of elements per wavelength have been utilized within the constraints of available computer resources and time.

In what follows Figs. 5.17–5.20 refer to data recovered from a two-slab method and Figs. 5.21–5.24 refer to data recovered from a slab-substitution method. In each case the first and second set of four plots are attenuation and wave speed. The final two sets of four plots for each case are frequency and time-domain longitudinal moduli.

Figures 5.17 and 5.18 show wave speed and attenuation recovered from transmitted axial displacement from two slabs of different thickness. Transmitted fields were averaged over an aperture whose

radius equals the source radius. Averaging simulates a piezoelectric transducer of finite radius whose output voltage and current are proportional to the average total axial field incident upon its face. Results for two different source radii are shown, $ka = 10, 50$, and for two different measurement locations: water/slab interface, $L_1 + L$, and backwall/vacuum interface, $L_1 + L + L_2$. There is some improvement in attenuation and wave speed estimates between 10MHz and 100MHz when data is collected at the backwall/vacuum interface, but increasing aperture radius of source and receiver ($ka = 50$) clearly gives the greatest improvement in accuracy of reconstructed properties especially for attenuation. Recording waves at the backwall/vacuum interface simulates a receiver in the water bath while recording waves at the water/slab interface represents a receiver abutting or actually attached to the slab.

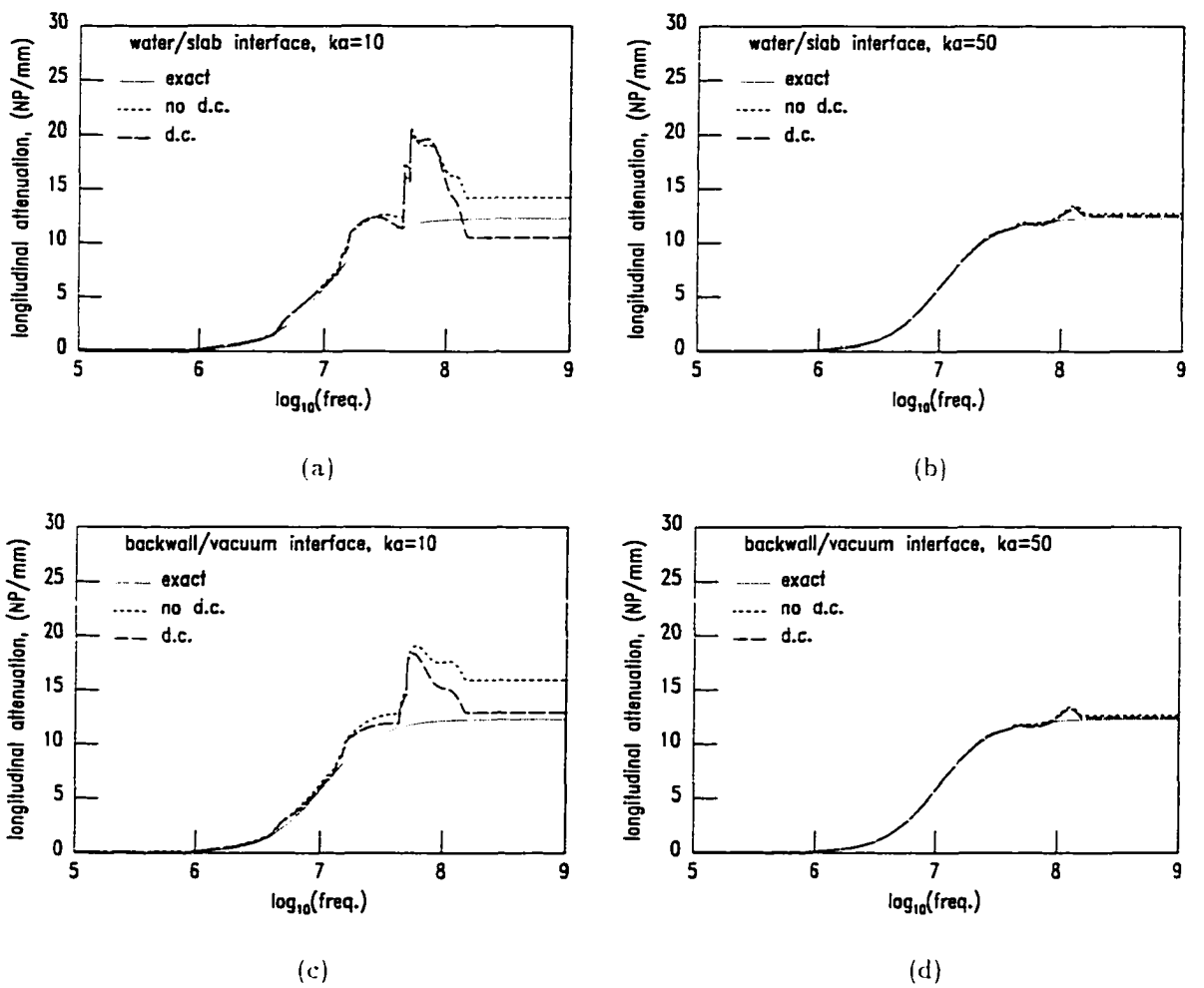

Figure 5.17 Two-slab method: reconstructed and exact longitudinal wave attenuation versus frequency for waves recorded at the water/slab interface with $ka = 10, 50$, (a) and (b), respectively, and the backwall/vacuum interface with $ka = 10, 50$, (c) and (d)

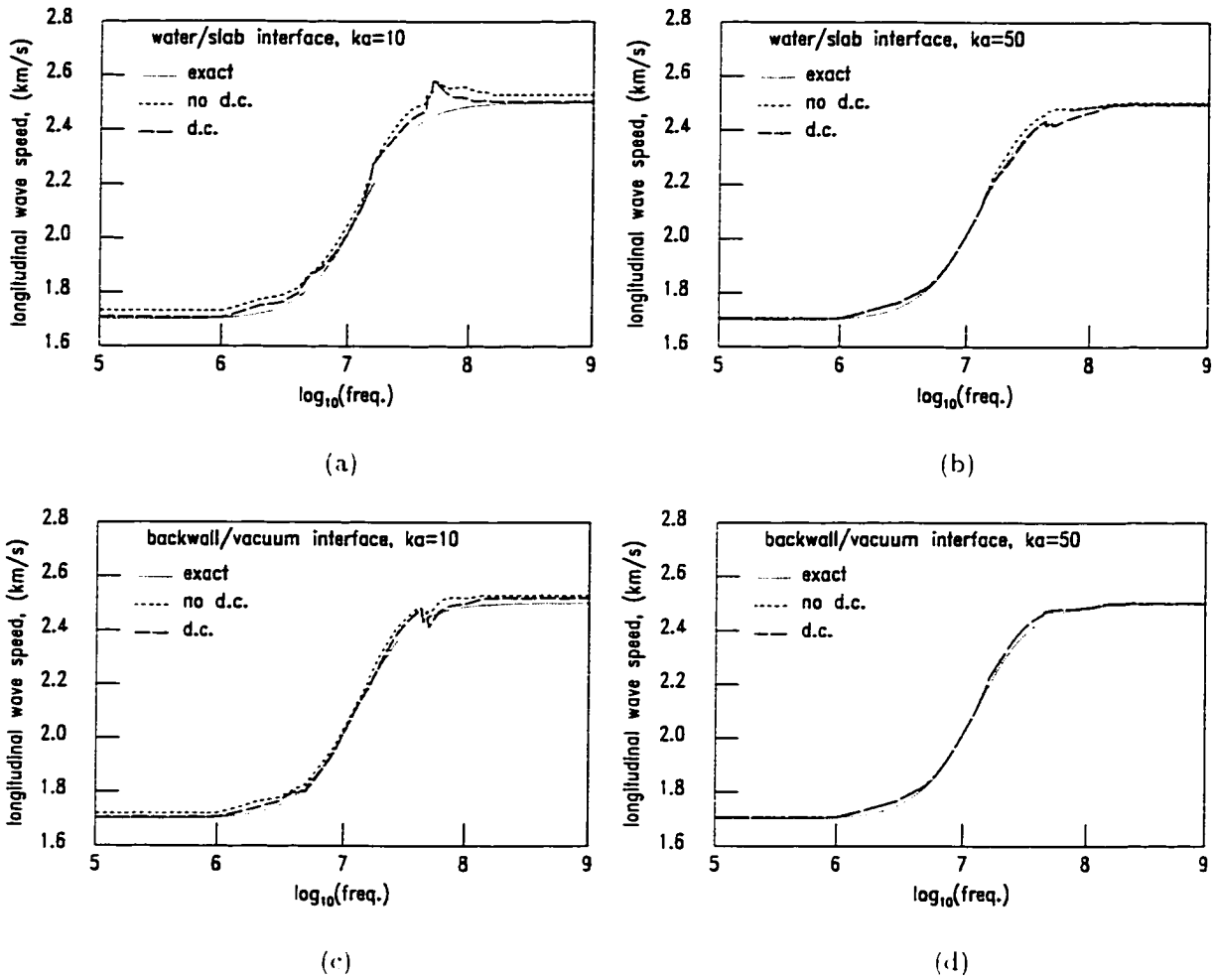

Figure 5.18 Two-slab method: reconstructed and exact longitudinal wave speed versus frequency for waves recorded at the water/slab interface with $ka = 10.\ 50.$ (a) and (b), respectively, and the backwall/vacuum interface with $ka = 10.\ 50.$ (c) and (d)

Attenuation and wave speed recovered with and without diffraction correction is also shown in Figs. 5.17 and 5.18. Again improvement is relatively slight in comparison with increasing aperture radius. If overall distance between source and receiver doubles or triples then a diffraction correction could be more important because decay due to beam spreading increases with distance. Results suggest that for pulsed measurements it is beneficial to keep source and receiver as close together as possible as long as re-reflections do not overlap. For continuous wave measurements close proximity of source and receiver can introduce systematic errors in measurements that are caused by standing waves set up between source and receiver.

Possible causes for the large discrepancy in recovered attenuation could be internal re-reflections

corrupting recorded waves when the slab is at its thinnest ($L = 10\mu m$ at 100MHz). This cause is ruled out for two reasons. First, attenuation at $f_0 = 100$MHz is about $\alpha_l = 0.012NP/\mu m$ and the reflection coefficient is about $|R_0^+| = 0.2475$; therefore, upon one roundtrip through the slab a wave is reduced in amplitude by $(0.2475)^2 \exp(-2 \cdot 0.012 \cdot 10) = 0.04818$ or, in other words, a re-reflection is only about 5% of the directly transmitted wave. This is not enough to account for the nearly 60% increase in attenuation. Besides, if extra attenuation was due in some way to internal re-reflections then the same effect should appear in axisymmetric cases when aperture width increases and in one dimensional results, but in both cases discrepancies are less than or on the order of 5% as shown in Figs. 5.6(b) and 5.7(b). Numerical approximation error is also an unlikely source because there are at least twenty elements per shear wavelength in the slab at 100MHz. Another possible source of systematic error is shear/longitudinal mode coupling inside the slab at the slab/water interface giving rise to axial displacements on the slab surface that do not correspond to displacements due to purely plane wave modes. If this is true then the effect is reduced for increasing aperture radius because such mode coupling occurs farther out from the axis of symmetry near the 'edge' of the ultrasonic beam's inner plane wave region. As the axial displacement is averaged over the receiver, mode coupling effects are weighted less overall relative to the plane wave portion of the field when the aperture is wider. A check on this possibility is left for further work.

The two components of longitudinal modulus are computed from attenuation and wave speed estimates. The best correspondence between exact and estimate occurs for measurement at the back-wall with $ka = 50$ as seen in Fig. 5.19(d). In general it appears that discrepancies in attenuation are smoothed when computing the modulus. In fact, when frequency dependent moduli are inverted to obtain their time dependent counterparts the resulting moduli, Fig. 5.20, all capture the general decaying-exponential trend of the data. For the worst case, Fig. 5.20(a), one might estimate the short-time limiting modulus to be about 7GPa instead of 6.25GPa which is about a 12% increase.

Figures 5.21 and 5.22 show estimates from attenuation and wave speed for the slab-substitition method for two different thicknesses of the slab. Diffraction corrections were not applied in these cases. Recall that a wave is recorded at the same location with or without the slab placed in the propagation path between source and receiver. A visual comparison of attenuation estimated with a two-slab method, Fig. 5.17, and a slab-substitition method, Fig. 5.21, suggests that the two-slab method offers an improved estimate of high frequency attenuation in all cases. It appears that whatever the cause of gross discrepancies in attenuation and wave speed, compare Figs. 5.18 and 5.22, the effect is partially 'cancelled out' when ratios of complex amplitudes are taken for waves transmitted through

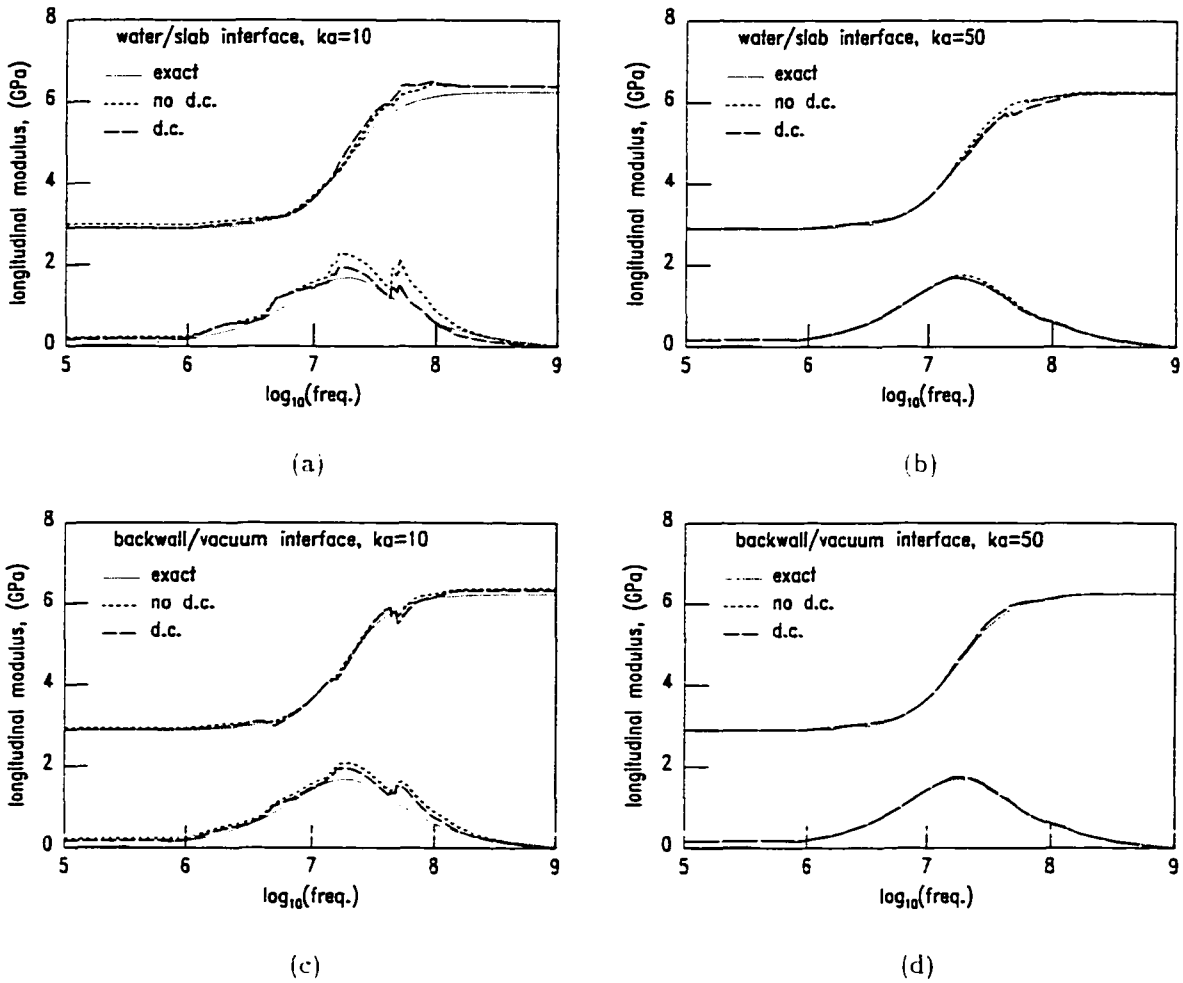

Figure 5.19 Two-slab method: reconstructed and exact longitudinal modulus versus frequency for waves recorded at the water/slab interface with $ka = 10, 50$. (a) and (b), respectively, and the backwall/vacuum interface with $ka = 10, 50$. (c) and (d)

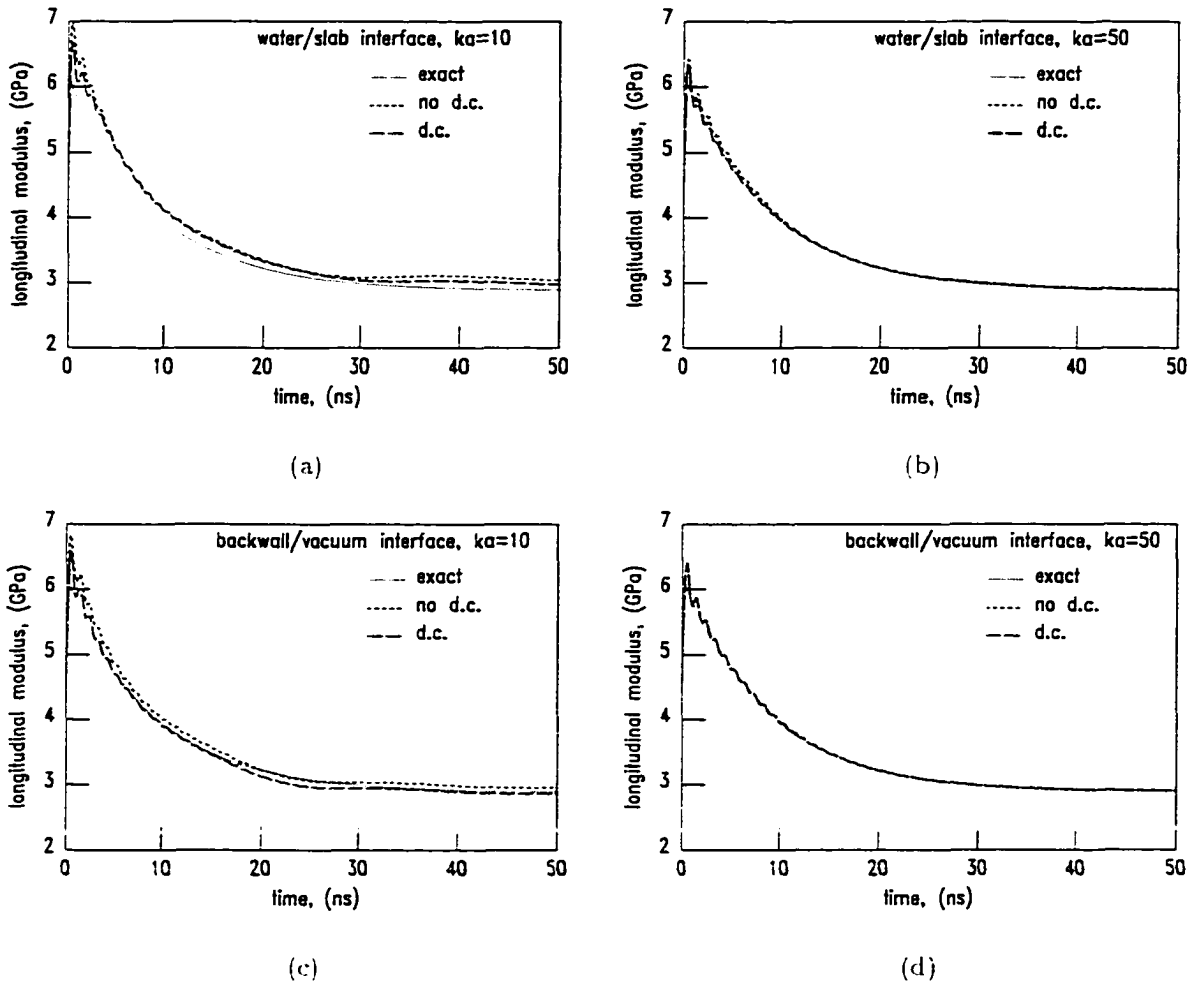

Figure 5.20 Two-slab method: reconstructed and exact longitudinal modulus versus time for waves recorded at the water/slab interface with $ka = 10, 50$. (a) and (b), respectively, and the backwall/vacuum interface with $ka = 10, 50$. (c) and (d)

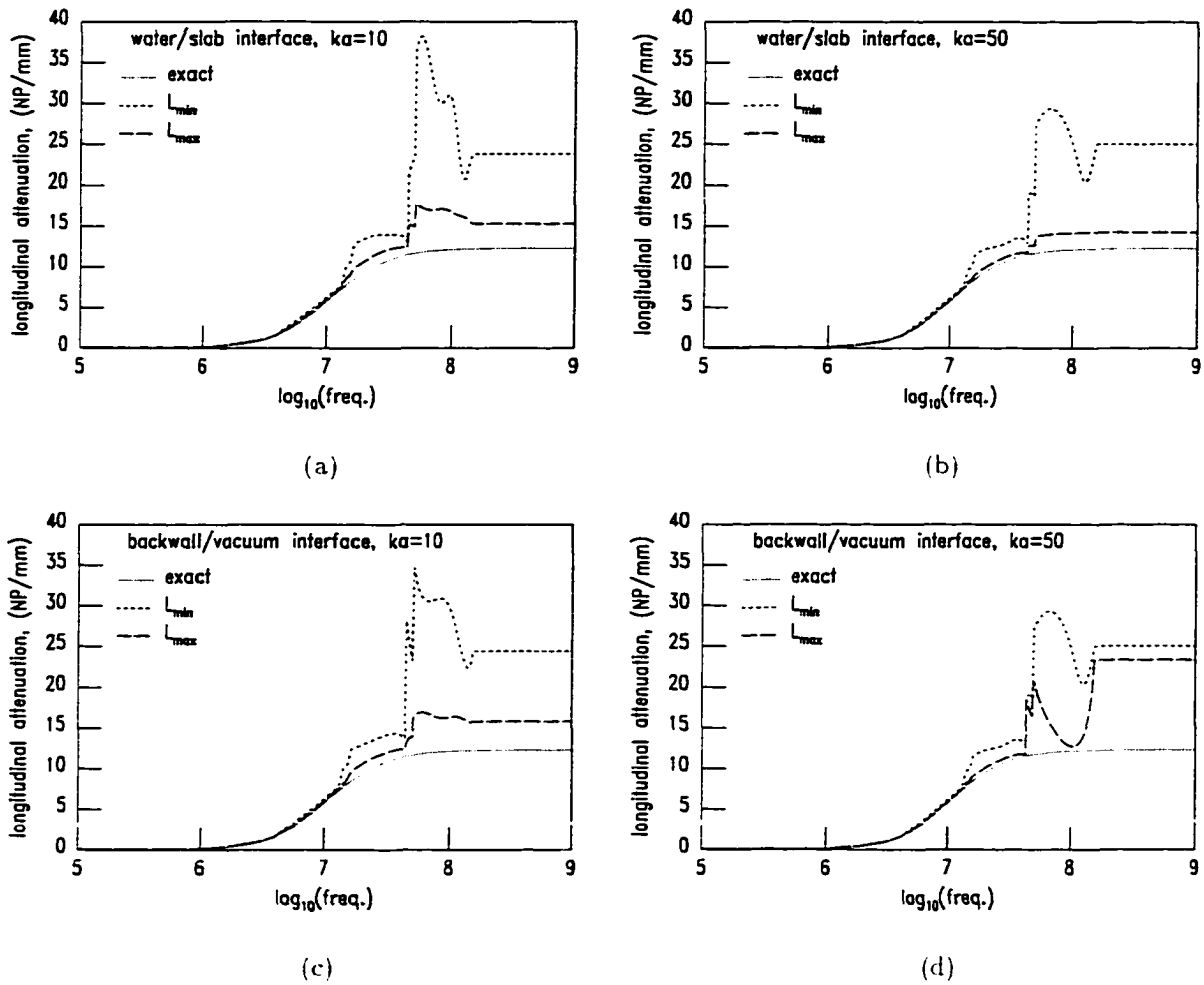

Figure 5.21 Slab-substution method: reconstructed and exact longitudinal wave attenuation versus frequency for waves recorded at the water/slab interface with $ka = 10, 50$. (a) and (b), respectively, and the backwall/vacuum interface with $ka = 10, 50$. (c) and (d)

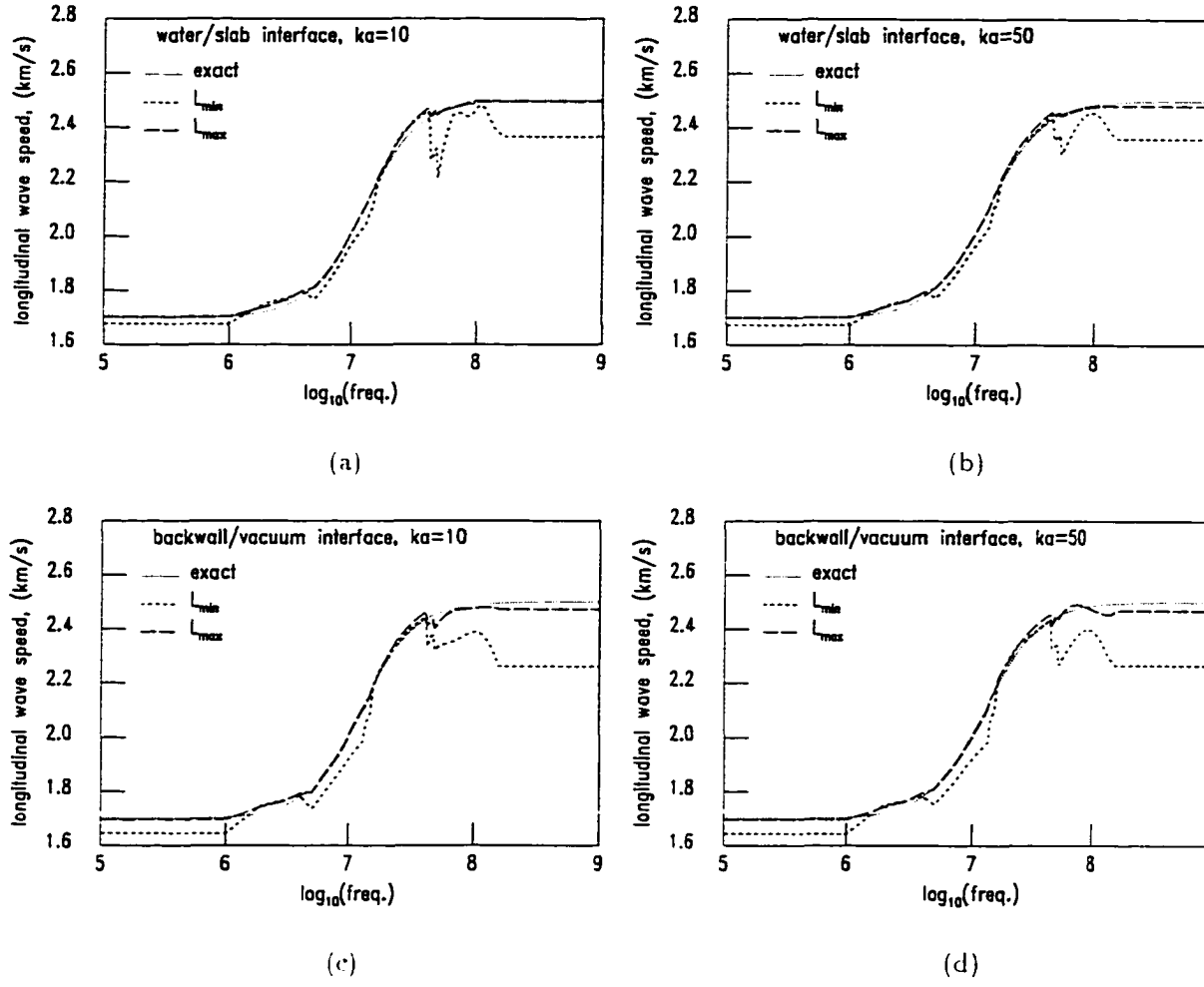

Figure 5.22 Slab-substution method: reconstructed and exact longitudinal wave speed versus frequency for waves recorded at the water/slab interface with $ka = 10, 50$. (a) and (b), respectively, and the backwall/vacuum interface with $ka = 10, 50$. (c) and (d)

two slabs of different thicknesses. If one is to use a slab-substition method then Figs. 5.21 and 5.22 imply that a slab thickness should be chosen so that transmitted waves undergo significant attenuation. For example, at 100MHz $L_{min} = 10\mu m$ and $L_{max} = 70\mu m$ so that one-way attenuation of a transmitted wave amplitude is $\exp(-\alpha_l L_{min}) = 0.8869$ and $\exp(-\alpha_l L_{max}) = 0.4317$, respectively. Attenuation and wave speed estimates are generally improved when the thicker slab is employed. Again, in spite of greater dicrepancies at higher frequencies the frequency and time-domain moduli, Figs. 5.23 and 5.24, respectively, all show reasonable agreement with the exact curve. Reasonable implies that a model for the modulus, if extracted from any of the estimates, would fall within about five or ten percent of the exact modulus both in amplitude and rate of decay. This may not be accurate enough to determine what molecular mechanisms are causing relaxation but it is generally accurate enough for engineering forward models. In terms of ease of use the slab-substitution method is favored because it requires only one slab per frequency band.

Hankel Transform Inverse Method Results

The Hankel transform method, described in Chapter 4, is not a distinctly different method for recovering material properties, but it does represent a different method of data collection. Rather than a receiver with a radius similar to that of the transmitter, assume a relatively small 'point-like' receiver that can be scanned along a radial outward from the axis of symmetry. The receiver stops at discrete points along the radial and records axial displacement as a function of time. Recorded displacements are summed to approximate a Hankel transform given below. For a finite aperture transmitter there will be some radius ($N\Delta r$) beyond which continued scanning yields relatively negligible displacement and at that point further outward scanning ceases. In practice such a device would be approximated by a small piezoelectric hydrophone or a laser beam from a laser interferometer. These devices can have small but finite radius. Effects of finite receiver radius are not considered here but is left for further work. The two propagator methods, two-slab and slab-substitution, are re-examined with wave data collected that approximates a Hankel transform of order zero with transform parameter, ξ, set to zero:

$$u_z^0(z,t) = \int_0^\infty u_z(r,z,t) r dr \tag{5.46}$$

$$\approx (\Delta r)^2 \left\{ \sum_{i=1}^{N} i u_z(i\Delta r, z, t) - \frac{N}{2} u_z(N\Delta r, z, t) \right\}. \tag{5.47}$$

In principle all radial dependence of the wave is integrated out; therefore, only a plane wave remains and no diffraction correction is required.

Data processing

The finite element method is a full field method, that is, at any time step displacement is computed at all node points in the mesh. This fact makes calculating an approximate Hankel transform straightforward. At each time step axial displacement along a chosen radial is summed according to eq. 5.47 and the result is output to a file. Resulting time traces for Hankel transformed axial displacement are processed according to procedures described in Figs. 5.15 and 5.16 except that a diffraction correction is not necessary.

Discussion of results

Figures 5.25 and 5.27 show attenuation and wave speed recovered at water/slab and backwall/vacuum interfaces with two-slab and slab-substitution Hankel transform methods, respectively. Previous results show that a smaller transmitter radius degrades accuracy of recovered quantities more relative to a larger aperture; therefore, it is sufficient to study the case when $ka = 10$. Compare Hankel transform results with previous two-slab results, Figs. 5.17(a), (c) and 5.18(a), (c), and slab-substitution results, Figs. 5.21(a), (c) and 5.22(a), (c), respectively. For the two-slab Hankel transform method there is clear improvement in reconstructed attenuation and wave speed especially at high frequencies. The deviation in attenuation in Fig. 5.25(a) is assumed to be due to an internal re-reflection contaminating the first transmitted pulse. Notice that both water/slab and backwall/vacuum interface results in Fig. 5.25(a) and (b) are indistinguishable to within a line-width suggesting any deviations from exact values are systematic errors arising from sources other than measurement location. For the slab-substitution method, Fig. 5.27, there is some improvement in high frequency attenuation and wave speed but large discrepancies still remain. A close comparison of Figs. 5.27(a) and (b) and Figs. 5.27(c) and (d) reveals that for two different measurement locations the reconstructed attenuation and wave speed are nearly identical. Discrepancies are reduced when a thicker slab is employed suggesting that whatever causes systematic errors between exact and recovered attenuation is suppressed more as the total attenuation, αL, increases. A more thorough investigation of these differences is left for further work. Figures 5.26(a) and 5.28 show frequency-domain moduli and Figs 5.26(b) and 5.29 show time-domain moduli. A general observation is that a slab-substitution Hankel transform method with a thicker slab and a two-slab method with or without Hankel transform processing gives frequency and time-domain moduli with practically the same quality, at least in a visual comparison.

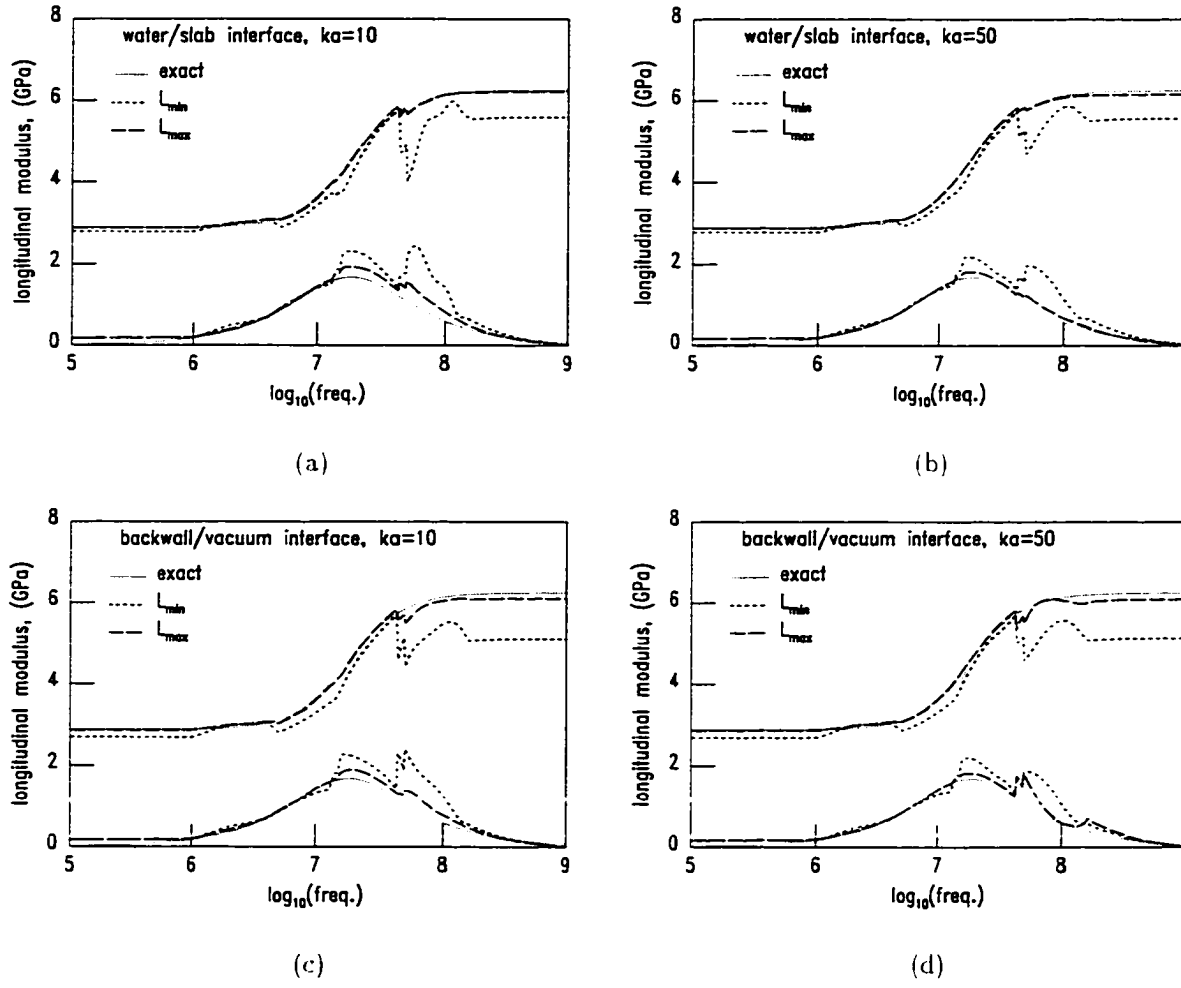

Figure 5.23 Slab-substution method: reconstructed and exact longitudinal modulus versus frequency for waves recorded at the water/slab interface with $ka = 10, 50$. (a) and (b), respectively, and the backwall/vacuum interface with $ka = 10, 50$. (c) and (d)

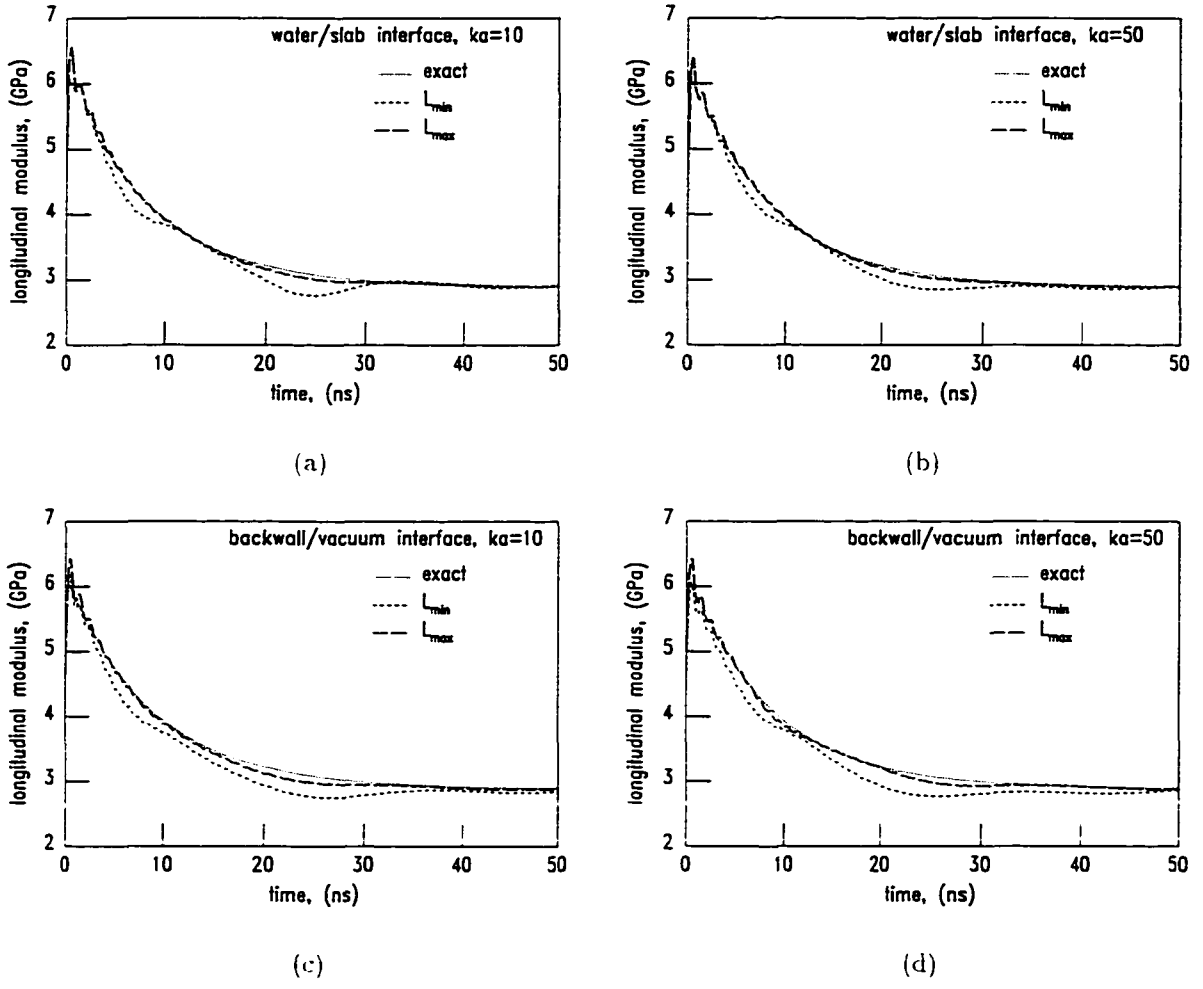

Figure 5.24 Slab-substution method: reconstructed and exact longitudinal modulus versus time for waves recorded at the water/slab interface with $ka = 10, 50$, (a) and (b), respectively, and the backwall/vacuum interface with $ka = 10, 50$, (c) and (d)

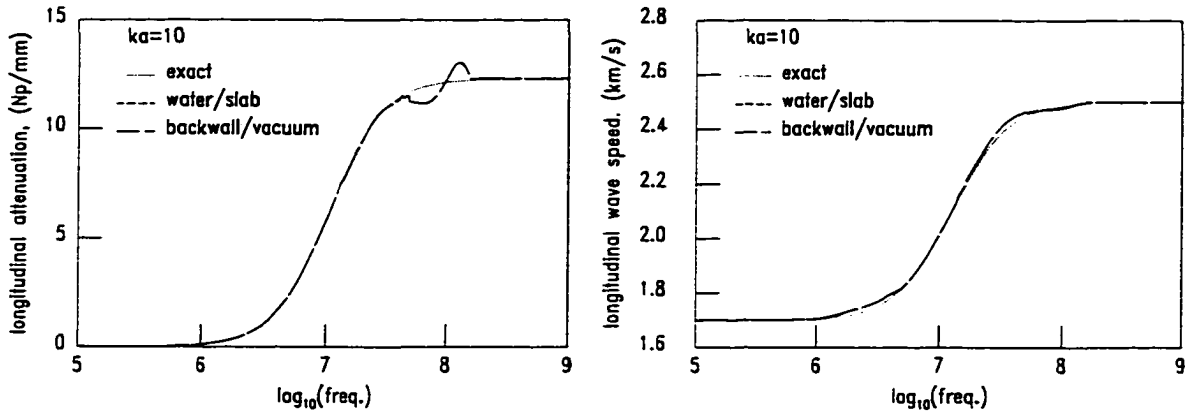

(a) (b)

Figure 5.25 Two-slab Hankel transform method: reconstructed and exact longitudinal wave attenuation and wave speed, (a) and (b), respectively, versus frequency for waves recorded at the water/slab and backwall/vacuum interface with $ka = 10$

Wave Splitting Inverse Method Results

Propagator inverse methods described above can recover attenuation and wave speed versus frequency from transmitted wave data. From attenuation and wave speed a frequency dependent modulus is computed. Attenuation and wave speed cannot be recovered with a single measurement over a frequency band sufficiently wide enough to reconstruct, ultimately, the time dependent relaxation modulus. A time domain modulus is computed from its frequency domain counterpart via an inverse Fourier transform. The inverse Fourier transform requires knowledge of the modulus over a broad frequency spectrum relative to the source bandwidth at a particular center frequency, f_0: therefore, a series of measurements at different center frequencies and slab thicknesses are required so that a composite modulus can be created as a function of frequency. This paradigm is fundamental and must be employed for recovery of data necessary for wave splitting inverse algorithms.

In contrast with propagator methods, wave splitting inverse methods require time domain reflection and transmission kernels. For homogeneous and isotropic viscoelastic media the specific wave splitting inverse algorithm described in Chapter 3 requires a transmission kernel for a single slab thickness. As in propagator methods the same restrictions apply for recovery of the frequency dependent transmission kernel, that is, a piece of the kernel is determined over a frequency band with a slab thickness

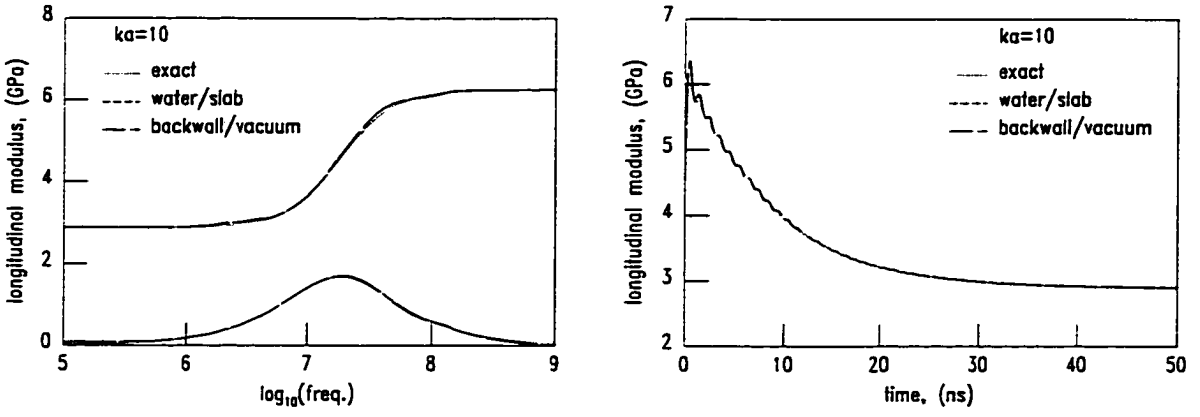

Figure 5.26 Two-slab Hankel transform method: reconstructed and exact longitudinal modulus versus frequency and time. (a) and (b), respectively, for waves recorded at the water/slab and backwall/vacuum interface with $ka = 10$

appropriate for that particular range of frequencies. Unfortunately, a slab thickness appropriate for measurements at a center frequency of one megahertz is at least one order of magnitude greater than the thickness appropriate for a center frequency of one hundred megahertz considering the specific attenuation (material parameters) chosen for the model problem. This presents a unique challenge not encountered with propagator methods. Transmission kernel data measured at several different slab thicknesses must be converted to an equivalent transmission kernel valid for one overall slab thickness. In other words, if a slab thickness of one millimeter is appropriate for measurement at one megahertz and one tenth of a millimeter is appropriate for one hundred megahertz then transmission kernel data measured at one hundred megahertz must be translated to a thickness of one millimeter or vice versa. Only when all data is translated to the same thickness can the transmission kernel be estimated. Translating transmission kernel data from one slab thickness to another is explored under conditions of finite source and receiving aperture and location of measurement. As before transmitted waves are averaged over the receiver aperture to simulate a piezoelectric transducer. It is shown that a reasonable estimate for the time domain transmission kernel is obtained for a relatively thick and thin slab, respectively, but only the transmission kernel for a thin slab is suitable for recovery of the time domain relaxation modulus. Reasons for this point and overall discussion of the results conclude this section.

Data processing

Examples of time domain transmission kernels are shown in Chapter 3. A distinguishing feature of transmission kernels with front and back wall impedance mismatch, $T_f(0, L, t)$, are finite jumps at times corresponding to multiples of a wave's round trip time through the slab, τ_0. In principle, all of the round trips must be accounted for, but in practice only the first round trip is utilized because higher order internal reflections are usually highly attenuated compared to the first transmitted wave and because greater deviation from a plane wave accumulates in higher order transmitted waves. From the definition of the scattering operator, $\mathcal{T}_f$, in eq. 3.87 with front and backwall impedance mismatch, the first round trip through the slab ($j = 0$) is

$$u^+(L, t + \tau_0/2) = \mathcal{T}_f u^+(0, t) = t_0^+ t_L^+ d_0 u^+(0, t) + t_0^+ t_L^+ \left[T_f * u^+\right](0, t). \tag{5.48}$$

Upon Fourier transforming this equation the transmission kernel is written formally as

$$\tilde{T}_f(0, L, \omega) = \frac{1}{t_0^+ t_L^+} \tilde{\mathcal{T}}_f(0, L, \omega) - d_0 \tag{5.49}$$

$$= \frac{1}{t_0^+ t_L^+} \left[\frac{\tilde{u}^+(L, \omega)}{\tilde{u}^+(0, \omega)}\right] - d_0. \tag{5.50}$$

From a simple bounce diagram approach (see appendix, eq. A.12) the frequency domain transmission and reflection operators for times less than one round trip through the slab are written by inspection:

$$\tilde{\mathcal{T}}_f(0, L, \omega) = \tilde{t}_{0,f}^+(\omega) \tilde{t}_{L,b}^+(\omega) d_0 \tilde{P}_N(\omega) \tag{5.51}$$

$$\tilde{\mathcal{R}}_f(0, L, \omega) = \tilde{r}_{0,f}^+(\omega) \tag{5.52}$$

where subscript 'N' implies normalized slab propagator (see appendix, eq. A.6) and 'f' and 'b' imply front and backwall. The 't's are front and backwall impedance-mismatched transmission coefficients. Assuming material on either side of the viscoelastic slab is water the term $\tilde{t}_{0,f}^+(\omega)\tilde{t}_{L,b}^+(\omega)$ becomes

$$\tilde{t}_{0,f}^+(\omega)\tilde{t}_{L,b}^+(\omega) = 1 - (\tilde{r}_{0,f}^+(\omega))^2 \tag{5.53}$$

where

$$\tilde{r}_{0,f}^+(\omega) = \frac{Z_w - \tilde{Z}_{ve}(\omega)}{Z_w + \tilde{Z}_{ve}(\omega)} \tag{5.54}$$

$$\tilde{Z}_{ve}(\omega) = \sqrt{\rho_{ve} \tilde{M}(\omega)} \tag{5.55}$$

$$Z_w = \rho_w c_w. \tag{5.56}$$

The wave propagator, $\tilde{P}_N(\omega)$, has the form

$$\tilde{P}_N(\omega) = e^{-(\alpha(\omega) - \alpha_\infty)L} e^{-i\omega L(1/c(\omega) - 1/V_{ref})} \tag{5.57}$$

where

$$\lim_{\omega \to \infty} \alpha(\omega) = \alpha_\infty \tag{5.58}$$

$$\lim_{\omega \to \infty} c(\omega) = V_{lg}. \tag{5.59}$$

Finally, the desired frequency dependent transmission kernel for the first transmitted wave is

$$\tilde{T}_f(0, L, \omega) = \frac{1}{1 - (r_0^+)^2} \left[(1 - (\tilde{r}_{0,f}^+(\omega))^2) d_0 \tilde{P}_N(\omega) \right] - d_0. \tag{5.60}$$

The zero and infinite frequency limits are

$$\lim_{\omega \to 0} \tilde{T}_f(0, L, \omega) = \frac{1}{1 - (r_0^+)^2} \left[(1 - (\tilde{r}_{0,f}^+(0))^2) d_0 \right] - d_0 \tag{5.61}$$

$$\lim_{\omega \to \infty} \tilde{T}_f(0, L, \omega) = 0. \tag{5.62}$$

Figure 5.30 outlines steps for recovery of a relaxation modulus from a transmission kernel valid for one effective slab thickness, L_{eff}, created from transmission kernels determined at different thicknesses and frequency bands.

'Star product' for combining transmission kernels

In Chapter 3 an algebraic composition or product of operators, called a star product, was introduced. It is an essential building block for invariant embedding methods and a key to constructing general one-dimensional integro-differential equations for reflection and transmission kernels. Equations 3.33-3.36 are the star product operator equations for addition of a thin slab at the left most interface of an existing slab.

In general, the star product of two operator scattering matrices is given in eq. 3.32 and repeated here with subscipt '1' and '2' denoting slab one and slab two, respectively.

$$\underline{\mathcal{S}}_{1+2} = \underline{\mathcal{S}}_1 * \underline{\mathcal{S}}_2. \tag{5.63}$$

The appropriate star product for combining transmission operators for two slabs, eq. 3.33, is

$$\mathcal{T}_{f,1+2}^+ = \mathcal{T}_{f,2}^+ \left[1 - \mathcal{R}_{f,1}^- \mathcal{R}_{f,2}^+ \right]^{-1} \mathcal{T}_{f,1}^+. \tag{5.64}$$

Due to the spatial symmetry of the viscoelastic slab $\mathcal{R}_{f,1}^- = \mathcal{R}_{f,1}^+$ and superscipts can be dropped. The transmission operators and kernels are known to be functions only of frequency; therefore, operator ordering can be ignored. With these simplifications the transmission kernel star product becomes

$$\mathcal{T}_{f,1+2} = \frac{\mathcal{T}_{f,1} \mathcal{T}_{f,2}}{1 - \mathcal{R}_{f,1} \mathcal{R}_{f,2}} \tag{5.65}$$

For cases to be considered the $\mathcal{T}_{f,1} = \mathcal{T}_{f,2}$ and $\mathcal{R}_{f,1} = \mathcal{R}_{f,2}$, that is, operators for the same slab are combined to yield a transmission operator in the frequency domain for a slab twice the original thickness. Equation 5.65 becomes

$$\tilde{\mathcal{T}}_f(0, 2L, \omega) = \frac{(\tilde{\mathcal{T}}_f(0, L, \omega))^2}{1 - (\tilde{\mathcal{R}}_f(0, L, \omega))^2}. \tag{5.66}$$

In order for this star product to be practically useful some approximations must be made. As was done for the slab-substitution method, the reflection operator is approximated by the reflection coefficient at f_0 or $\tilde{\mathcal{R}}_f(0, L, \omega) \approx \tilde{r}^+_{0,f}(f_0) = R^+_0|_{f_0}$; therefore,

$$\tilde{\mathcal{T}}_f(0, 2L, \omega) = \frac{(\tilde{\mathcal{T}}_f(0, L, \omega))^2}{1 - (R^+_0)^2} \tag{5.67}$$

where R^+_0 is selected from Table 5.2 for the relevant f_0.

The star product method can be continued, in principle, to obtain an equivalent transmission kernel for a slab of thickness $3L$, $4L$, $5L$, etc. When finished the transmisson kernel must be recovered for input into the inverse algorithm. For a star product of 'j' identical slabs the transmission operator and kernel are, respectively,

$$\tilde{\mathcal{T}}_f(0, jL, \omega) = \frac{(\tilde{\mathcal{T}}_f(0, L, \omega))^j}{(1 - (R^+_0)^2)^{j-1}} \tag{5.68}$$

$$\tilde{T}_f(0, jL, \omega) = \frac{1}{1 - (r^+_0)^2} \tilde{\mathcal{T}}_f(0, jL, \omega) - (d_0)^j \tag{5.69}$$

$$(d_0)^j = e^{-j\tilde{n}_0\tau_0/4} = e^{-\alpha_\infty jL}. \tag{5.70}$$

Of course combining two transmission operators to obtain the transmission operator of a slab twice as thick, for example, begs the question 'can the transmission operator for a slab with half the thickness, $L/2$, be obtained from a transmission operator for slab with thickness L?' Under current conditions and assumptions the answer is yes. With eq. 5.67 the transmission operator for a slab with thickness L is

$$\tilde{\mathcal{T}}_f(0, L/2, \omega) = \sqrt{[1 - (R^+_0)^2]\tilde{\mathcal{T}}_f(0, L, \omega)} \tag{5.71}$$

and the corresponding transmission kernel is

$$\tilde{T}_f(0, L/2, \omega) = \frac{1}{1 - (r^+_0)^2} \tilde{\mathcal{T}}_f(0, L/2, \omega) - (d_0)^{1/2} \tag{5.72}$$

$$(d_0)^{1/2} = e^{-\alpha_\infty L/2}. \tag{5.73}$$

In general, for halving the original slab 'j' times the resulting transmission kernel is

$$\tilde{T}_f(0, L/2^j, \omega) = \frac{1}{1 - (r^+_0)^2} \left[\prod_{i=1}^{j} \left[1 - (R^+_0)^2\right]^{1/2^i}\right] \left[\tilde{\mathcal{T}}_f(0, L, \omega)\right]^{1/2^j} - [d_0]^{1/2^j} \tag{5.74}$$

$$[d_0]^{1/2^j} = e^{-\alpha_\infty L/2^j}. \tag{5.75}$$

The term, r_0^+, is the front-wall 'hard' reflection coefficient defined by eq. 3.76. It is assumed that $r_0^+ \approx R_0^+|_{f_0=100MHz}$ in all cases.

Discussion of results

Table 5.4 gives estimates for high-frequency wavefront attenuation, d_0, when $L = 100\mu m$ and $f_0 = 100$MHz. Estimates for d_0 versus aperture radius confirms again that increasing aperture radius relative to wavelength gives the greatest improvement in accuracy of measured quantities. Figures 5.31 and 5.32 show frequency domain transmission kernels that have been created by translating transmission kernel fragments recovered within each frequency band to an effective slab length, L_{eff}, and then combining translated fragments together to form a complete kernel. Where there is overlap in kernel fragments at band edges the fragments are simply averaged together. For each frequency band the actual slab thickness is given in Table 5.5 with the corresponding L_{eff} at the top of each column. For example, at $f_0 = 100$MHz the transmission kernel was translated from an actual slab thickness of $100\mu m$ to an effective slab thickness of $1mm$ by application of eqs. 5.68–5.70, a ten-fold increase in slab thickness ($j = 10$). For translating from a $1mm$ thick slab to a $0.125mm$ slab requires application of eqs. 5.74 and 5.75 with $j = 3$, a decrease in slab thickness of eight times.

When kernel data are translated to $L_{\text{eff}} = 1mm$ as in Fig. 5.31, the resulting time-domain transmission kernels in Figs. 5.31(b) and (d) immediately reveal several important points. Ignoring for the moment deterioration in the recovered kernel due to various systematic effects such as aperture width, the kernels have a peak at about $200ns$. This implies that an incident wave convolved with any of these kernels to produce a transmitted wave will be delayed in time relative to the incident wave by about $200ns$ plus, of course, the time delay for the wavefront to traverse the slab, $\tau_0/2 = 400ns$, or about $600ns$ in total. The low frequency limiting wave speed is $1700m/s$ and the time delay across the slab for a wave traveling at this speed is about $588ns$. The main point is that the slab is a filter and is effectively eliminating high frequencies from transmitted waves. While this is not a surprising result it has profound consequences for recovering the relaxation modulus. In contrast Fig. 5.32 shows frequency and time domain transmission kernels for an effective slab length of $0.125mm$. In particular notice the difference in short-time response of Figs. 5.32(b) and (d) compared with Figs. 5.31(b) and (d). The kernels for $L_{\text{eff}} = 0.125mm$ peak near time zero as opposed to $200ns$ for kernels with $L_{\text{eff}} = 1mm$. As time goes to zero in Figs. 5.31(b) and (d) the kernels show increased oscillation due to loss of high frequency information. Figure 5.33 demonstrates the effect that slab thickness has on frequency and time response of the transmission kernel. In Fig. 5.33(a) normalized magnitude spectra for $L_{\text{eff}} = 1mm$

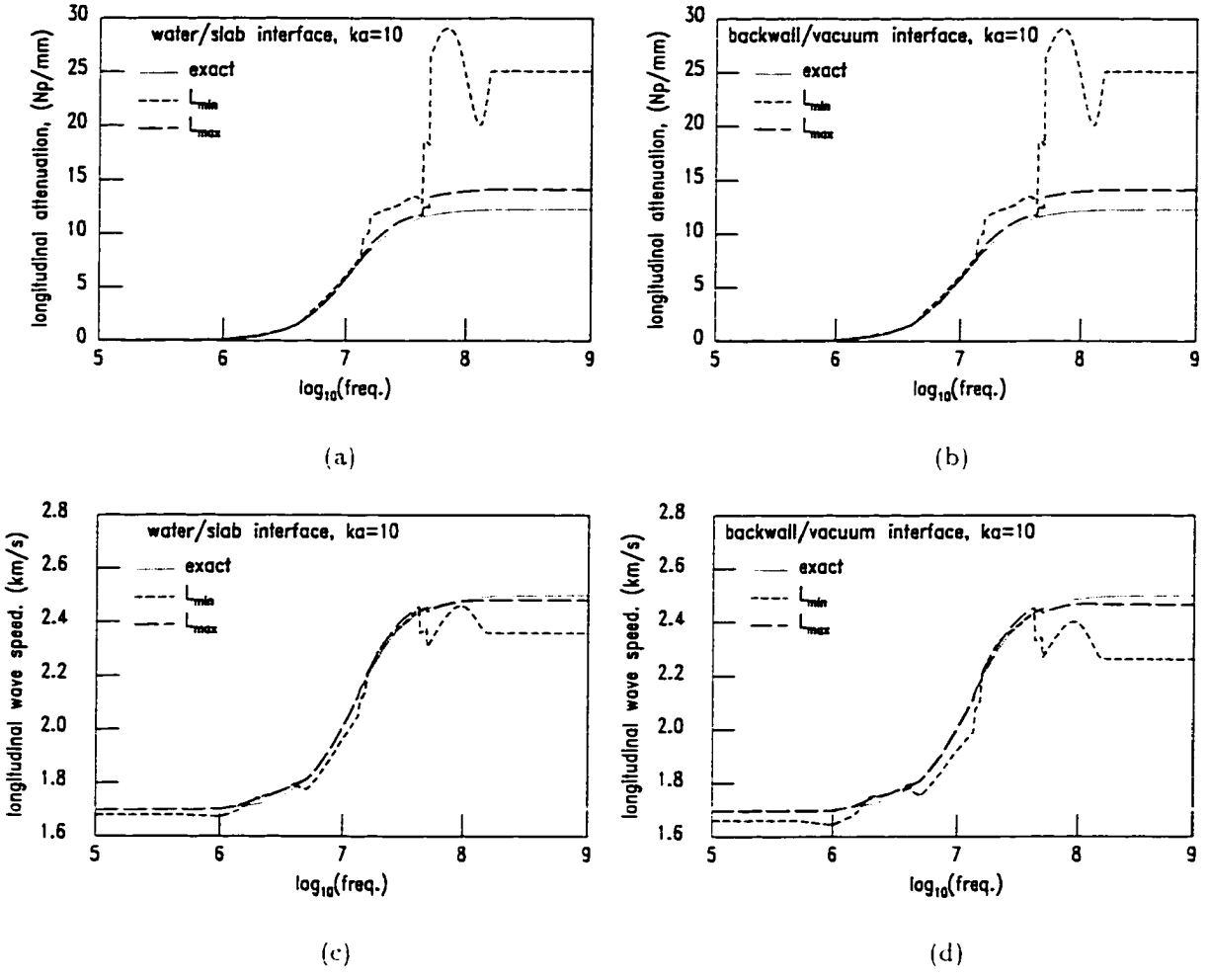

Figure 5.27 Slab-substitution Hankel transform method: reconstructed and exact longitudinal wave attenuation and wave speed versus frequency for waves recorded at the water/slab interface. (a) and (c). and backwall/vacuum interface. (b) and (d). with $ka = 10$

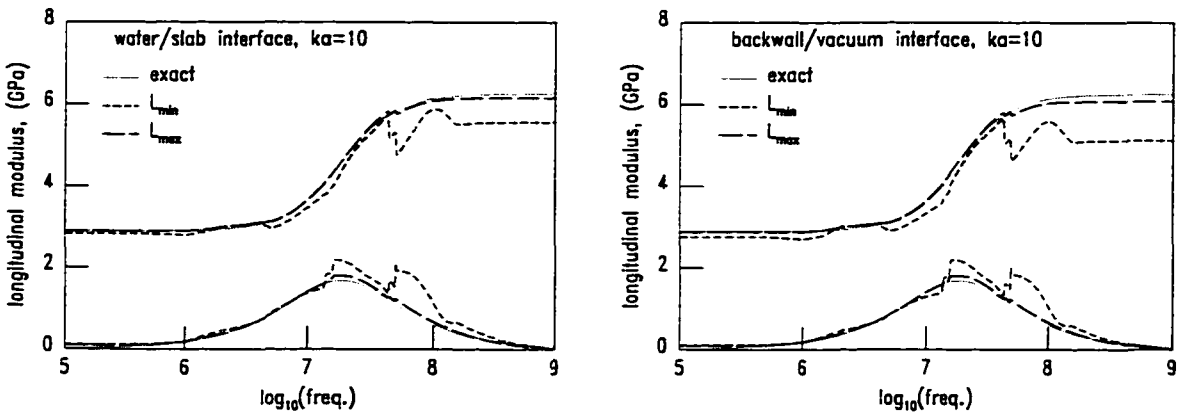

(a) (b)

Figure 5.28 Slab-substitution Hankel transform method: reconstructed and exact longitudinal modulus versus frequency for waves recorded at the water/slab interface, (a), and backwall/vacuum interface, (b), with $ka = 10$

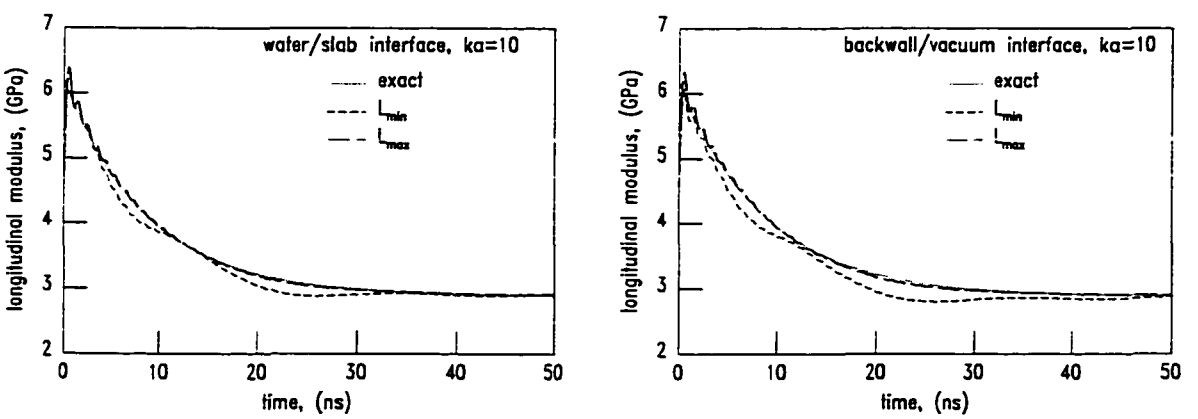

(a) (b)

Figure 5.29 Slab-substitution Hankel transform method: reconstructed and exact longitudinal modulus versus time for waves recorded at the water/slab interface, (a), and backwall/vacuum interface, (b), with $ka = 10$

1. Assume water's acoustic impedance, Z_w, and slab thickness, L, are known then estimate r_0^+ and d_0 from a transmission measurement at the highest available frequency (100MHz in this case)

2. From $r_0^+ \approx R_0^+(f_0 = 100\text{MHz})$ (see Table 5.2) estimate V_{lg} and τ_0 and from d_0 estimate $\alpha_\infty \approx \alpha(f_0 = 100\text{MHz})$ and $\dot{n}_0$

3. Given: raw time trace of transmitted wave, $u^+(L,t)$, at f_0 and averaged over radius, a

4. Window in time the first transmitted pulse without internal re-reflections (if possible)

5. FFT the windowed transmitted wave and calculate spectrum, $\tilde{u}^+(L,\omega)$

6. Window the useful frequency bandwidth of transmitted wave spectrum

7. Repeat steps 2-6 for the incident wave, $u^+(0,t)$, recorded with slab removed at the position of the slab's front interface

8. Compute estimate of transmission kernel:

$$\tilde{T}_f(0,L,\omega) = \frac{1}{1-(r_0^+)^2}\left[\frac{\tilde{u}^+(L,\omega)}{\tilde{u}^+(0,\omega)}\right] - d_0,$$

   where $\tilde{T}_f(0,L,\omega) = \tilde{u}^+(L,\omega)/\tilde{u}^+(0,\omega)$

9. Repeat steps 2-8 for another source center frequency, f_0, and appropriate slab thickness, L

10. Translate all transmission kernel estimates for various bandwidths and slab thicknesses to one effective slab thickness, L_{eff}, by means described in the text

11. Combine transmission kernel estimates translated to one effective slab thickness to form an overall estimate of the transmission kernel versus frequency

12. Extend low and high frequency transmission kernel data to zero frequency and 1GHz, respectively

13. Compute estimate of time domain transmission kernel (IFFT):

$$T_f(0,L_{\text{eff}},t) \quad = \quad \mathcal{F}^{-1}\left[\tilde{T}_f(0,L_{\text{eff}},\omega)\right]$$

14. With wave splitting inverse algorithm estimate time domain relaxation modulus, $M(t)$, with $T_f(0,L_{\text{eff}},t)$, d_0, r_0^+, L_{eff}, ρ_w, c_w and ρ_s as inputs, specifically: $(\rho_w, c_w, \rho_s, r_0^+) \Rightarrow V_{lg}$, $(V_{lg}, L_{\text{eff}}) \Rightarrow \tau_0$, $(d_0, \tau_0) \Rightarrow \dot{n}_0$, and $(d_0, r_0^+, \tau_0, \dot{n}_0, T_f(0,L_{\text{eff}},0)) \Rightarrow \ddot{n}_0$

Figure 5.30 Data processing for time domain relaxation modulus recovery from estimated transmission kernel for an effective slab thickness, L_{eff}

Table 5.4 Estimates from FEM calculations for wavefront attenuation, d_0, infinite frequency attenuation, α_∞, and derivative of normalized creep compliance at short time, $\dot{n}_0$, for $f_0 = 100$MHz and $L = 100\mu m$: exact values for computing percent difference are $d_0 = 0.2926$, $\alpha_\infty = 12.29$ Np/mm and $\dot{n}_0 = 61.44(10^6)s^{-1}$ (b.w., w., v., and s. denote backwall, water, vacuum and slab, respectively)

radius	interface	d_0	d_0 $\Delta\%$	α_∞ (Np/mm)	α_∞ $\Delta\%$	$\dot{n}_0$ (Ms^{-1})	$\dot{n}_0$ $\Delta\%$
$ka = 10$	w./s.	0.1795	-38.7	17.12	39.3	87.15	41.8
	b.w./v.	0.1448	-50.5	19.32	57.2	98.44	60.2
$ka = 50$	w./s.	0.2834	-3.16	12.61	2.62	62.44	1.63
	b.w./v.	0.2788	-4.73	12.77	3.92	63.20	2.86

Table 5.5 Actual slab thicknesses, L, for corresponding center frequency, f_0, and effective slab thickness, L_{eff}

	$L_{\text{eff}} = 1mm$	$L_{\text{eff}} = 0.125mm$
f_0 (MHz)	L (μm)	L (μm)
1.0	1000.0	1000.0
3.16	496.0	496.0
10.0	250.0	250.0
31.6	249.6	249.6
100.0	100.0	62.5

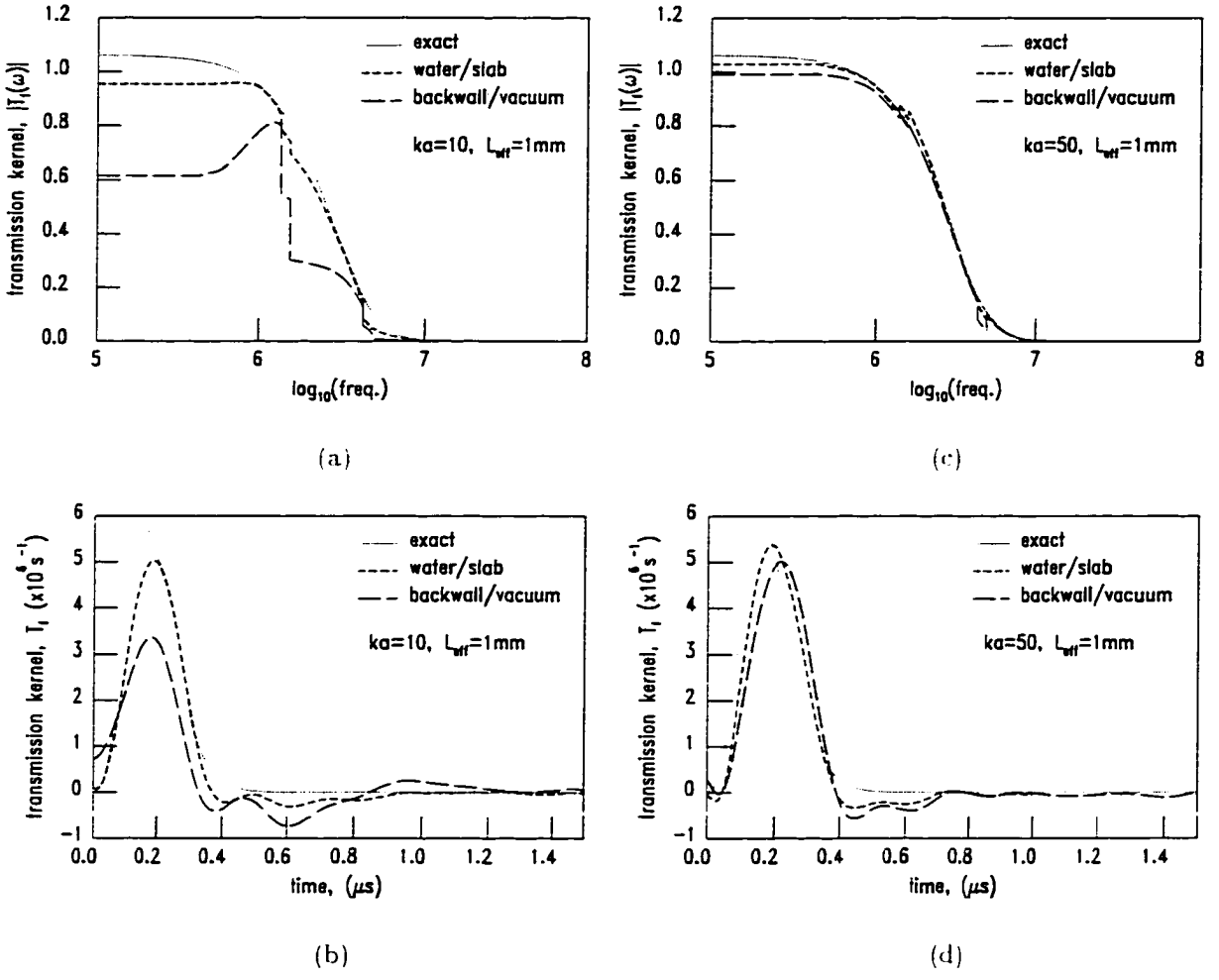

Figure 5.31 Wave splitting inverse method: reconstructed and exact transmission kernel versus frequency and time for waves recorded at the water/slab and backwall/vacuum interface and $L_{\text{eff}} = 1mm$ for $ka = 10$. (a) and (b), and for $ka = 50$. (c) and (d)

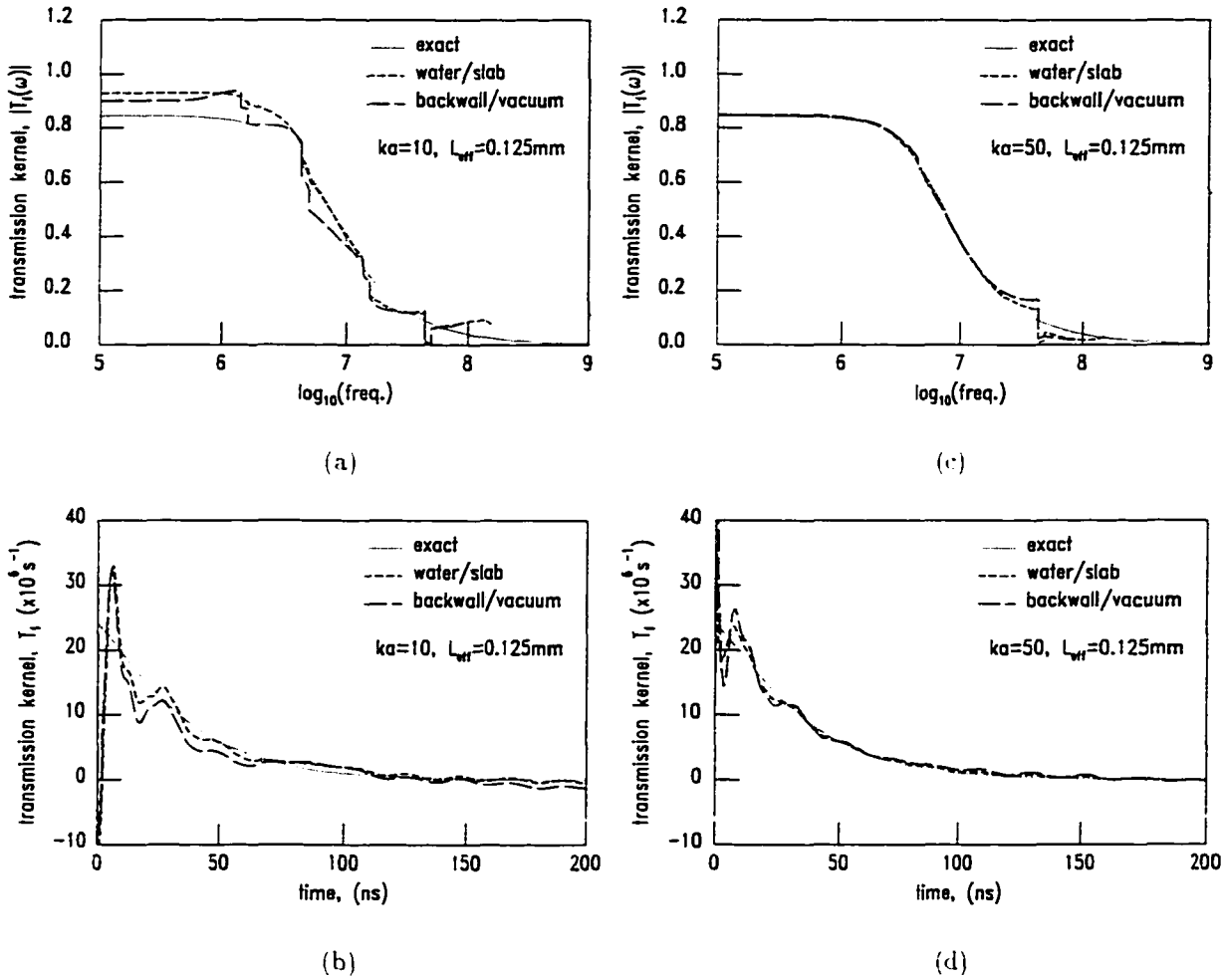

Figure 5.32 Wave splitting inverse method: reconstructed and exact transmission kernel versus frequency and time for waves recorded at the water/slab and backwall/vacuum interface and $L_{\text{eff}} = 0.125mm$ for $ka = 10$. (a) and (b), and for $ka = 50$. (c) and (d)

exact kernels for and $0.125mm$ are plotted along with the magnitude spectrum of the relaxation modulus. The kernel spectrum for $1mm$ becomes negligible even before the modulus has reached its low to high frequency transition region. On the other hand the kernel spectrum for $0.125mm$ has a non-zero overlap with the modulus through the high frequency regime at 100MHz.

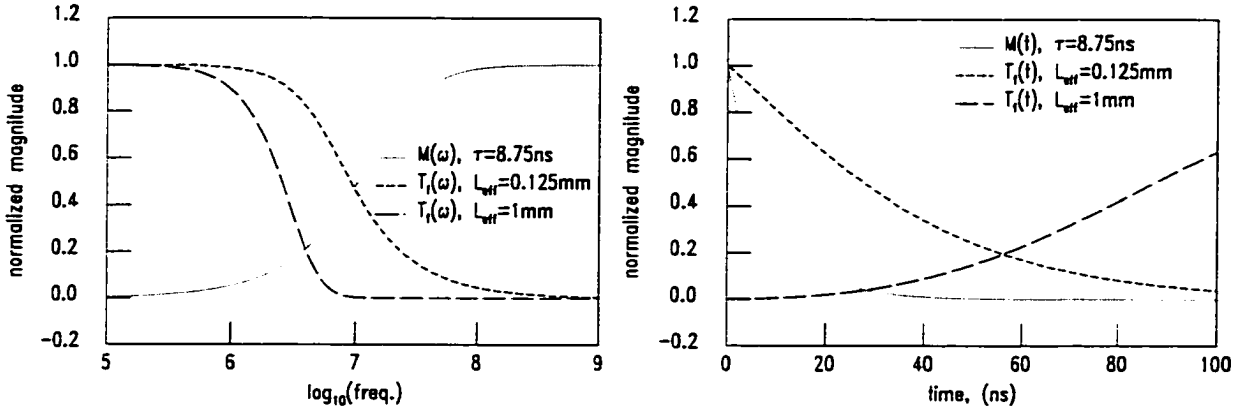

(a) (b)

Figure 5.33 Wave splitting inverse method: comparison of transmission kernels for $L_{\text{eff}} = 0.125,\ 1mm$ with relaxation modulus: normalized magnitude spectra. (a). short-time behavior. (b)

Figure 5.33(b) shows the first one hundred nanoseconds of the modulus and two exact transmissions kernels. Recall that the wave splitting inverse algorithm reconstructs a relaxation modulus progressively from time zero: therefore, quality of the short-time portion of the transmission kernel directly influences short-time quality of the reconstructed modulus. If the short-time portion of the transmission kernel is sensitive to small changes, for example noise, then it is difficult to obtain an accurate reconstruction of the modulus for short time. With this regard the kernel for $L_{\text{eff}} = 0.125mm$ has the advantage that its short-time features are emphasized. A more insightful point is that essential time scales inherent in the kernel for $L_{\text{eff}} = 0.125mm$ is commensurate with time scales of the modulus whereas time scales of the kernel for $L_{\text{eff}} = 1mm$ is at least an order of magnitude greater. In other words important time domain features of the kernel for the thinner slab occur on approximately the same time scale as decay of the modulus, but just the opposite is true for the kernel for the thicker slab. A consequence of the this disparity in time scales is that no estimate for the time-domain modulus could be recovered with the wave splitting algorithm from approximate kernels shown in Figs. 5.31(b) and (c). Several attempts to 'help' the algorithm failed. Only with the exact kernel would the inverse algorithm produce a modulus. On the other hand, Fig. 5.34 shows the estimates for the modulus obtained with approximate kernels

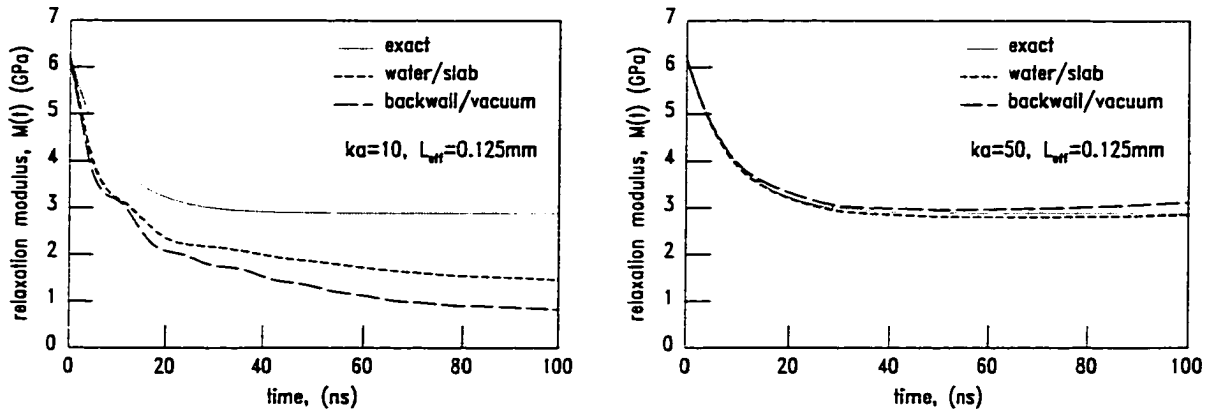

Figure 5.34 Wave splitting inverse method: reconstructed and exact longitudinal relaxation modulus versus time for waves recorded at the water/slab and backwall/vacuum interface and $L_{\text{eff}} = 0.125mm$ for $ka = 10$. (a), and for $ka = 50$. (b)

presented in Figs. 5.32(b) and (d). The algorithm had no difficulty producing modulus estimates, but clearly the approximate kernels for $ka = 50$ produced much better modulus estimates especially in long-time response.

Summary

Three methods for measurement of viscoelastic properties are compared and contrasted: two propagator methods (two-slab and slab-substitution) and a novel method denoted as wave splitting. Another method, the Hankel transform method, is applied to propagator inverse methods and shown to improve recovered attenuation and wave speed for the smaller aperture, $ka = 10$. The finite element method serves as a numerical test bed for illustrating effects of variables such as aperture radius, measurement location, etc., on longitudinal modulus reconstruction. Results show that propagator inverse methods are more robust in terms of collection of measurable data and are not restricted to a single slab thickness. On the other hand, it is shown that, in principle, wave splitting inverse methods can recover moduli if transmission kernel data measured at various slab lengths is translated to a single equivalent slab length. It is shown that a transmission kernel with decay time on the order of the decay time of the modulus is necessary for recovery of a time-domain modulus with the wave splitting inverse algorithms. This point implies a transmission kernel for a thinner slab with thickness appropriate for measurements

at the highest available frequencies ($\sim$ 100MHz) is required for modulus recovery. It is evident from results in all cases that aperture width has the greatest effect on accuracy of the reconstructed modulus especially for high frequencies. Surprisingly, a modulus reconstructed with wave data recorded at the water/slab interface is generally less accurate at high frequencies than a modulus reconstructed with data taken at the backwall/vacuum interface. Another surprise is that an often used diffraction correction provides almost negligible improvement in estimating moduli from wave data that includes decay due to beam spreading. Earlier in this chapter it is demonstrated that diffraction corrections could effectively remove decay due to geometric beam spreading from a wave propagating in a single homogeneous acoustic medium. In situations where distances between source and receiver are much greater than considered here, diffraction could be more significant; therefore, a diffraction correction could be more important.

CHAPTER 6 VISCOELASTIC MEDIA WITH MULTIPLE RELAXATIONS

Introduction

A simple single-exponential model for viscoelastic moduli manifests most of the relevant properties of real materials and is sufficient for studying questions posed in previous chapters. However, forward modeling of real materials requires a model that incorporates multiple relaxation mechanisms. In general, materials have moduli that are best represented by a continuous spectrum of relaxation times [13].

In a numerical model a continuous spectrum is usually approximated by a discrete sum of decaying exponentials (a Prony series). There are at least two ways to approximate a continuous spectrum of relaxations with a Prony series model. The first assumes a spectrum composed of a finite sum of Dirac delta functions with appropriate amplitudes and translations, for example,

$$h_{hn}(\tau) \approx \sum_{i=1}^{N_p} A_i \delta(\tau - \tau_i). \tag{6.1}$$

Integration over the spectrum is reduced to a finite sum of decaying exponentials. The second method assumes the spectrum is piecewise linear, then integration over the spectrum is accomplished with the trapezoidal rule. In this case the spectrum is effectively a Prony series but with amplitudes defined by the width of the chosen intervals of integration. Both of these methods are described in detail in chapter 2. Example calculations with both methods follow.

One question that is studied is "how many relaxation times are necessary in a forward model to approximate accurately a continuous spectrum for a given source bandwidth?" The answer will depend on relative bandwidth between modulus and source. A particular representative example is chosen with parameters described in Chapter 2. For the first method a continuous spectrum is approximated by a discrete sum of exponentials beginning with a single exponential. In each subsequent run the discrete relaxation spectrum is increased incrementally by one relaxation mechanism, that is, by adding one decaying exponential. As more relaxations are added, waves are recorded at a particular location and

convergence of the wave is observed as the number of relaxation mechanisms increases. This approach is repeated for a second method except that the number of integration intervals is increased in each run. As the number of exponentials or integration intervals is increased, it is shown that computed waveforms converge to the same result for both methods. Finally, a short section follows that describes the computation time required for a given number of relaxations and elements in a mesh.

Approximate Models for Continuous Relaxation Spectra

As described in a previous Chapter 2, two common models for viscoelastic moduli are the KWW and HN functions; they are, respectively,

$$\theta_{kww}(t) = e^{-(t/\tau_{kww})^{\beta}} H(t) \qquad 0 < \beta \leq 1 \tag{6.2}$$

$$\tilde{\theta}_{hn}(\omega) = 1 - \frac{1}{[1 + (i\omega\tau_{hn})^{\alpha}]^{\gamma}} \qquad 0 < \alpha, \gamma \leq 1. \tag{6.3}$$

These functions do not form a Fourier transform pair, but both of these functions are derived from continuous distributions of relaxations or relaxation spectra (see Chapter 2). The KWW function is a time domain relaxation function and is also known as a 'stretched exponential function.' The HN function is a frequency domain function first introduced by Havriliak [21] for modeling relaxation in dielectric materials.

Alvarez [1, 2] has described approximate interconnections between the KWW and HN functions. In particular for various values of the KWW parameter, β, he has optimized the HN parameters, (α, γ), such that the HN function is a 'best fit' for the KWW function with given β. He has summarized values for β and corresponding values for (α, γ) in a useful table. For each set of $(\beta; \alpha, \gamma)$ he also gives the ratio between the characteristic relaxation times, τ_{hn}/τ_{kww}. For calculations here $\tau_{hn} = 875$ns, $(\alpha, \gamma) = (0.8091, 0.5105)$ and $\tau_{hn} = 2.9174\tau_{kww}$, which is a model for a KWW function with $\beta = 0.5$ and $\tau_{kww} \approx 300$ns. The relaxation spectra are shown in Fig. 6.1 and normalized moduli and source spectrum are plotted in Fig. 6.2.

Approximating a continuous spectrum of relaxations with a discrete sum of exponentials requires a method of optimizing for unknown amplitudes and characteristic relaxation times. The discrete spectrum is represented by relaxation times and amplitudes, (τ_i, A_i), and is a model for the continuous spectrum $h_{hn}(\tau)$ (eq. 2.40). The discrete modulus in time and frequency is

$$\theta_p(t) = \sum_{i=1}^{N_p} A_i e^{-t/\tau_i} H(t) \tag{6.4}$$

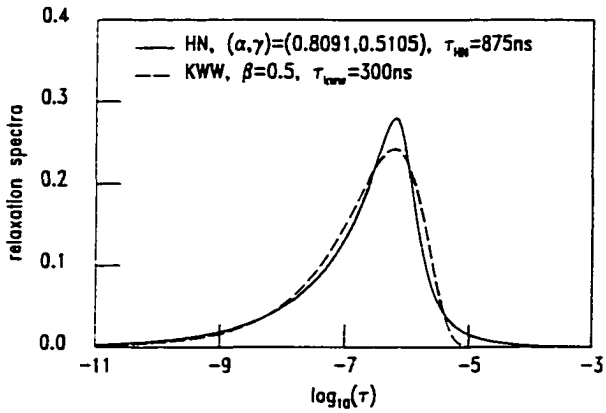

Figure 6.1 Relaxation spectrum for a KWW function with $\beta = 0.5$ compared with a 'best fit' HN spectrum

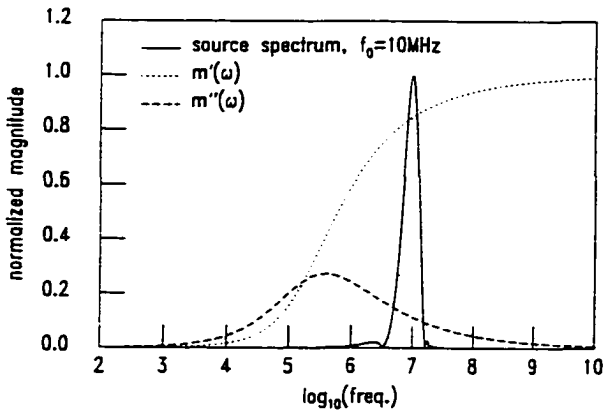

Figure 6.2 Normalized source spectrum for $f_0 = 10$MHz compared with normalized material modulus computed with HN parameters given in Fig. 6.1

$$\dot{\theta}_p(\omega) = \sum_{i=1}^{N_p} A_i \frac{i\omega\tau_i}{1 + i\omega\tau_i} \tag{6.5}$$

where

$$\sum_{i=1}^{N_p} A_i = 1 \tag{6.6}$$

and $\tau_1 < \tau_2 < \ldots < \tau_{N_p}$. The subscript 'p' denotes Prony series. Given N_p exponentials there are $2N_p$ unknowns to fit. A modified Levenberg-Marquardt algorithm (SNLS1E) available in the public domain software library known as SLATEC[1] was employed to fit the real part of the normalized relaxation modulus, $m'(\omega)$, computed with given HN parameters, to $m'(\omega)$ computed with the frequency-domain Prony series model, eq. 6.5. A reasonable initial guess is required for convergence. An optimization utilizing both real and imaginary components of $m(\omega)$ or $m''(\omega)$ alone yielded no significant difference in computed amplitudes and relaxation times. For reference normalized components of the (HN) longitudinal modulus, eq. 6.3, are

$$m'(\omega) = \frac{M'(\omega) - M_e}{M_g - M_e} = 1 - \frac{\cos^\gamma(o)\cos(\gamma o)}{\left[1 + \cos\left(\frac{\alpha\pi}{2}\right)(\omega\tau)^\alpha\right]^\gamma} \tag{6.7}$$

$$m''(\omega) = \frac{M''(\omega)}{M_g - M_e} = \frac{\cos^\gamma(o)\sin(\gamma o)}{\left[1 + \cos\left(\frac{\alpha\pi}{2}\right)(\omega\tau)^\alpha\right]^\gamma} \tag{6.8}$$

$$o = \arctan\left[\frac{\sin\left(\frac{\alpha\pi}{2}\right)(\omega\tau)^\alpha}{1 + \cos\left(\frac{\alpha\pi}{2}\right)(\omega\tau)^\alpha}\right]. \tag{6.9}$$

[1]SLATEC is a software library of mathematical subroutines in FORTRAN that was created by researchers at Sandia National Laboratory, Albuquerque, New Mexico.

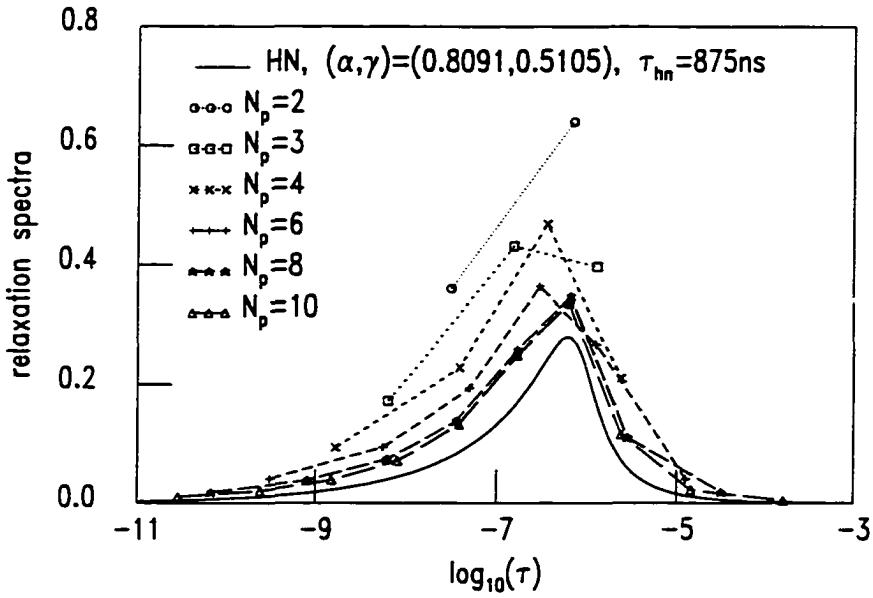

Figure 6.3 Relaxation spectra: continuous versus discrete for increasing number of exponentials in discrete spectra (lines are guides for the eye)

Figure 6.3 shows graphically the optimized results for increasing N_p. The lines are provided as guides for the eye. As the number of exponentials increases, discrete spectra slowly approach the continuous spectrum in shape and magnitude. Table 6.1 lists actual amplitudes and relaxation times.

Approximations to the continuous HN spectrum for the second method are shown in Fig. 6.4 where N_c designates the number of points in a piecewise linear approximation and $N_c - 1$ is the number of intervals. Actual integration points are given in Table 6.2. No special optimization was applied to determine location of points or number of intervals. Other integration schemes such as Simpson's rule or Gaussian quadrature were also considered, but will be left for further work.

Real and imaginary components of normalized longitudinal modulus, $\hat{m}(\omega)$, are shown in Fig. 6.5 computed with optimized parameters given in Table 6.1 for $N_p = 1, 2, 3$. The bumpy appearance of the modulus for $N_p = 2, 3$ occurs because the relaxation times in the discrete spectrum are so relatively far apart that their overlap can be discerned. In spite of this waves computed with $N_p = 3$ are practically equivalent to waves computed with a discrete spectrum having $N_p = 10$. Wave speed and attenuation for various N_p compared with a continuous HN spectrum are shown in Fig. 6.6. Attenuation plotted in Fig. 6.6(b) shows that, for a Dirac delta spectrum, attenuation approaches a finite limit at high frequency whereas attenuation for an HN spectrum is not bounded for increasing frequency. The reason

Table 6.1 Discrete spectra for increasing N_p, see Fig. 6.3

$N_p = 1$		
#	τ_i (ns)	A_i
1	628.1	1.000

$N_p = 2$		
#	τ_i (ns)	A_i
1	30.54	0.3598
2	713.6	0.6402

$N_p = 3$		
#	τ_i (ns)	A_i
1	6.215	0.1720
2	155.1	0.4315
3	1307.	0.3965

$N_p = 4$		
#	τ_i (ns)	A_i
1	1.673	0.09331
2	38.10	0.2283
3	365.5	0.4684
4	2440.	0.2100

$N_p = 5$		
#	τ_i (ns)	A_i
1	0.6816	0.06026
2	13.59	0.1416
3	126.4	0.2972
4	711.4	0.4107
5	5491.	0.09019

$N_p = 6$		
#	τ_i (ns)	A_i
1	0.3130	0.04084
2	5.520	0.09416
3	49.47	0.1939
4	302.1	0.3638
5	1290.	0.2667
6	12640.	0.04058

$N_p = 7$		
#	τ_i (ns)	A_i
1	0.1858	0.03109
2	2.927	0.06998
3	24.69	0.1398
4	147.3	0.2632
5	639.3	0.3607
6	2745.	0.1168
7	30790.	0.01848

$N_p = 8$		
#	τ_i (ns)	A_i
1	0.06840	0.01782
2	0.8219	0.03829
3	6.148	0.07412
4	34.94	0.1379
5	169.8	0.2578
6	676.7	0.3470
7	2890.	0.1093
8	32280.	0.01766

$N_p = 9$		
#	τ_i (ns)	A_i
1	0.06940	0.01788
2	0.8247	0.03813
3	6.127	0.07388
4	34.63	0.1368
5	166.3	0.2523
6	646.4	0.3385
7	2414.	0.1162
8	14260.	0.02185
9	159700.	0.0045-42

$N_p = 10$		
#	τ_i (ns)	A_i
1	0.02931	0.01035
2	0.2453	0.02049
3	1.521	0.03852
4	7.924	0.07100
5	37.77	0.1328
6	170.3	0.2492
7	650.3	0.3359
8	2426.	0.1156
9	14470.	0.02165
10	165100.	0.004447

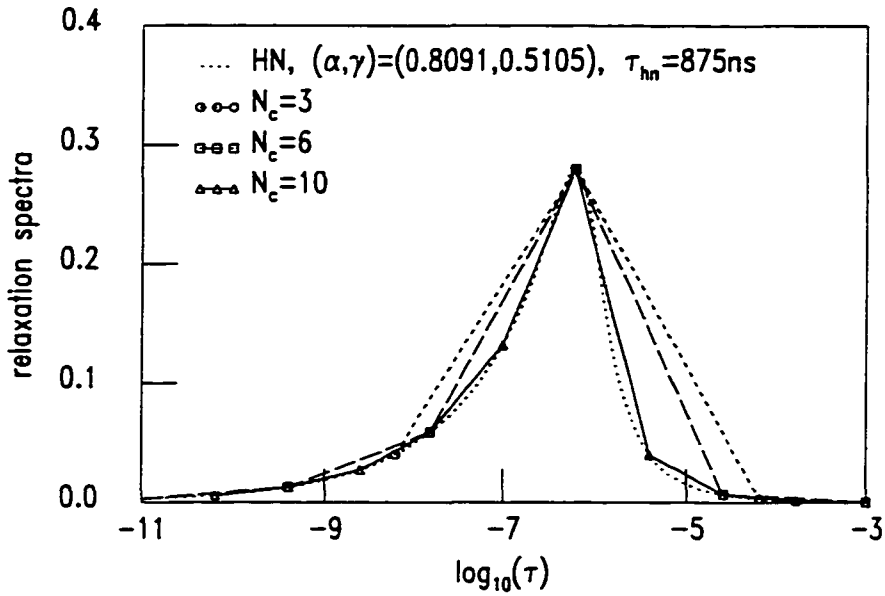

Figure 6.4 Relaxation spectra: continuous versus piecewise linear for increasing number of integration intervals

Table 6.2 Points, N_c, that define numerical integration intervals of continuous spectra, see Fig. 6.4

$N_c = 3$		
#	τ_i (ns)	A_i
1	6.281	0.04014
2	628.1	0.2800
3	62810.	0.003006

$N_c = 6$		
#	τ_i (ns)	A_i
1	0.009954	0.002782
2	0.3963	0.01275
3	15.78	0.05913
4	628.1	0.2800
5	25000.	0.006621
6	995400.	0.0003102

$N_c = 10$		
#	τ_i (ns)	A_i
1	0.06281	0.005954
2	0.3963	0.01275
3	2.500	0.02735
4	15.78	0.05913
5	99.54	0.1322
6	628.1	0.2800
7	3963.	0.03995
8	25000.	0.006621
9	157800.	0.001397
10	995400.	0.0003102

for this is that contributions to high frequency attenuation come from the small but non-zero tail in the relaxation spectrum for decreasing relaxation time. For comparison low and high frequency limits of a Dirac delta spectrum and an HN spectrum are, respectively,

$$\lim_{\omega\to 0}\alpha(\omega) = \left[\left(\frac{c_g^2-c_e^2}{2c_e^3}\right)\sum_{i=1}^{N_p}A_i\tau_i\right]\omega^2 \quad \text{(Dirac delta)} \tag{6.10}$$

$$\lim_{\omega\to\infty}\alpha(\omega) = \left[\left(\frac{c_g^2-c_e^2}{2c_g^3}\right)\sum_{i=1}^{N_p}A_i\frac{1}{\tau_i}\right] \tag{6.11}$$

$$\lim_{\omega\to 0}\alpha(\omega) = \left[\left(\frac{c_g^2-c_e^2}{2c_e^3}\right)\sin\left(\frac{\alpha\pi}{2}\right)\gamma\tau_{hn}^{\alpha}\right]\omega^{1+\alpha} \quad \text{(HN)} \tag{6.12}$$

$$\lim_{\omega\to\infty}\alpha(\omega) = \left[\left(\frac{c_g^2-c_e^2}{2c_g^3}\right)\sin\left(\frac{\gamma\alpha\pi}{2}\right)\frac{1}{\tau_{hn}^{\gamma\alpha}}\right]\omega^{1-\gamma\alpha} \quad (0<\gamma,\ \alpha\leq 1). \tag{6.13}$$

When $\gamma = \alpha = 1$ attenuation limits for an HN spectrum revert to a Dirac delta spectrum with a single relaxation.

For low frequencies HN attenuation behaves as $\omega^{1+\alpha}$ with $0 < \alpha \leq 1$. This suggests that with proper choice of parameters an HN spectrum could be a model, over a limited frequency range, for materials with power law attenuation, that is, $\alpha(\omega) = \alpha_0\omega^y$, $1 \leq y \leq 2$. Mammalian tissue is an example of such a material [12]. Wismer [54] presents finite element results for pulsed acoustic pressure wave propagation in materials with power law attenuation. Her numerical work was motivated by theoretical studies on time domain PDE's for lossy media with power law attenuation (Szabo [45, 46]). Wismer's method utilizes a Z-transform to convert a pressure wave equation including attenuation from frequency domain to discrete time. In her approach a power law attenuation model, transformed to discrete time with the Z-transform method, requires a series expansion that is shown to diverge, but reasonable results were obtained if only a small number of terms (< 7) are included in the expansion. In comparison, methods for lossy wave propagation developed here show no computational instability or signs of divergence for increasing number of exponential terms.

Model Calculations

A computational domain with only one material type is assumed. Material properties are given in eqs. 5.3, 5.4 and 5.5 with spectral properties described in this chapter. A finite aperture source is assumed with $f_0 = 10\text{MHz}$, $a = 500\mu m$ and $ka \approx 13$. Grid spacing is $\Delta r = \Delta z = 5\mu m$ and the time step is $\Delta t = 1.8\text{ns}$. The number of elements in the mesh is $500 \times 500 = 250,000$ and the total number of unkowns is $2 \times 501 \times 501 = 502,002$. Under these conditions there are about thirty-four elements

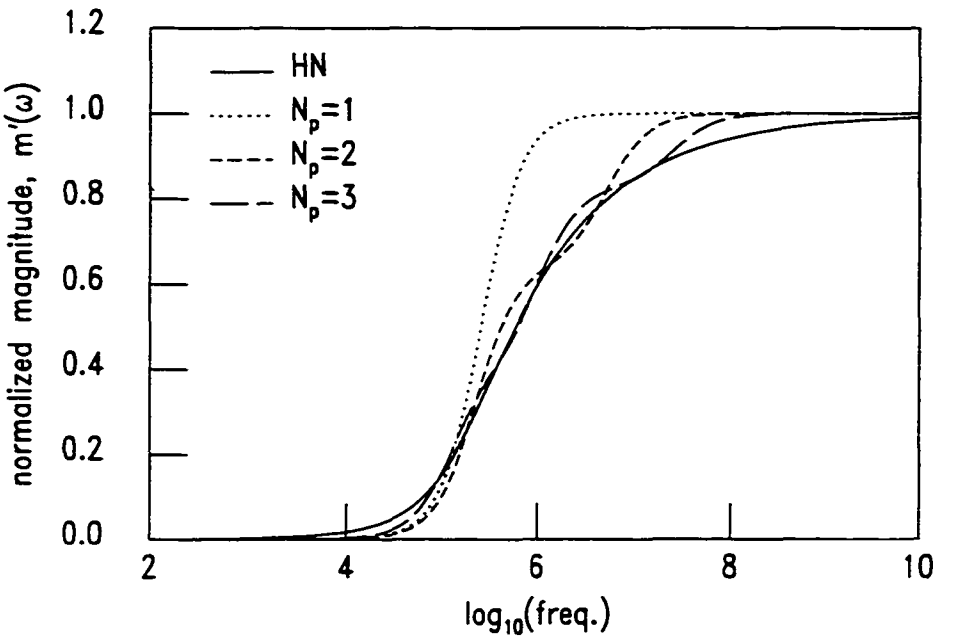

(a)

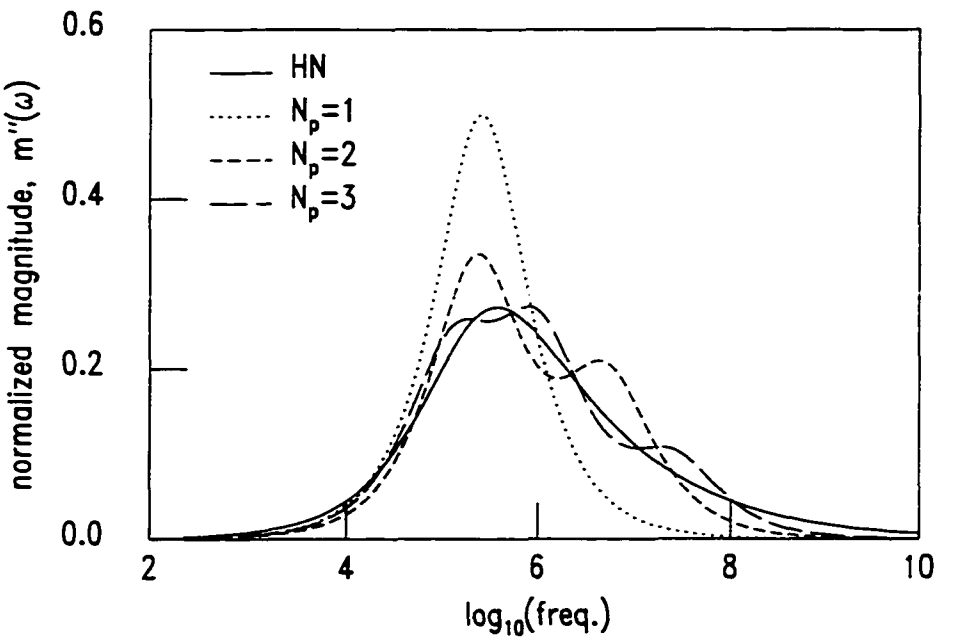

(b)

Figure 6.5 Real, (a), and imaginary, (b), components of longitudinal modulus, $\tilde{m}(\omega)$, computed for increasing N_p and compared with exact HN modulus

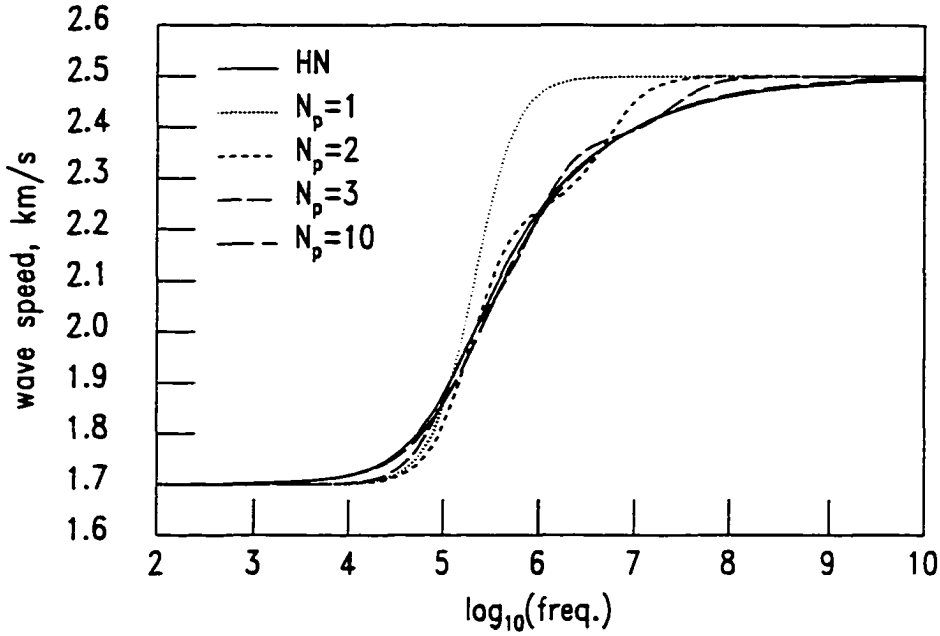

(a)

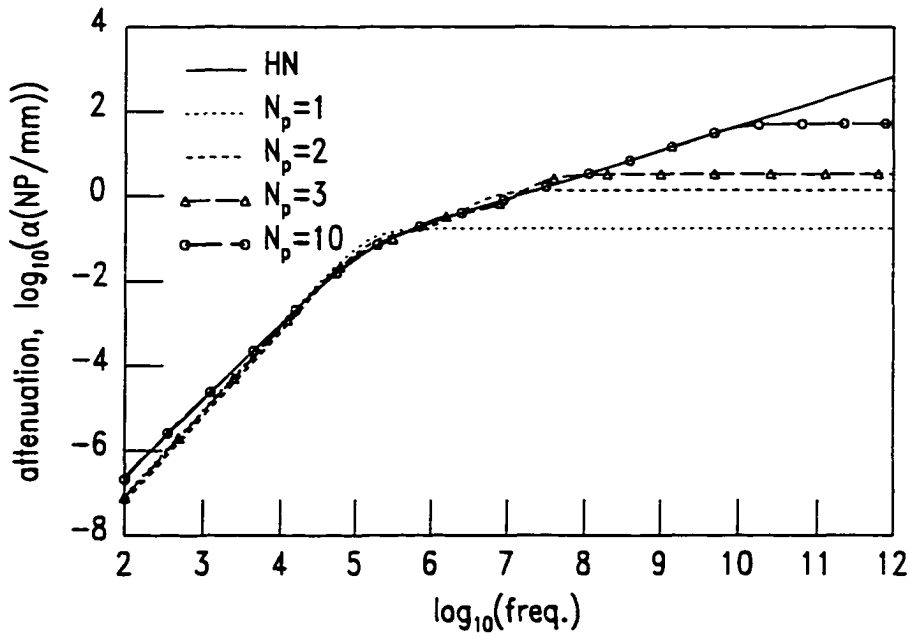

(b)

Figure 6.6 Comparison of wave speed. (a). and attenuation. (b). for HN-spectrum and Dirac delta spectra

per shear wavelength—more than adequate to model shear wave propagation accurately.

Figures 6.7 and 6.8 show axial displacement recorded at four different positions along the z-axis. In each plot the solid line represents a wave computed with a Dirac delta spectrum that contains ten relaxations (see Table 6.1). For comparison waves are also computed with $N_p = 1, 2, 3$. When $N_p = 3$ the wave is almost indistinguishable from that computed with $N_p = 10$. With just one relaxation the model cannot capture appropriate rates of decay of the longitudinal wave and especially the shear wave which appears at late time in each figure. With $N_p = 2$ the computed waveform is a fair approximation to the case with $N_p = 10$ and $z = 250, 500 \mu m$, but correspondence deteriorates with increasing distance from the source. In all cases the same results hold for off axis positions but are not shown.

Figure 6.9 compares waves computed with a Dirac delta spectrum, $N_p = 10$, and spectral density integrated by trapezoidal rule with increasing number of integration intervals, $N_c = 3, 6, 10$ (see Table 6.2 and Fig. 6.4). With $N_c = 6$ the Dirac delta and integrated spectral density produce waves indistinguishable to within a line width. A trade off is that six exponentials are required for an integrated spectral density while only three exponentials were required for convergence of the Dirac delta spectrum. Further work will investigate other methods for spectra integration that require fewer exponentials to achieve convergence.

Computer Run-Time Information

The computer employed for all axisymmetric calculations was a Silicon Graphics Power Onyx with eight 194 MHz MIPS-R10000 CPU's and 2048 Mbytes of random access memory. The computer is owned jointly by the Condensed Matter Physics group, Iowa State University, and the Scalable Computing Laboratory in Ames Laboratory. Although the Onyx is capable of running multiprocessor parallel code, it serves as a research computer for many users ($\sim$ 15) running serial programs. A series of timing runs was made for increasing number of elements and relaxation times. The results are shown in Fig. 6.10. The time represented along the ordinate axis is total time spent in the system[2] and not the total clock-on-the-wall running time which is largely dependent on the number of users at any given moment. Programs were submitted and run under a queuing system known as DQS[3].

[2]The UNIX function for run time measurement is 'time.'

[3]DQS is an experimental batch queuing system developed at the Supercomputer Computations Research Institute at Florida State University.

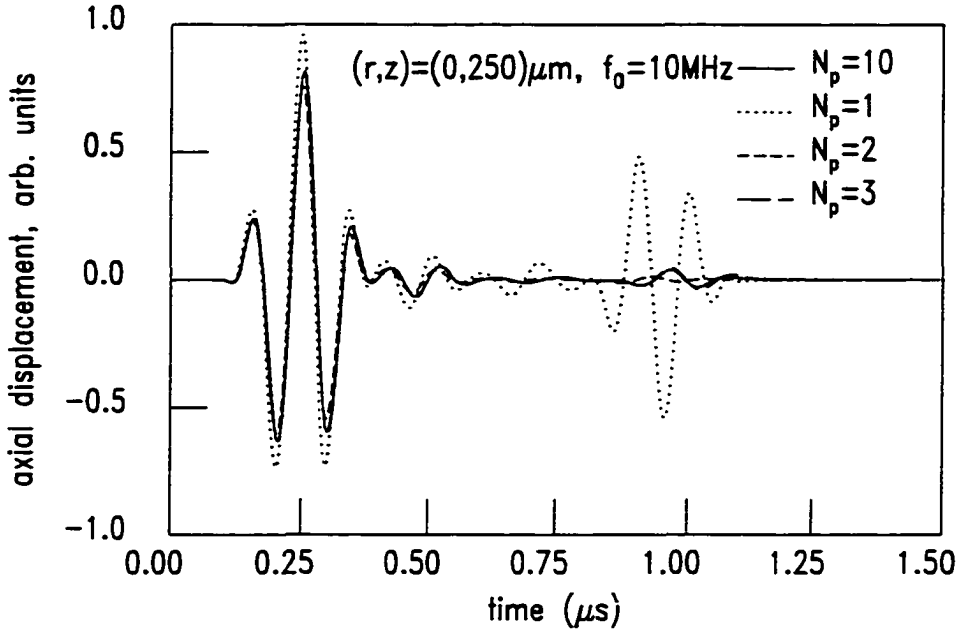

(a)

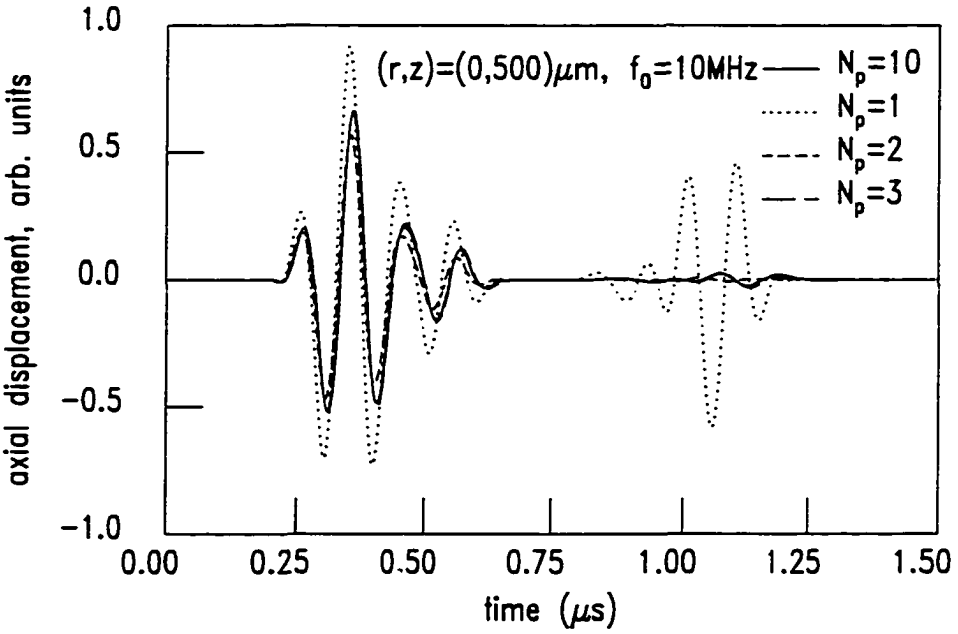

(b)

Figure 6.7 Axial displacement on the axis of symmetry for increasing number of relaxations included in discrete spectrum: (a) $z = 250\mu m$. (b) $z = 500\mu m$

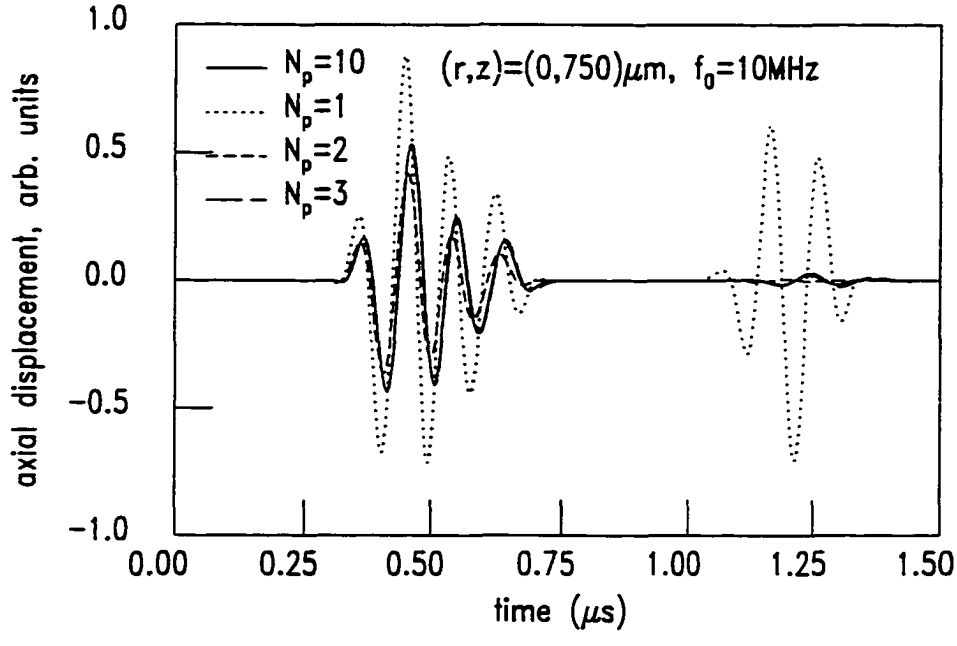

(a)

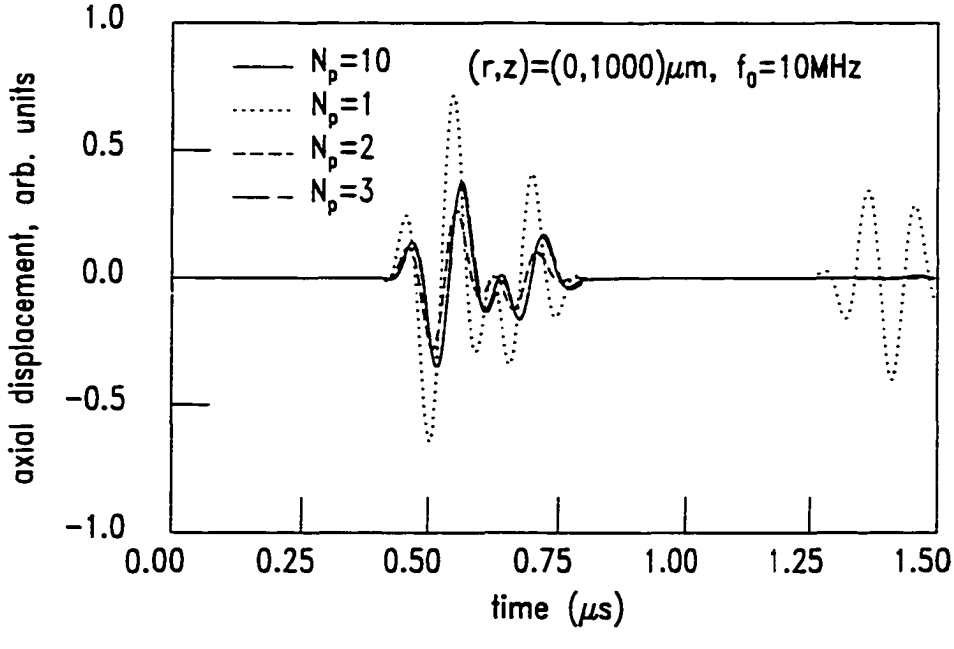

(b)

Figure 6.8 Axial displacement on the axis of symmetry for increasing number of relaxations included in discrete spectrum: (a) $z = 750\mu m$. (b) $z = 1000\mu m$

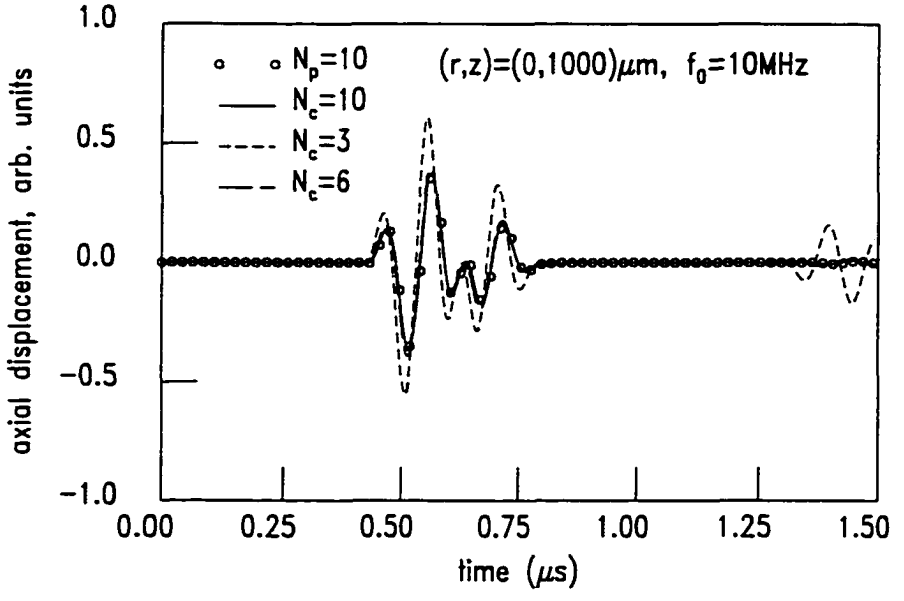

Figure 6.9 Axial displacement at $z = 1000\mu m$ on the axis of symmetry comparing waves computed with the relaxation spectrum integrated by trapezoidal rule with increasing number of integration intervals

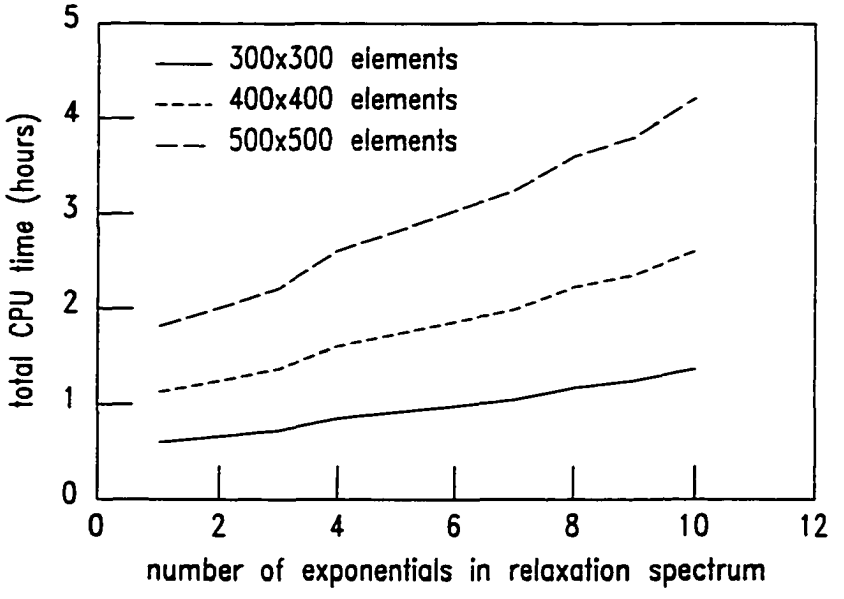

Figure 6.10 Elapsed CPU time in hours versus mesh size and number of exponentials in the relaxation spectrum

Summary

Real viscoelastic materials have a continuous distribution of relaxation times. Relaxation distributions are modeled by a finite sum of decaying exponentials. In one case a distribution is modeled by a Dirac delta spectrum whose amplitudes and relaxation times are optimized in a least squares sense to fit a continuous HN distribution. With another closely related method a continuous spectrum is integrated with a trapezoidal rule, but no optimization was attempted for this case. A representative calculation is presented showing that as little as three decaying exponentials are required to model accurately ultrasonic wave proagation in a medium assumed to have a continuous HN relaxation spectrum. No instability or divergence of the computed solution was observed in any of the calculations. A section is included that describes the actual computer employed for calculation and in-system run times for various mesh sizes and relaxation spectra.

CHAPTER 7 CONCLUDING REMARKS AND FURTHER WORK

Accurate and robust numerical forward models such as the finite element method running on presently available computers have forged complete industries and active areas of research, for example, computational mechanics. With recent introduction of teraFLOP computers and petaFLOP computers on the drawing board, computational science and engineering is quickly carving out its own unique niche from within the traditional theorist/experimentalist paradigm. True three dimensional modeling with suffucient resolution to provide important insight into field/material interaction is now possible for many problems and soon to be a reality for others such as time-domain wave propagation problems.

With accurate forward models and powerful computers, new methods for material property measurement wil be tested more quickly to determine feasibility, and existing methods can be modeled to determine optimal experimental arrangements. In this vein an investigation of inverse methods for recovery of linear, viscoelastic moduli from ultrasonic waves is presented. A system consisting of viscoelastic solid immersed in a water bath is modeled with a time-domain finite element method to study effects of certain variables on the accuracy of the reconstructed moduli. In principle present states of stress, strain and displacement in a viscoelastic medium require knowledge of these variables for all previous time. Numerically this fact implies storing displacement history for each node in the finite element mesh. A method is presented where time dependence of bulk and shear moduli is modeled as a finite sum of decaying exponentials. When this is done it is shown that only displacement data from one previous time step needs to be retained to account for displacement time history at a point. The FEM visoelastic model is tested against an inverse Laplace-Hankel transform method and is shown to give equivalent results for all cases considered.

The viscoelastic finite element method is employed as numerical test-bed for studying two existing inverse methods, two-slab and slab-substitution, and one new and novel method called wave splitting. With the FEM as a test bed it is shown that in principle all three methods can provide estimates of the longitudinal modulus, but two-slab and slab-substitution methods are clearly more robust because

they do not require measured data for a single slab thickness. For the former two propagator methods increasing source and receiver aperture diameter improves accuracy of reconstructed moduli.

Further work will focus mainly on developing the FEM forward model to accomodate more general geometric domains. At the present only regions that are topologically equivalent to rectangular regions can be modeled but geometries encountered in usual nondestructive testing situations include non-simply connected regions. On another front the code will be ported to a parallel computing environment such as a PC-cluster or workstation cluster. A parallel environment is appropriate for attempting full three dimensional calculations. On yet another front more sophisticated models for material properties will be developed. One type of material of immediate interest is a finite element model of materials such as metals with microscopically random properties, at least random about some mean value. Such a model could serve as a test bed for ultrasonic wave propagation in stochastic media.

APPENDIX: DERIVATION OF LAPLACE-DOMAIN SCATTERING KERNELS

Due to spatial homogeneity of the viscoelastic slab a simple bounce diagram model is sufficient to derive Laplace domain reflection and transmission kernels. A prototype bounce diagram is shown in Fig. A.1. Assume a wave is incident on the slab at '1a' with Laplace domain amplitude of one (i.e. Dirac delta in time). The slab is assumed impedance matched to the elastic half spaces at $z = 0$, L, respectively. Reflection and transmission coefficients for a viscoelastic half-space are, respectively,

$$\tilde{r}(s) = \frac{\sqrt{s\tilde{n}(s)} - 1}{\sqrt{s\tilde{n}(s)} + 1} \tag{A.1}$$

$$\tilde{t}(s) = 1 + \tilde{r}(s). \tag{A.2}$$

A wave incident upon either of the two elastic half-spaces from within the slab experiences a reflection of $-\tilde{r}(s)$ and a transmission of $1 - \tilde{r}(s)$. The wave propagator for the slab is

$$\tilde{P}(s) = d_0 \tilde{P}_0(s) \tilde{P}_N(s) \tag{A.3}$$

$$d_0 = d(z = 0) = e^{-n_0 \tau_0/4} \tag{A.4}$$

$$\tilde{P}_0(s) = e^{-s\tau_0/2} \tag{A.5}$$

$$\tilde{P}_N(s) = e^{-\tilde{b}(s)/2} \tag{A.6}$$

$$\tau_0 = \tau(z = 0) = \frac{2L}{c} \tag{A.7}$$

$$\tilde{b}(s) = s\tau_0 \left[\sqrt{s\tilde{n}(s)} - 1\right] - \frac{1}{2}\dot{n}_0 \tau_0 \tag{A.8}$$

$$\dot{n}_0 = \dot{n}(t)|_{t=0}. \tag{A.9}$$

where subscript 'N' implies 'normalized.' For a non-viscoelastic slab $\tilde{P}_N(s)$ equals one, identically.

By inspection the total Laplace-domain reflection kernel is

$$\begin{aligned} \tilde{R}(s) &= 2\mathrm{a} + 3\mathrm{a} + 4\mathrm{a} + 5\mathrm{a} + \ldots \\ &= \tilde{r} + \tilde{r}(\tilde{r}^2 - 1)\tilde{P}^2 \left[1 + \tilde{r}^2\tilde{P}^2 + \tilde{r}^4\tilde{P}^4 + \ldots\right] \\ &= \tilde{r} + \tilde{r}(\tilde{r}^2 - 1)\tilde{P}^2 \sum_{i=0}^{\infty} \left[\tilde{r}\tilde{P}\right]^{2i} \end{aligned} \tag{A.10}$$

$$= \tilde{r}\left[\frac{1-\tilde{P}^2}{1-\tilde{r}^2\tilde{P}^2}\right]. \tag{A.11}$$

The total transmission kernel is

$$\begin{aligned}
\tilde{T}(s) &= 2a + 3a + 4a + \ldots \\
&= (1-\tilde{r}^2)\tilde{P}\left[1 + \tilde{r}^2\tilde{P}^2 + \tilde{r}^4\tilde{P}^4 + \ldots\right] \\
&= (1-\tilde{r}^2)\tilde{P}\sum_{i=0}^{\infty}\left[\tilde{r}\tilde{P}\right]^{2i} \qquad (A.12) \\
&= \frac{(1-\tilde{r}^2)\tilde{P}}{1-\tilde{r}^2\tilde{P}^2}. \qquad (A.13)
\end{aligned}$$

For $|s| \to \infty$ the transmission kernel as written does not approach zero. To eliminate the "high frequency" asymptote and to remove inherent time delay, redefine the transmission kernel as follows:

$$\tilde{T}(s) \to e^{+s\tau_0/2}\left[\tilde{T}(s) - d_0 e^{-s\tau_0/2}\right]; \tag{A.14}$$

therefore,

$$\begin{aligned}
\tilde{T}(s) &= \frac{(1-\tilde{r}^2)\tilde{P}e^{+s\tau_0/2}}{1-\tilde{r}^2\tilde{P}^2} - d_0 \qquad (A.15) \\
&= d_0 e^{-\tilde{b}(s)/2}\left[1 - \tilde{r}\tilde{R}\right] - d_0. \qquad (A.16)
\end{aligned}$$

Define

$$\begin{aligned}
\tilde{v}(s) &= \tilde{r}\tilde{P}^2(s)e^{s\tau_0} \qquad (A.17) \\
&= \tilde{r}d_0^2 e^{-\tilde{b}} \qquad (A.18)
\end{aligned}$$

then the reflection kernel, eq. A.10, can be rewritten in the following manner:

$$\tilde{R}(s) = \tilde{r} + \sum_{i=0}^{\infty}\left[\tilde{r}^2\tilde{v} - \tilde{v}\right]\left[\tilde{r}\tilde{v}\right]^i e^{-(i+1)s\tau_0}. \tag{A.19}$$

The inverse Laplace transform, $R(t)$, is

$$R(t) = r(t) + \sum_{i=0}^{\infty}\mathcal{S}((i+1)\tau_0)\left[r*r*v - v\right]\left[*r*v\right]^i \tag{A.20}$$

where $r(t) = \mathcal{L}^{-1}[\tilde{r}]$ and $v(t) = \mathcal{L}^{-1}[\tilde{v}]$ and $\mathcal{S}(\tau_0)$ is a delay operator: $\mathcal{S}(\tau_0)f(t) = f(t-\tau_0)$.

Define

$$\begin{aligned}
\mathcal{L}[\dot{n}] &\equiv \dot{\tilde{n}} \qquad (A.21) \\
&= s\tilde{n}(s) - 1 \qquad (A.22)
\end{aligned}$$

or $s\dot{\bar{n}} = 1 + \dot{\bar{n}}$. The half space reflection coefficient becomes

$$\tilde{r} = \frac{\sqrt{1+\dot{\bar{n}}} - 1}{\sqrt{1+\dot{\bar{n}}} + 1} \tag{A.23}$$

and

$$\sqrt{1+\dot{\bar{n}}} = \frac{1+\tilde{r}}{1-\tilde{r}}. \tag{A.24}$$

Rationalizing the denominator of eq. A.23 gives

$$\tilde{r} = \frac{2 - 2\sqrt{1+\dot{\bar{n}}} + \dot{\bar{n}}}{\dot{\bar{n}}} \tag{A.25}$$

or, after eliminating the square root, it becomes

$$\dot{\bar{n}}\tilde{r} = 2 - 2\left[\frac{1+\tilde{r}}{1-\tilde{r}}\right] + \dot{\bar{n}}. \tag{A.26}$$

After rearranging and collecting terms the result is

$$4\tilde{r} - \dot{\bar{n}} + 2\dot{\bar{n}}\tilde{r} - \dot{\bar{n}}\tilde{r}^2 = 0 \tag{A.27}$$

$$\Longrightarrow 4r(t) - \dot{n}(t) + 2\dot{n} * r - \dot{n} * r * r = 0. \tag{A.28}$$

Define

$$\mathcal{L}[\ddot{n}] \equiv \dddot{\bar{n}} \tag{A.29}$$

$$= s\ddot{\bar{n}} - \dot{n}_0 \tag{A.30}$$

then the inverse Laplace transform of $\tilde{b}(s)$ is found as follows:

$$\begin{aligned}
\tilde{b}(s) &= s\tau_0\left[\sqrt{s\dot{\bar{n}}} - 1\right] - \frac{1}{2}\dot{n}_0\tau_0 \\
&= s\tau_0\left[\sqrt{1+\dot{\bar{n}}} - 1\right] - \frac{1}{2}\dot{n}_0\tau_0 \\
&= s\tau_0\left[\frac{1}{2}\dot{\bar{n}}(1-\tilde{r})\right] - \frac{1}{2}\dot{n}_0\tau_0 \\
&= \frac{\tau_0}{2}\left[(s\dot{\bar{n}} - \dot{n}_0 + \dot{n}_0) - (s\dot{\bar{n}} - \dot{n}_0 + \dot{n}_0)\tilde{r} - \dot{n}_0\right] \\
&= \frac{\tau_0}{2}\left[\ddot{\bar{n}} - \ddot{\bar{n}}\tilde{r} - \dot{n}_0\tilde{r}\right] \qquad \text{(A.31)} \\
\Longrightarrow b(t) &= \frac{\tau_0}{2}\left[\ddot{n}(t) - \ddot{n} * r - \dot{n}_0 r(t)\right]. \qquad \text{(A.32)}
\end{aligned}$$

From the transmission kernel equation, eq. A.16, define

$$\tilde{e}(s) = d_0 e^{-\tilde{b}/2} - d_0 \tag{A.33}$$

then

$$\begin{aligned} \partial_s \tilde{e} &= -\frac{1}{2} d_0 e^{-\tilde{b}/2} \partial_s \tilde{b} \\ &= -\frac{1}{2} [\tilde{e} + d_0] \partial_s \tilde{b} \\ &= -\frac{1}{2} \tilde{e} \partial_s \tilde{b} - \frac{1}{2} d_0 \partial_s \tilde{b} \qquad \text{(A.34)} \\ \Longrightarrow e(t) &= -\frac{1}{2} d_0 b(t) - \frac{1}{2t} e * (tb). \qquad \text{(A.35)} \end{aligned}$$

With eq. A.33 the transmission kernel, eq. A.16, is inverted as follows:

$$\begin{aligned} \tilde{T}(s) &= \tilde{e} - [\tilde{e} + d_0] \tilde{r} \tilde{R} \qquad \text{(A.36)} \\ \Longrightarrow T(t) &= e(t) - d_0 r * R - e * r * R. \qquad \text{(A.37)} \end{aligned}$$

Finally, $\tilde{v}(s)$ is inverted as follows:

$$\begin{aligned} \tilde{v}(s) &= \tilde{r} d_0^2 e^{-\tilde{b}} \\ &= \tilde{r} [\tilde{e} + d_0]^2 \\ &= d_0^2 \tilde{r} + 2 d_0 \tilde{e} \tilde{r} + \tilde{e}^2 \tilde{r} \qquad \text{(A.38)} \\ \Longrightarrow v(t) &= d_0^2 r(t) + 2 d_0 e * r + e * e * r. \qquad \text{(A.39)} \end{aligned}$$

A detailed derivation of the time domain reflection and transmission kernels, $R(t)$ and $T(t)$, for an isotropic viscoelastic slab has been given. Intermediate variables, $b(t)$, $e(t)$, $r(t)$ and $v(t)$, facilitate the derivation. These results are analogous to the electromagnetic case presented in Fuks [15].

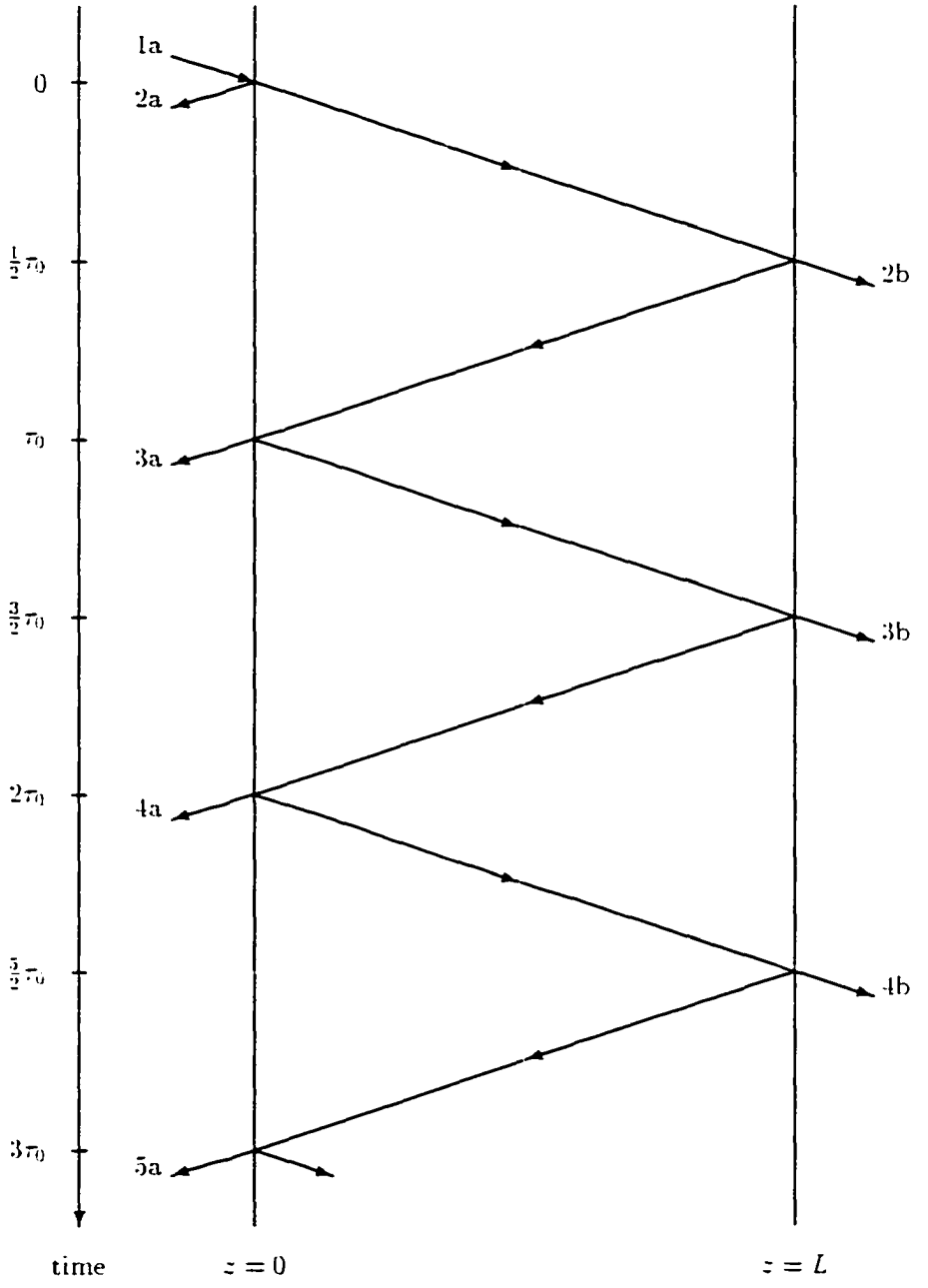

Figure A.1 Bounce diagram for a viscoelastic slab

BIBLIOGRAPHY

[1] F. Alvarez, A. Alegría, and J. Colmenero. "Relationship between the time domain Kohlrausch-Williams-Watts and frequency domain Havriliak-Negami relaxation functions". *Physical Review B*. 44(14):7306–7312, 1 Oct. 1991.

[2] F. Alvarez, A. Alegría, and J. Colmenero. "Interconnection between the frequency domain Havriliak-Negami and Kohlrausch-Williams-Watts relaxation functions". *Physical Review B*. 47(1):125–130, 1 Jan. 1993.

[3] J. Archer-Hall and D. Gee. "A single integral computer method for axisymmetric transducers with various boundary conditions". *NDT International*. 13:95–101, June 1980.

[4] B. Auld. *Acoustic Fields and Waves in Solids*. volume I and II. Krieger Publishing Co., Malabar, Florida, second edition, 1990.

[5] R. Bass. "Diffraction effects in the ultrasonic field of a piston source". *Journal of the Acoustical Society of America*. 30(7):602–605, July 1958.

[6] G. Benson and O. Kiyohara. "Tabulation of some integral functions describing diffraction effects in the ultrasonic field of a circular piston source". *Journal of the Acoustical Society of America*. 55(1):184–185, January 1974.

[7] S. Chan, M. Mina, S. Udpa, L. Udpa, and W. Lord. "Finite element analysis of multilevel acoustic fresnel lenses". *IEEE Transactions on Ultrasonics, Ferroelectrics and Frequency Control*. 43(4):670–677, July 1996.

[8] R. Christensen. *Theory of Viscoelasticity: An Introduction*. Academic Press, New York, second edition, 1982.

[9] I. Currie. *Fundamental Mechanics of Fluids*. McGraw-Hill Publishing Co., New York, 1974.

[10] M. Davison and R. Winther. "A general approach to splitting and invariant embedding for linear wave equations". *Mathematical Analysis and Applications*. 188(3):158–181, 1994.

[11] R. Dougherty. *Direct and Inverse Scattering of Classical Waves at Oblique Incidence to Stratified Media via Invariant Embbeding Equations.* Doctoral dissertation. Iowa State University. Ames. Iowa. 1986.

[12] F. Duck. *Physical Properties of Tissue.* Academic Press. New York. 1990.

[13] J. Ferry. *The Viscoelastic Properties of Polymers.* John Wiley and Sons. New York. third edition. 1980.

[14] D. Flanagan and T. Belytschko. "A uniform strain hexahedron and quadrilateral with hourglass control". *International Journal for Numerical Methods in Engineering.* 17:679–706. 1981.

[15] P. Fuks. A. Karlsson. and G. Larson. "Direct and inverse scattering from dispersive media". *Inverse Problems.* 10:555–571. 1994.

[16] P. Fuks. G. Kristensson. and G. Larson. "Permittivity profile reconstructions using transient electromagnetic reflection data". Technical Report CODEN:LUTEDX/(TEAT-7009)/. Dept. of Electromagnetic Theory. Lund Institute of Technology. Lund. Sweden. 1990.

[17] B. Gestblom and E. Noreland. "Transmission methods in dielectric time domain spectroscopy". *Journal of Physical Chemistry.* 81(8):782–788. 1977.

[18] G. Gonzalez. *Microwave Transistor Amplifiers: Analysis and Design.* Prentice-Hall. Upper Saddle River. New Jersey. 2nd edition. 1997.

[19] G. Harrison. *The Dynamic Properties of Supercooled Liquids.* Academic Press. London. 1976.

[20] B. Hartmann and J. Jarzynski. "Immersion apparatus for ultrasonic measurements in polymers". *Journal of the Acoustical Society of America.* 56(5):1469–1477. 1974.

[21] S. Havriliak and S. Negami. "A complex plane representation of dielectric and mechanical relaxation processes in some polymers". *Polymer.* 8:161–210. 1967.

[22] T. Hughes. *The Finite Element Method.* Prentice-Hall. Englewood Cliffs. New Jersey. 1987.

[23] H. Jeong and D. Hsu. "Experimental analysis of porosity-induced ultrasonic attenuation and velocity change in carbon composites". *Ultrasonics.* 33(3):195–203. 1995.

[24] Jian-Ming Jin. *The Finite Element Method in Electromagnetics.* John Wiley and Sons. New York. 1993.

[25] U. Kaatze, V. Kühnel, and G. Weiss. "Variable pathlength cells for precise hypersonic spectrometry of liquids up to 5GHz". *Ultrasonics*. 34:51-58. 1996.

[26] A. Karlsson. "Inverse scattering for viscoelastic media using transmission data". *Inverse Problems*. 3:691-709. 1987.

[27] D. Kelley and R. Luebbers. "Piecewise linear recursive convolution for dispersive media using FDTD". *IEEE Transactions on Antennas and Propagation*. 44(6):792-797. June 1996

[28] A. Khimunin. "Numerical calculation of the diffraction corrections for the precise measurement of ultrasound absorption". *Acustica*. 27(4):173-181. 1972.

[29] G. Kino. *Acoustic Waves: Devices, Imaging and Analog Signal Processing*. Prentice-Hall. Englewood Cliffs. New Jersey. 1987.

[30] R. Kline. "Measurement of attenuation and dispersion using an ultrasonic spectroscopy technique". *Journal of the Acoustical Society of America*. 76(2):498-504. 1984.

[31] G. Kristensson. "Direct and inverse scattering problems in dispersive media: Green's functions and invariant embedding". In R. Kleinman, R. Kress, and E. Martensen, editors. *Direct and Inverse Boundary Value Problems*. volume 37. pages 105-119. FRG. 1989. Mathematisches Forschungsinstitut Oberwolfach.

[32] C. Lee, M. Lahham, and B. Martin. "Experimental verification of the Kramers-Kronig relationship for acoustic waves". *IEEE Transactions on Ultrasonics, Ferroelectrics and Frequency Control*. 37(1):286-294. 1990.

[33] W. Lord, R. Ludwig, and Z. You. "Developments in ultrasonic modeling with finite element analysis". *Journal of Nondestructive Evaluation*. 9(2/3):129-143. 1990.

[34] R. Ludwig. *The Finite Element Modeling of Ultrasonic NDT Phenomena*. Doctoral dissertation. Colorado State University. Fort Collins, Colorado. 1986.

[35] R. Ludwig, D. Moore, and W. Lord. "A comparitive study of analytical and numerical transient force excitations on an elastic half-space". *IEEE Transactions on Ultrasonics, Ferroelectrics and Frequency Control*. 36(3):342-350. May 1989.

[36] J. Oden and W. Armstrong. "Analysis of nonlinear, dynamic coupled thermoviscoelasticity problems by the finite element method". *Computers and Structures*. 1:603-621. 1971.

[37] J. Oden and J. Reddy. *Variational Methods in Theoretical Mechanics.* Springer-Verlag. Berlin. 1983.

[38] R. Redheffer. "Difference equations and functional equations in transmission line theory". In E. Beckenbach. editor. *Modern Mathematics for the Engineer.* 2. chapter 12. pages 282–337. McGraw-Hill. New York. 1961.

[39] P. Rogers and A. Van Buren. "An exact expression for the Lommel diffraction correction integral". *Journal of the Acoustical Society of America.* 55(4):724–728. April 1974.

[40] C. Scruby and L. Drain. *Laser Ultrasonics: Techniques and Applications.* Adam Hilger. Bristol. England. 1990.

[41] H. Seki. A. Granato. and R. Truell. "Diffraction effects in the ultrasonic field of a piston source and their importance in the accurate measurement of attenuation". *Journal of the Acoustical Society of America.* 28(2):230–238. March 1956.

[42] I. Sneddon. *The Use of Integral Transforms.* McGraw-Hill Book Co.. New York. 1972.

[43] P. Stucky and W. Lord. "Finite element modeling of ultrasonic waves in viscoelastic media". In D. O. Thompson and D. E. Chimenti. editors. *Review of Progress in Quantitative Non-Destructive Evaluation.* volume 16a. pages 113–120. Plenum Press. New York. 1997.

[44] P. Stucky and W. Lord. "Spurious modes in finite element models for ultrasonic waves in fluid-solid systems". In D. O. Thompson and D. E. Chimenti. editors. *Review of Progress in Quantitative Non-Destructive Evaluation.* volume 17a. Plenum Press. New York. 1998. (to be published).

[45] T. Szabo. "Time domain equations for lossy media obeying a frequency power law". *Journal of the Acoustical Society of America.* 96(1):491–500. July 1994.

[46] T. Szabo. "Causal theories and data for acoustic attenuation obeying a frequency power law". *Journal of the Acoustical Society of America.* 97(1):14–24. Jan. 1995.

[47] R. Taylor. K. Pister. and G. Goudreau. "Thermomechanical analysis of viscoelastic solids". *International Journal for Numerical Methods in Engineering.* 2:45–59. 1970.

[48] R. Thompson and T. Gray. "Analytic diffraction corrections to ultrasonic scattering measurements". In D. O. Thompson and D. E. Chimenti. editors. *Review of Progress in Quantitative Non-Destructive Evaluation.* volume 2A. pages 567–586. Plenum Press. New York. 1983.

[49] N. Tschoegl. *The Phenomenological Theory of Linear Viscoelastic Behavior: An Introduction.* Springer-Verlag. Heidelberg. Germany. 1989.

[50] V. Uhlendorf. K. Richmann. and W. Berger. "Ultrasonic absorption and velocity measurements at mW peak power level in the range 50-500MHz with variable pathlength cell". *Journal of Physics E.* 18:151-157. 1985.

[51] A. Williams. "The piston source at high frequencies". *Journal of the Acoustical Society of America.* 23(1):1-6. January 1951.

[52] A. Williams. "Integrated signal on circular piston receiver centered in a piston beam". *Journal of the Acoustical Society of America.* 48(1):285-289. January 1970.

[53] G. Williams and D. Watts. "Non-symmetrical dielectric relaxation behavior arising from a simple empirical decay function". *Transactions of the Faraday Society.* 66:80-85. 1970.

[54] M. Wismer and R. Ludwig. "An explicit numerical time domain formulation to simulate pulsed pressure waves in viscous fluids exibiting arbitrary frequency power law attenuation". *IEEE Transactions on Ultrasonics. Ferroelectrics and Frequency Control.* 42(6):1040-1049. Nov. 1995.

[55] J. Wu. "Determination of velocity and attenuation of shear waves using ultrasonic spectroscopy". *Journal of the Acoustical Society of America.* 99(5):2871-2875. 1996.

[56] T. Xue. *Finite Element Modeling of Ultrasonic Wave Propagation with Application to Acoustic Microscopy.* Doctoral dissertation. Iowa State University. Ames. Iowa. 1996.

[57] T. Xue. W. Lord. and S. Udpa. "Numerical analysis of the radiated fields of ultrasonic transducers". *Journal of Nondestructive Evaluation.* 14(3):137-147. 1995.

[58] T. Xue. W. Lord. and S. Udpa. "Transient fields of pulsed transducers in solids". *Research in Nondestructive Evaluation.* 7:31-53. 1995.

[59] T. Xue. W. Lord. and S. Udpa. "Numerical analysis of the radiated fields of circular pistons and time-delay spherically focused arrays". *IEEE Transactions on Ultrasonics. Ferroelectrics and Frequency Control.* 43(1):78-87. Jan. 1996.

[60] Z. You. *Finite Element Study of Ultrasonic Imaging.* Doctoral dissertation. Iowa State University. Ames. Iowa. 1991.

[61] Z. You and W. Lord. "Finite element study of elastic wave interactions with cracks". In D. O. Thompson and D. E. Chimenti, editors, *Review of Progress in Quantitative Non-Destructive Evaluation*, volume 8A, pages 109–116. Plenum Press, New York, 1989.

[62] Z. You, M. Lusk, R. Ludwig, and W. Lord. "Numerical simulation of ultrasonic wave propagation in anisotropic and attenuative solid materials". *IEEE Transactions on Ultrasonics, Ferroelectrics and Frequency Control*, 38(5):436–445, Sept. 1991.

[63] D. Zellouf, Y. Jayet, N. Sint-Pierre, J. Tatibouët, and J. Baboux. "Ultrasonic spectroscopy in polymeric materials: application of the Kramers-Kronig relations". *Journal of Applied Physics*, 80(5):2728–2732, 1996.

IMAGE EVALUATION
TEST TARGET (QA-3)

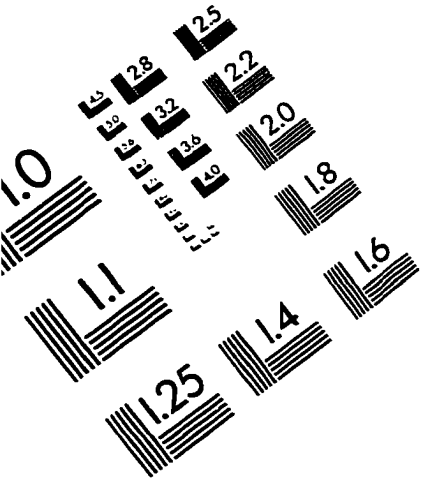

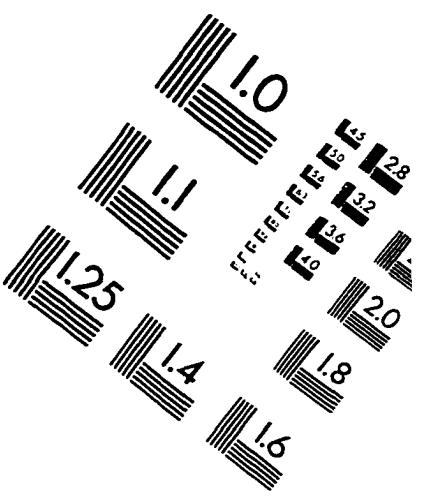

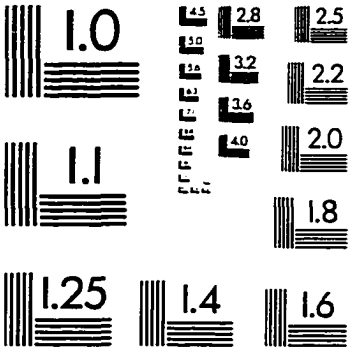

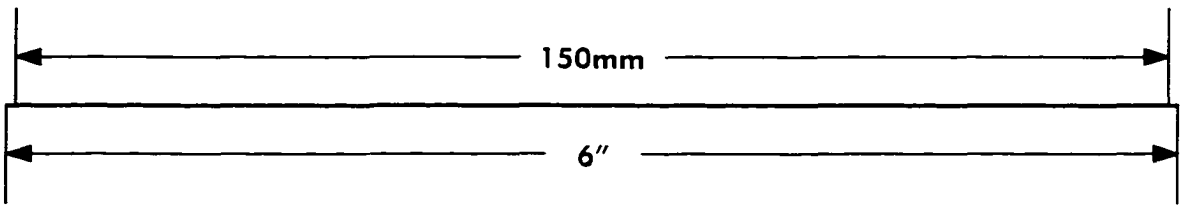

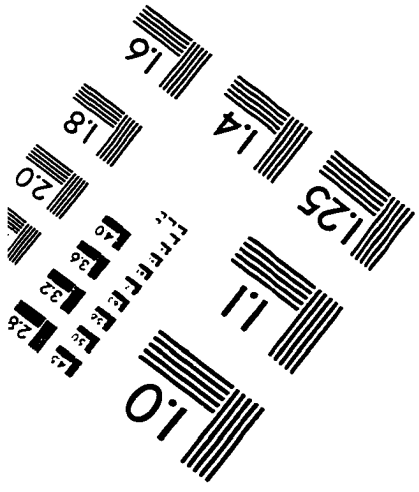

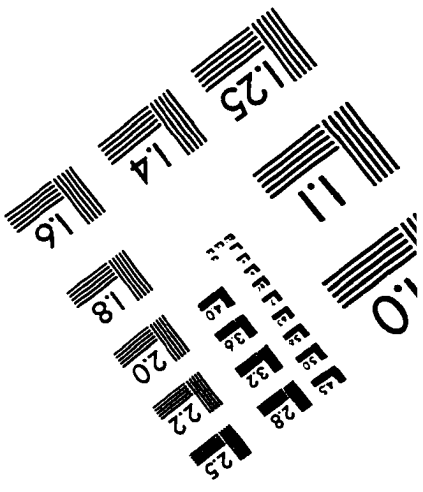

APPLIED IMAGE, Inc
1653 East Main Street
Rochester, NY 14609 USA
Phone: 716/482-0300
Fax: 716/288-5989